DEEP VIRTUAL PION PAIR PRODUCTION

by

Dilini Lakshani Bulumulla
B.S. May 2014, University of Peradeniya, Sri Lanka
M.S. May 2017, Old Dominion University

A Dissertation Submitted to the Faculty of
Old Dominion University in Partial Fulfillment of the
Requirements for the Degree of

DOCTOR OF PHILOSOPHY

PHYSICS

OLD DOMINION UNIVERSITY
August 2023

Approved by:

Charles E. Hyde (Director)

Moskov Amaryan (Member)

Balša Terzić (Member)

Alexander Godunov (Member)

John Cooper (Member)

ABSTRACT

DEEP VIRTUAL PION PAIR PRODUCTION

Dilini Lakshani Bulumulla
Old Dominion University, 2023
Director: Dr. Charles E. Hyde

This experiment investigates the deep virtual production of both $\sigma-$ and $\rho-$ mesons, with a particular focus on the microscopic structure of the σ mesons. While the ρ meson is an ordinary $q\bar{q}$ pair, the σ meson is composed of not only the typical $q\bar{q}$ pair, making it a topic of controversy for nearly six decades. Although the existence of the $\sigma-$ meson is now well-established, its microscopic structure remains poorly understood. The primary objective of this thesis is to contribute to the understanding of the σ meson by analyzing its deep virtual production. The main focus of this study was on the $ep \rightarrow e'p'\pi^+\pi^-$ reaction, which is a crucial process for investigating both the $\sigma-$ and $\rho-$ mesons. Specifically, this reaction is sensitive to the pure glue component of the $\sigma-$ meson's wave function near the threshold in the $\pi\pi-$ system. In order to separate the $\sigma-$ and $\rho-$ meson channels, we analyzed the angular distribution in the $\pi\pi$ rest frame. By focusing on this reaction and employing this technique, we aimed to gain a better understanding of the structure of both the $\sigma-$ and $\rho-$ mesons. The model has developed according to Lehmann-Dronke to understand the $\sigma-$ and $\rho-$ mesons separately. To conduct our experiment, we chose to use the data from the Hall B CLAS12 "Run Group A" with an electron beam energy of 10.6 GeV incident on the LH_2 target. The CLAS12 detector in Hall B has a large acceptance, making it an ideal choice for our study. By using this data, we were able to obtain accurate and reliable measurements of the $ep \rightarrow e'p'\pi^+\pi^-$ reaction and further our understanding of the $\sigma-$ and $\rho-$ mesons.

To Amma, Appachchi, Chanura and my two beautiful daughters, Nathalie and Amelia

ACKNOWLEDGMENTS

I would like to begin by expressing my heartfelt appreciation to my advisor, Prof. Charles E. Hyde, for his unwavering guidance and encouragement throughout my Ph.D. studies. Without his support and motivation, this project would not have come to fruition.

I would also like to extend my gratitude to the rest of my thesis committee - Prof. Moskov Amaryan, Prof. J.W. Van Orden, Prof. Alexander L. Godunov, Prof. Balša Terzić, and Prof. John Cooper - for their invaluable feedback and insights during my annual review.

Furthermore, I am deeply grateful to the CLAS12 Collaboration, the scientists, post-docs, and graduate students I have had the privilege to collaborate with over the past six years. I owe a great debt of gratitude to Dr. Raffaella De Vita, who is the Analysis Coordinator in CLAS12 RG-A and, Dr. Derek Glazier, who is the coordinator of the CLas12root analysis package, who provided me with their expertise and assistance during the analysis. Special thanks also go to Dr. Latifa Elouadrhiri, whose guidance and encouragement were instrumental to the success of this experiment.

I am particularly indebted to Dr. Mac Mestayer, with whom I worked on the Drift Chamber Calibration project over the past five years. His flexibility, sense of humor, and dedication to our work made it a truly enjoyable experience. I would also like to thank the DC Group, especially Dr. Taya Chetry, Dr. Florian Hauenstein, with whom I collaborated on the DC Calibration project and Caleb Fogler, who has been my calibration partner over the last four years for, the teamwork and collaboration.

I would like to acknowledge all the professors and classmates in the Physics Department at Old Dominion University, as well as the Operations Manager, Ms. Lisa Okun, for her unwavering support throughout my journey at ODU. I would like to express my gratitude to all my friends and family in Sri Lanka for their continuous support since my first day in the USA. A special thanks go to Jayendrika Tiskumara and Amali Premathilaka, who have always been there for us whenever we needed them. Most importantly, I would like to thank my loving parents for their unwavering love and encouragement. Without their support, this accomplishment would not have been possible. Finally, I want to express my deepest gratitude to my partner, Chanura, for being my rock through all the ups and downs. Your patience and unwavering support have given me the strength to see this through. And last but not least, to my two little daughters, Nathalie and Amelia, who have been the light of my life over the past five years and who have given me the extra strength and motivation to accomplish this feat.

TABLE OF CONTENTS

Page

Chapter

APPENDICES

LIST OF TABLES

Table Page

LIST OF FIGURES

Figure Page

CHAPTER 1

INTRODUCTION

The atom is the fundamental unit of matter, which defines an element's structure. Originally, the word "atom" came from the Greek word meaning indivisible, as they were thought to be the smallest things in the universe. Later research discovered that atoms consist of three particles: electrons, protons, and neutrons. In 1897, J.J. Thompson discovered the electron, a structure-less particle whose interaction with matter can be described by Quantum Electrodynamics (QED). The proton was discovered in 1919 by E. Rutherford, and the neutron in 1932 by J. Chadwick. In a nuclear atom, protons and neutrons are collectively referred to as nucleons. In addition, there are even smaller particles called "quarks," which are elementary particles that makeup matter. A proton consists of two "Up" quarks (each with a 2/3 positive charge) and one "Down" quark (with a 1/3 negative charge). Neutron consists of two "Down" quarks and one "Up" quark. Other subatomic particles, known as gluons, hold the quarks together. Quantum Chromodynamics (QCD) describes the strong interaction between quarks via the exchange of gluons and is responsible for keeping nucleons and nuclei together.

The famous QCD Lagrangian [1] describes the information about the dynamic of the system. The Lagrangian can be represented as:

$$\mathcal{L} = -\frac{1}{4}\mathrm{Tr}\left[G_{\mu\nu}G^{\mu\nu}\right] + \sum_{f} \bar{\psi}_f (i\partial\!\!\!/ + gA\!\!\!/ - m_f)\psi_f, \tag{1}$$

where :
$\bar{\psi}_f$: Quark-field spinors for a quark flavor,
$G^{\mu\nu}$: Gluon field tensor,
$A\!\!\!/$: Gauge covariant derivative,
m_f: Quark mass of flavor f.

The QCD Lagrangian has a short form separating the terms for gluons and quarks: ($\mathcal{L} = \mathcal{L}_g + \mathcal{L}_q$). Accordingly, in Eq. (1), the first term represents the gluon term, in which gluons interact with each other, and their self-interaction is represented by the gluon field tensor and the second term represents the quark contribution, including quark-gluon interactions.

Depending on the distance between quarks or equivalently their interaction energy, the q-q interaction potential will vary. The strong coupling constant (α_S) parameterizes the strength of the interaction between quarks and gluons.

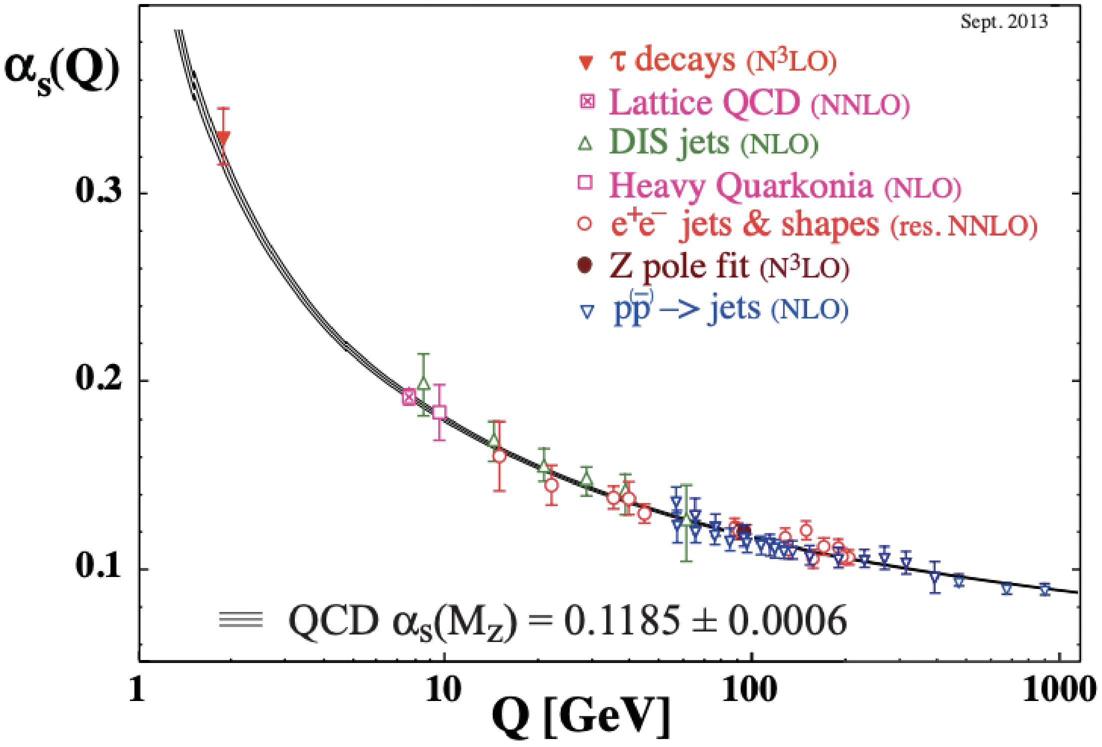

FIG. 1. The Strong coupling constant (α_s) as a function of energy scale Q (GeV). Various results provide a very precise and stable world average value of $\alpha_s(M_Z^2)$ consistent with QCD predictions of Asymptotic Freedom, as well as a clear indication of the energy dependence of α_s [2].

Fig. 1 clearly illustrates that the strong coupling constant (α_s) depends on the energy scale Q (GeV). Two important factors that lead to the strong coupling constant (α_s), Asymptotic freedom and confinement. Essentially, asymptotic freedom refers to fact that at very short distances ($\ll$ hadron size $\approx 10^{-15}$ m), interactions between quark and gluon become very small [1] (See Fig. 1), which leads to the existence of free quarks and gluons inside the hadrons. Quarks and gluons (called partons) are the relevant degrees of freedom at short distances, and their interactions may be explained very well by perturbative quantum chromodynamics (pQCD).

Then confinement refers that at very large distances ($\geq$ hadron size $\approx 10^{-15}$m) interactions between quarks and gluons become very large (α_s increases), thereby making it impossible to isolate gluons and quarks, which means it is impossible to directly observe color-charged particles (such as q and g). Since quarks and gluons clump together into hadrons as elementary particles, understanding QCD in confinement regime presents a significant challenge. Additionally, gluons are also consistent with confinement as the form of glueballs, but this is harder to identify experimentally. Even though that QCD explains as much as possible about the interaction of nucleon constituents, we need to continue to strive for a deeper understanding. There are many unanswered questions regarding the nucleon and other hadrons, one of which is how the nucleon is built from quarks and gluons. Even if there is a lack of analytical information for this question and many other questions (how does the interior of the nucleons look like?, how much of nucleon spin is carried by quarks and gluons? etc.), experimental advances and nucleon structure play a main role of understanding the nucleon of the system.

Various hard reactions can produce small-size configurations of quarks and gluons, including Deep Inelastic Scattering (DIS), Semi-inclusive DIS, Drell-Yan Process, and hard exclusive reactions [1]. Moreover, there is an essential characteristic of hard-reactions: they can be separated into perturbative and non-perturbative phases. In QCD, this feature is called the factorization property, which can be explained with the factorization theorem [3]. As mentioned before, hard reactions enable us to create small-size quark and gluon configurations and describe them in terms of perturbative quantum mechanics because of their asymptotic freedoms. The non-perturbative stage describes the reaction of a specific hadron to a given configuration [1].

The hard exclusive reaction, which is the heart of this dissertation work, provides us with a way to study nucleon structure. The hard exclusive reaction types are as follows [1]:

$$\gamma^*(q) + T(p) \to \gamma(q') + T'(p'), \qquad \gamma^*_L(q) + T(p) \to M(q') + T'(p'). \tag{2}$$

The above two reactions (Eq. (2)) explain a photon γ^* with high energy and large virtuality ($Q^2 \gg M_N^2$) scatters off the hadronic target T and produces a real photon γ or a meson

(M) and a low mass hadronic Target T'. It is relevant to these two reactions Eq. (2) to use Deep Virtual Compton Scattering (DVCS) and Deep Virtual Meson Production (DVMP) processes, as in DVCS, the electron scatters off a quark by exchanging a virtual photon with the quark, which then absorbs the virtual photon, which then emits a real photon when the parent nucleon reabsorbed the quark. DVMP is also performed similarly to DVCS. However instead of emitting a real photon, DVMP emits a meson as the final product. These DVCS and DVMP processes have shown to be effective in evaluating hadronic structure over the past decade since they allow us to access the three-dimensional structure of hadrons.

Detailed information about the structure of nucleons is contained in the Generalized Parton Distributions (GPDs). Through Deep Virtual Compton Scattering and Deep Virtual Meson Production, we can precisely measure the GPDs of a nucleon and systematically explore its quark structure. To extract information about the quark structure of nucleons (GPD), clear and comprehensive approaches are needed. Since we selected high Q^2 and high W^2 region (where the "handbag" diagram dominates) for this thesis to looked at the hard exclusive meson production. The 12 GeV upgrade of Thomas Jefferson Lab is to explore the internal structure of the nucleon at a resolution scale $< 10^{-15}$ m. There has been an exciting development in hadronic research in Hall B as the physics program in CLAS12 (Cebaf Large Acceptance Spectrometer at 12 GeV) has opened up a new avenue. This project will provide complementary measurements for analyzing proton structure for both ground and excited states, as well as 3D imaging and gluonic excitation. The project's core objective is to comprehend how strong forces unify protons and how the dominant mass of hadrons emerges. From 2017 to 2019, the CLAS12 Run Group-A (RG-A) collected data (139 "PAC" days), starting with the engineering run in the Winter of 2017 and collecting more data in the Spring of 2018, Fall of 2018, and Spring of 2019. It is anticipated that all of these data will significantly impact the field of hadronic science as they are analyzed.

As part of the CLAS12 service, I participated in the DC Monitoring Project, DC Calibration Project (see Appendix C), DC Fault Finder Project, and analyzed the data as part of my thesis. The main goal of this thesis project is to understand deep virtual production of the ρ and σ mesons in high Q^2 (photon virtuality) and high W^2 (Center of mass energy) range. This document is organized as follows:

The first chapter lays the theoretical frameworks and background of the nucleon structure in the partonic picture. The introduction part describes the evaluation of particle physics and continues the chapter from electron scattering to the deep virtual era by including reaction kinematics and various kinematics quantities.

The second chapter represents an outline of the apparatus of the CLAS12 detector. This chapter includes the overview of the standard Hall B CLAS12 equipment setup, CLAS12 experiments parameters, CLAS12 Simulation and Reconstruction Software, and Data Processing.

Chapter three of this thesis is centered around the analysis framework. Specifically, it covers particle identification methods, with a particular focus on the Event Builder. The chapter also provides different identification methods for electrons, protons, pi-plus, and pi-minus particles.

The fourth chapter describes the Monte-carlo generator that we produced, and the separate section describes the radiative correction part added to that generator.

Chapter five of this thesis pertains to the analysis of a specific type of event selection process, namely, the selection of exclusive $ep \rightarrow ep\pi^+\pi^-$ events from the available data. The chapter offers a detailed description of the topology that was employed in the analysis, in addition to outlining the various cuts made for particle identification and event selection purposes.

Furthermore, the chapter six includes a separate computation of the tracking efficiency, specifically for the forward detector (FD) and central detector (CD).

Chapter seven of the thesis pertains to cross-section analysis. Specifically, the chapter describes the extracted cross-section, the cross-section model used in the analysis, and the final cross-section results obtained from the study.

Chapter eight of my thesis represents my final conclusion based on our research.

The Appendix section of this thesis covers several important calculations that are relevant to the topic at hand. Additionally, it includes a description of service projects to which I have contributed, as well as my own attempts at particle identification.

1.1 ELECTRON-PROTON SCATTERING

Studying nucleons and hadrons through electron-proton scattering is one of the basic methods of determining their structure. It can be interpreted as a beam of an electron with energy E is scattered from a stationary proton with mass M. There are two types of scattering.

- Elastic Scattering - Outgoing protons remain intact; this process dominates at low energies.

- Inelastic Scattering - The proton that is being scattered is in an excited state (a different mass) or has been broken up into fragments. This process is known as “Deep Inelastic Scattering” at high Center-of-Mass energies.

1.1.1 ELASTIC SCATTERING

Among the processes that dominate at low energies is the elastic electron-proton scattering ($e + p \to e + p$), in which the outgoing proton remains intact. A famous gold foil experiment [4] was conducted by Rutherford in 1911, which demonstrated that the atom had a heavy nucleus. Using a point-like target and non-relativistic electron, Rutherford calculated the cross-section of the interaction, $\beta_e \gamma_e \ll 1$. The Rutherford cross-section is as follows:

$$\left(\frac{d\sigma}{d\Omega}\right)_{Rutherford} = \frac{\alpha^2}{4E^2 \sin^4\left(\frac{\theta}{2}\right)}, \tag{3}$$

where α is the QED fine structure constant, E is the energy of the incident particle, and θ is the angle of the scattered electron. In order to derive the Rutherford cross-section in Eq. (3), one must consider the scattering of non-relativistic electrons in the static coulomb potential of protons $V(r) = \frac{\alpha}{r}$. Therefore, only the Coulomb interaction contributes significantly, not the magnetic (spin-spin) interaction. Rutherford cross-section Eq. (3) can be modified as Mott cross-section in electron-proton scattering since electrons behave relativistically (but proton recoil can still be neglected), according to Eq. (4). Again this can be written as follows:

$$\left(\frac{d\sigma}{d\Omega}\right)_{Mott} = \frac{\alpha^2}{4E^2 \sin^4\left(\frac{\theta}{2}\right)} \cos^2\left(\frac{\theta}{2}\right). \tag{4}$$

There was a discrepancy between Rutherford’s (Eq. (3)) and Mott’s (Eq. (4)) cross-section formulae, which assume that the target is point-like and spin-less, which is not in good agreement with the experimental result. For non-point-like and spin-less (extended) target, the Mott scattering cross-section formulae of Eq. (4) has to be modified as in Eq. (5) [5]. In this Eq. (5), the extended proton charge distribution is taken into account:

$$\left(\frac{d\sigma}{d\Omega}\right)_{Mott} \to \frac{\alpha^2}{4E^2 \sin^4\left(\frac{\theta}{2}\right)} \cos^2\left(\frac{\theta}{2}\right) |F(q^2)|^2, \tag{5}$$

where $F(q^2)$ is the three-dimensional Fourier transform of the charge distribution.

The kinematics of electron elastic scattering at the rest of a proton target can be visualized as shown in Fig. 2. Virtuality of the exchange photon can be described as the negative of q^2, defined in Eq. (6), which is always positive. In the ultra-relativistic limit for the electron:

$$Q^2 = -q^2 \to 4EE' \sin^2\left(\frac{\theta}{2}\right) > 0. \tag{6}$$

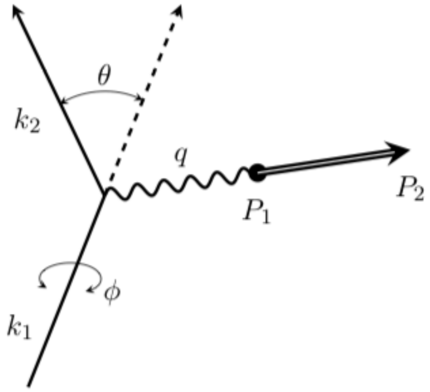

FIG. 2. This diagram illustrates the kinematics of elastic scattering that occurs between an electron and a rest proton on a target. Where: $k_1 = (E_1 = E, \overrightarrow{p}_1)$ represents the four-momentum of the incident electron, $k_2 = (E_2 = E', \overrightarrow{p}_2)$ represents the four-momentum of the scattered electron, $P_1 = (M, 0)$ is the target proton and P_2 is the recoil proton. The four-momentum of the exchanged photon is q. Virtuality of the exchange photon can be defined as the negative of q^2. Thus $Q^2 = -q^2 = -(k_2 - k_1)^2$. Here θ is the electron-scattering angle. For unpolarized scattering, the cross-section is independent of ϕ the azimuthal angle of $\overrightarrow{p}_2$).

For low Q^2, the form factor $F(Q^2)$ represents, via a Fourier transform, which describes how different the nucleon is from a point-like particle. Two form factors exist for the elastic electron scattering of spin 1/2 particles; one enables the proton's spin state to remain the same at all times, and the other allows the spin state to flip during the scattering process. In this context, Dirac and Pauli forms factors are defined as $F_1(Q^2)$ and $F_2(Q^2)$, respectively. By calculating the following matrix element (Eq. (7)) of the electromagnetic current, we can determine $F_1(Q^2)$ and $F_2(Q^2)$:

$$\langle p'|j^{\mu}(0)|p\rangle = \bar{N}(p')\left(F_1(Q^2)\gamma^{\mu} + F_2(Q^2)\frac{i\sigma_{\mu\nu}q^{\nu}}{2M_N}\right)N(p), \tag{7}$$

where N and $\bar{N}$ are the initial and final nucleon spinors, M_N is the nucleon mass and j^{μ} is the electromagnetic current. $F_1(Q^2)$ and $F_2(Q^2)$ are the Dirac and Pauli form factors respectively. $F_1(Q^2)$ is related to the charge distribution of the nucleon, and $F_2(Q^2)$ is related to the magnetic moment of the nucleon. Once $Q^2 \to 0$ (corresponding to the exchange of low virtuality photons), we have the following relations between the neutron and proton:

$$F_{1p} = 1, \qquad F_{2p} = \kappa_p, \qquad F_{1n} = 0, \qquad F_{2n} = \kappa_n, \tag{8}$$

where $\kappa_p = \mu_p - 1$ and $\kappa_n = \mu_n$ are the anomalous magnetic moment of proton and neutron, respectively, with $\mu_p = 2.7928$ and $\mu_n = -1.9130$ in the units of nucleon magnetons [6]: It is possible to express these $F_1(Q^2)$ and $F_2(Q^2)$ form factors in terms of electric and magnetic Sachs form factors [7],

$$G_E(Q^2) = F_1(Q^2) - \frac{Q^2}{(2M_N)^2} F_2(Q^2), \tag{9}$$

$$G_M(Q^2) = F_1(Q^2) + F_2(Q^2). \tag{10}$$

These equations are valid for both protons and neutrons (with their respective form factors). In the limit of $Q^2 \to 0$, the Sachs form factors are

$$G_{Ep}(0) = 1, \qquad G_{Mp}(0) = \mu_p, \qquad G_{En}(0) = 0, \qquad G_{Mn}(0) = \mu_n. \tag{11}$$

The Rosenbluth formula describes the differential elastic scattering cross-section for electron-proton scattering in terms of electric and magnetic form factors, G_E and G_M as follows:

$$\frac{d\sigma}{d\Omega} = \frac{\alpha^2}{4E^2 \sin^4\left(\frac{\theta}{2}\right)} \frac{E'}{E} \left(\frac{G_E^2 + \tau G_M^2}{1+\tau} \cos^2\left(\frac{\theta}{2}\right) + 2\tau G_M^2 \sin^2\left(\frac{\theta}{2}\right) \right), \tag{12}$$

with $\tau = \frac{Q^2}{4M^2}$. By introducing the degree of polarization of the virtual photon $\epsilon = (1 + 2(1 + \tau)\tan^2\left(\frac{\theta}{2}\right))^{-1}$, we can simplify Rosenbluth formulae (see Eq. (12)):

$$\frac{d\sigma}{d\Omega} = \left(\frac{d\sigma}{d\Omega}\right)_{Mott} \frac{\epsilon G_E^2 + \tau G_M^2}{\epsilon(1+\tau)} = \frac{\tau}{\epsilon(1+\tau)} \left(\frac{\epsilon G_E^2}{\tau} + G_M^2 \right). \tag{13}$$

It is now clear that Sachs form factors eliminate mixed terms from the cross-section term and only depend on the square of G_E, and G_M. To extract the form factors of measured cross-sections, the Rosenbluth separation is usually used [7]. The world data for G_{Ep} and G_{Mp} obtained from the Rosenbluth separation can be found in Fig 3. The results for the Rosenbluth separation were calculated in the 1970s as ratios of G_{Ep}/G_D and $G_{Mp}/\mu_p G_D$. G_D is the dipole form factor, which is given below by Eq. (14). As we can see, these ratios appear to be closer to one but decrease with an increase in Q^2:

$$G_D = \frac{1}{(1 + Q^2/0.71\text{GeV}^2)^2}, \tag{14}$$

The extraction of electric form factor G_E becomes very problematic for the high Q^2 range. This could be based on several reasons; one obvious reason is, $\frac{1}{\tau}$ term in front of

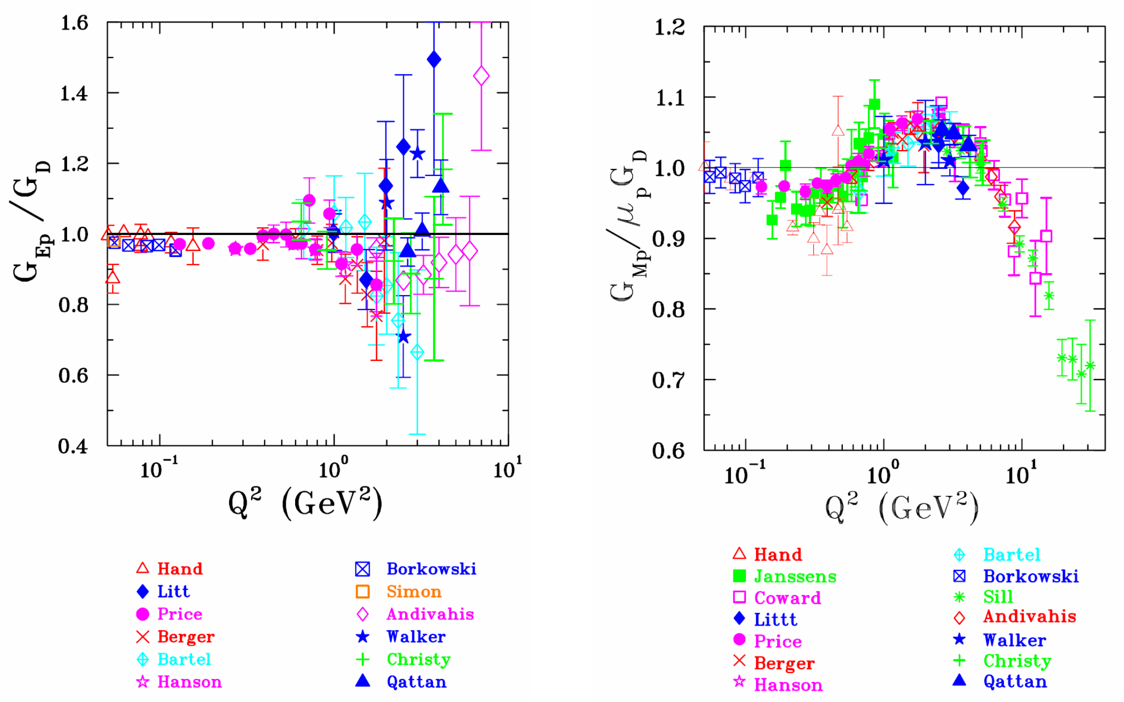

FIG. 3. World data for G_{Ep} (left) and G_{Mp} (right) were obtained by the Rosenbluth separation method [8].

G_E (see Eq. (13)), automatically reduce the cross-section as Q^2 increases; and second, even at small Q^2 taking into account that $G_M^2 \sim \mu_p^2 G_E^2$, we can see that the term with G_E^2 is reduced by the factor of $\mu_p^2 = 7.8$ [8]. The measurements of G_E at large Q^2 can be refined by scattering longitudinally polarized electrons and analyzing the recoil polarization of the scattered protons. It has been demonstrated at the Thomas Jefferson National Accelerator Facility in Virginia (JLab) that such polarized beam of electrons scattering experiments are practically the same [9, 10]. In their study, the proton form factor ratio was found to be clearly deviating from unity with a small statistical error as compared to previous measurements. Fig. 4 shows the e.m FF ratio (G_E/G_M) for the polarization experiments together with the Rosenbluth separation. Further, JLab Hall A and Hall C have repeated the same unpolarized experiments [11, 12], respectively and their results are shown in Fig. 4 as open and filled triangles. See more details in reference [8].

1.1.2 DEEP INELASTIC SCATTERING (DIS)

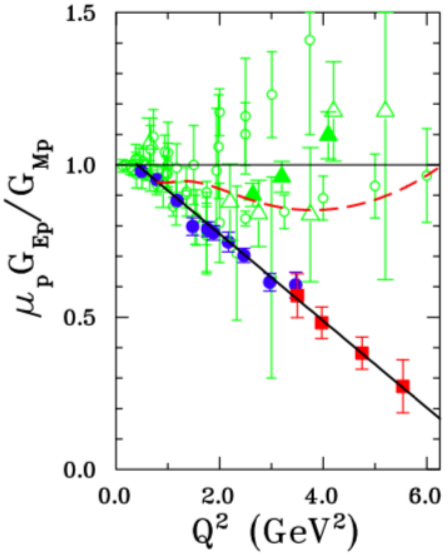

FIG. 4. Comparison of electro-magnetic form factor ratio from two Jlab polarization experiments referenced in [9, 10], and Rosenbluth separation. The dashed curve is a re-fit of Rosenbluth data, including an estimate of two-photon exchange effects [8].

For high-energy electron-proton scattering, most of the scattering occurs at inelastic energy levels. For inelastic scattering $e^-p \to e^-X$, shown in Fig 5, a hadronic final state resulting from break-ups of the proton into small units which are difficult to measure all at once. For this case, we can introduce four more variables in addition to the previous section, 1.1.1. Those are:

- the energy exchange of virtual photon: $\nu = \frac{q \cdot P}{M} \to E - E'$ (Target rest frame).
- the invariant mass W of the hadronic final state

$$W^2 = (P+q)^2 = (M^2 + 2P \cdot q - Q^2) \quad \Leftrightarrow \quad W^2 - M^2 = 2P \cdot q + q^2, \tag{15}$$

  - $W^2 = M^2$ for the elastic case;
  - $W^2 \gg M^2$ for the highly inelastic case;

- $x = \frac{Q^2}{2P \cdot q}$: Bjorken-$x$ variable. In DIS, this longitudinal momentum fraction of the struck quark in the nucleon.

  - ○ x is always in the range $0 \leqslant x \leqslant 1$;
  - ○ $x = 1$ for the elastic case;
  - ○ $x < 1$ for the inelastic regime.
- $y = \frac{P \cdot q}{P \cdot k}$: the fractional energy transfer from the electron to the nucleon

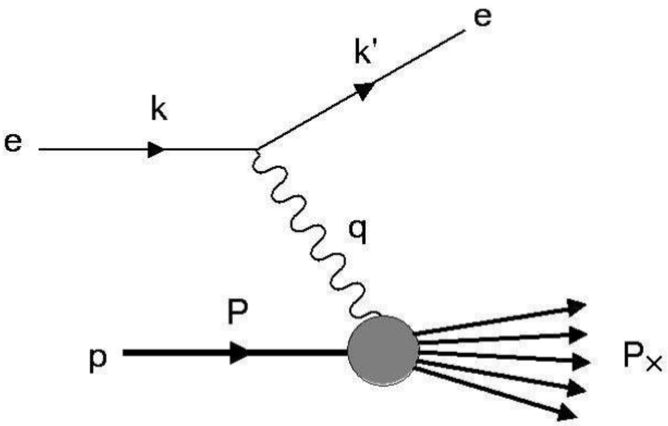

FIG. 5. The diagram demonstrating the kinematics of deep inelastic scattering, $e^- p \to e^- X$, where k is the four-momentum of the incident electron, k' is the four-momentum of the scattered electron, and q is the four-momentum of the exchanged virtual photon. This figure is referenced from [13].

If the electron-proton scatters at large momentum transfer Q^2, the proton has a high probability of break-up into small parts and the final hadronic state is very complicated, then this process is named as "Deep ($Q^2 \gg M^2$) Inelastic ($W^2 \gg M^2$) Scattering" (DIS). The Deep inelastic regime is generally defined as $Q^2 > 1$ GeV^2 and $W^2 > 4$ GeV^2. As a result of these conditions, the nucleon's internal structure can be explored at a high enough resolution. This $W^2 > 4$ GeV^2 regime excludes the region of elasticity and inelastic scattering to well-isolated nucleon resonances. The inclusive differential cross-section for DIS can be written as follows:

$$\frac{d^2\sigma}{d\Omega d\nu} = \frac{1}{2M}\frac{E'}{E}|\mathcal{M}|^2, \tag{16}$$

where:

$$|\mathcal{M}|^2 = \frac{\alpha^2}{q^4} L_{\mu\nu} T^{\mu\nu}, \tag{17}$$

Here $L_{\mu\nu}$ and $T^{\mu\nu}$ are the leptonic and hadronic tensors, respectively. Fig. 6 shows the interaction at the leptonic vertex and the hadronic vertex corresponds to the forward limit of the optical theorem [1]. The leptonic ($L_{\mu\nu}$) tensor and hadronic ($T^{\mu\nu}$) tensor can be described as following equations:

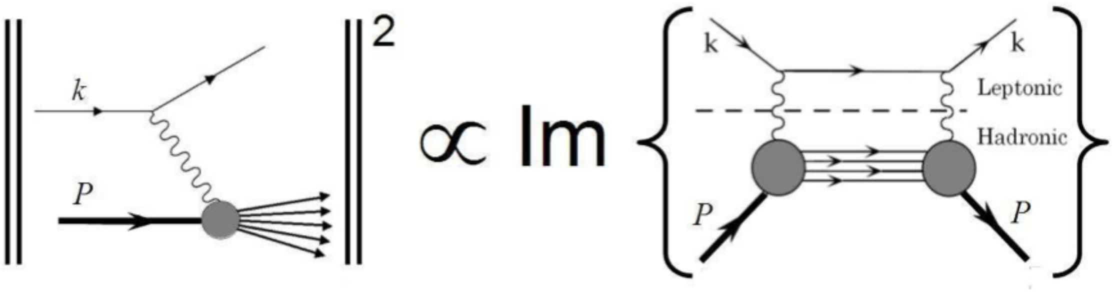

FIG. 6. A diagram depicts the optical theorem that relates the squared amplitude $|\mathcal{M}|^2$ of the DIS process with the imaginary part of the forward scattering amplitude. The leptonic tensor represents the upper part, and the hadronic tensor represents the lower part of the right picture respectively. This figure was taken from Ref. [13].

$$L^{\mu\nu} = \frac{1}{2}Tr[(\not{k}' + m_e)\gamma_\mu(\not{k} + m_e)\gamma_\nu] = 2(k'_\mu k_\nu + k'_\nu k_\mu - (k \cdot k' - m_e^2)). \tag{18}$$

The hadronic tensor can be expressed as the Fourier transform of the forward matrix element

---

[1] The optical theorem relates the imaginary part of the forward scattering process to the total cross-section.

of two electromagnetic currents at two separate points

$$T^{\mu\nu} = \frac{1}{4\pi}\sum_{spins}\int d^4 z e^{iq\cdot z} < p|J^{\mu}(z)J^{\nu}(0)|p >, \tag{19}$$

where J^{μ} is the quark electromagnetic current at the space-time z and can defined as:

$$J^{\mu}(z) = \sum_i Q^i \bar{q}_i(z)\gamma^{\mu}q^i(z), \tag{20}$$

with i as the quark flavor, Q as its charge, and $(\bar{q}, q)$ as the quark field. The hadronic tensor Eq. (19) can be decomposed as [14]:

$$T^{\mu\nu}(p,q) = \left(-g^{\mu\nu} + \frac{q^{\mu}q^{\nu}}{q^2}\right)W_1(\nu,q^2) + \frac{1}{M^2}\left(p^{\mu} - \frac{p\cdot q}{q^2}q^{\nu}\right)\left(p^{\nu} - \frac{p\cdot q}{q^2}q^{\nu}\right)W_2(\nu,q^2). \tag{21}$$

The structure functions of the nucleon are represented by $W_{1,2}(\nu, q^2)$. By applying current conservation in the leptonic tensor, $q_{\mu}L^{\mu\nu} = q_{\nu}L^{\mu\nu} = 0$, all $q_{\mu,\nu}$ terms are suppressed and we can get final effective formula for the hadronic tensor:

$$T^{\mu\nu}(p,q)_{eff} = -W_1(\nu,q^2)g^{\mu\nu} + \frac{W_2(\nu,q^2)}{M^2}p^{\mu}q^{\nu}. \tag{22}$$

The Eq. (23) shows that the unpolarized cross-section depends on two independent variables, q^2 and ν

$$\frac{d^2\sigma}{d\Omega d\nu} = \frac{\alpha^2}{4E^2\sin^4\left(\frac{\theta}{2}\right)}\frac{E'}{E}\left(W_2\cos^2\left(\frac{\theta}{2}\right) + 2W_1\sin^2\left(\frac{\theta}{2}\right)\right). \tag{23}$$

The $W_{1,2}(\nu, Q^2)$ structure functions, which involve elastic electron scattering off the proton's point-like constituents, can be expressed using the spin-independent structure functions F_1 and F_2 [2]. The Callan-Gross relation links F_1 and F_2, stating that $2xF_1(x) = F_2(x)$. This relation is valid only when the proton's only point-like constituents are spin-1/2 fermions.

$$\begin{aligned} W_1(\nu,Q^2) &= \sum_q e_q^2\frac{q(x)}{M} \equiv \frac{1}{M}F_1(x), \\ W_2(\nu,Q^2) &= \sum_q e_q^2 xq(x) \equiv F_2(x), \end{aligned} \tag{24}$$

where $x = x_B = \frac{Q^2}{2M\nu}$ is the Bjorken variable, e_q is the quark charge, and $q(x)$ is the parton distribution function which describes the probability that the struck parton q carries a fraction x of the proton's longitudinal momentum p [14]. In Fig. 7, the F_2 structure function

---

[2] These F_1 and F_2 are different from elastic Dirac and Pauli form factors in Eq. (9) and Eq. (10)

for the proton is plotted for Q^2 for different values of x, for various fixed target experiments, and the "HERA" results. A picture of the phenomenon appears below, illustrating that at high x values, the structure-function F_2 does not vary with Q^2, a phenomenon known as Bjorken scaling. Nevertheless, the scaling property is violated as x decreases below ~ 0.1 due to the evolution of structure functions caused by gluon radiation. More and more gluons are radiated as Q^2 increases which in turn split into $q\bar{q}$ pairs, leading to the growth of the gluon and the $q\bar{q}$ sea quark density with increasing Q^2 at low x. This result is expected in QCD and calculated using DGLAP [3] equations [15].

If the beam and target are longitudinally polarized, the difference in cross-section under reversal of the electron and nucleon spin projections allows the measurement of the polarized structure functions: g_1 and g_2 [14]

$$\begin{aligned} g_1(x) &= \frac{1}{2}\sum_q e_q^2 \Delta q(x), \\ \Delta q(x)(x) &= q_+(x) - q_-(x), \end{aligned} \tag{25}$$

where $q_\pm(x)$ are spin-dependent parton distribution functions whose spin orientations are parallel and anti-parallel to the longitudinal spin of the nucleon. In the case of unpolarized cross-section $q(x) = q_+(x) + q_-(x)$ (see Eq. (24)). The structure-function $g_2(x)$ does not have a simple probabilistic interpretation. It is related to a quark-gluon correlation inside the nucleon.

Whenever a nucleon approaches light speed in a particular direction, x is the longitudinal momentum fraction carried by the quark, which absorbs the virtual photon in a DIS event. Therefore, the parton distribution function (PDF) describes the probability of finding partons (quarks and gluons) in a hadron following their fractions of proton momentum. According to this PDF formalism, partons in a fast-moving nucleon have a longitudinal momentum distribution and a spin distribution, but their transverse momentum distributions are assumed to be confined to values $\ll \sqrt{Q^2}$ and are integrated over in the scattering process. In the DIS process, the soft structure function (long-distance, "soft" structure of the nucleon-QCD factorization) is the well-known unpolarized and polarized PDFs, $q(x)$ and $\Delta q(x)$, respectively. These PDFs are obtained as one-dimensional Fourier transforms in the

---

[3] Dokshitzer, Gribov-Lipatov, Altarelli-Parisi.

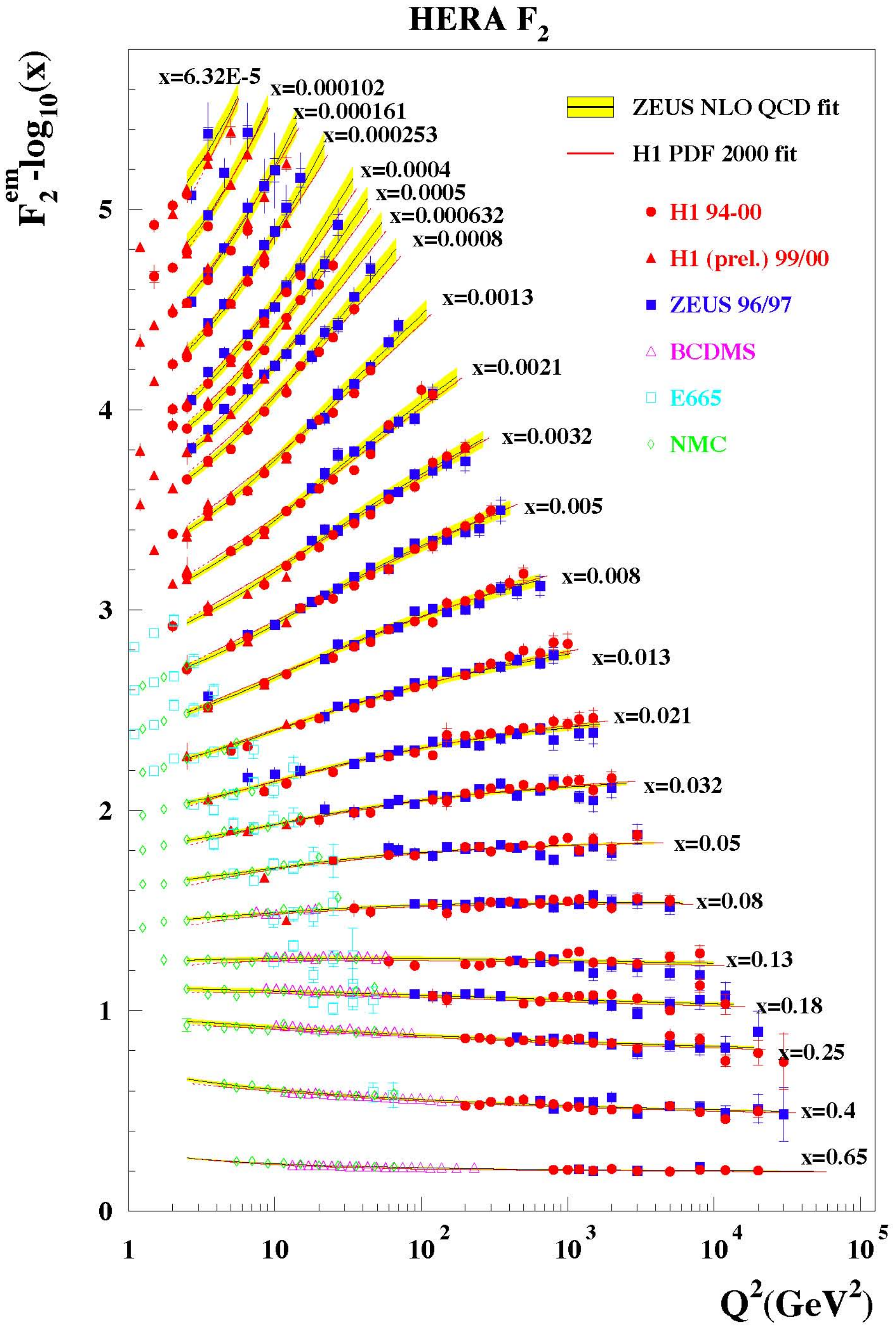

FIG. 7. A diagram depicting the F_2 structure function of the proton as a function of Q^2 for different values of x. There is a combination of measurements from the fixed target experiment as well as the HERA results [16].

light-like variable $y^- = (y^0 - y^3)/\sqrt{2}$ (at zero values of the other coordinates) as [17]:

$$\begin{aligned} q(x) &= \frac{p^+}{4\pi}\int dy^- e^{ixp^+y^-} < p|\bar{\psi}_q(0)\gamma_+\psi_q(y)|p > \Big|_{y^+=\overrightarrow{y}_\perp=0}, \\ \Delta q(x) &= \frac{p^+}{4\pi} dy^- e^{ixp^+y^-} < pS_\parallel|\bar{\psi}_q(0)\gamma_+\gamma^5\psi_q(y)|pS_\parallel > \Big|_{y^+=\overrightarrow{y}_\perp=0}, \end{aligned} \tag{26}$$

where, ψ_q quark field of flavor q, p is the initial and final state nucleon momentum: In the DIS case, the initial and final momentum are the same due to the optical theorem, $S_\parallel$ is the longitudinal projection of nucleon spin, and p^+ is the light-cone four-momentum. Once defined the vector $p^\mu = (p^0, p^1, p^2, p^3)$, then light-cone components are defined by $p^\pm \equiv (p^0 \pm p^3)/\sqrt{2}$ and $p_\perp = (p^1, p^2)$. The Eq. (26) is called "non-local" matrix element since the two quark fields are at different space-time points. A further advantage is that the DIS process can be easily described in a reference frame where the virtual photon and the target nucleon are anti-collinear along the z-axis (light-front frame). It is possible to extract PDFs over a large x using data from targets such as JLAB and COMPASS, as well as from collider experiments like HERA. As x increases, valence quark distributions dominate, and sea quark contributions dominate as x decreases. The property is illustrated in Fig. 8 at $Q^2 = 20$ GeV^2 and $Q^2 = 10,000$ GeV^2. Fig. 8 shows good agreement with the QCD prediction and the data to extract the PDF [14]. The PDFs are extracted by fitting the data to F_2. The elastic form factors and the deep inelastic structure functions by themselves cannot give a full understanding of the nucleon's structure. Through the investigation of exclusive electroproduction processes, scientists have discovered a new avenue for study of nucleons. This will be discussed in the following section 1.2.

1.2 DEEP VIRTUAL EXCLUSIVE SCATTERING

Recent years have seen the development of a new approach to studying nucleon structure, Deep Exclusive Scattering (DES), which involves the exclusive electroproduction of a photon or meson on the nucleus at large Q^2. The following reactions can be used to represent these:

$$\begin{aligned} e + N &\to e + N + \gamma, \\ e + N &\to e + N + \text{meson}(M). \end{aligned} \tag{27}$$

The first reaction $eN \to eN\gamma$ named Deeply Virtual Compton Scattering (DVCS), and the second reaction, $eN \to eNM$ represents Deep Virtual Meson Production(DVMP). As a result of these processes, we gain a better understanding of nucleon constituents. Essentially, deep virtual processes correspond to deep inelastic scattering with large Q^2 and W^2. (i.e

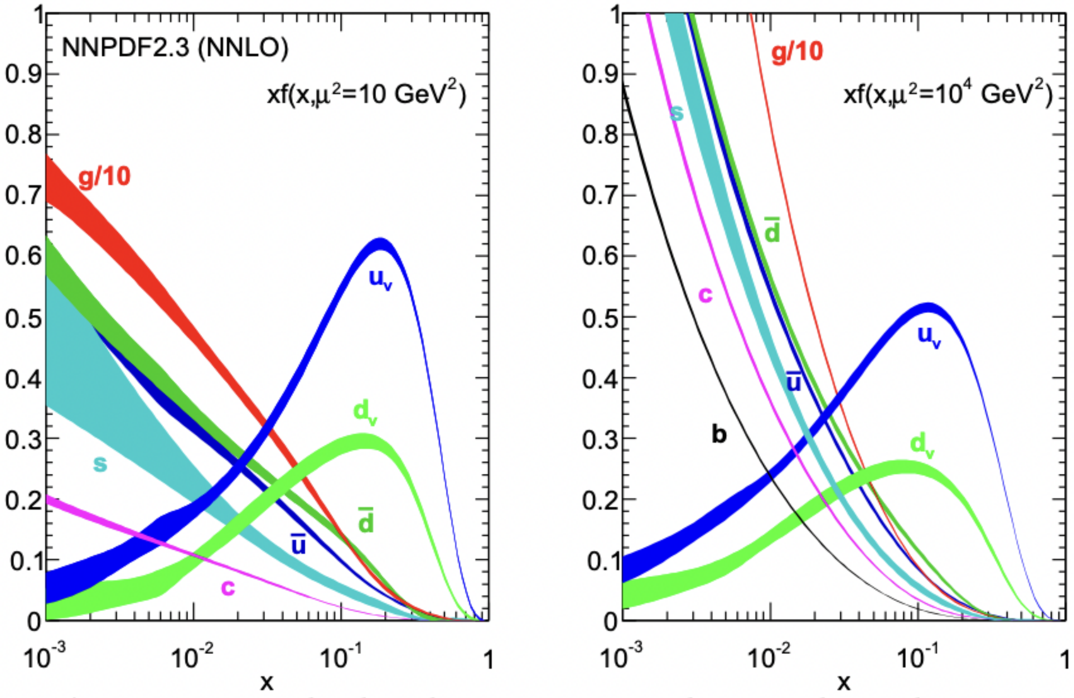

FIG. 8. The diagram illustrates the PDFs $xq(x)$ (for $q = u_v, d_v, \bar{u}, \bar{d}, s, c, b, g$), and their associated uncertainties using the NNLO MRST parametrization at $Q^2 = \mu^2 = 10$ GeV^2 and $10,000$ GeV^2. This figure and text were taken from Ref. [2].

$Q^2 > 1.0$ GeV^2 and $W^2 > 4.0$ GeV^2 as discussed in previous section). In particular, at the large Q^2 regime, exclusive electroproduction processes can be described in terms of the quark degree of freedom. In the Bjorken limit[4], QCD factorization theorems state that the exclusive electroproduction of photons and mesons is dominated by a mechanism in which the production process happens in the reaction of the longitudinally polarized virtual photon interacts with only one parton (quark or anti-quark). According to Fig. 9, this feature can be represented by a "handbag diagram". For one photon exchange approximation, these exclusive electroproduction processes can be written in terms of the virtual photon, such as $\gamma^*(Q^2) + N \to M + N(M = \gamma, Meson)$. Further, kinematically, the forward exclusive limit can be found by $-t \lesssim \Lambda^2_{QCD} \lesssim 1.0$ GeV^2 [18]. It is contained in the Generalized Parton Distributions (GPDs) that describe the spatial parton distribution in the transverse plane and their longitudinal momentum fraction. As a result, we can obtain a three-dimensional

---

[4] $Q^2 \to \infty$, $2P \cdot q \to \infty$ and then $\frac{x_B}{2P \cdot q}$ is fixed.

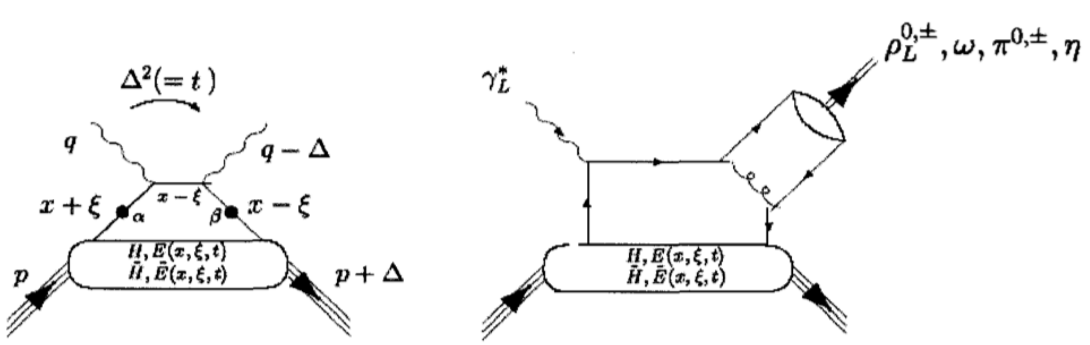

FIG. 9. Handbag diagrams illustrating the DVCS and DVMP processes (left and right, respectively) [19].

picture of nucleons. The nucleon quark structure can be systematically explored using the DVCS and DVMP electroproduction mechanisms.

1.2.1 GENERALIZED PARTON DISTRIBUTION

According to studies conducted by D. Muller [20], X. Ji [21], and A. Radyushkin [22] about twenty years ago, DVCS amplitudes in the forward direction can be divided into "hard" and "soft" parts in the Bjorken regime. The "hard" part consists of the virtual Compton process at the quark level that is perturbatively calculable in QCD, and the lower blob which is representing a "soft" part, parameterized in terms of the four structure functions: $H, E, \widetilde{H}, \widetilde{E}$, called as GPDs, illustrated in Fig. 9. The GPDs depend on three independent variables x, ξ, and, t:

- x-momentum fraction of the struck quark in the quark loop. $-1 \leq x \leq 1$;
- ξ-longitudinal momentum fraction of the transfer $\Delta = P - P'$. In the Bjorken limit, $\xi \sim x_B/(2 - x_B)$
- t-squared momentum transfer between the initial and final nucleons, $t = \Delta^2 = (P' - P)^2$.

Light-cone frame, when the partons move along z direction at light speed, the non-perturbative object shown in the lower blob of Fig. 9 can be parameterized in terms of the matrix element of the bi-local quark operator, which is expressed as the four GPDs:

$$\left|\frac{P^+}{2\pi}\int dy^- e^{ixP^+y^-} < P^{+\prime}|\bar{\psi}_\beta(-\frac{y}{2})\psi_\alpha(\frac{y}{2})|P>\right|_{y^+=\overrightarrow{y}_\perp=0} =$$

$$\frac{1}{4}\Bigg\{\gamma^-_{\alpha\beta}\Bigg[H^q(x,\xi,t)\bar{N}(P'^+)\gamma^+N(p)+E^q(x,\xi,t)\bar{N}(P'^+)i\sigma^{+k}\frac{\Delta_k}{2M_N}N(p)\Bigg]+$$

$$(\gamma_5\gamma^-)_{\alpha\beta}\Bigg[\widetilde{H}^q(x,\xi,t)\bar{N}(P'^+)\gamma^+\gamma_5N(p)+\tilde{E}^q(x,\xi,t)\bar{N}(P'^+)\gamma_5\frac{\Delta_k}{2M_N}N(p)\Bigg]\Bigg\}, \tag{28}$$

where $N(p)$ is the nucleon spinor and $\alpha\beta$ are un-contracted spinor indices. The left part of this Eq. (28) represents the Fourier integral along the light-cone distance y^- of a quark-quark correlation function. This process depicts the removal of a quark from a nucleon of initial momentum P at the space-time point $y/2$, followed by its subsequent reinsertion into a final nucleon of momentum P'^+ at the space-time point $-y/2$. This process occurs with equal light-cone time ($y^+ = 0$) and zero transverse separation ($\overrightarrow{y}_\perp = 0$) between the quarks [19]. The right side, the first line of this Eq. (28) corresponds to the vector part ($\gamma^-_{\alpha\beta}$) of the current, and on the right side, the last line of this Eq. (28) corresponds to the axial vector part $(\gamma_5\gamma^-)_{\alpha\beta)}$ of the current. These two nucleon structures are encoded in terms of four GPDs: $H^q(x,\xi,t)$ (parameterizing a vector transition), $E^q(x,\xi,t)$ (parameterizing a tensor transition), $\widetilde{H}^q(x,\xi,t)$ (parameterizing an axial vector transition) and $\tilde{E}^q(x,\xi,t)$ (parameterizing a pseudo-scalar transition).

Each of the four GPD configurations H, E, $\widetilde{H}$, $\tilde{E}$, corresponds to the quark helicity and nuclear spin orientation, as shown in Fig. 10. GPDs H and E are spin-independent functions and are therefore called "unpolarized" GPDs, while $\widetilde{H}$ and $\tilde{E}$ are spin-dependent functions and are therefore called "polarized" GPDs.

Previously, we mentioned that the GPDs are determined by three variables: x, ξ, and t. Since x varies between -1 and 1, the momentum fraction ($x+\xi$ or $x-\xi$) of the quark can be either positive or negative. It is, therefore, possible to create and name the DGLAP region as $x > \xi$ and $x < -\xi$. There are two types of scattering in this DGLAP region: scattering on quarks, for $x > \xi$, and scattering on anti-quarks, for $x < -\xi$. GPDs reduce to parton distributions in the forward limit (when nucleon momentum is transferred) where H becomes the quark density distribution $q(x)$, $\widetilde{H}$ becomes the helicity distribution $\Delta(q)$, and the following relationships hold:

$$H^q(x,0,0) = \begin{cases} q(x) & x > 0 \\ -\bar{q}(-x) & x < 0 \end{cases}, \tag{29}$$

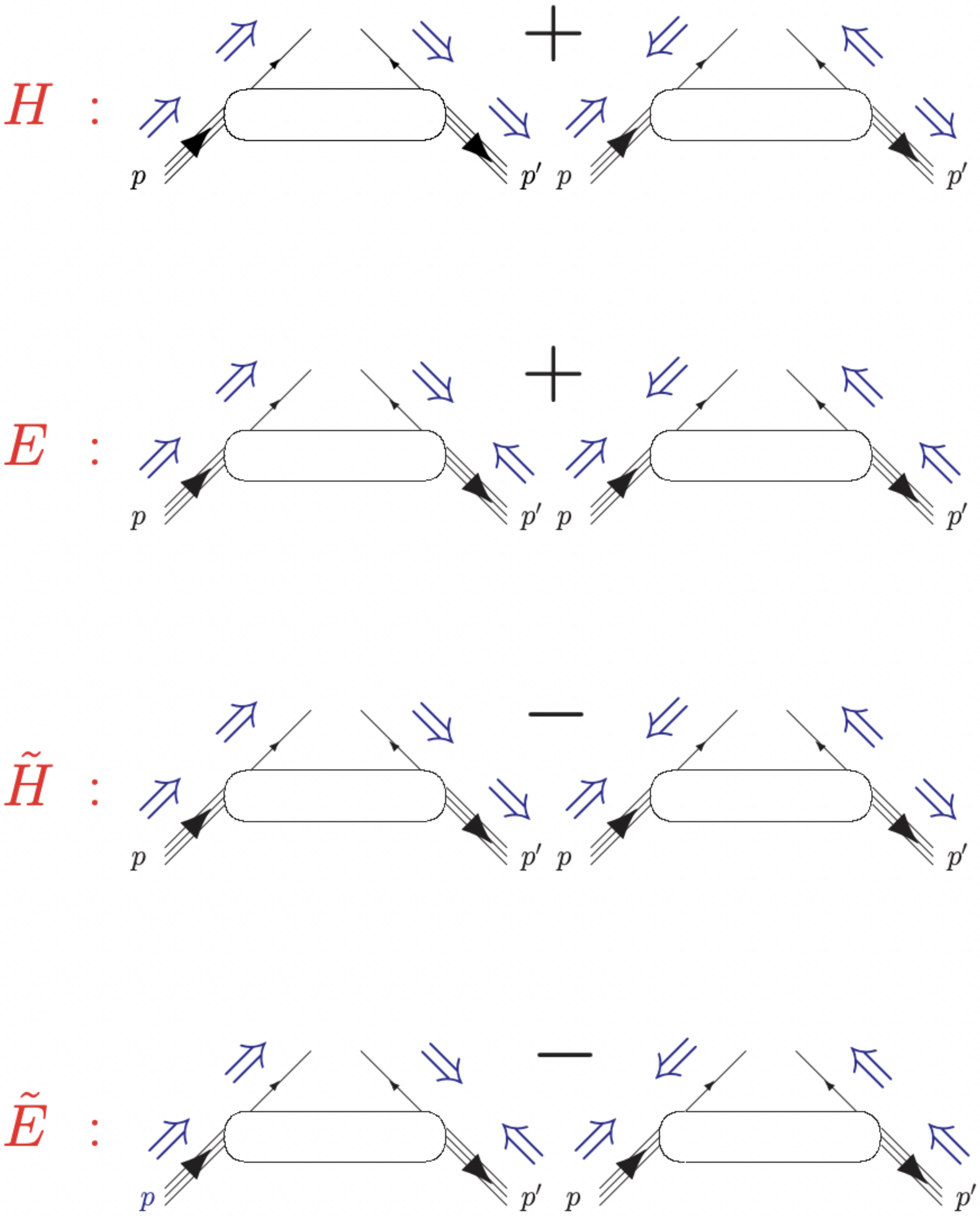

FIG. 10. These four GPDs, H, E, $\widetilde{H}$, and $\widetilde{E}$, relate to the different quark spin orientations and quark helicity [17].

$$\widetilde{H}^q(x,0,0) = \begin{cases} \Delta q(x) & x > 0 \\ \Delta \bar{q}(-x) & x < 0 \end{cases}. \tag{30}$$

As the forward limit approaches, E and $\widetilde{E}$ disappear. However, if at finite momentum transfer (not in the forward limit), there are model-independent sum rules relate to the first moment of GPDs to the elastic form factors [17]:

$$\begin{aligned} &\int_{-1}^{+1} dx H^q(x,\xi,t) = F_1^q(t), \qquad &&\int_{-1}^{+1} dx E^q(x,\xi,t) = F_2^q(t), \\ &\int_{-1}^{+1} dx \widetilde{H}^q(x,\xi,t) = G_A^q(t), \qquad &&\int_{-1}^{+1} dx \widetilde{E}^q(x,\xi,t) = G_P^q(t), \end{aligned} \tag{31}$$

where $F_1^q(t)$, $F_2^q(t)$, $G_A^q(t)$, and, $G_P^q(t)$ represent elastic Dirac FF, Pauli FF, axial FF and pseudo-scalar FF, respectively. A summary of the above discussed components of GPDs is presented in the following Table 1. The second moment of the H^q and E^q are in the following

	Nucleon helicity non-flip	**Nucleon helicity non-flip**
$\tau = \gamma^\mu$ Unpolarized quarks	H Dirac FF	E Pauli FF
$\tau = \gamma^\mu \gamma_5$ Polarized quarks	$\widetilde{H}$ Axial FF	$\widetilde{E}$ Pseudo-scalar FF

TABLE 1. Summary table for GPDs as a component of the quark density in the nucleon.

form [14].

$$\begin{aligned}\int_{-1}^{+1} dx x H^q(x,\xi,t) &= A^q(t) + 4\xi^2 C^q(t),\\ \int_{-1}^{+1} dx x E^q(x,\xi,t) &= B^q(t) - 4\xi^2 C^q(t),\end{aligned} \tag{32}$$

By combining the two equations above Eq. (32),

$$\int_{-1}^{+1} dx x[H^q(x,\xi,t) + E^q(x,\xi,t)] = A^q(t) + B^q(t). \tag{33}$$

According to Xiangdong Ji, there exists a gauge-invariant decomposition of nucleon spin [21]:

$$\frac{1}{2} = J_{quarks} + J_{gluons}, \tag{34}$$

where J_{quarks} and J_{gluons} are total(spin +orbital) quarks and gluons angular momentum. Following Ji's sum rule [21]: H and E are the second moments of unpolarized GPDs to the quark's total angular momentum:

$$\sum_q \int_{-1}^{+1} dx x[H^q(x,\xi,t) + E^q(x,\xi,t)] = \sum_q [] A^q(0) + B^q(0)] = 2J_{quarks}. \tag{35}$$

J_{quarks} can be decomposed as: $J_{quarks} = \sum_q (S_q + L_q)$, where $S_q = \frac{\Delta q}{2} = \frac{1}{2}\int_0^1 dx[q_+(x) - q_-(x)]$ and L_q is the quark spin and orbital angular momentum. Several polarized DIS experiments (e.g., EMC collaboration [23]) have measured Δq, and Eq. (35) provides a model-independent approach to determining the quark orbital angular momentum. Therefore, Eq. (34) can be utilized to determine the contribution of the gluon.

1.3 HARD MESON ELECTROPRODUCTION

The process of Deeply Virtual Meson Production (DVMP) involves the scattering of a virtual photon off a nucleon target, which produces a meson (e.g., ρ_L, ω_L, ϕ_L, π^0, $\pi^\pm$, η, $K^\pm$, K^0, etc.). At leading order and twist, the unpolarized GPDs (H and E) are sensitive to the longitudinal polarization of vector meson channels, namely ρ_L, ω_L, and ϕ_L. On the other hand, the polarized GPDs ($\widetilde{H}$ and $\widetilde{E}$) are only sensitive to the pseudo-scalar channels, such as π^0, $\pi^\pm$, η, $K^\pm$, and K^0.

Exclusive electroproduction, particularly the Deeply Virtual Meson Production (DVMP) process, provides valuable insights into both the reaction dynamics and the nucleon structure of the target. The DVMP process is represented by the second reaction in Eq. (27):

$$e(k) + N(p) \to e'(k') + N'(p') + M(p_M). \tag{36}$$

In the one-photon exchange approximation, the DVMP process can be expressed in terms of the exchange of a virtual photon (γ^*):

$$\gamma^*(q) + N(p) \to N'(p') + M(p_M). \tag{37}$$

The final state of meson electroproduction can be characterized by five independent variables, derived from the 4-vectors of the incident and scattered electrons (k and k') and the virtual photon ($q = k - k'$). If there is no polarization of either the electron or the proton, four kinematic variables are sufficient to describe the final state, namely the squared 4-momentum of the virtual photon ($Q^2 = -q^2$), the virtual photon energy ($\nu = E - E'$), the Bjorken variable ($x_B = \frac{Q^2}{2p \cdot q}$), and the squared 4-momentum transfer between the target and recoiling nucleon ($t = (p' - p)^2$). Additionally, the angle Φ_h between the leptonic and hadronic planes (see Fig. 11) can be defined.

If the meson decays into a pair of pions (π_1 and π_2), three extra variables are needed to describe the final state. These include the invariant mass of the two pions ($M_{\pi_1\pi_2} = \sqrt{(p_1 + p_2)^2}$), where p_1 and p_2 are the 4-vectors of π_1 and π_2, respectively, as well as θ_1 and ϕ_1, the π_1 decay angles in the meson rest frame. For this analysis, θ_1 and ϕ_1 are defined in the helicity frame, which is the rest frame of the meson. In the helicity frame, the z-axis is defined by the direction of the meson in the $\gamma^* N$ center-of-mass system and the rest-frame angles are referred to as $\cos(\Theta_R)$ and Φ_R (see Fig. 11).

1.3.1 DEEP EXCLUSIVE TWO PION PRODUCTION

This thesis is primarily concerned with deep virtual two-pion production, focusing on charged and neutral pion pairs. Specifically, two reactions are examined: $ep \to e'p'\pi^+\pi^-$ and $ep \to e'p'\pi^0\pi^0$ (Note that the second reaction is skipped from this thesis). The former involves iso-spin $I = 1$ and angular momentum $J = 1$, resulting in the production of the $\rho(770)$ meson. In the latter, iso-spin $I = 0$ and angular momentum $J = 0$ are present, leading to the production of the σ meson, as well as the $f_0(500)$ and $f_0(980)$ mesons.

- $ep \to e'p'\pi^+\pi^-$
    - Isospin $I = 1$, Angular momentum $J = 1$
        - $\rho(770)$: ρ meson.
    - Isospin $I = 0$, Angular momentum $J = 0$
        - $f_0(500)$: σ meson, $f_0(980)$.

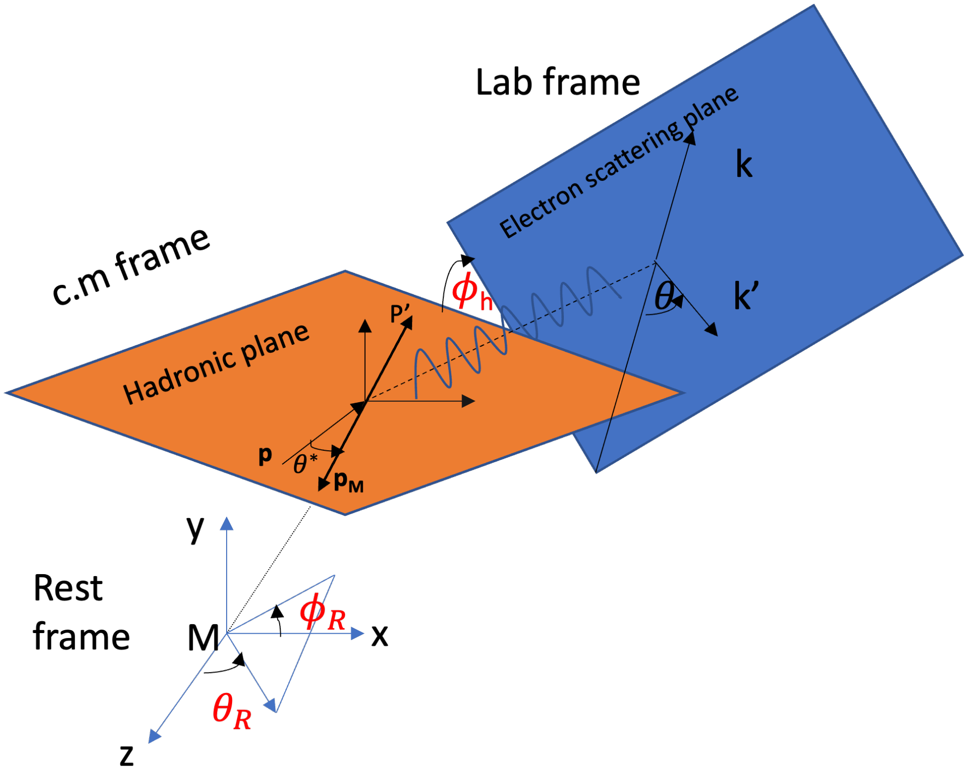

FIG. 11. Relevant kinematics variables for the description of the exclusive meson electroproduction in the rest frame.

- $ep \to e'p'\pi^0\pi^0$
    - $*$ Isospin $I = 0$, Angular momentum $J = 0$
        - $*$ $f_0(500)$: σ meson, $f_0(980)$.

Our focus is on the analysis of the $\pi\pi$ partial waves with isospin zero ($I = 0$) and isospin one ($I = 1$) channels for the two reactions of charged and neutral pion pairs. Although an isospin two ($I = 2$) channel is also possible, it is expected to be very small. For the isospin one ($I = 1$) channel, the allowed orbital angular momentum is $J = 1$, while for the isospin zero ($I = 0$) channel, both $J = 0$ and $J = 2$ are allowed.

Resonances are observed in both reactions. In the charged pion pair reaction, the $\rho(770)$ resonance, which is a spin one particle with isospin one ($I = 1$) and angular momentum

$J = 1$ is present. For the isospin zero ($I = 0$) channel, the $f_0(500)$ resonance, also known as the sigma-meson, and the $f_0(980)$ resonance are observed, both having angular momentum $J = 0$. In the neutral pion pair reaction, only the isospin zero, spin-zero channel ($I : J = 0 : 0$) is present, and both the $f_0(500)$ (sigma-meson) and $f_0(980)$ resonances are observed. A summary of the poles for each resonance is shown in Table 2.

$J^\pi; I$	Resonance	Re[Pole] (MeV)	Im[Pole] (MeV)
$0^+; 0$	$f_0(500)$	450 ± 20	-275 ± 12
	$f_0(980)$	990 ± 20	-40 ± 20
$1^-; 1$	$\rho(770)$	770 ± 5	-148 ± 1
$2^+; 0$	$f_2(1270)$	1275 ± 1	-185 ± 3

TABLE 2. $\pi\pi$ final state Quantum Numbers [2].

1.4 FACTORIZATION OF EXCLUSIVE MESON PRODUCTION

The factorization theorem states that the amplitude of exclusive production [24]

$$\gamma_L^* + T \to F + T', \tag{38}$$

factorizes at large invariant collision energy $W \to \infty$, large virtuality of longitudinally polarized photon $Q^2 \to \infty$ at fixed $x_B = \frac{Q^2}{2p.q}$(Bjorken limit) and with $-t, M_T^2, M_F^2 \ll Q^2$. In this limit, the scattering amplitude can be written as [24],

$$\mathcal{M} \to \Sigma_{i,j} \int_0^1 dz \int dx_1 f^{T'}_{\frac{i}{T}}(x_1, x_1 - x_B, t) H_{i,j}(\frac{x_1}{x_B}, Q^2, z) \Phi^F_j(z) \tag{39}$$
$$+power - suppressed - corrections(\frac{t}{Q^2}...).$$

In this expression, where $f^{T'}_{i,T}$ are the $T \to T'$ skewed parton distribution (essentially different terminology for GPDs), $\Phi^F_j(z)$ is the distribution amplitude of hadronic state F, and $H_{i,j}$ is the hard part computable in perturbative QCD. The distribution amplitude $\Phi(x)$ is the amplitude for the mesonic state F to be found in an elementary $q\bar{q}$ state, with the quark carrying a fraction z of the total light cone momentum of the F. Therefore, the dominant amplitude in exclusive meson electroproduction at the Bjorken limit, for $-t \ll Q^2$ and for the longitudinally polarized photon can be factorized according to the handbag diagram, which is shown in Fig. 12.

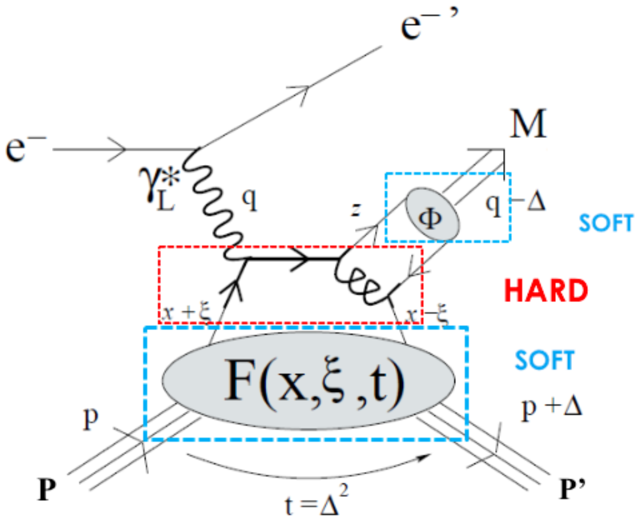

FIG. 12. Handbag diagram for deeply virtual meson production, coupling to quark GPDs and quark DAs. Diagrams involving gluon GPDs and/or gluon DAs are shown in Fig. 14.

This Fig. 12 splits into HARD and SOFT parts: the interaction of the virtual photon and a quark of the nucleon (HARD), calculable through perturbative QCD, the parton interaction with the proton (SOFT), which describes in terms of GPD (non-perturbative part), and another non-perturbative soft part is described the meson production.
The x is the quark momentum fraction of the proton, and ξ is the skewness parameter describing the longitudinal component of the momentum transfer which x in the Bjorken limit $Q^2 \to \infty$ can be expressed in terms of the Bjorken variable x_B

$$\xi \to \frac{x_B}{2 - x_B}. \tag{40}$$

$x \pm \xi$ are parton + momentum fraction, and z, $1 - z$ are parton momentum fraction in the mesonic initial and final state (see Fig. 12).

The handbag diagram is calculated in the light cone referential, shown in Fig. 13. The referential is defined by the components, + and −:

$$a^{\pm} = \frac{a^0 \pm a^3}{\sqrt{2}}, \tag{41}$$

The coordinate a^0 is here denoted by the time t and a^3 by the spatial coordinate z. By neglecting the mass of particles in play, the incident and recoil protons move along the positive z at the speed of light (+ axis). The meson produced moves at the speed of light in the direction of the negative z (− axis). The virtual photon moves in the direction of the positive z at a speed higher than the light because of its negative mass Q^2: it is, therefore, outside the cone of light and has two components + and − (Fig. 13).

Factorization can be applied to any low-mass hadronic final state. The lowest order(LO) Feynman diagrams (lowest order in both α_{QED} and α_s) for the $\gamma^*+p \to p+\pi+\pi$ amplitude are illustrated in Fig. 14. Those are leading order diagrams for exclusive deep virtual production of two pions (Fig. 14). The permutations of the ordering of the vertices must also be included. The blob connecting to the external pions represents the two pion Distribution Amplitude (DA). The blob connecting to the two external nucleon states represents the nucleon Generalized Parton Distributions (GPDs). The internal lines are quark (or anti-quark) propagators, and the springy lines are gluons. These diagrams from Lehmann-Dronke [24], they mostly discussed the hard exclusive pion pairs. Basically, they have analyzed the angular distribution of two pions using the leading order amplitude of hard exclusive electro-production of two pions (hard means high Q^2). The hard exclusive production of pion pairs exhibits an interesting feature where the isoscalar state ($I = 0$) of two pions can be produced

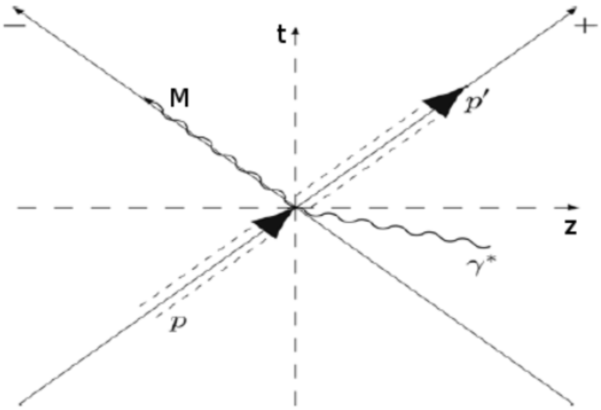

FIG. 13. Referential light cone for the exclusive production of meson.

not only from a collinear $q\bar{q}$ pair but also from two collinear gluons. It's important to note that measuring the isospin zero state can offer valuable insights into the gluon content of the two-pion system. Furthermore, the production of the pion pair in the isoscalar state is dominated by the gluon distribution amplitude, as its contribution is twice that of the quark distribution amplitude. Based on the evidence, it appears that the production of hard pairs in the isoscalar state is primarily related to the gluon structure of the σ-meson [24].

1.5 DEEP VIRTUAL EXCLUSIVE SCATTERING CROSS-SECTION

This section attempts to generalize the vector meson production formalism of Schilling and Wolf [25] to the more general case of a meson pair in $l = 0, 1, \ldots$ partial waves. The dependence on the $\pi\pi$, $m_{\pi\pi}$ is given explicitly in terms of the Omnés functions derived from $\pi\pi$ scattering phase-shifts, as described in [24, 26] and computed in [27, 28].

The critical aspect of [25] is to develop the $\gamma^* p \to p' h$ scattering amplitude in terms of the helicity states of the incident and scattered electron and proton, as well as the final state two-meson system h. This approach was first developed in detail by Jacob and Wick [29]. The present notes deal only with an unpolarized proton without polarization analysis in the final state. Averaging over the initial proton helicity and summing over the final proton helicity is always assumed in the expressions of the cross-section, even if not explicitly stated. The differential cross-section for the $\vec{e}p \to ep\pi\pi$ reaction with a polarized electron beam (helicity

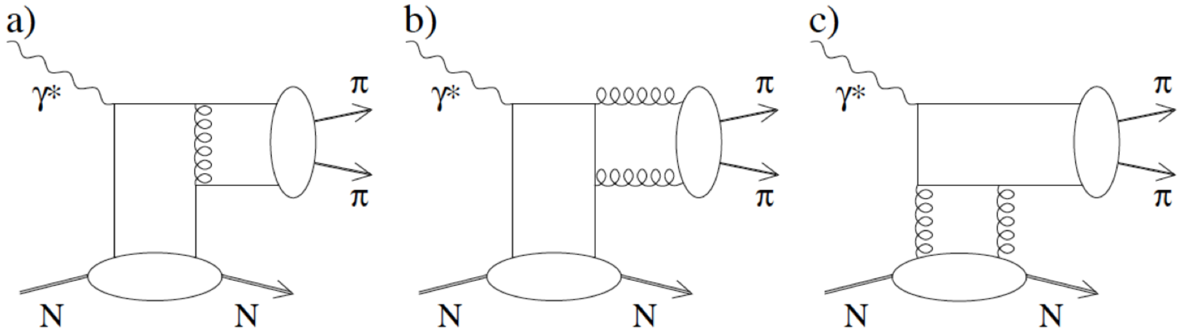

FIG. 14. The typical leading order (LO) diagrams for hard exclusive pion pair production include three distinct channels labeled (a), (b), and (c). Channel (a) involves the convolution of a Flavor-Diagonal quark- Generalized Parton Distribution (GPD) with a qq-Two-Pion Distribution Amplitude (DA). Channel (b) involves the convolution of a Flavor-Diagonal quark-GPD with a gluon-Two-Pion DA. Finally, channel (c) involves the convolution of a Gluon-GPD with a qq-Two-Pion DA. These channels represent important contributions to the hard exclusive pion pair production process and provide insight into the underlying dynamics of the process [24].

h) incident on an unpolarized Hydrogen target has the following form (in the limit $m_e \ll k$)

$$d\sigma(h) = \frac{(2\pi)^4}{4k \cdot P}\frac{1}{2}\sum_{h',s,s'}\left|\sum_d \mathcal{M}_d(h,h',s,s')\right|^2 d\Phi^{(8)}(k+P;k',P',p_1,p_2), \qquad (42)$$

The Lorentz-Invariant Phase Space (LIPS) is (e.g., `pdg.lbl.gov`)

$$\begin{aligned} d\Phi^{(8)}(k+P;k',P',p_1,p_2) &= \delta^{(4)}\left(k^\mu + P^\mu - k'^\mu - P'^\mu - p_1^\mu - p_2^\mu\right) \\ &\left(\frac{d^3\mathbf{k}'}{(2\pi)^3 2E'_e}\right)\left(\frac{d^3\mathbf{P}'}{(2\pi)^3 2E'_p}\right)\left(\frac{d^3\mathbf{p}_1}{(2\pi)^3 2E_1}\right)\left(\frac{d^3\mathbf{p}_2}{(2\pi)^3 2E_2}\right). \end{aligned} \qquad (43)$$

The $\pi\pi$ phase space can be separated out:

$$\begin{aligned} d\Phi^{(8)}(k+P;k',P',p_1,p_2) &= d\Phi^{(5)}(k+P;k',P',P_{1,2})d\Phi^{(2)}(P_{1,2};p_1,p_2)(2\pi)^3 dP_{1,2}^2 \\ &= \frac{\delta^{(4)}\left(k^\mu + P^\mu - k'^\mu - P'^\mu - P_{1,2}^\mu\right)}{(2\pi)^9}\left[\frac{d^3\mathbf{k}'}{2E'_e}\right]\left[\frac{d^3\mathbf{P}'}{2E'_p}\right]\left[\frac{d^3\mathbf{P}_{1,2}}{2E_{1,2}}\right] \\ &\times \frac{\delta^{(4)}\left(P_{1,2}^\mu - p_1^\mu - p_2^\mu\right)}{(2\pi)^6}\left[\frac{d^3\mathbf{p}_1}{2E_1}\right]\left[\frac{d^3\mathbf{p}_2}{2E_2}\right] dM_{1,2}^2(2\pi)^3. \end{aligned} \qquad (44)$$

The electron scattering kinematics can be written in semi-invariant form

$$\left[\frac{d^3\mathbf{k}'}{2E'_e}\right] = \frac{y dx_B dQ^2 d\phi_e^{\text{Lab}}}{4x_B}. \tag{45}$$

In the $\gamma^* + P$ CM frame (equivalently $P_{1,2} + P'$ CM):

$$\begin{aligned} \delta^{(4)}\left(k^\mu + P^\mu - k'^\mu - P'^\mu - P^\mu_{1,2}\right)\left[\frac{d^3\mathbf{P}'}{2E'_p}\right]\left[\frac{d^3\mathbf{P}_{1,2}}{2E_{1,2}}\right] &= \frac{\left|\mathbf{P}^{\text{CM}}_{1,2}\right| d\cos\theta^{\text{CM}}_{1,2} d\phi^{\text{CM}}_{1,2}}{4\sqrt{W^2}} \\ &= \frac{dt d\phi^{\text{CM}}_{1,2}}{8\left|\mathbf{q}^{\text{CM}}\right|\sqrt{W^2}}, \end{aligned} \tag{46}$$

with the Lorentz invariant definitions of $d\phi^{\text{CM}}_{1,2}$ and $\mathbf{q}^{\text{CM}}$ given Appendix B.0.3. Similarly, in the $\pi\pi$ rest frame:

$$\frac{\delta^{(4)}\left(P^\mu_{1,2} - p^\mu_1 - p^\mu_2\right)}{(2\pi)^6}\left[\frac{d^3\mathbf{p}_1}{2E_1}\right]\left[\frac{d^3\mathbf{p}_2}{2E_2}\right] dM^2_{1,2}(2\pi)^3 = \frac{\beta^{\text{Rest}} dM^2_{1,2} d\cos\Theta_R d\Phi_R}{8(2\pi)^3}, \tag{47}$$

with $\beta^{\text{Rest}} = \sqrt{1 - 4m^2_\pi/M^2_{1,2}}$.

In summary, the 8-fold differential invariant phase space is expressed as (with $\phi_h = \phi^{\text{CM}}_{1,2}$)

$$\begin{aligned} d^8\Phi &= \frac{y dx_B dQ^2 d\phi_e^{\text{Lab}}}{4x_B}\,\frac{dt d\phi^{\text{CM}}_{1,2}}{8\left|\mathbf{q}^{\text{CM}}\right|\sqrt{W^2}}\,\frac{\beta^{\text{Rest}} dM^2_{1,2} d\cos\Theta_R d\Phi_R}{8(2\pi)^3} \\ &= \frac{y\beta^{\text{Rest}}}{32(4\pi)^3 x_B\left|\mathbf{q}^{\text{CM}}\right|\sqrt{W^2}}\left(dx_B dQ^2 d\phi_e^{\text{Lab}}\right)\left(dt d\phi_h\right)\left(dM^2_{1,2} d\cos\Theta_R d\Phi_R\right). \end{aligned} \tag{48}$$

1.5.1 ELECTRON AND HADRON TENSORS

The scattering amplitude has the general form

$$i\mathcal{M} = -e\overline{u}(k', h_2)\gamma_\mu u(k, h_1)\frac{1}{q^2}\left\langle P'\pi\pi\left|\hat{J}^\mu(q)\right|P\right\rangle, \tag{49}$$

We will expand the currents in the photon polarization basis defined in appendix B.0.4. Thus

$$\begin{aligned} i\mathcal{M} &= -e\sum_\lambda \overline{u}(k', h_2)\gamma\cdot\epsilon^\dagger(\lambda)u(k, h_1)\frac{1}{q^2}\left\langle P'\pi\pi\left|\epsilon(\lambda)\cdot\hat{J}(q)\right|P\right\rangle \\ &= \sum_\lambda j(\lambda)\frac{1}{q^2}J(\lambda). \end{aligned} \tag{50}$$

The scattering amplitude squared is

$$\begin{aligned} |\mathcal{M}|^2 &= e^2\sum_{h_1,h'_1,h_2}\overline{u}(k', h_2)\gamma_\mu u(k, h_1)\rho(h_1, h'_1)\overline{u}(k, h'_1)\gamma_\nu u(k', h_2) \\ &\qquad\frac{1}{Q^4}\left\langle P'\pi\pi\left|J^\mu(q)\right|P\right\rangle\left\langle P\left|J^\nu(q)\right|P'\pi\pi\right\rangle \\ &= \mathcal{L}_{\mu\nu}\frac{4\pi\alpha}{Q^4}\mathcal{H}^{\mu\nu}, \end{aligned} \tag{51}$$

with the Lepton Tensor

$$\mathcal{L}_{\mu\nu} = \mathrm{Tr}\left\{ \left(\not{k}' + m\right) \gamma_\mu \left(\not{k} + m\right) \left[\frac{1 + \gamma_5 \not{\xi}_e}{2}\right] \gamma_\nu \right\},$$

and the Hadron Tensor

$$\mathcal{H}^{\mu\nu} = \left\langle P'\pi\pi \left| J^\mu(q) \right| P \right\rangle \left\langle P \left| J^\nu(q) \right| P'\pi\pi \right\rangle . \tag{52}$$

The electron tensor simplifies to

$$\begin{aligned}
\mathcal{L}_{\mu\nu} &= \mathcal{L}_{S,\mu\nu} + \mathcal{L}_{A,\mu\nu} \\
\mathcal{L}_{S,\mu\nu} &= \frac{1}{2}\mathrm{Tr}\left\{ \not{k}'\gamma_\mu \not{k} \gamma_\nu + m^2 \gamma_\mu \gamma_\nu \right\} = 2k'_\mu k_\nu - \left(2k' \cdot k - 2m^2\right) g_{\mu\nu} + 2k_\mu k'_\nu \\
&= K_\mu K_\nu - q_\mu q_\nu - Q^2 g_{\mu\nu}, \qquad \text{with } K_\mu = (k + k')_\mu \\
\mathcal{L}_{A,\mu\nu} &= \frac{m}{2}\mathrm{Tr}\left[\gamma_\mu \not{k} \gamma_5 \not{\xi}_e \gamma_\mu + \not{k}' \gamma_\mu \gamma_5 \not{\xi}_e \gamma_\nu\right] = 2mi\epsilon_{\alpha\beta\gamma\delta}\left(\delta^\alpha_\mu k^\beta + k'^\alpha \delta^\beta_\mu\right) \xi^\gamma \delta^\delta_\nu \\
&= 2mi\epsilon_{\alpha\beta\mu\nu} q^\alpha \xi^\beta .
\end{aligned} \tag{53}$$

In the ultra-relativistic limit $m\xi^\beta \to hk^\beta$.

Symmetric Lepton Tensor

Express the Lepton tensor on a helicity basis (definitions of coordinates in B.0.3):

$$\begin{aligned}
\mathcal{L}_{S,\mu\nu} &= \sum_{\lambda,\lambda' \in \{0,\pm 1\}} \epsilon_\mu(\lambda) \mathcal{L}_S(\lambda,\lambda') \epsilon_\mu(\lambda')^\dagger, \\
\mathcal{L}_S(\lambda,\lambda') &= \epsilon^\mu(\lambda)^\dagger \mathcal{L}_{S,\mu\nu} \epsilon^\nu(\lambda').
\end{aligned} \tag{54}$$

The individual terms are (note, generally $\delta_Q \ll 1$):

$$\begin{aligned}
\mathcal{L}_S(0,0) &= \frac{Q^2}{(q \cdot P)^2 (1 + \delta_Q)} P^\mu \left[K_\mu K_\nu - q_\mu q_\nu - Q^2 g_{\mu\nu}\right] P^\nu, \\
&= \frac{Q^2}{(q \cdot P)^2 (1 + \delta_Q)} \left[(P \cdot K)^2 - (q \cdot P)^2 - Q^2 M^2\right], \\
&= \frac{Q^2}{(1 + \delta_Q)} \left[\left(\frac{2 - y}{y}\right)^2 - (1 + \delta_Q)\right], \\
\mathcal{L}_S(\lambda,\lambda')_{\lambda\lambda' \neq 0} &= \frac{\lambda\lambda'}{2} \left\{ \left[K \cdot X(q)\right]^2 + Q^2 \left(1 + \lambda\lambda'\right) \right\}, \\
\mathcal{L}_S(\lambda = \pm 1, 0) &= -\lambda \sqrt{\frac{Q^2}{2(1 + \delta_Q)}} \left[K \cdot X(q)\right] \frac{2 - y}{y}.
\end{aligned} \tag{55}$$

with

$$\begin{aligned} K\cdot X(q) &= \frac{\epsilon_{\alpha\beta\gamma\delta}}{(q\cdot P)\sqrt{1+\delta_Q}}K^{\alpha}Y^{\beta}q^{\gamma}P^{\delta}, \\ &= \frac{2\mathcal{N}_Y\, Y(q)^2}{(q\cdot P)\sqrt{1+\delta_Q}} = -\frac{2\mathcal{N}_Y}{(q\cdot P)\sqrt{1+\delta_Q}}, \\ &= -\frac{(2k\cdot P)\sqrt{Q^2\left[1-y-\frac{Q^2M^2}{(2k\cdot P)^2}\right]-(m_e^2y^2)(1+\delta_Q)}}{(q\cdot P)\sqrt{1+\delta_Q}}. \end{aligned} \tag{56}$$

In the target rest frame and taking the limit $m_e \to 0$:

$$K\cdot X(q) = -|\mathbf{k}_{\perp}|. \quad . \tag{57}$$

In general

$$\begin{aligned} [K\cdot X(q)]^2 &= \frac{4Q^2}{y^2(1+\delta_Q)}\left[1-y-y^2\frac{\delta_Q}{4}-\frac{m_e^2y^2}{Q^2}(1+\delta_Q)\right] \\ &= \frac{Q^2}{(1+\delta_Q)}\left[\left(\frac{2-y}{y}\right)^2-(1+\delta_Q)\right]-4m_e^2 \\ &= \mathcal{L}_S(0,0)-4m_e^2. \end{aligned} \tag{58}$$

Now define

$$\epsilon = -\frac{\mathcal{L}_S(+,-)+\mathcal{L}_S(-,+))}{\mathcal{L}_S(+,+)+\mathcal{L}_S(-,-)} = \frac{[K\cdot X(q)]^2}{[K\cdot X(q)]^2+2Q^2}. \tag{59}$$

This virtual photon polarization parameter ϵ describes both the degree of longitudinal and transverse-linear polarization of the virtual photons. Similarly

$$\begin{aligned} \frac{\mathcal{L}_S(0,0)}{\mathcal{L}_S(+,+)+\mathcal{L}_S(-,-)} &= \frac{[K\cdot X(q)]^2+4m_e^2}{[K\cdot X(q)]^2+2Q^2}, \\ &= \epsilon+\delta_C, \\ \delta_C &= \frac{2m_e^2}{Q^2}(1-\epsilon) = \frac{4m_e^2}{[K\cdot X(q)]^2+2Q^2}. \end{aligned} \tag{60}$$

In summary (with $\lambda, \lambda' = (1,0,-1)$):

$$\mathcal{L}_S(\lambda,\lambda') = \frac{Q^2}{1-\epsilon}\left[\begin{array}{rrr} 1, & -\sqrt{\epsilon(1+\epsilon+2\delta_C)}, & -\epsilon \\ -\sqrt{\epsilon(1+\epsilon+2\delta_C)}, & 2(\epsilon+\delta_C), & \sqrt{\epsilon(1+\epsilon+2\delta_C)} \\ -\epsilon, & \sqrt{\epsilon(1+\epsilon+2\delta_C)}, & 1 \end{array}\right]. \tag{61}$$

The trace is

$$\sum_{\lambda} \mathcal{L}_S(\lambda, \lambda) = \frac{2Q^2}{1-\epsilon}(1+\epsilon+\delta_C). \tag{62}$$

These Lorentz-invariant helicity amplitudes are defined in the electron scattering coordinate system $X(q)$, $Y(q)$, $\eta(q)$, $\widetilde{\eta}(q)$. However, we prefer to define the $\gamma * + p \to h + p$ in the hadronic coordinate system, which is rotated by the angle Φ_h about the $Z(q)$ direction. The rotation of a spin-1 tensor is defined by:

$$\begin{aligned} \mathcal{L}_S^{(h)}(\lambda, \lambda') &= e^{iL_z\Phi_h}\mathcal{L}_S e^{-iL_z\Phi_h} \\ &= \frac{Q^2}{1-\epsilon}\left[\begin{array}{rl} 1, & -\sqrt{\epsilon(1+\epsilon+2\delta_C)}e^{i\Phi_h}, -\epsilon e^{2i\Phi_h} \\ -\sqrt{\epsilon(1+\epsilon+2\delta_C)}e^{-i\Phi_h}, & 2(\epsilon+\delta_C), \sqrt{\epsilon(1+\epsilon+2\delta_C)}e^{i\Phi_h} \\ -\epsilon e^{-2i\Phi_h}, & \quad\sqrt{\epsilon(1+\epsilon+2\delta_C)}e^{-i\Phi_h}, 1 \end{array}\right]. \end{aligned} \tag{63}$$

This agrees with Eq. (44) of [25], except that the signs of the $\mathcal{L}(\pm 1, 0)$ and $\mathcal{L}(0, \pm 1)$ terms are reversed. The normalized photon-helicity density-matrix in the hadronic coordinate system is (neglecting electron mass):

$$\begin{aligned} \rho_\gamma^{(h)}(\lambda, \lambda') &= \frac{1-\epsilon}{2Q^2}\mathcal{L}_S^{(h)}(\lambda, \lambda'), \\ \mathrm{Tr}\left[\rho_\gamma^{(h)}\right] &= 1+\epsilon. \end{aligned} \tag{64}$$

We then have

$$\frac{1}{Q^4}\mathcal{L}_S^{(h)}(\lambda, \lambda') = \frac{1}{2Q^2}\,\frac{1}{1-\epsilon}\rho_\gamma^{(h)}(\lambda, \lambda'). \tag{65}$$

The factor of $1/\left[2Q^2(1-\epsilon)\right]$ is generally absorbed into the definition of a virtual photon flux factor Γ in Eq. (132).

Hadronic Tensor

The development of the Hadronic Tensor follows [25], with an extension to consider the exclusive production of a superposition of hadronic channels of arbitrary spin J and isospin I. The amplitude for exclusive virtual photo-production of a hadronic channel (*e.g.,* $\pi^+\pi^-$) of spin, isospin J, I, and helicity λ_h is described by

$$\begin{aligned} T(W^2, t)^{(\lambda_h, \lambda)}_{(\lambda_f, \lambda_i)} &= \sum_{J,I} T_{J,I}(W^2, t)^{(\lambda_h, \lambda)}_{(\lambda_f, \lambda_i)}, \\ T_{J,I}(W^2, t, m_h^2, Q^2)^{(\lambda_h, \lambda)}_{(\lambda_f, \lambda_i)} &= \left\langle P_h\lambda_h; P'\lambda_f \left|\epsilon(\lambda)\cdot J(q)\right| P\lambda_i\right\rangle, \end{aligned} \tag{66}$$

with λ_i, λ_f the initial and final helicity states of the nucleon. The label of the specific I_z channel is suppressed for simplicity since it is common to all terms in the sum. Furthermore, the hadronic amplitudes have the parity symmetry ([25], Eq. (72)):

$$T_{J,I}^{(-\lambda_h,-\lambda'_N|-\lambda,-\lambda_N)}(x_B,t,Q^2) = (-1)^{\lambda_h-\lambda'_N-(\lambda-\lambda_N)} T_{J,I}^{(\lambda_h,\lambda'_N|\lambda,\lambda_N)}(x_B,t,Q^2). \tag{67}$$

The amplitude for the hadronic system to decay with polar and azimuthal angles Θ_R and Φ_R in the decay rest frame is

$$\mathcal{M}\left(W^2,t\,|\Theta_R,\Phi_R\right)^{(\lambda_h,\lambda)}_{(\lambda_f,\lambda_i)} = \sum\nolimits_{J,I} \mathcal{D}^J_{0,\lambda_h}\left(\Phi_R,\Theta_R,-\Phi_R\right)^* T_{J,I}(W^2,t)^{(\lambda_h,\lambda)}_{(\lambda_f,\lambda_i)}. \tag{68}$$

With an unpolarized target and no analysis of the final state nucleon polarization, the helicity elements of the Hadronic tensor are (m_h^2, Q^2 variables suppressed for clarity):

$$\begin{aligned} H(\lambda,\lambda';\lambda_h,\lambda'_h) &= \epsilon(\lambda)_\mu H^{\mu\nu}\epsilon^\dagger(\lambda')_\nu \\ &= \sum_{J,I|J',I'} \frac{1}{2}\sum_{\lambda_i,\lambda_f} T_{J,I}(W^2,t)^{(\lambda_h,\lambda)}_{(\lambda_f,\lambda_i)} T^\dagger_{J',I'}(W^2,t)^{(\lambda'_h,\lambda')}_{(\lambda_f,\lambda_i)}. \end{aligned} \tag{69}$$

The virtual photon helicity density matrix $\rho_\gamma(\lambda,\lambda')$ was defined above. As a consequence, the final state hadronic system has a helicity polarization matrix:

$$\begin{aligned} \widetilde{H}(\lambda_h,\lambda'_h) &= \sum_{\lambda,\lambda'} H(\lambda,\lambda';\lambda_h,\lambda'_h)\rho_\gamma(\lambda,\lambda') \\ &= \sum_{J,I|J',I'}\sum_{\lambda,\lambda'}\frac{1}{2}\sum_{\lambda_i,\lambda_f} T_{J,I}(W^2,t)^{(\lambda_h,\lambda)}_{(\lambda_f,\lambda_i)}\rho_\gamma(\lambda,\lambda') T^\dagger_{J',I'}(W^2,t)^{(\lambda'_h,\lambda')}_{(\lambda_f,\lambda_i)}. \end{aligned} \tag{70}$$

Suppressing all kinematic variables except the decay angular distribution and also suppressing the summed over helicity variables, we obtain a matrix expression for the hadronic angular distribution:

$$\widetilde{W}(\Theta_R,\Phi_R) = \sum_{J,I|J',I'} D^J_{0,\lambda_h}\left(\Phi_R,\Theta_R,-\Phi_R\right)^* T_{J,I}(W^2,t)\rho_\gamma T^\dagger_{J',I'}(W^2,t) D^{J'}_{0,\lambda'_h}\left(\Phi_R,\Theta_R,-\Phi_R\right). \tag{71}$$

The Wigner D-functions have the form

$$D^J_{m',m}(\alpha,\beta,\gamma) = e^{-im'\alpha} d^J_{m',m}(\beta) e^{-im\gamma}. \tag{72}$$

with the d-functions given in §B.0.4. Therefore, the integrated hadronic flux is

$$\begin{aligned} \int_{-1}^{1} d\cos\Theta_R \int_0^{2\pi} d\Phi_R \widetilde{W}(\Theta_R,\Phi_R) &= \sum_{J,I|J',I'} \frac{4\pi}{2J+1}\delta_{J,J'} T_{J,I}(W^2,t)\rho_\gamma T^\dagger_{J',I'}(W^2,t) \\ &= \sum_{J,I} \frac{4\pi}{2J+1}\delta_{J,J'} T_{J,I}(W^2,t)\rho_\gamma T^\dagger_{J,I}(W^2,t). \end{aligned} \tag{73}$$

The distribution $\widetilde{W}$ also depends upon the kinematic variables W^2, Q^2, t, m_h. The m_h-dependence of each channel is described by the Omnes functions $\Omega_{J,I}(m_h)$:

$$T_{J,I} = T_{J,I}(W^2, Q^2, t)\Omega_{J,I}(m_h). \tag{74}$$

1.6 $\pi\pi$ MASS DISTRIBUTION (OMNÉS FUNCTION)

The mass-dependent Omnés functions can be determined by accurately extracting the $\pi\pi$ phase shifts from available data sources. The expression that relates the $\pi\pi$ Omnés function to the phase shift can be found in references [24] and [28]:

$$\Omega_l^I(m_{\pi\pi}) = \exp\left\{ i\delta_l^I(m_{\pi\pi}) + \frac{m_{\pi\pi}^2}{\pi} Re\left[\int_{4m_\pi^2}^{\infty} ds \frac{\delta_l^I(s)}{s(s - m_{\pi\pi}^2 - i\epsilon)} \right] \right\}. \tag{75}$$

The analysis of the Omnés functions was conducted in detail in reference [28], and the estimated cross-sections were based on the findings of that work. Fig. 15 presents the phases and amplitude of the Omnés function for both the S and D waves with $I = 0$ and $I = 2$, as determined by M. R. Pennington [28]. Meanwhile, Fig. 16 displays the $\pi\pi$ Omnés function result for $L = 1$, which corresponds to the ρ-meson. The Omnés function for the ρ-meson is well-established at present.

In the $I = 0$, $L = 0$ channel, both the $f_0(500)$ (sigma-meson) and $f_0(980)$ resonances are present, as shown in Fig. 15(a) and Fig. 15(b). On the other hand, in the $I = 0$, $L = 2$ channel, the $f_0(1270)$ resonance is present, as shown in Fig. 15(c) and 15(d). There is also considerably less structure in the isospin $I = 2$ channel. For the spin-zero ($L = 0$) resonance, Fig. 15(a) shows that there is an angle of π in the phase motion, while for the spin-two ($L = 2$) resonance, the phase goes through $\frac{\pi}{2}$ rather strongly.

1.7 DEEP SIGMA ($f_0(500)$)

For nearly six decades, the existence and characteristics of the sigma meson have been the subject of controversy. However, its existence is now well-established. The pole position of the sigma meson has been determined to be $449^{+22}_{-16} - i(275 \pm 12)$, as reported in [32]. Despite this, the microscopic structure of the sigma meson is not yet well understood. It is believed to be a mixture of tetraquark and $\pi\pi$ molecules, but it also contains sub-dominant $q\bar{q}$ components and purely gluonic content. Therefore, the sigma meson can be regarded as a superposition of all $q\bar{q}$, tetraquark, $\pi\pi$ molecules, and glueball.

1.8 DEEP ρ MESON PROBLEM

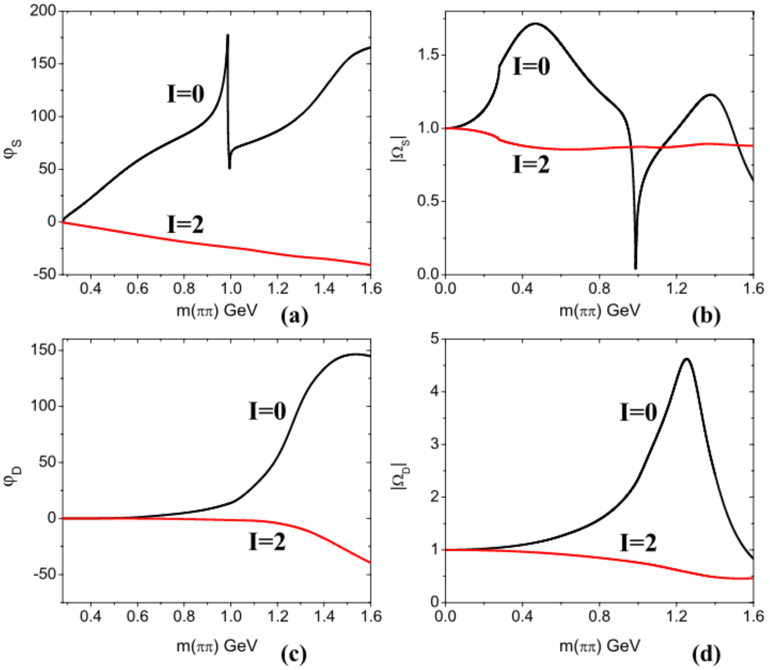

FIG. 15. The figure presents the phases (left) and moduli (right) of the Omnés functions for both the $J = 0$ (top) and $J = 2$ (bottom) partial waves with $I = 0$ and $I = 2$, as reported in reference [30, 31].

Deep virtual production of ρ meson is still quite a puzzle. Fig. 17 shows the deep ρ longitudinal cross-section as a function of W at fixed Q^2. Fig. 17 shows two particular GK (Goloskokov, Kroll) and VGG (Vanderhaegen, Guidal, Guichon) GPD-based calculations that provide quantitative results for the longitudinal part of the exclusive meson cross-section. The red dashed line shows the results of the GK model, while the blue solid line shows the VGG model. As we can see, they give a good description of the high and intermediate W region, down to $W \approx 5$ GeV. At high W, the slow rise of the cross- section is due to the gluon and sea contributions, while the valence quark contributes only at small W. At lower W values, where the new CLAS data lies, both GK and VGG models failed to reproduce the data [33].

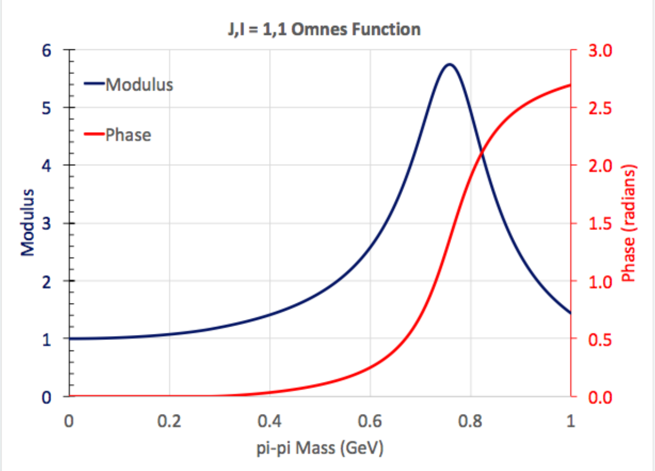

FIG. 16. The phases and moduli of the Omnés function for $L = 1$ (ρ-meson).

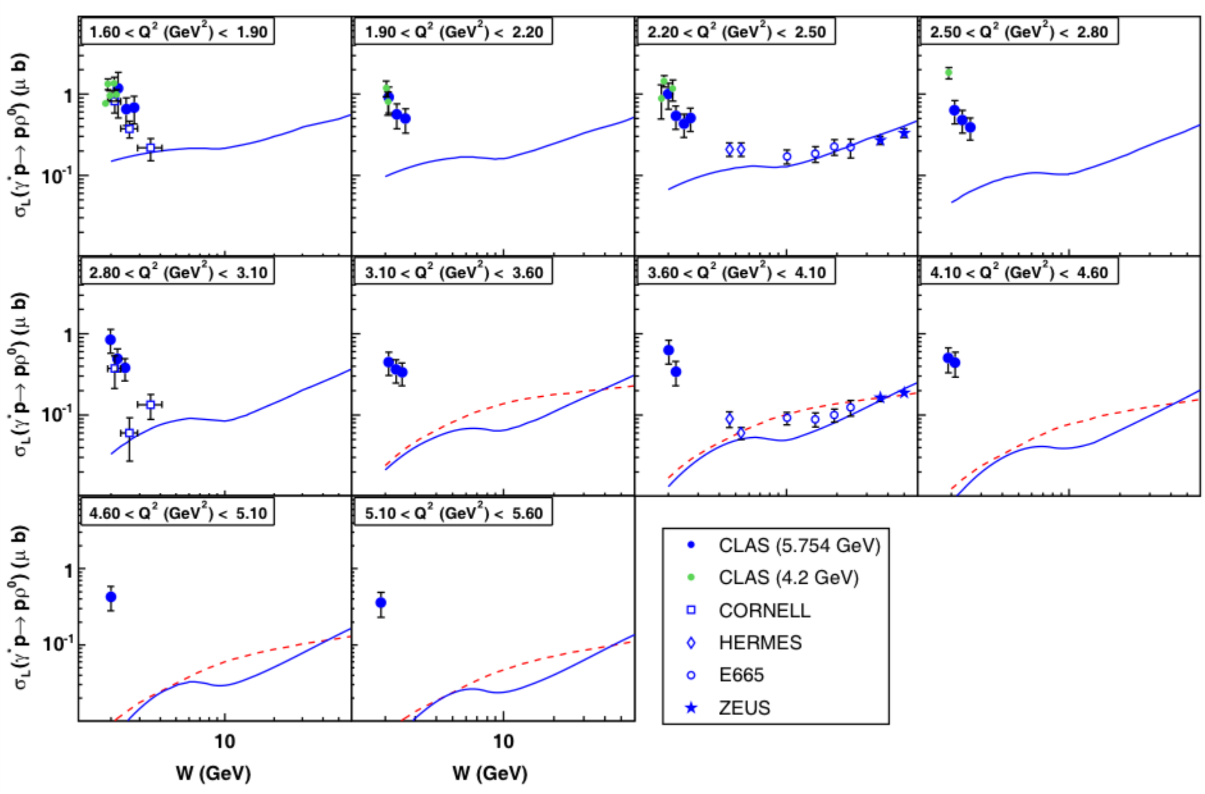

FIG. 17. The longitudinal cross-section as a function of the invariant mass W at a fixed virtuality Q^2 is shown in the context of the reaction $\gamma^* + p \rightarrow p\rho$. The calculation is presented using two different models: the Goloskokov-Kroll (GK) model, represented by the red dashed curve, and the Vanderhaegen-Guidal-Guichon (VGG) model, represented by the blue solid curve. The comparison of the results from these models provides insights into the underlying dynamics of the reaction and can be used to test the validity of theoretical predictions against experimental data [33].

CHAPTER 2

EXPERIMENTAL SETUP

The CLAS12 experiment, which stands for CEBAF Large Acceptance Spectrometer at 12 GeV, is located in experimental Hall B at Jefferson Lab (JLab). This experiment has made significant contributions to the field of hadronic physics and is particularly valuable for investigating the new physics of Generalized Parton Distributions (GPDs), as well as the internal dynamics and 3D imaging of the nucleon and quark hadronization processes. These investigations are conducted by measuring exclusive and semi-inclusive processes.

The CLAS12 experiments include the Run Group-A (RG-A) science program, which comprises 13 experiments carried out by an international collaboration and organized into five topical categories. The data examined in this thesis study comes from the "Deep Exclusive Processes ($E12-12-007$)" category within the RG-A program. The CLAS12's large acceptance, operation at high luminosity ($L = 10^{35}\text{cm}^{-2}\text{s}^{-1}$), and use of 11 GeV polarized electrons on a liquid hydrogen target make it a highly suitable platform for my thesis project.

The RG-A program has gathered data during three distinct running periods: spring 2018 (126 mC), fall 2018 (99 mC), and spring 2019 (60 mC), and the total charge collected represents approximately half of the approved RG-A beam time [34]. The Fall 2018 in-bending data-set, which covers Run 5032-5419, was the largest data-set in the experiment. For this run range total accumulated charge of 41.8 mC from the CLASQADB was calculated by Christopher Dilks, and considering the set beam energy of 10.6 GeV, the integrated luminosity of the experiment can be determined. For a fixed target experiment, the luminosity is defined as the number incident beam particles times the number density of nuclei in the target, times the target length. Considering only the liquid hydrogen in the target and assuming no target boiling effects, the integrated luminosity was calculated to be 5.46348×10^{10} $/\mu b$.

2.1 THE CLAS12 DETECTOR

The CLAS12 detector is divided into two parts: the Forward Detector (FD) and the Central Detector (CD). The FD is composed of six sectors, which are symmetrically arranged and defined by toroidal superconducting magnet coils. Charged particle tracking is provided by 18 drift chambers, with 36 layers in each sector, and six layers of micromesh gas detectors (micromegas) located downstream of the target area and in front of the High-Threshold Cherenkov counter (HTCC). Time-of-flight information is obtained from two layers of time-of-flight detectors (FTOF) for particle identification. Electron, photon, and neutron detection are provided by the triple-layer electromagnetic calorimeter (PCAL), EC (inner), and EC (outer). The heavy gas Cherenkov counter (LTCC) is used for separating high-momentum pions from kaons and protons. The CD consists of 6-8 layers of silicon strip detectors with stereo readout, 6 layers of micromegas arranged as a barrel around the target, 48 scintillator bars to measure the particle flight time from the target (CTOF), and a central neutron detector. The CLAS12 Forward Tagger (FT) is located between the FD and beamline and extends the detection capability of electrons and photons at small polar angles from 2° to 5°. The FD covers the polar angle range from 5° to 35°, while the CD covers the polar angle range from roughly 35° to 125° [35]. Additional information on each detector can be found in Ref. [35]. Ref. [36] provides further details of sub-detectors of the FD and CD. The FD and CD consisted of the following sub-detectors:

- The Forward Detectors(FD):
    - TORUS magnet
    - High Threshold Cherenkov Counter (HTCC)
    - Drift Chambers (DC)
    - Low Threshold Cherenkov Counter (LTCC)
    - Forward Time of Flight System (FTOF)
    - Preshower Calorimeter (PCAL)
    - Electromagnetic Calorimeter (EC)
    - Forward Tagger (FT)
    - RICH detector
- The Central Detector (CD):
    - Solenoid magnet
    - Silicon Vertex Tracker (SVT)
    - MicroMegas(MM)
    - Central Time of Flight (CTOF)

  - Central Neutron Detector (CND)

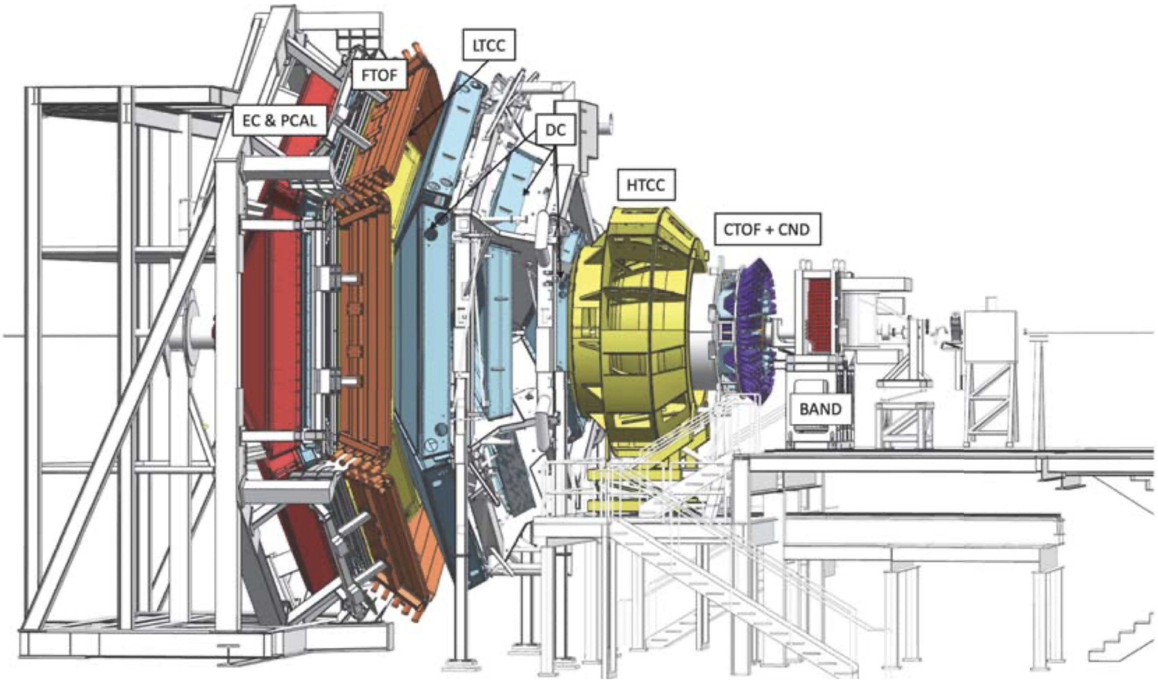

FIG. 18. The overview of the CLAS12 detector, which is a complex system in the Hall B beamline designed to detect scattered electrons and forward-going particles. The detector comprises several components, including the High Threshold Cherenkov Counter, torus magnet, drift chamber tracking system, time-of-flight scintillation counters, electromagnetic calorimeters, Silicon Vertex Tracker, Barrel Micromesh Tracker, Central Time-of-Flight system, and Central Neutron Detector. The Forward Tagger and Back Angle Neutron Detector are also installed to detect electrons, photons, and neutrons. In its operational configuration, the CLAS12 detector extends for 13 m along the beamline [35].

2.2 CLAS12 OFFLINE SOFTWARE

High-energy physics and nuclear experiments generate large amounts of data, requiring significant computing power for analysis. To improve the quality of physics data analysis, diverse groups within a large collaboration must work together. The CLAS collaboration is a team that provides location-independent access to data and flexibility in designing, operating, maintaining, and extending physics data processing applications to ensure productivity.

The CLAS12 offline software project offers the tools for efficient, repeatable, and understandable design, simulation, and data analysis. One of the main tools is the CLARA (CLAS12 Reconstruction and Analysis Framework), which covers all stages of physics data processing, including physics and detector simulations, high-level software triggers, reconstruction, analysis, and visualization applications. CLARA is built using a service-oriented architecture, where the relevant software applications are composed of interlocking building blocks called micro-services, which are linked together by data-stream pipes. The technology and algorithmic solutions, such as high-level programming languages or hardware deployment, are used to process the data. The specific software application implemented in CLARA is determined by the micro-services, which receive input data, process it, and produce output data organized into tabular structures called “banks” configured by the service developer [36].

The CLARA framework offers service work implementation in Java, C++, and Python programming languages. However, currently, all of the CLAS12 re-construction services that are deployed using the CLARA framework are written in Java [36]. This is because Java is considered to be a secure and robust programming language.

2.3 SIMULATION

The Geant4 Monte-Carlo (GEMC) package is a simulation tool that is commonly used in experimental particle physics to model the interactions of particles with matter. In particular, it is frequently used in simulations of the CLAS12 detector system to help researchers understand how the detectors respond to different types of particles and how they can be calibrated to improve accuracy. GEMC is especially useful in studying the geometrical acceptance and tracking efficiency of the CLAS12 detectors, as well as the detector response [37]. Accurately calculating these factors is essential for obtaining reliable measurements of the physical properties of the particles being studied. Overall, GEMC is a valuable tool in experimental particle physics research, and its use in the CLAS12 experiment is an excellent example of how it can be used to improve our understanding of particle interactions and detector performance.

GEMC is a C++ framework that leverages the powerful Geant4 toolkit to simulate the behavior of particles as they pass through matter. Geant4 is a widely-used toolkit for simulating the interactions of particles with matter, and it is especially well-suited for simulating complex experimental setups.

One of the key features of GEMC is its application-independent geometry description [37]. This means that GEMC can be used to simulate a wide variety of experimental setups, from high-energy physics experiments to medical imaging applications, without needing to modify the underlying code. The geometry is described in a simple and intuitive language, which makes it easy to create even complex geometries.

Another advantage of GEMC is its easy-to-use interface for building and running experiments [37]. The framework provides a user-friendly interface that allows users to easily set up and configure simulations, run them, and analyze the results. This makes it easy to explore different experimental designs and configurations and to optimize them for specific research goals.

Finally, GEMC also provides support for importing CAD and GDML files [37], which makes it easy to create complex geometries from existing 3D models. This is especially useful for designing experimental setups that involve complex shapes or geometries, such as medical imaging devices.

In GEMC, simulation parameters are stored in an application-independent external database. This means that the database can be used to define GEANT4 objects at runtime without needing to modify the underlying code. The database is typically populated with data and parameters that describe the experimental setup, such as the geometry, materials, mirrors, physics list, database constants, digitization, and electromagnetic fields [37].

The LUND format is a text file format utilized to store particle event data. It comprises of two rows; the first row contains header information that specifies the event and its kinematic properties, while the block of second rows include one row per particle, describing the characteristics of each particle.

The first row header information includes such as no of particles, Mass number of target, Atomic number of target, Target polarization, Beam polarization, xBj, $\sqrt{(W^2)}$, Q^2, Radiative factor, and phase space factor (see example below). Certain properties like the particle's momentum, position, and energy are employed by GEMC, whereas others are designated as UD (used designed), indicating that they are not used by GEMC but can be defined by the user for their specific purposes. In the second row, each row corresponds to a single particle, and it describes the properties of the particle such as index, charge, type (active or not), particle ID, index of parent, index of daughter, momentum x, momentum y, momentum z, energy of the particle, mass of the particle, vertex x, vertex y, and vertex z (see example below).

Following Fig. 19 is an example output for the deep two pion ($e'p'\pi^+\pi^-$) event with radiative correction.

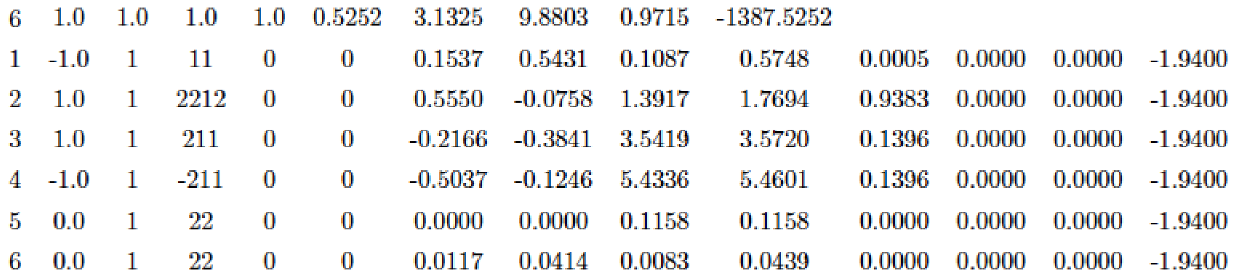

```
6  1.0   1.0   1.0   1.0  0.5252   3.1325   9.8803  0.9715  -1387.5252
1  -1.0  1     11    0    0        0.1537   0.5431  0.1087  0.5748      0.0005  0.0000  0.0000  -1.9400
2  1.0   1     2212  0    0        0.5550  -0.0758  1.3917  1.7694      0.9383  0.0000  0.0000  -1.9400
3  1.0   1     211   0    0       -0.2166  -0.3841  3.5419  3.5720      0.1396  0.0000  0.0000  -1.9400
4  -1.0  1     -211  0    0       -0.5037  -0.1246  5.4336  5.4601      0.1396  0.0000  0.0000  -1.9400
5  0.0   1     22    0    0        0.0000   0.0000  0.1158  0.1158      0.0000  0.0000  0.0000  -1.9400
6  0.0   1     22    0    0        0.0117   0.0414  0.0083  0.0439      0.0000  0.0000  0.0000  -1.9400
```

FIG. 19. An example output for the deep two pion ($e'p'\pi^+\pi^-$) event with radiative correction.

2.4 EVENT RECONSTRUCTION

The Event Reconstruction software, developed in the CLARA software framework, aims to reconstruct raw data from detectors or simulations. Its main objective is to accurately reconstruct events. The software is designed to produce physics output that includes particle identification and track parameters.

2.5 DATA FORMAT

In CLAS12, there are different types of data format through input to output. The raw data format is called as EVIO (Event Input-Output) which is the data format designed and maintained by the Jlab Data Acquisition Group. For the reconstruction and analysis, CLAS12 has developed High Performance Output (HIPO) format. This HIPO data format

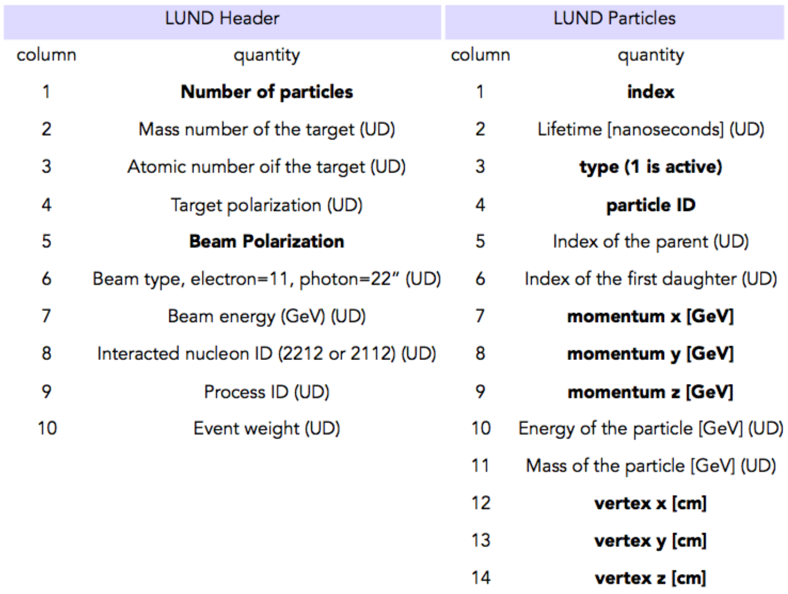

LUND Header		LUND Particles	
column	quantity	column	quantity
1	**Number of particles**	1	**index**
2	Mass number of the target (UD)	2	Lifetime [nanoseconds] (UD)
3	Atomic number oif the target (UD)	3	**type (1 is active)**
4	Target polarization (UD)	4	**particle ID**
5	**Beam Polarization**	5	Index of the parent (UD)
6	Beam type, electron=11, photon=22" (UD)	6	Index of the first daughter (UD)
7	Beam energy (GeV) (UD)	7	**momentum x [GeV]**
8	Interacted nucleon ID (2212 or 2112) (UD)	8	**momentum y [GeV]**
9	Process ID (UD)	9	**momentum z [GeV]**
10	Event weight (UD)	10	Energy of the particle [GeV] (UD)
		11	Mass of the particle [GeV] (UD)
		12	**vertex x [cm]**
		13	**vertex y [cm]**
		14	**vertex z [cm]**

FIG. 20. The format of the LUND file [38].

was designed to provide data compression, using LZ4 [36] which is the fastest compression algorithm currently available, and random access. HIPO data format is record based format with full indexed file structure. It stores data in separate records, with tags associated with each records. Each record is compressed and a pointer to the record is kept in the file's index table [36]. This feature of "hipo" format allow us to separating events during reconstruction based on the content of the event (e.g., number of reconstructed particles). Thus, the user can read portion of a data file according to the desired final state.

Furthermore, its compression and random access features, the HIPO format also includes a suite of utility programs such as file merging/splitting, faster bank reading, file statistics, event-by-event content display, and bank filtering for DST [36].

The HIPO library offers both Java and C++ implementations. The C++ version is built on top of the ROOT analysis framework, which enables HIPO files to be read from the ROOT framework. This extension of the ROOT base classes facilitates the reading and processing of HIPO files in the C++ environment [36].

2.6 DATA PROCESSING

Data processing for CLAS12 is carried out on the Jefferson Lab Scientific Computing

(SciComp) farm. The first step involves retrieving the decoded raw files from permanent tape storage. Subsequently, these files are reconstructed on the SciComp farm nodes, and the reconstructed output is then transferred to the cache disk, which is used for temporary storage. Finally, the data is copied to the Mass Storage System (mss) for permanent storage (as shown in Fig. 21).

The reconstructed output can be used to create “trains”, which are stored in a volatile disk for temporary storage and can be distributed to the analyzer. The train configuration may be adjusted over time, but the final train configuration used for publication preparation will be stored permanently on mss [36].

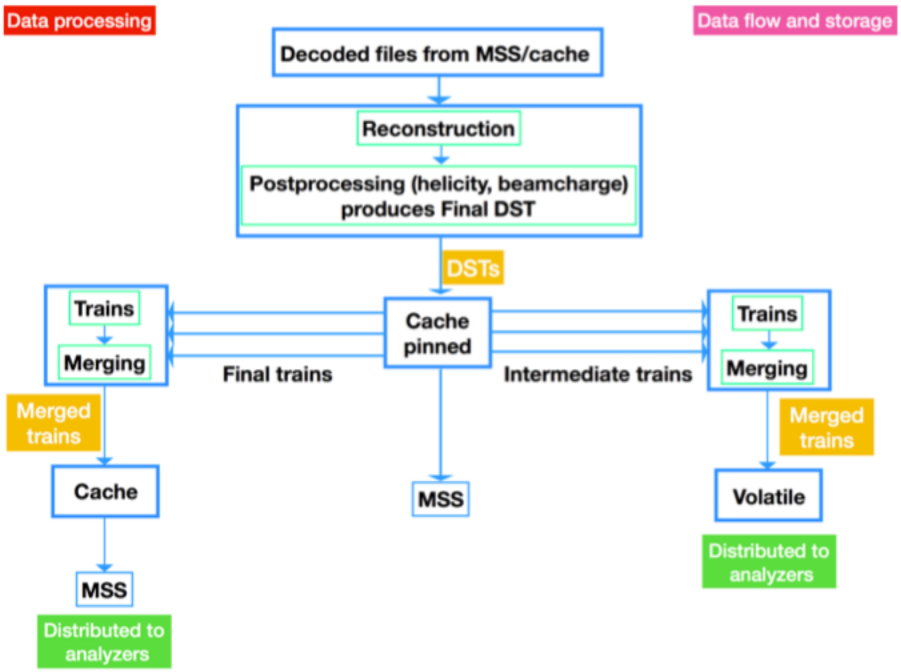

FIG. 21. A diagrammatic representation of the hierarchical data processing workflow in CLAS12 is shown below. The workflow consists of three stages: decoding, reconstruction, and creating analysis trains [34].

Decoding: Decoding is the first stage of data processing for CLAS12, which entails extracting hits from waveforms, translating data-acquisition/hardware nomenclature (associated with crate/slot/channel labels) into physical detector objects, performing special analyses dependent on serial event access, and converting the data from the input EVIO format to the HIPO data format [36]. This process is computationally intensive and performed in a single thread, since it results in a reduction of file size by a factor of approximately 5.

Reconstruction: The reconstruction is the second stage of data processing in CLAS12, which involves tracking, clustering, calorimetry, time-of-flight, and event building. This process runs in the multi-threaded CLARA framework and can be configured to produce various output data schema depending on the purpose during full-scale data processing or larger, special-purpose banks during preliminary calibration phases [36].

Trains: The final stage of data processing in CLAS12 involves creating analysis trains that perform event skimming, corrections, and common analysis plugins. Skimming involves filtering specific final states. The speed of skimming depends on how services are fed, and is currently slow since services are fed on an event-by-event basis. Trains are split into multiple output files based on final-state event selection. A train may include a plugin to correct ECAL sampling fraction and analysis filters for different final states. The IO services read events from HIPO files and process them through the analysis train. Using this process, an EVIO file of about 2 GB in size is typically reduced to a HIPO file of about 200 MB for physics analysis.

The CLAS12 analysis group has created a list of wagons, and for my analysis, I have utilized the nSIDIS Inclusive skim (skim22) in its “v1” version. The following topology has applied for the nSIDIS skim 22.

```
"nSidis:",
  "id: 22",
   "forward: 11:X+:X-:Xn",
   "  electron: Q2>1 && W>2 && p>2 && vz>-25 && vz<20",
```

This skim files has selected the electron in FD, $Q^2 > 1.0$ GeV^2, $W > 2$ GeV, $p > 2$ GeV, and z vertex in between -25 cm and 20 cm cuts.

CHAPTER 3

ANALYSIS FRAMEWORK

3.1 DATASET

This analysis used RG-A fall 2018 in-bending data acquired by the CLAS12 detector using an electron beam energy of 10.6 GeV incident on the liquid hydrogen (LH_2) target. This analysis used both Forward Detector (FD) and Central Detector (CD); considering that some of my hadrons (protons and pions) pass through the CD, both detectors are essential, even though CD tracking is not reliable at the moment. Currently, this analysis is proving to be quite challenging. We used the nSIDIS Inclusive skim (skim22) in its “v1” version files contain all the data with an electron in the FD, as detailed below.

3.2 EVENT BUILDER

Event Builder plays a fundamental role in the CLAS12 System. It is responsible for associating tracks with detectors. In CLARA’s Event Builder micro-service, where all relevant information from each detector is assigned to a track, data structures called “banks” are used to store the information provided by the Event Builder. A data bank is maintained for each sub-detector in CLAS12, which contains information specific to each detector, such as the coordinates of the hit x, y, z, timing information, energy, detector layers and etc. The names of the banks are prefixed with the abbreviation “REC”; these banks contain what have traditionally been referred to as Data Summary Tapes (DST), and that information help for the physics analysis. The “REC” banks mainly included REC::Particle, REC::Response (subcategories of REC::Calorimeter, REC::Scintillator, REC::Cherenkov, REC::Track, REC::Forward Tagger), REC::Traj, and REC::CovMat under physics banks. The REC::Particle is the most important bank for physics analysis, and the content of the REC::Particle bank is shown in Fig. 22. The different species of particles are assigned the values of the Particle ID (PID) in EB REC::Particle bank, which can be used directly for the physics analysis. The following section provides further information regarding how they assigned PIDs and particle identification refinement that was used to obtain clean particle samples.

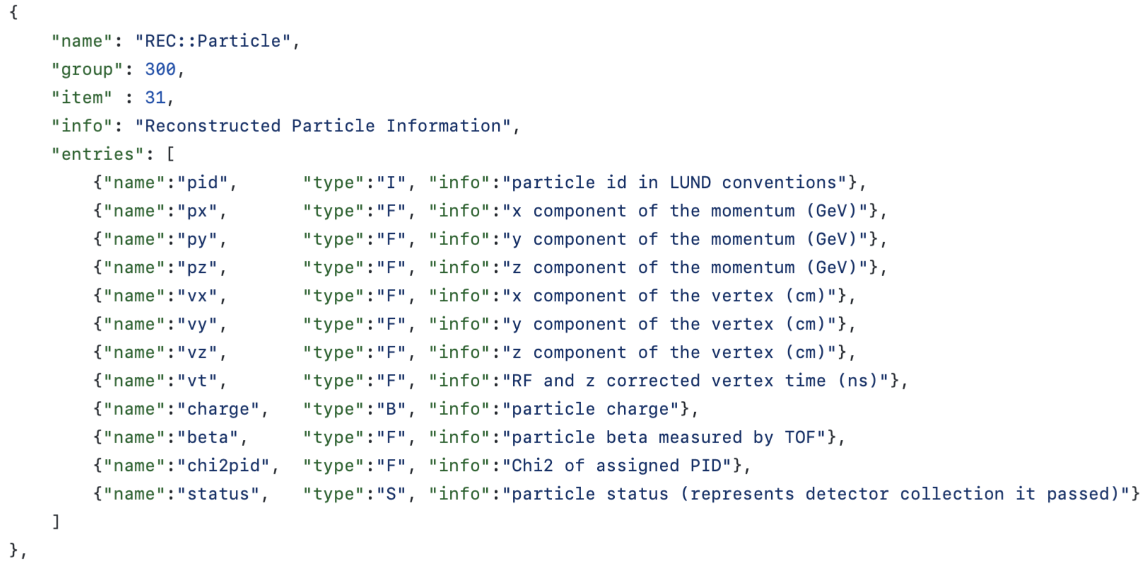

```
{
    "name": "REC::Particle",
    "group": 300,
    "item" : 31,
    "info": "Reconstructed Particle Information",
    "entries": [
        {"name":"pid",      "type":"I", "info":"particle id in LUND conventions"},
        {"name":"px",       "type":"F", "info":"x component of the momentum (GeV)"},
        {"name":"py",       "type":"F", "info":"y component of the momentum (GeV)"},
        {"name":"pz",       "type":"F", "info":"z component of the momentum (GeV)"},
        {"name":"vx",       "type":"F", "info":"x component of the vertex (cm)"},
        {"name":"vy",       "type":"F", "info":"y component of the vertex (cm)"},
        {"name":"vz",       "type":"F", "info":"z component of the vertex (cm)"},
        {"name":"vt",       "type":"F", "info":"RF and z corrected vertex time (ns)"},
        {"name":"charge",   "type":"B", "info":"particle charge"},
        {"name":"beta",     "type":"F", "info":"particle beta measured by TOF"},
        {"name":"chi2pid",  "type":"F", "info":"Chi2 of assigned PID"},
        {"name":"status",   "type":"S", "info":"particle status (represents detector collection it passed)"}
    ]
},
```

FIG. 22. Overview of the REC::Particle bank's content.

In the past (2019), I attempted to identify particles and tried my own PID algorithms, however, I was not able to achieve a better PID than the one we have in Event Builder. This study has been done using Coatjava version 5b.7.8. The results are in the Appendix.D.

3.3 ELECTRON IDENTIFICATION

In physics analysis, electrons are generally required as the first particle. The Event Builder assigned PID = 11 to identify the electron. There are several cuts applied in order to determine the electron PID in the event builder. Some cuts are designed to remove the Minimum Ionizing Particles (MIPS), such as negative π^-. The following cuts are assigned for the Event builder electron PID [34].

- Negative charge track in the Forward Detector.
- Cut on number of photo-electrons in High Threshold Cherenkov Counter (HTCC): $N_{phe} > 2.0$.
- Pre-Shower Calorimeter (PCAL) energy cut $PCAL_{dep} > 60$ MeV.
- Calorimeter Sampling Fraction (E_{dep}/p) vs E_{dep} cut $\pm 5\sigma$.

In the REC::Particle bank structure, the electron which defines the event time is entered as the first particle. The Central Detector does not have either Cherenkov detectors or Electromagnetic Calorimetry, and therefore cannot identify electrons.

3.3.1 NEGATIVE CHARGE TRACK IN THE FORWARD DETECTOR

When a charged particle passes through a strong magnetic field, the particle trajectory will be deflected. In the region of the Forward Detector, there is a strong toroidal magnetic field. This field deflects charged particle trajectories primarily along the polar angle. When the torus polarity is set to deflect negatively charged particles to smaller polar angles (towards the beam axis,) we label this the "inbending" configurations. Throughout a series of runs spanning many weeks, data is taken in both "inbending" or "outbending" configurartions. This thesis only examines the "inbending" data. In the reconstruction algorithm, charges are assigned based on the track curvature. Thus, only negative charge tracks are selected as candidate electrons, subject to the Cherenkov and Calorimetry cuts.

The HTCC contains CO_2, and therefore only, charged particles with speed $v \geq 0.9995\,c$ will produce a flash of blue light in this detector. The requirement on the number photo-electrons in the HTCC: $N_{phe} \geq 2$ reduces the negative pion (π^-) contamination in electron candidate tracks for momenta up to 4.9 GeV [34]. The Photomultiplier tubes (PMT) used in the Cherenkov counter record how many photons are emitted as a result of Cherenkov radiation by a charged track traversing the detector volume. The PMTs have a quantum efficiency of approximately 20% and a gain in excess of 10^6. After calibration, the PMT signal is quantified in 'photo-electrons' (phe): the number of primary electrons emitted from the photo-cathode (before gain) from the Cherenkov light flash. It is expected that an electron candidate track will produce more than 2 Phe, which is the minimum threshold for this cutoff [34]. The Fig. 23 shows the Number of photoelectron plot in HTCC to identify the electron candidate.

3.3.2 CUT ON MINIMAL PCAL ENERGY DEPOSITION

This minimal Preshower Calorimater (PCAL) energy deposition cut can be used to discriminate between electrons and negative pions (π^-). In the dense material of a calorimeter, high energy electrons, and gamma-rays produce a shower of secondary gamma-rays and electron-positron pairs. In contrast, pions and other heavier high-energy particles deposit energy only by ionization. At CEBAF energies, the pions are close to the minimum of the ionization *vs.* momentum curve and are called Minimum Ionizing Particles (MIPs). During the transit of an electron through the calorimeter detectors, the electron develops an extended

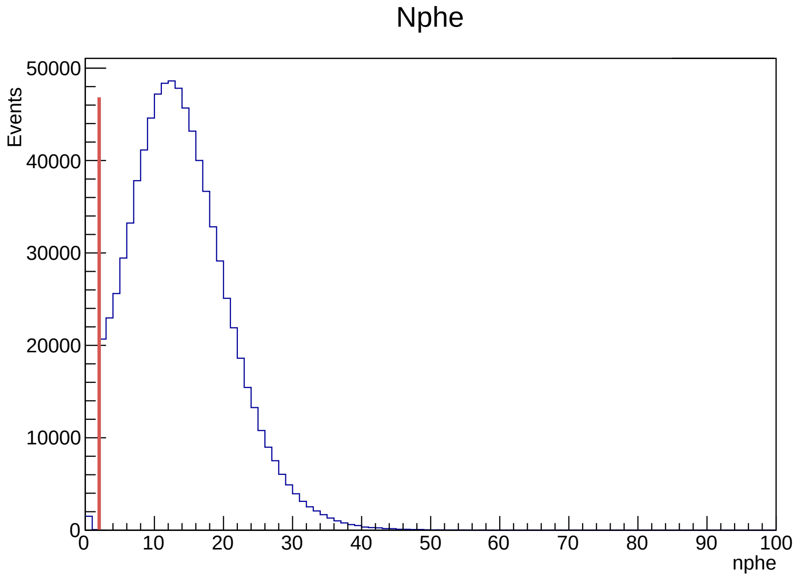

FIG. 23. Number of Photo-electrons in HTCC. $Nphe > 2$ cut has used to identify the electron.

electromagnetic shower, which ultimately deposits all of its energy in the three-layer FD ECal (PCAl, ECal-inner, ECal-outer). The pions, however, as MIPS deposit a much smaller energy, which is approximately independent of momentum therefore constant event-by-event. As a result, electrons and pions exhibit distinct energy signatures that can be exploited to choose candidate electron tracks [34]. Fig. 24 shows the energy deposited in the Preshower Calorimeter (PCAL) vs. Electromagnetic Calorimeter (ECAL = $(\mathrm{EC}_{inner} + \mathrm{EC}_{outer})$), which is consisted of inner and outer regions. Although the Event Builder used a cut of 0.06 GeV, we used a cut of 0.07 GeV in order to increase the accuracy of the electron selection. The Fig. 24 red vertical line indicates the 0.07 GeV cut that was applied in order to discriminate electrons from negative pions.

3.3.3 CUT ON THE SAMPLING FRACTION VS. MOMENTUM CUT

In the Electromagnetic Calorimeter (ECAL), when an electron emits an electromagnetic shower, it deposits a proportional amount of energy according to its momentum. By plotting ECAL's deposited energy divided by momentum ($ECAL_{total}/p$) as a function of momentum (p), it is possible to identify a good candidate for the electron. The $ECAL_{total}$ is the sum of the energy deposited in the PCAL, ECAL (inner), and ECAL (outer) and $\frac{ECAL_{total}}{p}$ named

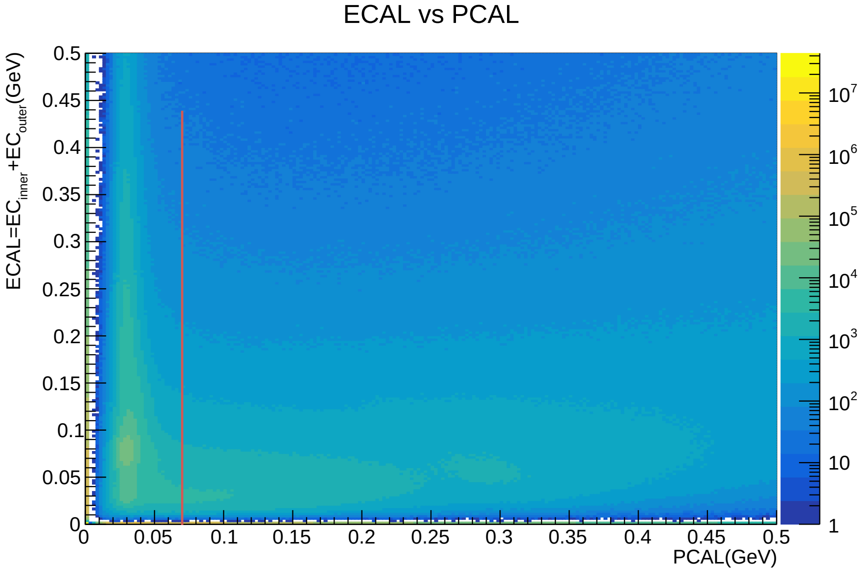

FIG. 24. $ECAL = EC_{inner} + EC_{outer}$ energy deposited as a function of PCAL energy deposited. In PCAL, a cut of 0.07 GeV removes pions (MIPs) below the vertical red line.

as Sampling Fraction. Electrons exhibit a nearly constant sampling fraction signature with a ratio of $\sim$ 0.25 across all momenta. This is evident in Fig. 25. The Fig. 25 illustrates the $\frac{ECAL_{total}}{p}$ sampling fraction as a function of momenta (p). However, the Event Builder applied a $\pm 5\sigma$ cut, whereas we applied a $\pm 3.5\sigma$ tight cut to suppress the misidentified pions as in Fig. 25. Moreover $P_e > 2.0$ GeV threshold has been applied in the Fig. 25.

3.3.4 PCAL FIDUCIAL CUT

The calorimeter generates electromagnetic showers when electrons hit it. It is possible that the shower of electrons will not be completely contained within the calorimeter volume if the electron strikes close to the edge of the detector. In this case, the reconstructed energy deposition is reduced, which will result in an incorrect sampling fraction. Furthermore, in this case, it is not possible to determine the cluster size accurately [34]. Consequently, electron identification power may be reduced in both cases. Therefore, we can use PCAL (U, V, W) coordinates to reject tracks that are too close to the edges. Note that, The PCAL detector in the CLAS12 experiment is composed of three layers of scintillator strips arranged in a repeating $U-V-W$ pattern, with each layer rotated by 60° with respect to the previous one. This configuration allows for more complete coverage of the detection area and improves the

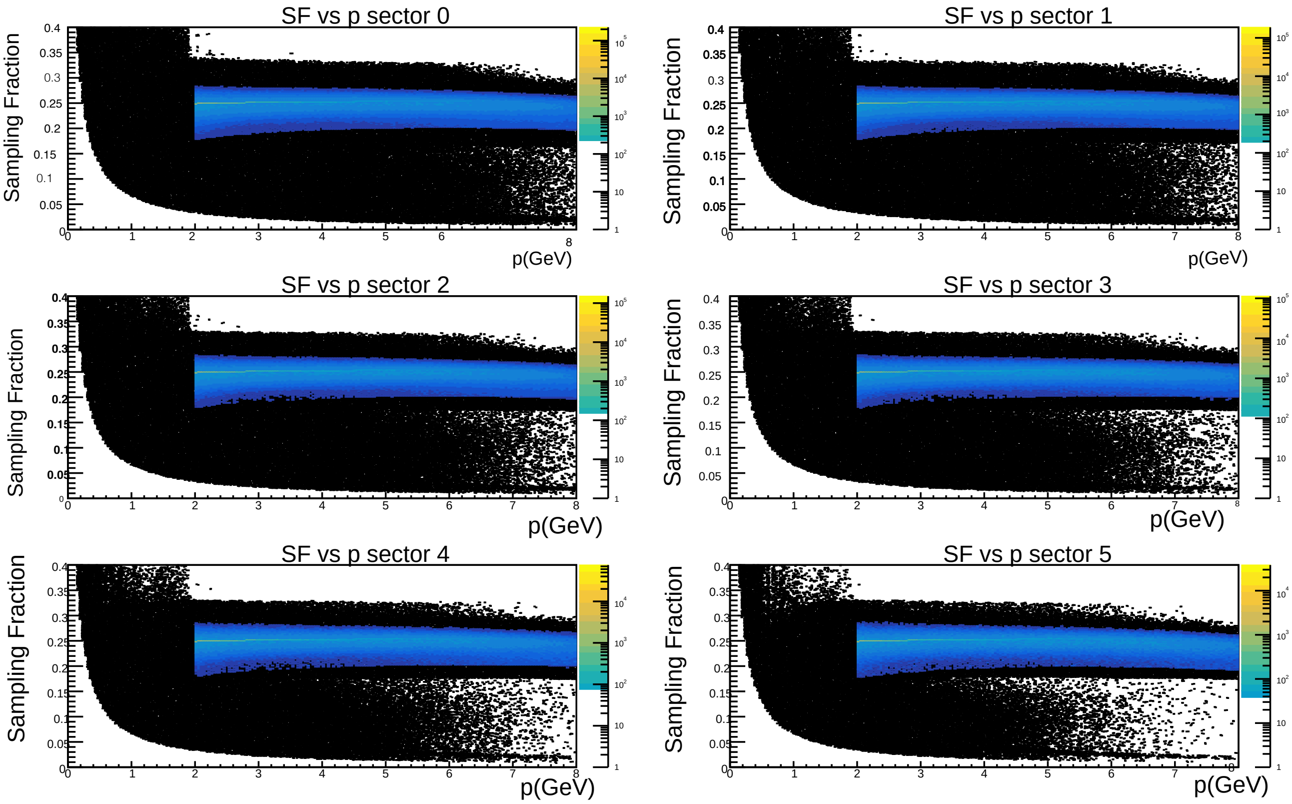

FIG. 25. For selecting an electron candidate, Energy deposited in the ECAL is divided by the momentum as a function of momentum for all 6 sectors. Black color plots are before applying sampling fraction cut (Nphe and PCAL minimal energy deposition cuts are already applied). Color plots applied ±3.5 sigma cut and $P_e > 2.0$ GeV threshold (colored) to suppress the pion misidentification.

accuracy of energy and position measurements. Each layer of scintillator strips is positioned perpendicular to the other two, forming a three-dimensional coordinate system to locate energy deposition. The U and V layers are parallel to the plane of the CLAS12 detector, while the W layer is perpendicular to it. Thus, to determine the cut borders, the sampling coordinates V and W are correlated with the local calorimeter coordinates. The Fig. 26 [34] shows the boundaries used in the RG-A Analysis note. Monte Carlo simulations of the sampling fraction as a function of the V and W coordinates (see Fig. 27 [34]) support the results of experimental experiments. Therefore following three PCAL cuts are used in the Clas12 RG-A Analysis note.

- loose: 1 scintillator bar (4.5 cm).

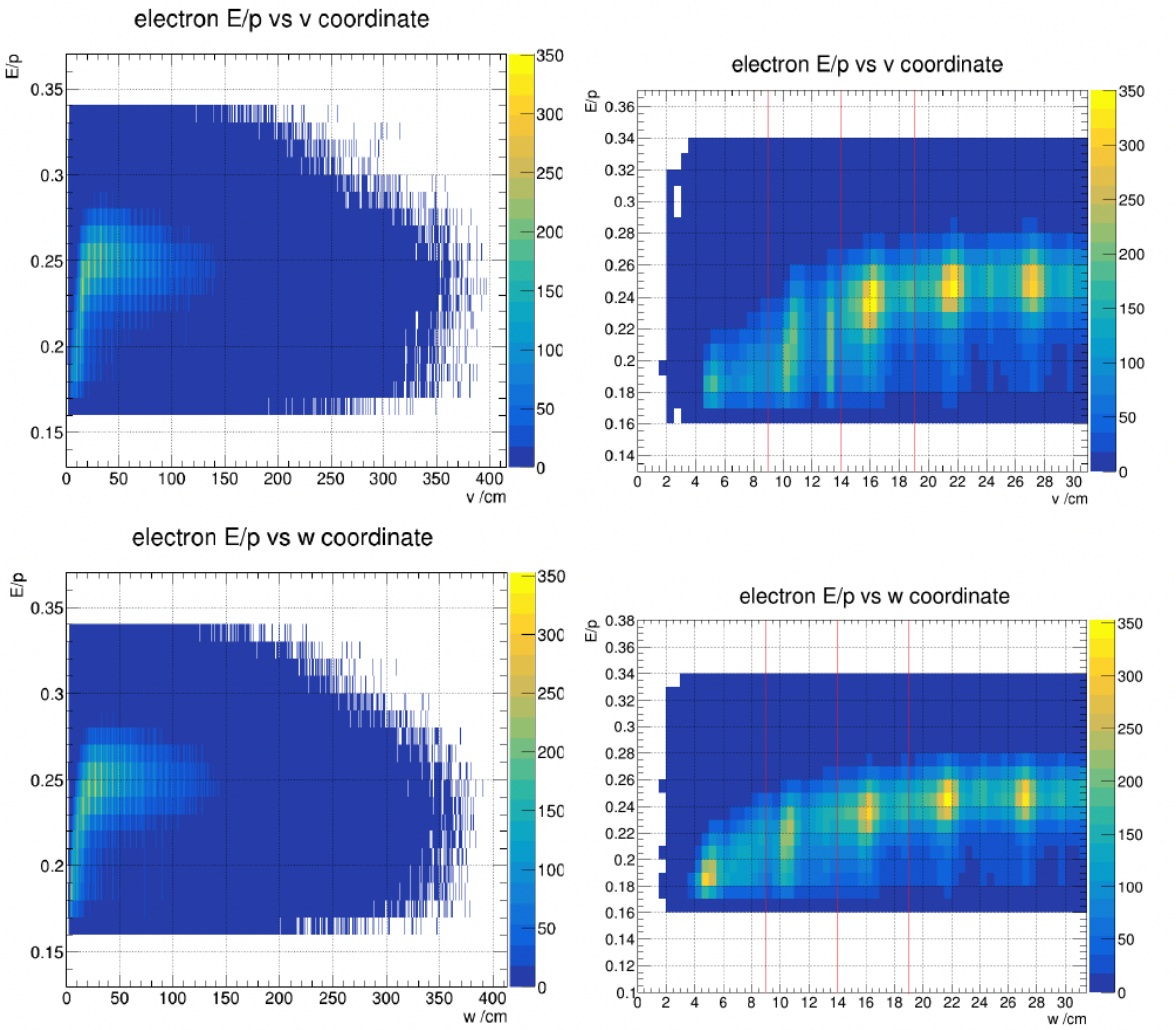

FIG. 26. In the left diagram, the sampling coordinates V (upper) and, W (lower) are correlated over the entire range (left), and in the right diagram, the sampling coordinates are zoomed to the relevant region (right) [34].

- medium: 2 bars (14.0 cm)-Used tight bars in this analysis.
- tight: 3 bars (19 cm).

When measuring beam-spin asymmetry (BSA), loose cuts may be used, whereas tight cuts may be required for the cross-section measurements. The 2-bars of 14 cm cut has been used to identify electrons for this study. Fig. 28 shows the PCAL fiducial cut before (left) and

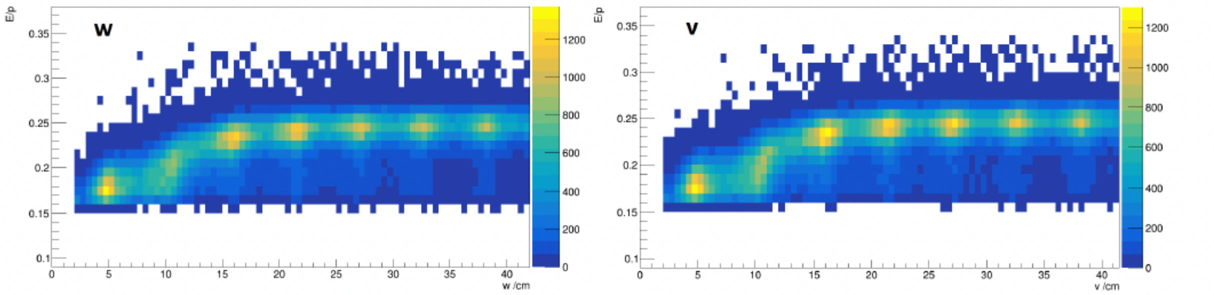

FIG. 27. Sampling Fraction as a function of V and W coordinated in MC Simulation [34].

after (right) the medium 2 bars cut.

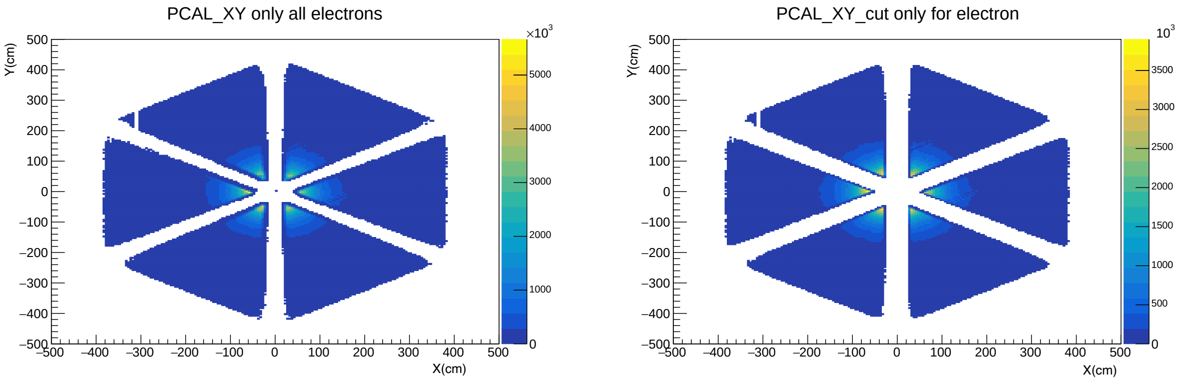

FIG. 28. PCAL fiducial cuts before (left) and after (right) medium cut 2 bars (14 cm).

3.3.5 DC FIDUCIAL CUTS

Drift Chamber (DC) fiducial cuts can be used to reject the poorly reconstructed tracks in the edges of the Drift Chamber (DC). DC fiducial cuts are derived from $chi2/NDF$ distributions from the track, according to the CLAS12 RG-A analysis note. These cuts are extracted in the local $\theta\phi-$plane and $xy-$plane. The second approach (cut extracted in $xy-$plane) in CLAS12 RG-A analysis note had been used for better results of electron identification. Because in this method, extrapolated cut borders are more stable [34]. The more details about these DC fiducial cuts are in CLAS12 analysis note [34] section 8.3. Fig. 29 illustrates the before and after DC fiducial cuts.

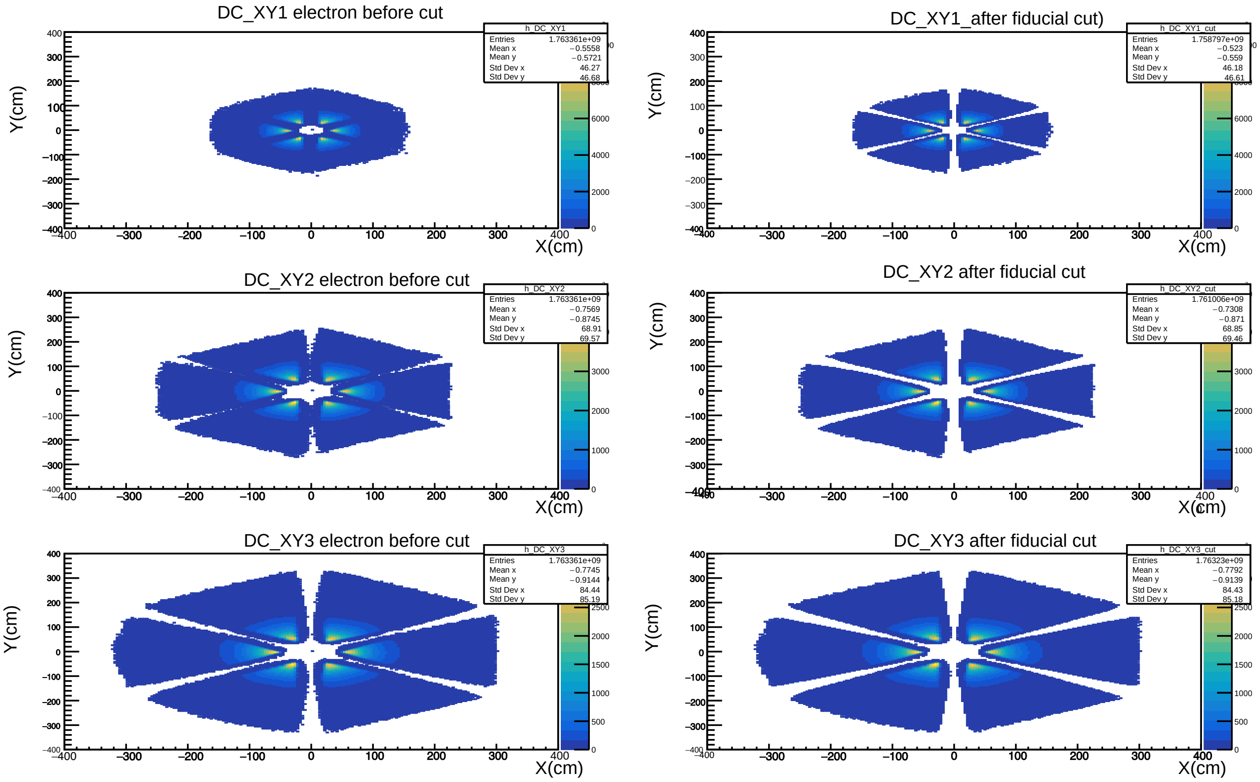

FIG. 29. DC fiducial cuts results for electron, region 1 before (top left) and after (top right), region 2 before (middle left) and after (middle right), and region 3 (bottom) before (bottom left) and after (bottom right).

3.3.6 Z-VERTEX CUT

The Z-vertex cut is necessary to ensure that electrons only originate from the hydrogen target. This cut primarily rejects electrons that have been scattered at the target cell's window. The Figure shows the z-vertex distribution of the electron in the in-bending torus field. The target is 5 cm long, centered at $z = -3$ cm, since the cut for the electron selection is set to $[-13, 12]$ cm.

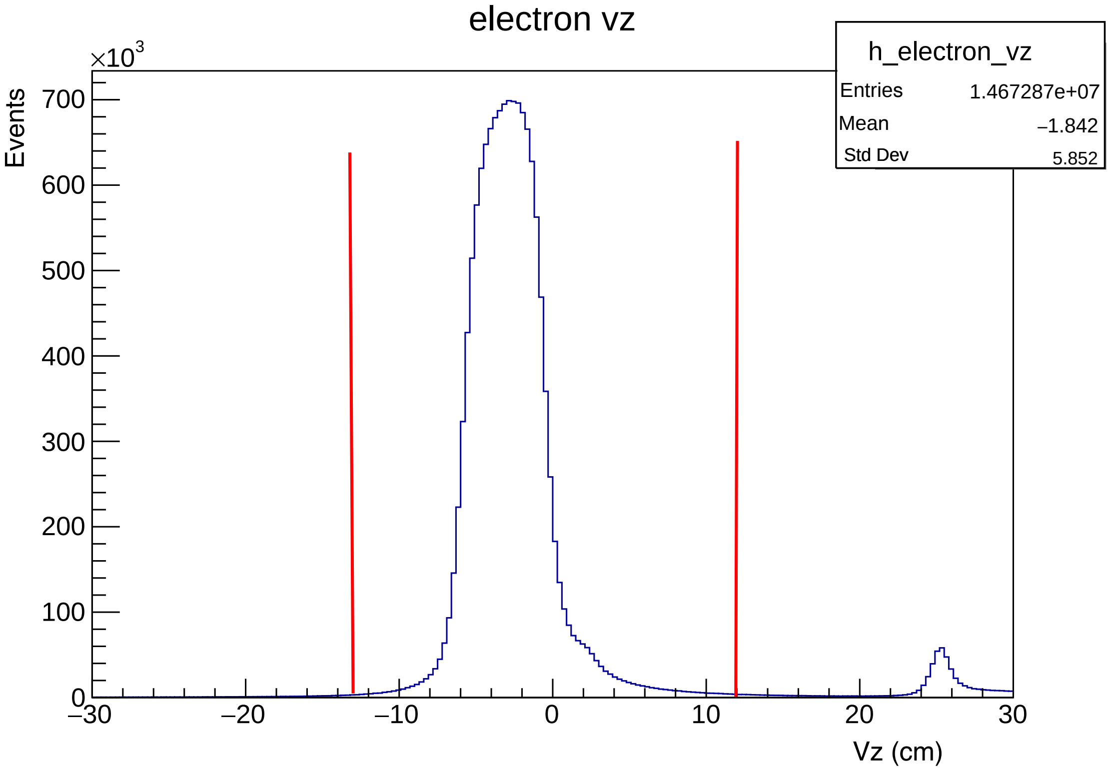

FIG. 30. z-vertex (cm) coordinates for electrons with an in-bending torus field. The red vertical lines represent the cut between -13 cm $< v_z < +12$ cm.

3.3.7 SUMMARY OF ELECTRON IDENTIFICATION

The CLAS12 event builder provides the loose particle ID, which is used as a basis for PID refinement. It is possible to achieve a better result of electron identification by making some additional cuts with the electron PID. All the cuts for the electron are summarized as follows.

- Event builder PID= 11.
- A cut on the minimal energy deposition in the PCAL > 0.07 GeV.
- A cut on the sampling fraction vs. momentum- ±3.5-Sigma region.
- PCAL fiducial cuts.
- DC fiducial cuts on regions 1, 2 and 3.
- A cut on the z-vertex position $[-13, 12]$ cm.

3.4 HADRON IDENTIFICATION

A discussion of the identification of proton, π^+, and π^- will be presented in this section. Chapter 2 of this thesis mentioned that the CLAS12 detector consists of two main detectors: Forward Detector (FD) and Central Detector (CD). Both FD and CD pass charged hadrons (protons, pions, kaons, deuteron). Therefore it is important to identify hadrons in both detectors separately. It is possible to identify charged hadrons using time-of-flight (TOF) detectors and CLAS12 drift chambers (DC). It is useful to utilize FTOF (consists of FTOF1B, FTOF1A, and FTOF2) and Drift Chamber for FD and CTOF for CD in order to identify hadrons. FTOF Panel 1B (one of the two layers of scintillator paddles in the FTOF system) is preferred because of its enhanced timing resolution over the other panels. But there is no preference in CD; only one timing response is available. The proton and pions are identified based on the timing difference between start-time and recorded time at the TOF detector, the trajectory length l, and the momentum p measured in the drift chambers. Eq. (76) shows the calculation of Δt. In this case, the PID is assigned to the track that which minimizes Δt:

$$\Delta t = t_{start\,time} - \left[t_{FTOF} - \frac{l}{\beta_h(p)} \right], \tag{76}$$

where: l-path length, p-track momentum, $\beta_h = \frac{v}{c} = \frac{p}{\sqrt{(p^2+m_h^2)}}$- the ratio of the velocity of the particle to the speed of light, and "h" represents the hadrons such as protons, pions etc.

Fig. 31 (left) illustrates the relationship between β and p for FTOF panel B, and there are some accidentals resulting from different beam buckets separated by 2 ns. However, a clear separation of pions, kaons, and protons is seen in Fig. 31 (left). At high momenta, it's difficult to separate pions and kaons. The Fig. 32 (left) illustrates the relationship between β and p for FTOF 1B for negatively charged particles, as well as the effect of accidentals. $\beta = 1$ is from the electrons.

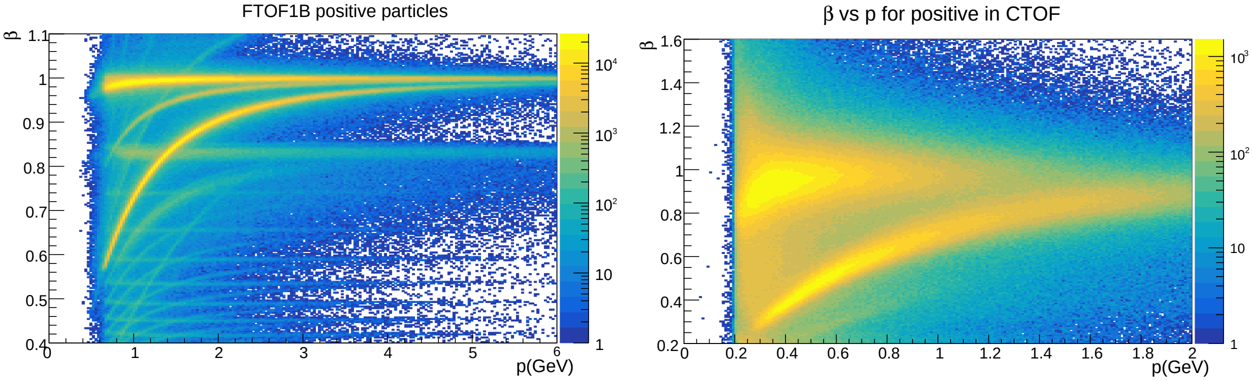

(a) (b)

FIG. 31. β as a function of momentum (p) for all sectors FTOF 1B (left) and CTOF (right) for positively charged particles.

A clear separation of particle species is apparent in Fig. 31 (left). Using slice fitting along the momentum axis, these distributions were investigated for positively charged particles in panel-1b in order to measure the separation between the species of particles using Gaussian widths [34]. More details about this particle separation is in CLAS12 RG-A analysis note [34]. However, the hadron identification has been assigned to the event builder PID. The

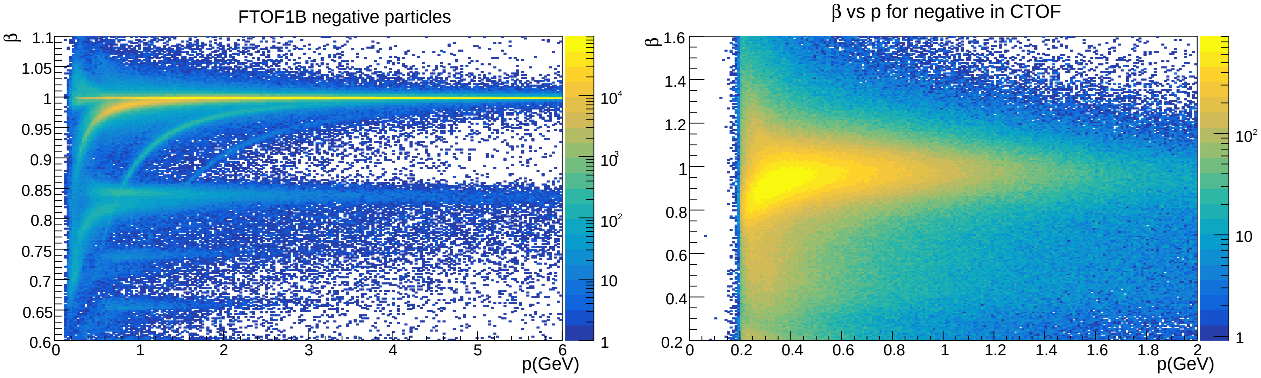

(a)

(b)

FIG. 32. β as a function of momentum (p) for FTOF 1B (left) and CTOF (right) for negatively charged particles.

Event Builder assigned PID for proton PID= 2212, for π^+ PID= 211 and for π^- PID= -211.

3.4.1 DC FIDUCIAL CUTS FOR HADRONS

For the DC fiducial cuts, two approaches have been used in the CLAS12 RG-A analysis, as discussed in section 3.3.5 in this thesis. The first approach (cut extracted in the local angle $\theta\phi$-plane) is used for hadrons with in-bending data. More details about this approach 1 is in RG-A CLAS12 analysis note [34] section 8. The Fig. 33 shows each π^+, π^-, and proton before (black) and after (colored) the DC fiducial cuts.

3.4.2 A CUT ON VERTEX DIFFERENCE BETWEEN ELECTRON AND HADRONS

The vertex difference between electrons and hadrons is cut to reject hadrons produced outside of the target region. At this point, we expect a common reaction vertex. This cut has been applied for both FD and CD. Fig. 34 shows the hadron vertex difference for proton, π^+ and π^- to the electron in the FD. The vertical red lines represent the cut $|V_z(electron) - V_z(hadron)| < 20$ cm. Moreover, this vertex difference between electron and hadrons cut has been applied for the proton, π^+, and π^- in the CD as well. Similar cut ($|V_z(e^-) - V_z(h)| < 20$ cm) is applied for the CD proton, π^+, and π^-. The Fig. 35 is evidence of that.

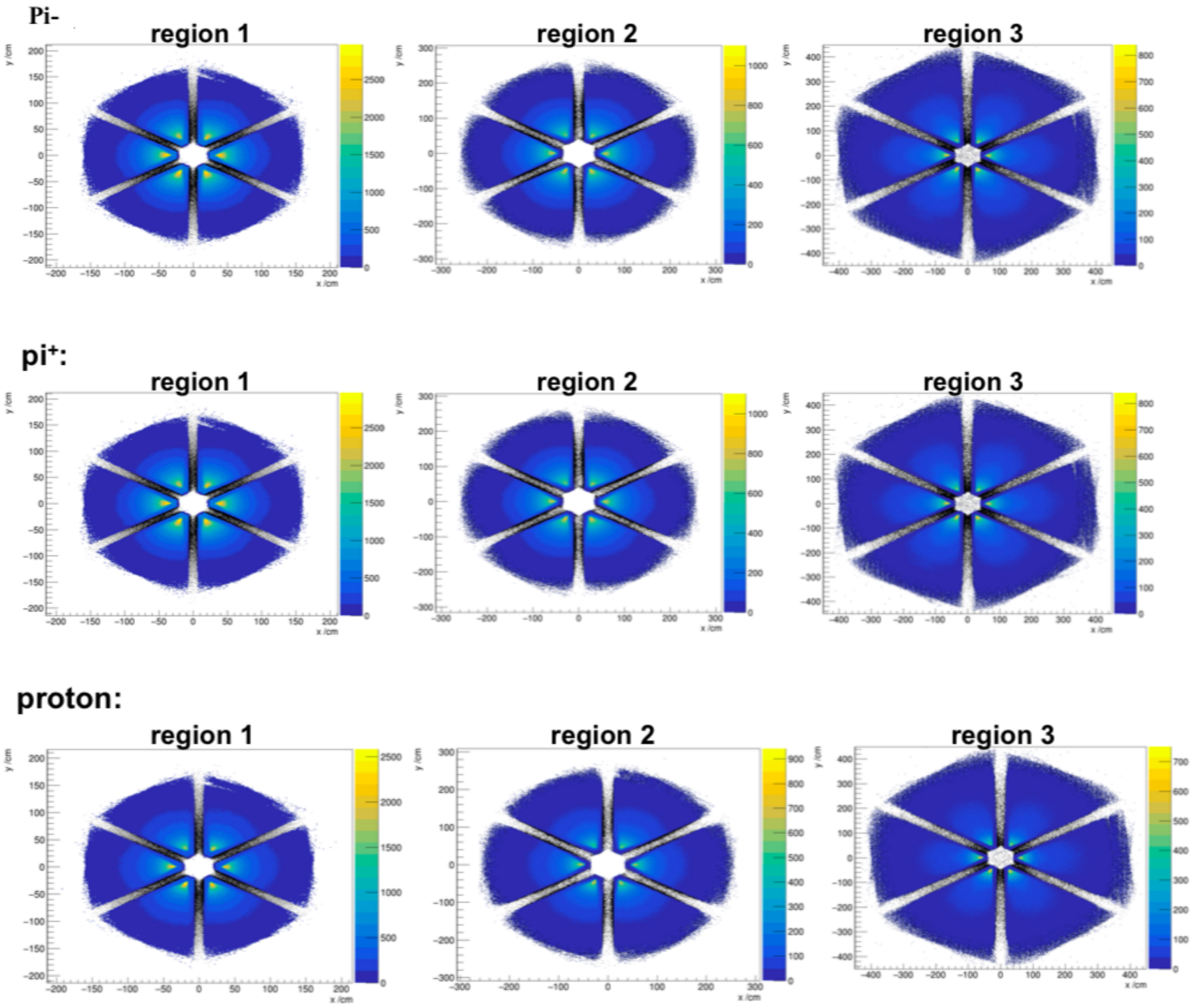

FIG. 33. Results before (black) and after (colored) DC fiducial cuts for π^- (top), π^+(*middle*) and proton (bottom).

3.4.3 CHI2PID CUT

A Chi2PID value (cut on the quality of the event builder PID) is assigned to each charged hadron by the Event Builder. The Fig. 36 shows the Chi2PID plots for proton, π^+, and π^- in FD for data. The same distributions are used in CLAS12 RG-A analysis note [34], but for the SIDIS π^+ and π^- MC and fitted using Gaussian distributions and 3σ cut has taken (see [34] section 8.2). For this analysis, the same cut values were used, since there is no difference between the Chi2PID cut for data and MC because it is given as multiples of sigma. Thus

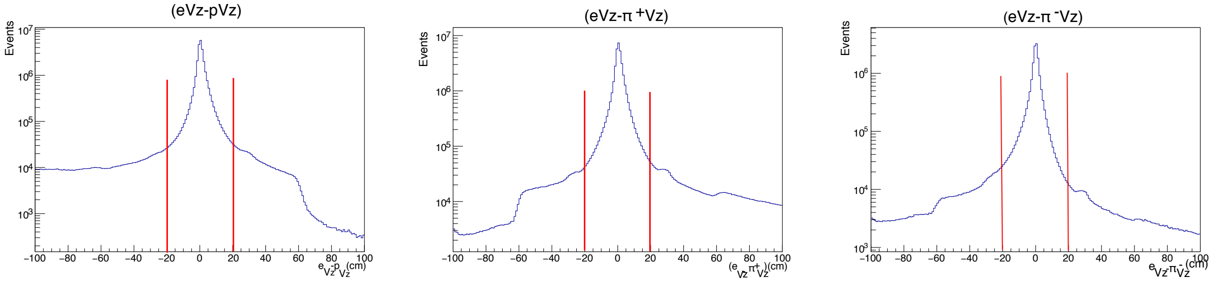

FIG. 34. Vertex difference between hadrons and electrons for FD. The red vertical line represents the cut $|V_z(electron) - V_z(hadron)| < 20$ cm.

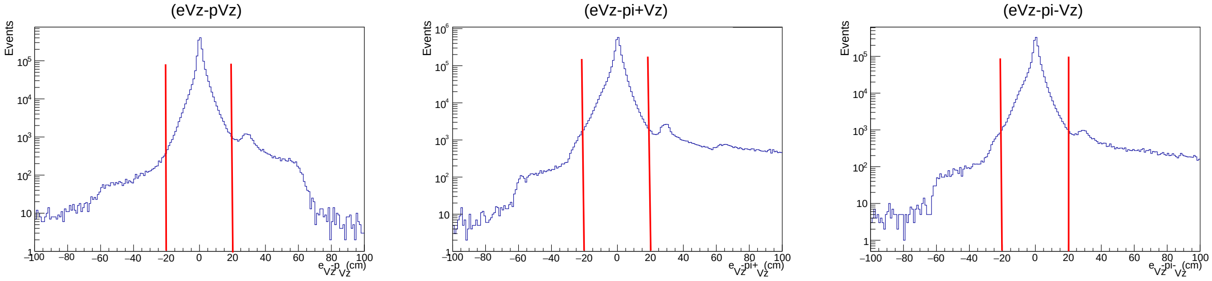

FIG. 35. Vertex difference between hadrons and electrons for CD. The red vertical line represents the cut $|V_z(electron) - V_z(hadron)| < 20$ cm.

for π^+ $|Chi2PID_{piplus}| < 2.64$ cut, for π^- $|Chi2PID_{piminus}| < 2.79$ cut and for the proton $|Chi2PID_{proton}| < 2.5$ (by eye) cut is used (see Fig. 36). But for the proton, π^+, and π^- in the CD, different chi2PID cuts have been used. Chi2PID distributions for three hadrons are shown in Fig. 37, with the red vertical lines representing each particle's Chi2PID cut.

3.4.4 DRIFT CHAMBER(DC) "CHI2" TRACK FITTING

The "Chi2" distribution is commonly used as a statistical tool to assess the quality of track reconstruction. The "REC::Track" bank provides this quantity, which can be used to evaluate the degree of similarity between the reconstructed track and the actual trajectory of the particle. The selection of a cut-off value for the "Chi2" distribution is a crucial aspect of such analyses, as it determines the level of precision and accuracy required. In

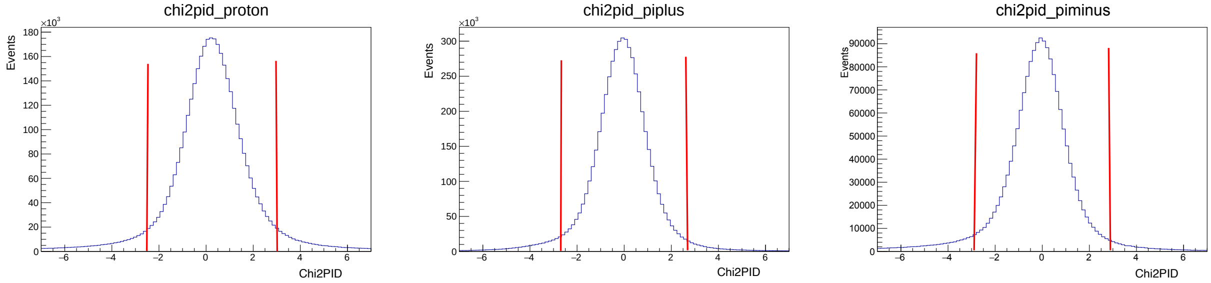

FIG. 36. ChiPID distributions for proton, π^+, and π^- in FD. The red vertical lines represents the cuts we used for the proton $|Chi2PID_{proton}| < 2.5$ (by eye), for π^+ $|Chi2PID_{piplus}| < 2.64$ cut for π^- $|Chi2PID_{piplus}| < 2.79$ cut.

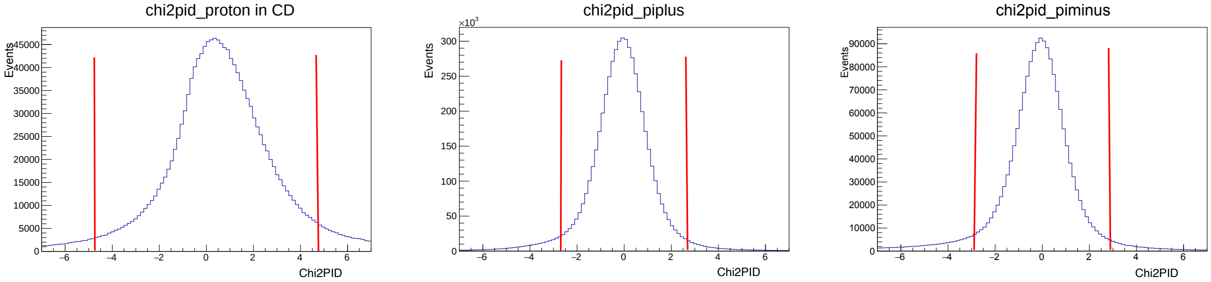

FIG. 37. ChiPID distributions for proton, π^+ and π^- in CD. The red vertical lines represents the cuts we used, for the proton $|Chi2PID_{proton}| < 4.7$, for π^+ $|Chi2PID_{piplus}| < 4.0$ cut, for π^- $|Chi2PID_{piplus}| < 4.1$ cut.

this particular instance, it appears that a cut-off of $Chi2 < 20$ was utilized to identify good quality tracking in the Drift Chamber (DC) "Chi2" distribution. This indicates that only tracks with a "$Chi2$" value below 20 were deemed to be of sufficient quality to be included in the analysis. The Fig. 38 is the Drift Chamber (DC) "$Chi2$" distribution and the red vertical line represent the $Chi2N < 20$ cut to identify the good quality of the tracking.

3.4.5 SUMMARY OF HADRON IDENTIFICATION

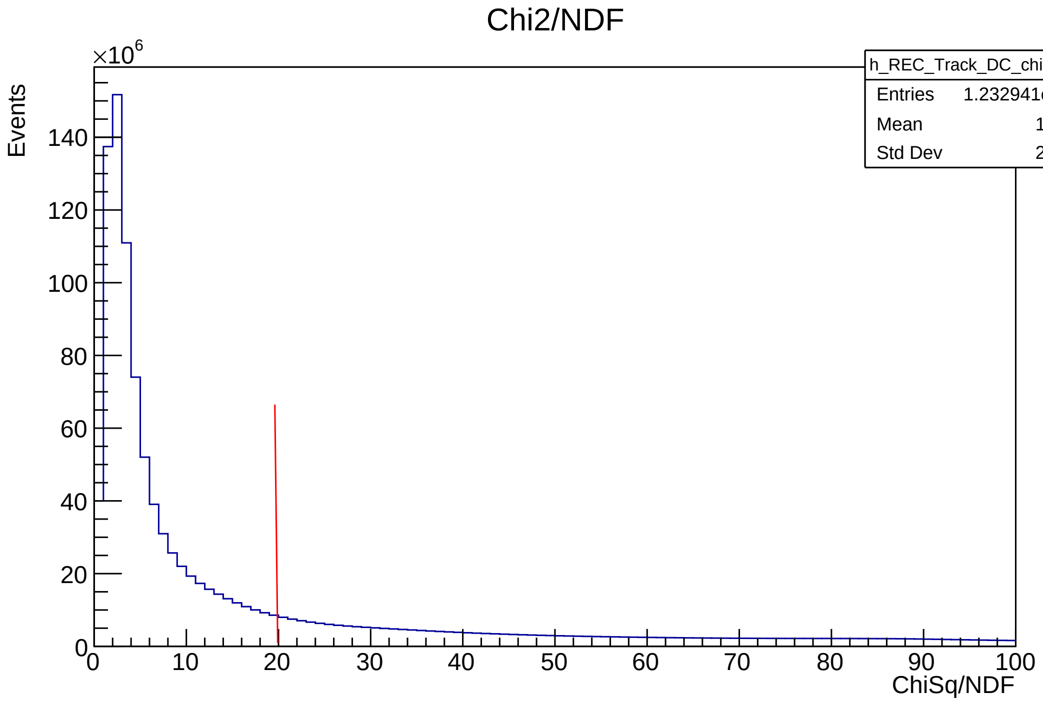

FIG. 38. The Chi2 distribution for the Drift Chamber tracking. The red vertical lines represent the cut $Chi2N < 20$ to identify the good quality tracking in the DC.

All the cuts for the hadron identification are summarized as follows,

- Event builder PID (Proton PID= 2212, π^+ PID= 211 and π^- PID= -211).
- DC fiducial cuts on region 1, 2, and 3, individually adjusted for all hadrons type: proton, π^+ and π^-.
- A cut on vertex difference to the electron $|V_z(electron) - V_z(hadron)| < 20$ cm for both FD and CD.
- Chi2PID cut from the event builder
  Particles in FD -for π^- $|Chi2PID_{piplus}| < 2.64$ cut, for π^+ $|Chi2PID_{piplus}| < 2.79$ cut and for the proton $|Chi2PID_{proton}| < 2.5$ (by eye) cut are used.
  Particles in CD -for π^- $|Chi2PID_{piplus}| < 4.1$ cut, for π^+ $|Chi2PID_{piplus}| < 4.0$ cut and for the proton $|Chi2PID_{proton}| < 4.7$ cut are used.
- Drift Chamber(DC) "$Chi2$" Track fitting.

3.5 MOMENTUM CORRECTION

When particles traverse the various detector materials in CLAS12, they lose energy and undergo changes in trajectory. In order to perform a cross-section analysis, momentum correction is essential. The CLAS12 collaboration uses a common momentum correction procedure (see more details [39]). The momentum correction procedure was based on the exclusive pion reaction. The most recent version of momentum correction for fall2018 inbending data can be found in [39].

CHAPTER 4

MONTE CARLO SIMULATION FOR $ep \rightarrow e'p'\ \pi^+\pi^-$

This chapter discusses the Monte-Carlo simulation we used in our analysis. For the purpose of evaluating the effects of several systematic, it is crucial to be able to match particles created by the Event Generator with particles that have been "detected" after they have been simulated and reconstructed by CLAS12. This study uses two Monte-Carlo simulations. One is our "Deep $\pi\pi$ Generator," and the other is Harut Avagyan's "Inclusive DIS Generator".

4.1 DEEP $\pi\pi$ GENERATOR

There are eight independent kinematic variables in the final state of the two-pion monte-carlo generator, including the following: $Q^2, x_B, \phi_e, M^2_{1,2}, t, \phi^*_{1,2}, \cos(\theta)_{\sigma-rest}, \phi_{\sigma-rest}$. The event generation proceeds as follows (with the fixed incident beam energy $k = 10.6$ GeV, and all variables generated uniformly within the given ranges):

1. Generate $x_B \in [x_{min}, x_{max}]$. For $k = 10.6$ GeV, an appropriate range is
   $x_{min} = 0.2, \qquad x_{max} = 0.8.$

2. Generate $Q^2 \in [Q^2_{min}, Q^2_{max}]$. Use $Q^{min} = 1$ GeV^2 and $Q^{max} = 10$ GeV^2. Energy-momentum conservation rules (Laboratory rest frame):

   $$\begin{aligned} k' &= \frac{k}{1 + \frac{k}{Mx_B}(1-\cos\theta_e)}, \\ Q^2 &= \frac{2k^2(1-\cos\theta_e)}{1 + \frac{k}{Mx_B}(1-\cos\theta_e)}. \end{aligned} \tag{77}$$

   Check that k' is physical: reject events with $k' < 0$ or $k' > k$. Calculate the invariant $W^2 = M^2 + Q^2(\frac{1}{x_B} - 1)$: reject events with $W^2 - M^2 < 4m^2_\pi$. Use the charged pion mass $m_\pi = 0.139$ GeV and neutral pion mass $m_\pi = 0.135$ GeV.

3. Generate $\phi_e \in [0, 2\pi]$. Calculate the components of the 4-vectors k', q. Define the three unit vectors $\hat{x_q}$, $\hat{y_q}$, $\hat{z_q}$ as 3-vectors in the laboratory rest frame. Define the boost vector 3-vector

   $$\boldsymbol{\beta}_{CM} = \left[\frac{\mathbf{q}}{\nu + M}\right]_{Lab}. \tag{78}$$

This boosts four vectors in the γ^*P CM frame back to the laboratory frame. Apply the boost $-\beta_{CM}$ to the four-vectors q and P to obtain their versions in the $\gamma^* P$ CM frame.

4. Generate the $\pi\pi$ invariant mass squared

$$M_{1,2}^2 \in \left[4m_\pi^2, (\sqrt{W^2} - M)^2\right]. \tag{79}$$

Calculate the two-pion momentum in the CM frame: $P_{1,2}^*$.

5. Generate $t \in [t_{max}, t_{min}]$ with the limits defined the t_{max} in the Eq. (174) and t_{min} in the Eq. (173). Calculate $cos\theta_{1,2}^*$ (see Appendix A). Check that $-1 < \cos(\theta_{1,2}^*) < 1$.

6. Generate $\phi_h \in [0, 2\pi]$. This is the azimuthal angle of the two-pion system with respect to the electron scattering plane. Compute the $\gamma^* P$ CM frame four-vectors $P_{1,2}^*$ and P'. Use the variables in the $\gamma^* P$ CM frame to evaluate the three unit vectors $\hat{x}_{1,2}^*$, $\hat{y}_{1,2}^*$, $\hat{z}_{1,2}^*$, as defined in Eqs. (177)-(179) Define the boost 3-vector

$$\boldsymbol{\beta}_{\sigma-\text{Rest}} = \left[\frac{\mathbf{P}_{1,2}}{E_{1,2}}\right]_{\gamma^* P\,\text{CM}}. \tag{80}$$

This will boost four-vectors from the σ-meson rest frame back to the $\gamma^* P$ CM frame.

7. Generate $\cos\theta_{\sigma-\text{Rest}} \in [-1, 1]$. This is the polar angle of the π^+ in the $\pi\pi$ rest frame, with respect to the $\hat{z}_{1,2}^*$ direction.

8. Generate $\phi_{\sigma-\text{Rest}} \in [0, 2\pi]$. This is the azimuthal angle of the π^+ in the $\hat{x}_{1,2}^*$, $\hat{y}_{1,2}^*$ plane. Compute the σ-Rest frame four-vectors p_1 and p_2 of the two pions.

9. Boost the four-vectors p_1, p_2 back to the $\gamma^* P$ CM frame.

10. Boost the four-vectors p_1, p_2, P' back to the laboratory frame.

4.2 RADIATIVE CORRECTION

Measuring the cross-section of the exclusive meson electroproduction can inform us about the nature of diffraction and the hadronic composition of the photon. Therefore radiative correction has been added to the "Deep $\pi\pi$ Generator," because electrons often emit photons due to their low mass. As a consequence, an electron's kinematics can be greatly altered. Based on the energy of the radiated photons, two categories of radiation effects can be distinguished: “hard” photons and “soft” photons. Due to the high energy of hard photons, they can be detected in CLAS12 or omitted from its exclusivity cuts in any case. As opposed to hard photons, soft photons have very low energy to be detected: most of them are either reabsorbed immediately (vacuum polarization) or possess a very low energy. As shown in Fig. 39, Feynman diagrams are included in the calculation of radiative corrections. There are Feynman diagrams from Born to the cross-section of the next order included in this Fig. 39. We used the Fortran code diffrad.f [41] to add the radiative correction part to the “Deep $\pi\pi$ Generator.” This code calculates the real and virtual-photon radiative corrections to the exclusive:

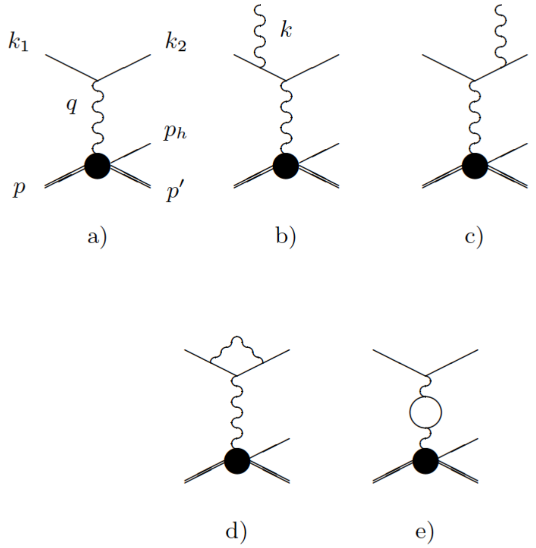

FIG. 39. Feynman diagrams for the radiative correction from Born and next-order cross-sections. (a) Born diagram, (b) initial-electron radiation, (c) final-electron radiation, (d) radiative loop between initial and final electron, and (e) vacuum polarization [40].

$$e(k_1) + p(P) \to e(k_2) + p(P') + V(p_V). \tag{81}$$

Here V represents the vector meson. The usual invariants are,

$$\begin{aligned}
P^2 &= M^2, \\
s_e &= (k+p)^2 = S + M^2, \\
Q^2 &= -q^2 = -(k_1 - k_2)^2 > 0, \\
x_B &= \frac{Q^2}{2q \cdot P}, \\
W^2 &= (q+P)^2 = M^2 + 2q \cdot P - Q^2, \qquad W \equiv \sqrt{W^2}, \\
t &= \Delta^2 < 0, \qquad \Delta^\mu = (q - p_V)^\mu, \\
y &= \frac{q \cdot P}{k \cdot P},
\end{aligned} \tag{82}$$

with the relation $Q^2 = x_B y S$, neglecting the lepton mass. The code is based on the formalism of [40]. The formalism is general and would seem to apply to any exclusive lepto-production process. Nonetheless, there is an implicit choice of a reference frame for the calculation of real-radiative effects that must be utilized in the analysis of data. In particular, the kinematics of radiative events:

$$e(k_1) + p(P) \to e(k_2) + p(P') + V(p_V) + \gamma(k), \tag{83}$$

are described at constant Q^2, x_B, and $t = \Delta^2 = (q - p_V)^2$, and as a function of $\Lambda^2 - M^2$, with

$$\Lambda^\mu = (P' + k)^\mu. \tag{84}$$

The radiative line shape is defined as a function of Λ^2, which is the missing mass squared if all particles other than the final proton and photon are detected. More specifically, all kinematic formulae are calculated without explicit reference to measured values of P'^μ or k^μ. This means that as Λ^2 varies, the energy and three-momentum direction of p_V^μ must also vary to keep Δ^2 constant.

Kinematics

The final state kinematics are most easily defined in the virtual photon plus target CM frame:

$$(\mathbf{q} + \mathbf{P})^{CM} = \mathbf{0} = (\mathbf{p}_V + \mathbf{\Lambda})^{CM}, \tag{85}$$

In this frame

$$\begin{aligned}
\nu^{CM} &= \left(q^0\right)^{CM} = \frac{W^2 - Q^2 - M^2}{2W}, \\
\left|\mathbf{q}^{CM}\right| &= \sqrt{\left(\nu^{CM}\right)^2 + Q^2} = \frac{1}{2W}\sqrt{\left(W^2 - Q^2 - M^2\right)^2 + 4Q^2W^2}, \\
&= \frac{1}{2W}\sqrt{\left(W^2 + Q^2 - M^2\right)^2 + 4Q^2M^2}, = \frac{1}{2W}\sqrt{\left(2q\cdot P\right)^2 + 4Q^2M^2}, \\
&= \frac{q\cdot P}{W}\sqrt{1 + \frac{4x_B^2M^2}{Q^2}}.
\end{aligned} \tag{86}$$

The “vector-meson” kinematics are

$$\begin{aligned}
E_V^{CM}(\Lambda^2) &= \frac{W^2 + m_V^2 - \Lambda^2}{2W} \qquad \text{with threshold } W \geq m_V, \\
\left|\mathbf{p}_V^{CM}\right|(\Lambda^2) &= \sqrt{\left(E_V^{CM}\right)^2 - m_V^2}.
\end{aligned} \tag{87}$$

Finally:

$$\begin{aligned}
t = \Delta^2 &= -Q^2 + m_V^2 - 2q\cdot p_V, \\
&= -Q^2 + m_V^2 - 2\left(\nu^{CM}E_V^{CM} - \left|\mathbf{q}^{CM}\right|\left|\mathbf{p}_V^{CM}\right|\cos\theta_{\gamma V}^{CM}\right).
\end{aligned} \tag{88}$$

For fixed values of (Q^2, x_B, t), there is a bound on the value of Λ^2. This bound is determined by the constraint that $\left|\cos\theta_{\gamma V}^{CM}\right| \leq 1$ (see Appendix A and Eq. (184)):

$$\left(\Lambda^2 - M^2\right)_{\text{Max}} = \left[\frac{Q^2 - t + m_V^2}{2x_B} + t\right]\left\{1 - \sqrt{1 - \frac{W^2}{Q^2}\frac{(t_0 - t)(t - t_\pi)}{\left[t + \left(Q^2 - t + m_V^2\right)/(2x_B)\right]^2}}\right\}. \tag{89}$$

Radiative Corrections

The diffrad radiative correction, as a function of the radiative cutoff Λ^2 is [40], Eq. (14):

$$\sigma(\Lambda^2)^{\text{Observed}} = \sigma^{\text{Born}}\left\{\left[e^{\delta_{\text{inf}}}\left(1 + \delta_{VR} + \delta_{vac}\right)\right]\right\}_{\Lambda^2} + \sigma_F(\Lambda^2). \tag{90}$$

The individual factorized terms are

$$\begin{aligned}
\delta_{\text{inf}}(\Lambda^2) &= \delta_S \log\frac{\left(\Lambda^2 - M^2\right)^2}{S'X'}, \qquad e^{\delta_{\text{inf}}} = \left[\frac{\left(\Lambda^2 - M^2\right)^2}{S'X'}\right]^{\delta_S}, \\
\delta_S &= \frac{\alpha}{\pi}\left[\log\frac{Q^2}{m_e^2} - 1\right], \\
\delta_{\text{VR}} &= \frac{\alpha}{\pi}\left\{\frac{3}{2}\log\frac{Q^2}{m_e^2} - 2 - \frac{1}{2}\log^2\frac{X'}{S'} + \text{Li}_2\left[\frac{S'X' - Q^2M^2}{S'X'}\right] - \frac{\pi^2}{6}\right\}, \\
\delta_{\text{Vac}} &= \sum_{\text{leptons}}\frac{2\alpha}{3\pi}\left[\log\frac{Q^2}{m_l^2} - \frac{5}{3}\right] + \text{ hadronic terms.}
\end{aligned} \tag{91}$$

These are functions of the following invariants ($S = 2k_1 \cdot P = s_e - M^2$):

$$\begin{aligned} S' &= 2\Lambda \cdot k_1 = 2(k_1 - k_2 + p - p_V) \cdot k_1 = -Q^2 + S - 2k_1 \cdot p_V, \\ X' &= 2\Lambda \cdot k_2 = 2(k_1 - k_2 + p - p_V) \cdot k_2 = Q^2 + S(1-y) - 2k_2 \cdot p_V, \\ S' - X' &= -2Q^2 + yS - 2q \cdot P_V = yS - Q^2 + t - m_V^2. \end{aligned} \tag{92}$$

Note also

$$\mathrm{Li}_2(1) = \frac{\pi^2}{6}. \tag{93}$$

$t_p \equiv (p' - p)^2$-Dependence

The Λ^2 dependence is calculated for constant $t = (q - p_V)^2$. However, $t_p \equiv (p' - p)^2$ is not constant. Strong variations of the cross-section as a function of t_p must be incorporated into the σ_F term. The exact dependence of the cross-section on t_p is described in [40]. This, as well as an approximate model, is also incorporated into diffrad.f. Assuming the Born cross-section for diffractive vector-meson production has an exponential dependence on t_p:

$$\frac{d\sigma}{dt_p} \sim b\sigma_0 e^{bt_p}, \tag{94}$$

then the radiative term

$$\delta_F = \frac{\sigma_F}{\sigma_{\text{Born}}} = 2\left(\Lambda^2 - M^2\right) b\delta_S \left\{ \frac{Q^2 + m_V^2}{2q \cdot P - Q^2 - m_V^2} \right\}. \tag{95}$$

`diffrad.f` Inconsistency

There is a factor of 4 inconsistency between the computations of S' and X' in the code diffrad.f and the publication [40].

Exclurad *vs.* Diffrad

The code exclurad [41] was developed after diffrad to incorporate explicitly the MAID[42] model of exclusive pion electro-production in the nucleon resonance region [43]. Eq. (55) of [43] has the identical form as Eq. (90), with the important simplification that the terms δ_{inf} and δ_{VR} are defined at the $\Lambda^2 = M^2$ limit. The observed cross-section, integrated up to a radiative limit of $v_{cut} = \Lambda^2 - M^2$ is

$$\begin{aligned} \left[\sigma(\Lambda^2)^{\text{Observed}}\right]_{\texttt{exclurad}} &= e^{\delta_{\text{inf},0}} \left[1 + \delta_{VR,0} + \delta_{vac}\right] \sigma_{\text{Born}} + \sigma_F, \\ e^{\delta_{\text{inf},0}(v_{cut}} &= \left(\frac{v_{cut}^2}{S_0' X_0'} \right)^{\delta_S}. \end{aligned} \tag{96}$$

As before, the radiative tail at fixed W^2, Q^2, t only extends up to $v_{\text{Max}} = \Lambda^2_{\text{Max}} - M^2$.

Radiative Lineshape

Ignoring the σ_F term for the moment, if the radiative tail is integrated all the way to v_{Max}, then the radiative factor

$$RF\left(v_{\text{Max}}\right) = \left(\frac{v_{\text{Max}}^2}{S_0' X_0'}\right)^{\delta_S}\left[1 + \delta_{VR,0} + \delta_{vac}\right], \tag{97}$$

is the effective radiative correction, to the lowest order Born cross-section, from all real and virtual radiative processes. The full radiative tail is usually obscured by inelastic channels. Thus the radiative cross-section can only be integrated up to a value $v_{cut} < v_{\text{Max}}$, defined by the inelastic channel. Then the ratio

$$\frac{RF\left(v_{cut}\right)}{RF\left(v_{\text{Max}}\right)} = \left(\frac{v_{cut}}{v_{\text{Max}}}\right)^{2\delta_S} < 1, \tag{98}$$

is the fractional decrease in the measured cross-section, due to the “missing” radiative events beyond v_{cut}.

Monte-Carlo Procedure

Radiative corrections can be incorporated into a general electro-production $ep \to eVN$ Monte Carlo by the following steps:

1. Generate scattered electron: *e.g.,* (Q^2, x_B, ϕ_e) (see section 4.1)

2. Generate final mesonic state: (m_V, t);

3. Calculate “on-shell” Radiative variables: $\Lambda^2_{\text{Max}}, S_0', X_0', \ldots$ and terms: $\delta_{\text{VR},0}$, $\delta_{\text{Vac},0}$;

4. Calculate radiation weight factor $RF\left(v_{\text{Max}}\right)$ (Eq. (97)):

5. Generate internal pre-radiation $q'(1)$ parallel to $\mathbf{k}_1$ with distribution

$$P(v_1) = \frac{\delta_S}{v_{\text{Max}}}\left(\frac{v_1}{v_{\text{Max}}}\right)^{\delta_S} : \qquad 0 \le v_1 < v_{\text{Max}}. \tag{99}$$

6. Generate internal post-radiation $q'(2)$ parallel to $\mathbf{k}_2$ with distribution (Appendix A)

$$P(v_2) = \frac{\delta_S}{v_{\text{Max}} - v_1}\left(\frac{v_2}{v_{\text{Max}} - v_1}\right)^{\delta_S} : \qquad 0 \le v_2 < v_{\text{Max}} - v_2. \tag{100}$$

7. Calculate Born cross-section at vertex kinematics:

$$\begin{aligned}\widetilde{Q}^2 &= -\widetilde{q}^2 = -(k_1 - q'(1) - q'(2) - k_2)^2, \\ \widetilde{W}^2 &= (\widetilde{q} + P)^2, \\ t_p(v) &= P'(v_1 + v_2) - P)^2. \end{aligned} \tag{101}$$

It remains to determine whether the last step removes the need to explicitly calculate σ_F.

CHAPTER 5

$ep \to e'p'\ \pi^+\pi^-$ EVENT SELECTION

To ensure a rigorous and accurate analysis, we apply various cuts to identify $ep \to e'p'\pi^+\pi^-$ events. Firstly, we select events that contain at least one electron, one proton, one positive pion, and one negative pion. We also include all possible combinations of e, p, π^+, and π^- within the events. By doing so, we increase the number of e, p, π^+, and π^- events that we can analyze. As discussed in the previous Chapter 3, both the Forward Detector (FD) and Central Detector (CD) are utilized in this analysis.

As mentioned in Chapter 1, this analysis focuses on events in the Deep Inelastic Scattering (DIS) region, where $Q^2 > 1$ $(\text{GeV/c})^2$ and $W > 2$ GeV. Fig. 40 shows the Q^2 vs. x_B distribution after applying the DIS cut of $Q^2 > 1$ $(\text{GeV/c})^2$ and $W > 2$ GeV.

It is important to note that we apply various other cuts, including fiducial cuts and momentum corrections, to ensure the accuracy of our analysis. These cuts are crucial in identifying and selecting the $ep \to e'p'\pi^+\pi^-$ events that are the focus of this study.

5.1 EXCLUSIVE EVENT SELECTION

5.1.1 MISSING TOTAL ENERGY AND MISSING TOTAL MASS CUTS FOR $H(e, e'p\pi^+\pi^-)X$

In our study, we utilized the missing mass technique to identify the $ep \to e'p'\pi^+\pi^-$ final state. As a first step in examining the exclusivity cut, we examined the distributions of missing total mass square and missing total energy for the events $(H(e, e'p\pi^+\pi^-)X)$, which allowed us to select the exclusive $e'p\pi^+\pi^-$ events. To define the exclusive variables, we employed four-momentum algebra. Specifically, we defined the exclusive variables as follows:

$$MM^2_{e'p\pi^+\pi^-} = (k_{beam} + P_{target} - k_{e'} - P'_p - p_{\pi^+} - p_{\pi^-})^2, \tag{102}$$

$$ME_{e'p\pi^+\pi^-} = (E_{beam} + M - E_{e'} - E_p - E_{\pi^+} - E_{\pi^-}). \tag{103}$$

The missing mass squared (MM^2) and missing energy (ME) are kinematic variables that are used to identify the presence of undetected particles. These variables are defined as

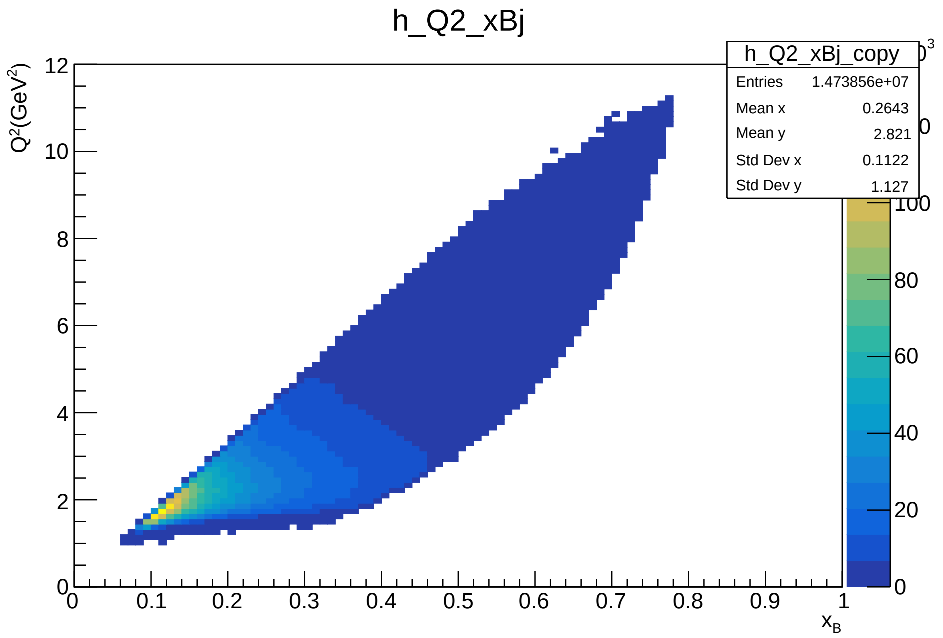

FIG. 40. Q^2 vs. x_B distributions after DIS cut, $Q^2 > 1$ $(\mathrm{GeV/c})^2$ vs. $W > 2$ GeV.

.

the difference between the total four-momentum of the initial particles and the total four-momentum of the detected particles. Referring to the figures, Fig. 41 shows the distribution of Missing Energy (E_X) for the $H(e,[e'p\pi^+\pi^-])X$ events. The red vertical lines represent a cut of $|E_X[e'p\pi^+\pi^-X]| < 0.4$ GeV used to select the $e'p\pi^+\pi^-$ final state. This means that events where the absolute value of the Missing Energy is greater than 0.4 GeV are excluded from the analysis as they do not correspond to the desired final state.

Fig. 42(a) shows the distribution of Missing Total Mass Square (M_X^2) for all $H(e,[e'p\pi^+\pi^-])X$ events without any cuts applied. The red lines in this figure represent a cut of $|M_X^2[e'p\pi^+\pi^-X]| < 0.2$ GeV^{2}used to select the $e'p\pi^+\pi^-$ final state. This means that events where the absolute value of the Missing Total Mass Square is greater than 0.2 GeV^2 are excluded from the analysis.

Fig. 42(b) shows the distribution of Missing Total Mass Square after applying the Missing Energy cut of $|E_X[e'p\pi^+\pi^-X]| < 0.4$ GeV shown in Fig. 41. This figure only includes events that pass both cuts, meaning that the selected events correspond to the $e'p\pi^+\pi^-$ final state with good accuracy.

5.1.2 P_T^{MISS} DISTRIBUTION

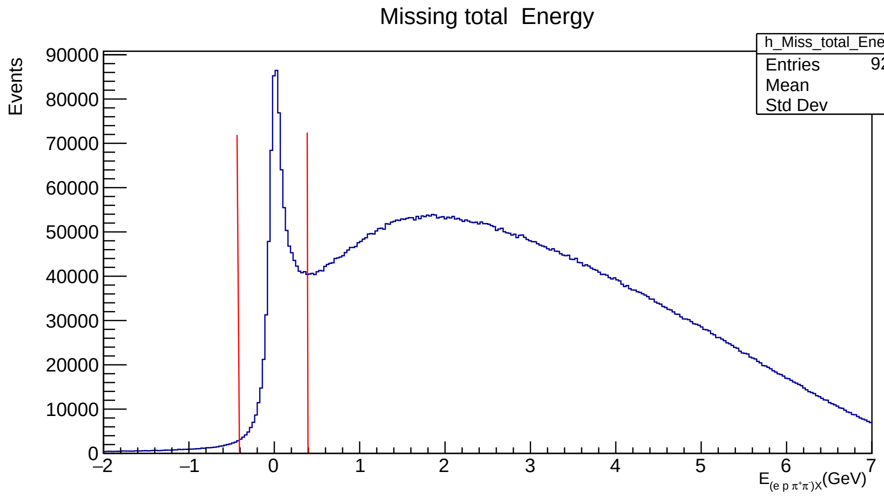

FIG. 41. Missing energy $E_X[e'p\pi^+\pi^-X]$ after $Q^2 > 1$ GeV^2 and $W > 2$ GeV. The red lines show the cut $|E_X[e'p\pi^+\pi^-X]| < 0.4$ GeV used to select the $e'p\pi^+\pi^-$ final state.

.

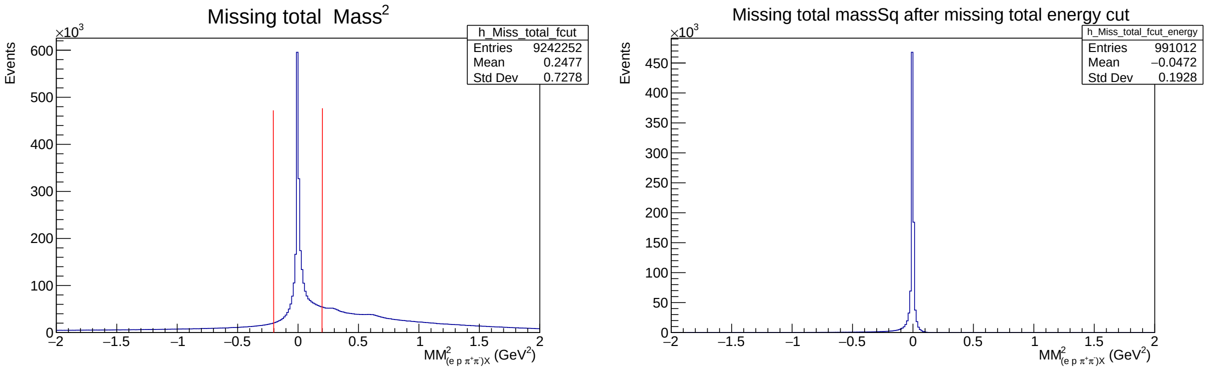

(a)

(b)

FIG. 42. The presented plots exhibit the fall 2018 in-bending RGA data. Fig. (a) on the left-hand side illustrates the Missing total mass square distribution of $H(e,[e'p\pi^+\pi^-])X$ events before the application of any cuts and the red lines show the cut $|M_X^2[e'p\pi^+\pi^-X]| < 0.2$ GeV^2 used to select the $e'p\pi^+\pi^-$ final state, while Fig. (b) on the right-hand side displays the Missing total mass square distribution after Missing energy cut $|E_X[e'p\pi^+\pi^-X]| < 0.4$ GeV.

The missing transverse momentum (p_T^{miss}) is defined as the component of the total momentum that is perpendicular to the direction of the electron scattering plane. The p_T^{miss} is calculated by measuring the momenta of all the detected particles in the event and then subtracting their vector sum from the vector sum of the initial particles. The resulting vector points in the direction of the missing momentum, and the magnitude of the vector gives the magnitude of p_T^{miss}:

$$\begin{aligned} \hat{y} &= \mathbf{p_{beam}} \times \mathbf{p_{e'}}, \qquad (104) \\ p_T^{\text{miss}} &= \hat{y} \cdot \mathbf{p_{e'p\pi^+\pi^-}}. \end{aligned}$$

The p_T^{miss} distribution is shown in Fig. 43. The exclusive events cut was implemented with a threshold of $|p_T^{\text{miss}}| < 1.0$ GeV (the vertical red lines in Fig. 43(a), indicating that events with missing transverse momentum above this threshold were excluded from further analysis. The right-hand plot in Fig. 43 plot shows the p_T^{miss} distribution after the Missing energy cut $|E_X[e'p\pi^+\pi^-X]| < 0.4$ GeV and missing mass square $|M_X^2[e'p\pi^+\pi^-X]| < 0.2$ GeV^2 cuts. This type of cut is often used to select events with low missing transverse momentum, as this may be indicative of the presence of new physics phenomena.

5.1.3 CONE ANGLE ANALYSIS

The study details an experimental investigation into the cone angle of various hadrons, including protons and pions with both positive and negative charges. Specifically, the cone angle was defined as the angle between the 3-momentum direction of the hadron and the missing direction, which was calculated from the incoming particles and the detected particles not belonging to the target final state. The primary aim of this investigation was to identify exclusive $e'p\pi^+\pi^-$ events. These events were identified through a thorough analysis of the cone angles, as detailed in Eqs. (105)-(107). By characterizing the properties of these exclusive events and the behavior of the involved particles, we aimed to deepen our understanding of these processes

$$\begin{aligned} \cos(\theta_{collinear-proton}) &= (\mathbf{p}_{e'\pi^+\pi^-} \cdot \mathbf{p_p})/(|\mathbf{p}_{e'\pi^+\pi^-}| * |\mathbf{p_p}|), \\ \theta_{collinear-proton} &= \cos^{-1}(\cos(\theta_{collinear-proton})), \qquad (105) \end{aligned}$$

$$\begin{aligned} \cos(\theta_{collinear-piminus}) &= (\mathbf{p}_{e'p\pi^+} \cdot \mathbf{p}_{\pi^-})/(|\mathbf{p}_{e'p\pi^+}| * |\mathbf{p}_{\pi^-}|), \\ \theta_{collinear-piminus} &= \cos^{-1}(\cos(\theta_{collinear-piminus})), \qquad (106) \end{aligned}$$

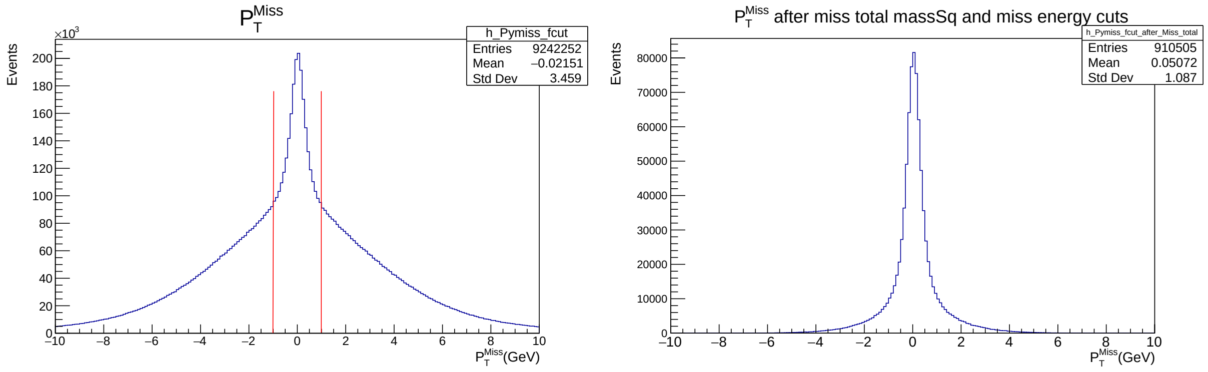

(a) (b)

FIG. 43. The presented plots exhibit the fall 2018 in-bending RGA data. Fig. (a) on the left-hand side illustrates the P_T^{Miss} distribution of $H(e,[e'p\pi^+\pi^-])X$ events before the application of any cuts, and the red lines show the cut $|P_T^{MISS}| < 1.0$ GeV used to select the $e'p\pi^+\pi^-$ final state, while Fig. (b) on the right-hand side displays the P_T^{MISS} distribution after Missing energy cut $|E_X[e'p\pi^+\pi^-X]| < 0.4$ GeV and missing mass square $|M_X^2[e'p\pi^+\pi^-X]| < 0.2$ GeV^2 cuts.

$$\cos(\theta_{collinear-piplus}) = (\mathbf{p}_{e'p\pi^-}\cdot\mathbf{p}_{\pi^+})/(|\mathbf{p}_{e'p\pi^-}| * |\mathbf{p}_{\pi^+}|),$$
$$\theta_{collinear-piplus} = \cos^{-1}(\cos(\theta_{collinear-piplus})), \tag{107}$$

where $\mathbf{p}_{e'\pi^-\pi^+}$-Miss proton 3-momentum $= \mathbf{k}-\mathbf{k'}-\mathbf{p_1}-\mathbf{p_2}$, $\mathbf{p}_{e'p\pi^+}$-Miss pi-minus 3-momentum $= \mathbf{k}-\mathbf{k'}-\mathbf{P'}-\mathbf{p}_1$, $\mathbf{p}_{e'p\pi^-}$-Miss pi-plus 3-momentum, $\mathbf{p_p}$- measured proton, $\mathbf{p}_{\pi^-}$- measured pi-minus, $\mathbf{p}_{\pi^+}$- measured pi-plus. The cone angle distributions for the proton, π^-, and π^+ particles are presented in Fig. 44 after applying the previously mentioned exclusive cuts. The red line in the figure corresponds to the criterion employed to choose the exclusive final state. The figures denoted as Fig. 45, Fig. 46, and Fig. 47 display the missing mass square distributions for the proton, π^+, and π^- particles, respectively, both before and after the implementation of exclusivity cuts, which are elaborated below. The missing mass distributions prior to the application of the exclusivity cuts are presented on the left-hand side of the figures, while the missing mass distributions after the exclusivity cuts are depicted on the right-hand side of the figures. Please find the exclusivity cuts listed below:

- $Q^2 > 1.0$ (GeV$^2/c$) and $W > 2.0$ (GeV) (Kinematic Cut).
- Missing Total Energy cut $|E_X[e'p\pi^+\pi^-X]| < 0.4$ GeV.
- Missing Total Mass Square Cut $|M_X^2[e'p\pi^+\pi^-X]| < 0.2$ GeV^2.

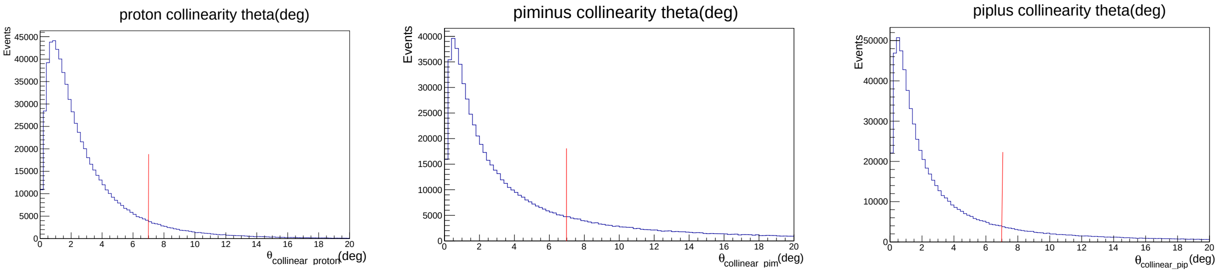

FIG. 44. Cone angle distributions for proton, π^+, and π^- in both FD and CD. The red vertical lines represent the cuts we used for the $\theta_{collinear-proton} < 7°$ (by eye), for π^+ $\theta_{collinear-piminus} < 7°$ cut, for π^- and $\theta_{collinear-piplus} < 7°$ cuts.

- P_T^{MISS} distributions are relative to the scattering plane. $|P_{ymiss}| < 1.0$ GeV.

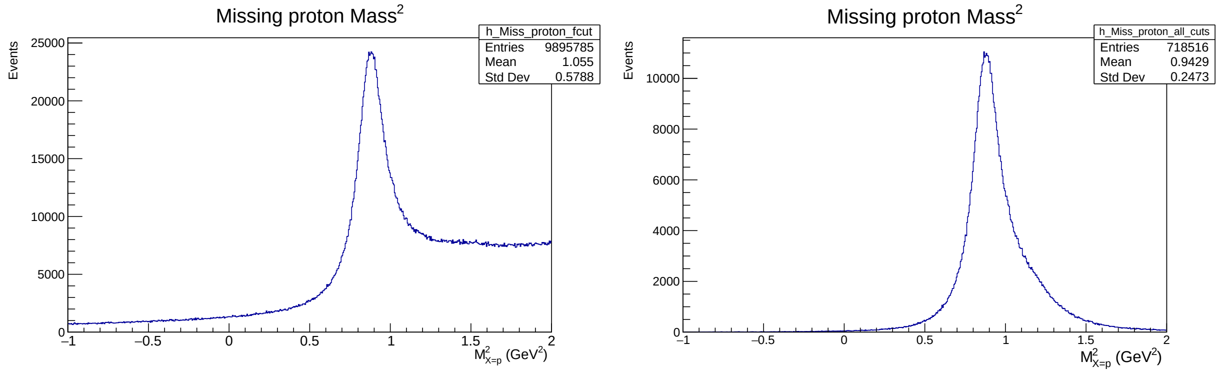

(a) (b)

FIG. 45. The presented plots exhibit the in-bending RGA data for the fall of 2018. Fig. (a) on the left-hand side portrays the Missing Proton Mass Square distribution of $H(e, [e'p\pi^+\pi^-])X$ events before the application of any cuts, while Fig. (b) on the right-hand side displays the Missing Proton Mass Square distribution subsequent to the exclusivity cuts detailed in cuts 5.1.3.

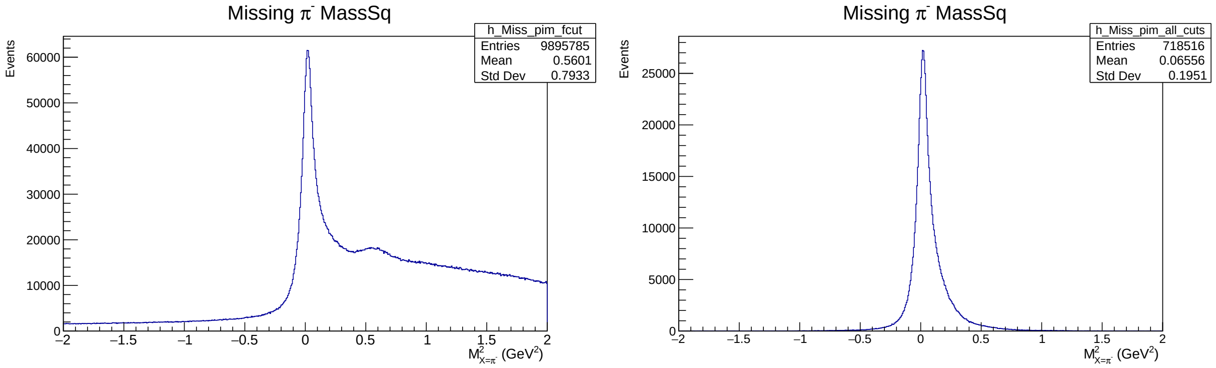

(a) (b)

FIG. 46. The presented plots exhibit the fall 2018 in-bending RGA data. Fig. (a) on the left-hand side illustrates the Missing π^- Mass Square distribution of $H(e,[e'p\pi^+\pi^-])X$ events before the application of any cuts, while Fig. (b) on the right-hand side displays the Missing π^- Mass Square distribution subsequent to the exclusivity cuts described in cuts 5.1.3.

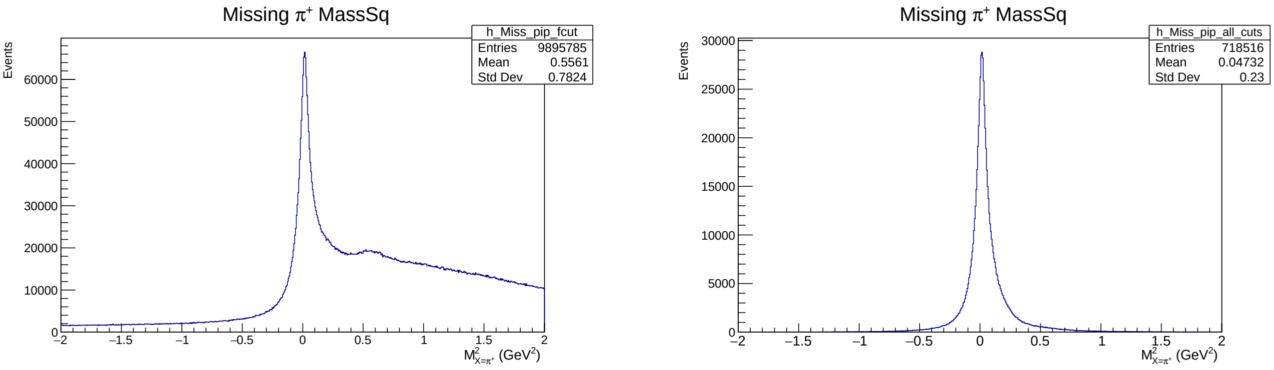

(a) (b)

FIG. 47. The provided plots showcase the in-bending RGA data for the fall of 2018. Fig. (a) on the left-hand side presents the Missing π^+ Mass Square distribution of $H(e,[e'p\pi^+\pi^-])X$ events, $M^2(\pi^+ + X)$, before implementing any cuts, while Fig. (b) on the right-hand side portrays the Missing π^+ Mass Square distribution subsequent to the exclusivity cuts outlined in cuts 5.1.3.

.

CHAPTER 6

EFFICIENCY STUDIES

The objective of this section is to investigate the effectiveness of the CLAS12 detector in detecting particles, with a focus on the Forward Detector (FD) and Central Detector (CD) separately. The tracking efficiency of the detector is a crucial factor in determining the cross-section of deep virtual two-pion production. To conduct this study, we utilized data from runs 5032-5419 of the Fall 2018 in-bending RGA pass-1 cooking data set, which is the same data set used in the previous section. Similar to this thesis topic, the exclusive analysis approach of exclusive two-pion production was employed for this efficiency study. The study evaluated tracking efficiencies for different particles, including electrons (e), protons (p), positively charged pions (π^+), and negatively charged pions (π^-), for both the FD and CD.

6.1 FD TRACKING EFFICIENCY

The FD tracking efficiency study was conducted to evaluate the performance of the tracking system for the exclusive $ep \to e'p\pi^+\pi^-$ reaction. The study aimed to determine the tracking efficiency for each particle, namely the electron (e), proton (p), positive pion (π^+), and negative pion (π^-), separately.

To achieve this goal, three-fold and four-fold coincidences were compared after applying fiducial cuts and initial exclusivity cuts (see section 3). Fiducial cuts are used to select events in a specific region of the detector where the tracking efficiency is known to be high, while exclusivity cuts are used to select events where only the desired particles are present in the final state.

The efficiency of each particle was determined bin-by-bin in θ vs. p space, where θ is the scattering angle and p is the momentum of the particle. This was done to take into account any dependence of the tracking efficiency on these variables.

Overall, the efficiency study was conducted using a data sample collected by the FD tracking system, which was in relatively good shape at the time. The study allowed us to assess the performance of the tracking system and identify any areas where improvements could be made to further enhance its efficiency.

4-fold case-$H(e, [e'p\pi^+\pi^-]_{FD})X$

The proposed method involves utilizing the detected data of the form $H(e, [e'p\pi^+\pi^-]_{FD})X$, where e, p, π^+, and π^- represent the detected electron, proton, positively charged pion, and negatively charged pion, respectively. The first step is to analyze the missing total mass square and missing total energy distributions.

$$MM^2_{e'p\pi^+\pi^-} = (k_{beam} + P_{target} - k_{e'} - P'_p - p_{\pi^+} - p_{\pi^-})^2, \tag{108}$$

$$ME_{(e'p\pi^+\pi^-)_{FD}} = (E_{beam} + M - E_{e'} - E_p - E_{\pi^+} - E_{\pi^-}). \tag{109}$$

Fig. 48 displays the distributions of Missing total mass square (left) and Missing total energy (right). The vertical red lines indicate the chosen "exclusivity cuts" at $|M_X^2| < 0.1$ GeV^2 and $|E_X| < 0.2$ GeV from the Missing total mass square and Missing total energy distribution, respectively. These exclusivity cuts were selected to define a specific set of events that satisfy the conditions for exclusive reactions. The events that do not meet the exclusivity cuts are referred to as "non-exclusivity cuts", where $|M_X^2| > 0.1$ GeV^2 and $|E_X| > 0.2$ GeV.

Our initial analysis consisted of examining the histogram of the missing π^- mass square ($M^2_{\pi^- + X}$), which was defined using Eq. (110). This calculation involves the four-momenta of the incoming beam (p_{beam}), the target nucleus (p_{target}), the detected π^- particle (p_{π^-}), and any undetected particles (p_X) in the final state of the collision. By utilizing the conservation laws of energy and momentum, we can infer the properties of the undetected particles from the measured momenta of the detected particles

$$(MM^2_{e'p\pi^+})_{4-fold} = (k_{beam} + P_{target} - k_{e'} - P'_p - p_{\pi^+})^2. \tag{110}$$

In this study, we have utilized a 4-fold missing π^- mass square distribution to investigate the properties of certain particles. To identify the region of interest, we have defined an "exclusive window" as having $(MM^2_{e'p\pi^+})_{4-fold}$ values between -0.13 GeV^2 and 0.17 GeV^2. This window represents the range of values where the desired particles are expected to be found.

In addition, we have defined a "background window" as having $|(MM^2_{e'p\pi^+})_{4-fold}|$ values between 0.2 GeV^2 and 0.5 GeV^2. This region is intended to capture the values where background events are likely to occur.

To analyze the data within these regions, we have created three histograms. These histograms are designed to represent the distribution of particles in the exclusive window,

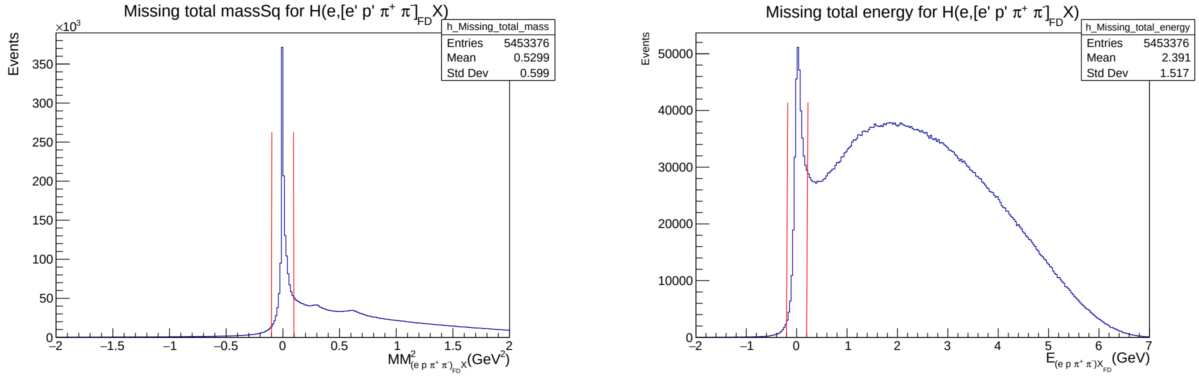

(a)

(b)

FIG. 48. The presented plots depict the fall 2018 in-bending RGA data for the exclusive reaction $H(e,[e'p\pi^+\pi^-]_{FD})X$. Specifically, Fig. (a) (left) displays the distribution of Miss total mass Sq (M_X^2) for the aforementioned events, while Fig. (b) (right) shows the distribution of Miss total energy (E_X). The exclusivity cuts applied to Fig. (a)(left) are set to $|M_X^2| < 0.1$ GeV^2, indicating that events with M_X^2 outside this range are discarded from the analysis. The exclusivity cut imposed on Fig. (b) (right) is $|E_X| < 0.2$ GeV, implying that events with E_X outside this range are excluded from the analysis.

the background window, and the overall distribution. By comparing these histograms, we can better understand the properties of the particles of interest and differentiate them from background events.

1. $h1\_pim\_4-fold\_exc \rightarrow Fill((MM^2_{e'p\pi^+})_{4-fold})$-
   Inside "Exclusive window." (see Fig. 50 yellow plot).

2. $h1\_pim\_4-fold\_exc\_notExc \rightarrow Fill((MM^2_{e'p\pi^+})_{4-fold})$-
   Passes non-exclusivity cuts inside the "Exclusive window." (see Fig. 50 cyan plot).

3. $h1\_pim\_4-fold\_bgnd\_notExc \rightarrow Fill((MM^2_{e'p\pi^+})_{4-fold})$-
   Passes non-exclusivity cuts inside the "Background window." (see Fig. 50 magenta plot).

The "SumW2" option was used to estimate the statistical error of the plots. This technique involves calculating the sum of the squares of the weights assigned to each bin in the histogram, where the weight represents the number of events that fall within that bin. The square root of the sum of the squares of the weights is then used as an estimate of the statistical error for each bin. In addition, it was necessary to impose a geometrical fiducial cut on the ϕ of the Fake pi-minus 3-vector for both the 3-fold and 4-fold cases in the absence of the kinematic fit. Consequently, each histogram presented a "somewhat" 4-fold coincidence, comprising either a genuine coincidence or a 3-fold coincidence in which the fake pi-minus direction pointed towards a valid region of the detector. Eq. (111), the term "$phi\_Rotation\_4-fold$"(ϕ^{4-fold}_{Rot}) is defined as follows:,

$$\phi^{4-fold}_{Rot} = \phi_{\pi^- + X} - \frac{\sin(\theta_{\pi^- + X})}{p_{\pi^- + X}} * 70°. \tag{111}$$

The "$phi\_Rotation\_4-fold$"(ϕ^{4-fold}_{Rot}) function has to rotated by 70° tilt due to the magnetic field. For the 4-fold case, we have used the geometric fiducial cuts shown below.

```
if(phi_Rotation_4-fold < -180) phi_Rotation_4fold+=360;
if(((-20 <phi_Rotation_4-fold) && (phi_Rotation_4fold < 20)) ||
((40 <phi_Rotation_4-fold) && (phi_Rotation_4-fold < 80)) ||
((100 <phi_Rotation_4-fold) && (phi_Rotation_4-fold < 140)) ||
((-80 <phi_Rotation_4-fold) && (phi_Rotation_4-fold < -40)) ||
((-140 <phi_Rotation_4-fold) && (phi_Rotation_4-fold < -100)) ||
((160 <phi_Rotation_4-fold) || (phi_Rotation_4-fold < -160))){
```

The plots are shown in Fig. 49, with the first one being Fig. 49(a); this figure displays a tilt due to the magnetic field (after applying ϕ fiducial cuts) and has been rotated by an angle of 70°. The second figure, Fig. 49(b), depicts the result after the application of geometrical cuts. The histograms $h1\_pim\_4f-old\_exc$, $h1\_pim\_4-fold\_exc\_notExc$, and $h1\_pim\_4-fold\_bgnd\_notExc$ are associated with the geometrical cuts.

3-fold case - $H(e, [e'p\pi^+]_{FD})Y$

Then the missing π^- mass square distribution is generated for 3-fold events described by the expression $H(e, [e'p\pi^+]_{FD})Y$. It is crucial to consider the detection or non-detection of π^- in the final state Y during the construction of the distribution.

$$(MM^2_{e'p\pi^+})_{3-fold} = (k_{beam} + P_{target} - k_{e'} - P'_p - p_{\pi^+} - p_{\pi^-})^2. \tag{112}$$

To analyze a specific region of interest and to separate signal events from background events, we have defined two regions, an "Exclusive Window" and a "Background Window,"

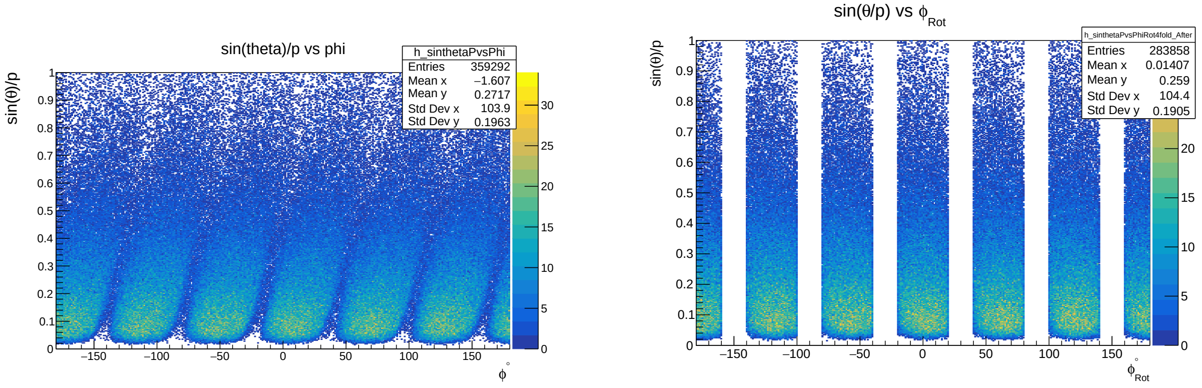

(a) (b)

FIG. 49. The plots depict the in-bending RGA data from the fall of 2018. Specifically, panel (a) (left) represents the $\sin(\theta)/p$ vs ϕ plot for Missing π^- in $H(e,[e'p\pi^+\pi^-]_{FD})X$ events before applying a geometrical fiducial cut (But after applied exclusivity cuts in panel (b)). In contrast, Fig. (48) (b) (right) displays the same plot after applying the geometrical fiducial cut.

based on the value of the missing mass squared $(MM^2_{e'p\pi^+})_{3-fold}$ for the reaction $ep \to e'p'\pi^+\pi^-$.

The “Exclusive Window” is defined as $(MM^2_{e'p\pi^+})_{3-fold} > 0.13$ GeV^2 and $(MM^2_{e'p\pi^+})_{3-fold} < 0.17$ GeV^2. This region corresponds to the expected signal region where the reaction $e'p \to e'p\pi^+\pi^-$ is expected to occur with a high probability.

On the other hand, the “Background Window” is defined as $(MM^2_{e'p\pi^+})_{3-fold} > 0.2$ GeV^2 and $(MM^2_{e'p\pi^+})_{3-fold} < 0.5$ GeV^2. This region corresponds to a wider range of missing mass squared values where we expect to observe background events.

To visualize these regions, we can define histograms that show the distribution of events in terms of the missing mass squared. For example, we can plot a histogram of the number of events as a function of $(MM^2_{e'p\pi^+})_{3-fold}$ for events that fall within the “Exclusive Window” and another histogram for events that fall within the “Background Window”. By comparing these histograms, we can distinguish between signal and background events and extract information about the properties of the reaction $ep \to e'p'\pi^+\pi^-$:

1. $h1\_pim\_3-fold\_exc \to Fill((MM^2_{e'p\pi^+})_{3-fold})$-
   Inside “Exclusive window.” (see Fig. 50 light green plot).

2. $h1\_pim\_3-fold\_bgnd \rightarrow Fill((MM^2_{e'p\pi^+})_{3-fold})$-
   Inside the "Background window." (see Fig. 50 red plot).

Similar geometrical fiducial cuts have been revised for the 3-fold case using the same methodology that was used to define the fiducial cuts for the 4-fold case. In the equation labeled as 113, the term "$phi\_Rotation\_3-fold$"(ϕ^{3-fold}_{Rot}) is defined in the following manner:

$$\phi^{3-fold}_{Rot} = \phi_Y - \frac{\sin(\theta_Y)}{p_Y} * 70^\circ. \tag{113}$$

```
if(phi_Rotation_3-fold < -180) phi_Rotation_3-fold+=360;
if(((-20 <phi_Rotation_3-fold) && (phi_Rotation_3-fold < 20)) ||
((40 <phi_Rotation_3-fold) && (phi_Rotation_3-fold < 80)) ||
((100 <phi_Rotation_3-fold) && (phi_Rotation_3-fold < 140)) ||
((-80 <phi_Rotation_3-fold) && (phi_Rotation_3-fold < -40)) ||
((-140 <phi_Rotation_3-fold) && (phi_Rotation_3-fold < -100)) ||
((160 <phi_Rotation_3-fold) || (phi_Rotation_3-fold < -160))){
```

Normalization

We aim to clarify the process of data normalization in this section. Since we lack an inclusive sample, the background of the 3-fold case needs to be computed using our existing histograms. As per Eq. (114), the normalization constant can be determined using the following calculation:

$$f\_bgnd = \frac{Integrate \text{ 3-fold}}{Integrate \text{ 4-fold } !Exc} \text{ in the background region,} \tag{114}$$

Then, the normalized background for the 3-fold is as follows:

$$\text{3-fold normalized background} = (f\_bgnd)(\text{4-fold !Exc integrated over the exclusive window of missing } \pi^- \; M^2), \tag{115}$$

Fig. 50 illustrates all the plots that we have defined.

Efficiency Calculation

- **Calculation of efficiency in data for π^- in the FD**

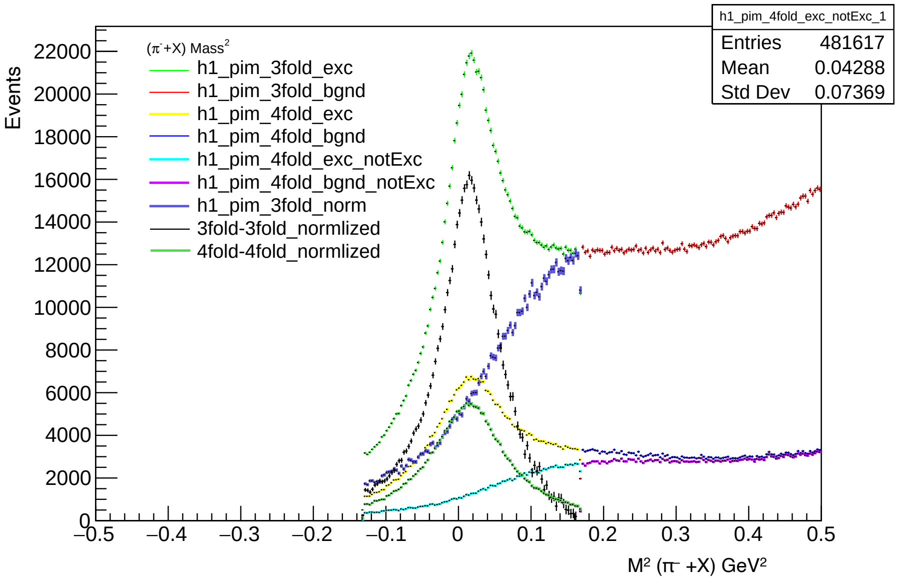

FIG. 50. Missing π^- mass square distributions for the fall-2018 pass1 data (only FD); Plots are named in the legend.

,

These histograms can be used to calculate the tracking efficiency of specific particles, such as π^-, by comparing the number of reconstructed tracks to the number of true tracks in the detector. To do this, one would need to analyze events where a known π^- particle was produced and passed through the detector. By comparing the reconstructed track of the π^- particle to the true track, the tracking efficiency can be calculated as the ratio of the number of reconstructed tracks to the number of true tracks. The histograms in the Fig. 50 can be used for the tracking efficiency calculation of π^- in the Forward Detector (FD) suggests that there are histograms in Fig. 50 that can be used to calculate the tracking efficiency of π^- particles in the Forward Detector (FD):

$$Efficiency = \frac{4\_fold - background}{3\_fold - normalized\_bgnd}, all\ in\ the\ "exclusive"\ window. \tag{116}$$

From Fig. 50, by subtracting the background 3-fold and 4-fold cases, the resultant histograms are “black” and “dark_green”, respectively:

$$\begin{aligned} Efficiency &= \frac{(h1\_pim\_4 - fold\_exc) - (h1\_pim\_4 - fold\_bgnd)}{(h1\_pim\_3 - fold\_exc) - (h1\_pim\_4 - fold\_exc\_notExc)}, \\ &= \frac{yellow - cyan}{light\_green - dark\_blue}, \\ &= \frac{black}{dark\_green}. \end{aligned} \tag{117}$$

$$Efficiency\_error = Efficiency * \sqrt{\frac{4 - fold\_err}{4 - fold} + \frac{3 - fold\_err}{3 - fold}}. \tag{118}$$

In the following manner, we can calculate the tracking efficiency by taking the integral of the “dark_green” and “black” histograms (see Fig. 50)

$$Tracking\ Efficiency\ \pi^-\ FD(Data) = 0.438923 \pm 0.001914. \tag{119}$$

- **Calculation of efficiency in simulation for π^- in the FD**

Similarly, We have computed the tracking efficiency for π^- in the forward detector (FD) using simulation. The simulation was performed using the same code as the data analysis and based on exclusive e, p, π^+, and π^- events extracted from SIDIS background merged (45nA) simulation files created by Orlando Soto. The simulation results are presented in Fig. 61, which is similar to Fig. 50.

$$Tracking\ Efficiency\ \pi^-\ FD(Simulation) = 0.402491 \pm 0.001824. \tag{120}$$

- **Bin-by-bin efficiency studies for π^- in the FD**

The same procedure has been applied to different bins of (p, θ) despite variations in efficiency, resulting in more accurate efficiency studies. The distribution of θ vs. p for π^- from $H(e, [e'p\pi^-\pi^+]FD)X$ in the CLAS12 FD data and simulation after applying PID, fiducial, and exclusivity cuts are presented in Fig. 51. The plot is enclosed by a red line, and we have divided it into four bands in polar angle θ (equally spaced between the minimum and maximum θ) and six equal bands in momentum ranging from 0.5 to 7.0 GeV/c.

The calculation of 1D efficiency calculation has followed for bin-by-bin studies. The efficiency calculations were carried out for each of the 6 sectors in FD. This bin-by-bin calculation has continued for both simulation and data separately.

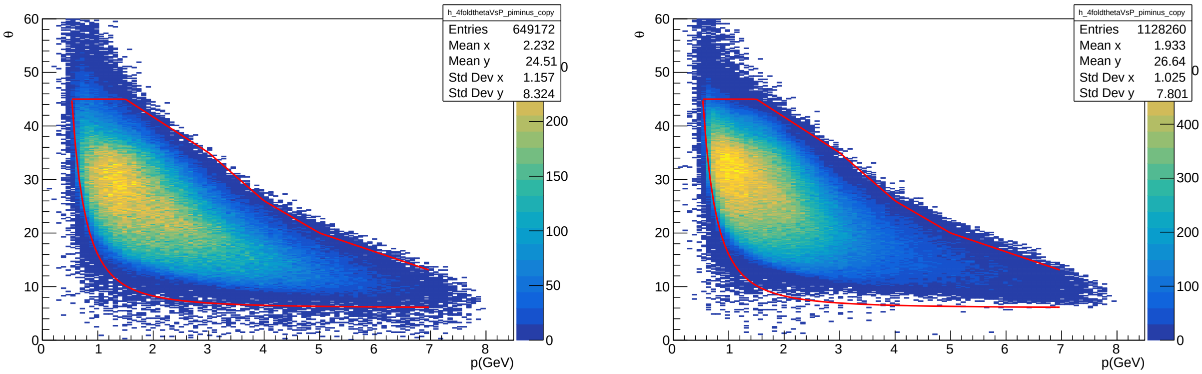

(a)

(b)

FIG. 51. The plot on the left displays the θ *vs.* p distribution of π^- tracks in the CLAS12 Forward Detector (FD) obtained from $H(e,[e'p\pi^-\pi^+]FD)X$ events after applying PID (particle identification), fiducial, and exclusivity cuts on the experimental data. The plot on the right shows the distribution of π^- in the CLAS12 FD based *simulated* $H(e,[e'p\pi^-\pi^+]FD)X$ events, after applying PID, fiducial, and exclusivity cuts.

The plots pertaining to certain bins located at the edges of the θ vs. p plot were affected by low statistics and, thus, appeared unsatisfactory. As a result, the efficiency calculations of these bins were not valid. Our study involved a correlation analysis of experimental data and simulation, examining each theta versus momentum bin across all six sectors of FD. A comparison of the resulting efficiency ratio from both sources was presented in Fig. 52. The analysis revealed that regions with a higher degree of statistics and acceptance demonstrated efficiency ratio values that approached unity, indicating a favorable agreement between the simulation and data. However, the bins located at the edges of the data set exhibited lower values of efficiency ratio due to a lack of statistical data.

$$ratio\_pim[ith][ip] = \frac{Data\_Efficiency[ith][ip]}{Simu\_Efficiency[ith][ip]}, \tag{121}$$

$$\begin{aligned} ratio\_pim\_error = {} & ratio\_pim[ith][ip] \\ & * \sqrt{\left(\frac{data\_error\_pim[ith][ip]}{Data\_Efficiency[ith][ip]}\right)^2 + \left(\frac{simu\_error\_pim[ith][ip]}{Simu\_Efficiency[ith][ip]}\right)^2}. \end{aligned} \tag{122}$$

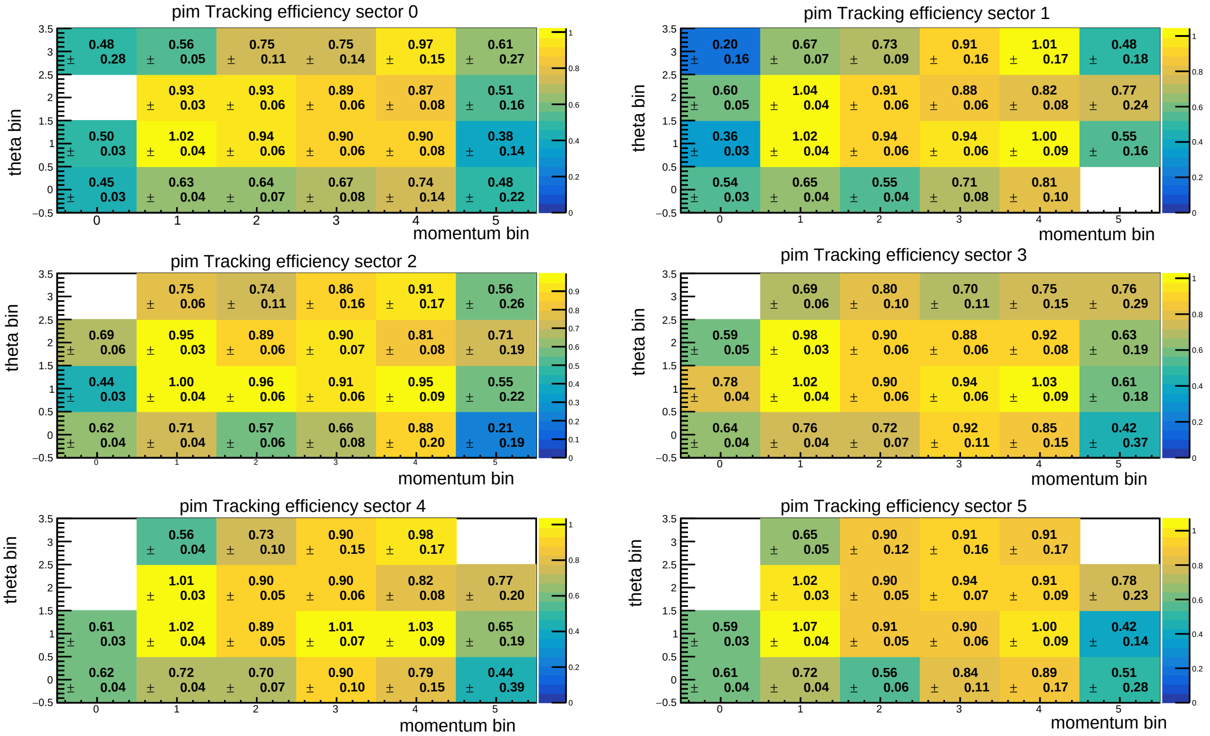

FIG. 52. Ratio of π^- efficiency extracted from 3-fold vs. 4-fold coincidence of the data, to the same efficiency extracted from simulation with background folding, for all 6 sectors in FD.

Calculation of π^+ tracking efficiency values in FD

The figure labeled Fig. 53 displays the ratio of proton efficiency obtained from 3-fold compared to 4-fold coincidence of data, in contrast to the efficiency extracted from simulation for all six sectors in the Forward Detector (FD). The methodology used in this study is similar to that used in a previous study involving π^- particles.When there is sufficient data and acceptance, the efficiency ratios are nearly equal to one. However, the efficiency is reduced at the edges of the data due to a lack of statistical data in those bins.

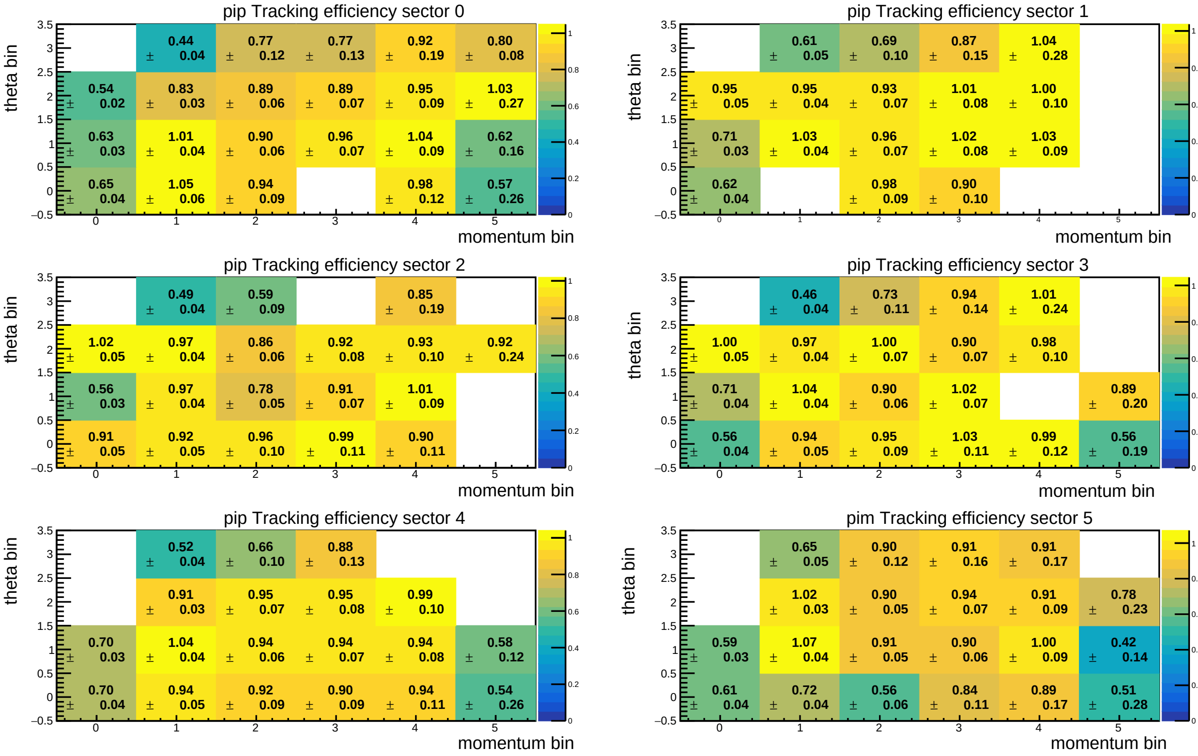

FIG. 53. Ratio of π^+ efficiency extracted from 3-fold vs. 4-fold coincidence of the data, to the same efficiency extracted from simulation with background folding, for all 6 sectors in FD.

Calculation of proton tracking efficiency values in FD

The figure labeled Fig. 54 displays the ratio of proton efficiency obtained 3-fold compared to the 4-fold coincidence of data, in contrast to the efficiency extracted from simulation for all six sectors in the Forward Detector (FD). The methodology used in this study is similar to that used in a previous study involving π^- particles. Fig. 54 also evidence that the efficiency ratios approach unity when there is enough data and acceptance, but at the edges of the data, efficiency decreases due to insufficient statistical data in those bins.

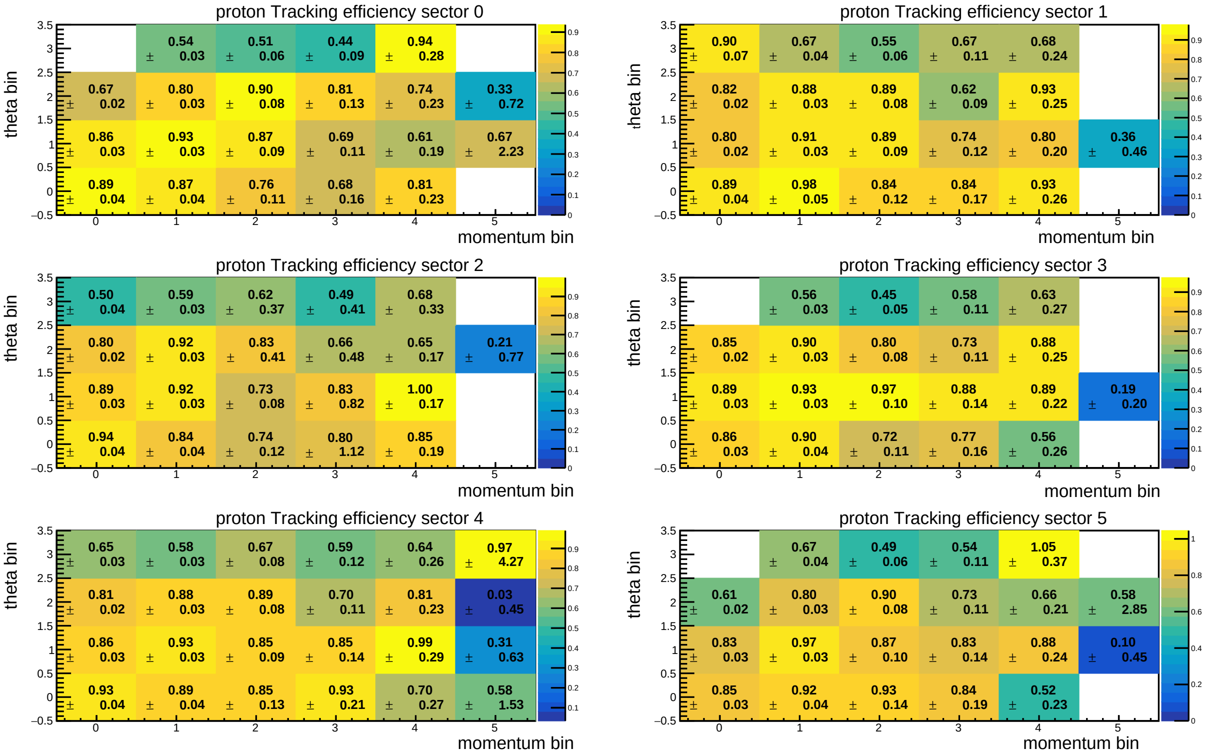

FIG. 54. Ratio of proton efficiency extracted from 3-fold vs. 4-fold coincidence of the data, to the same efficiency extracted from simulation with background folding, for all 6 sectors in FD.

6.2 CD TRACKING EFFICIENCY

Based on the available pass-1 data, the efficiency of the tracker has been shown to be in the range of $50 - 80\%$. This inefficiency is due to biases in the reconstruction code and the fact that the CD tracking is not optimal at the moment. Additionally, the detector alignment is not yet fully completed, which also contributes to the inefficiency.

Efficiency studies for pass-1 cooking are currently challenging, but the hope is that once these issues are resolved, the tracker efficiency will improve significantly. In particular, for pass-2 cooking, it is expected that the CVT efficiency should be close to $90 - 95\%$ over nearly the full azimuth acceptance of the detector, which would bring it much closer to the defined detector specifications.

As mentioned in the introduction, we have chosen the exclusive approach of two charged pions, specifically the $ep \to e'p\pi^+\pi^-$ reaction. Our approach involves comparing the number of CD tracks in exclusive kinematics with the number of CTOF hits consistent with exclusivity for $(e, e'p\pi^+)X$ where X is either missing or a detected exclusive π^-.

We have considered two cases: the 4-fold $(H(e, [e'p\pi^+])_{FD}[\pi^-]_{CD})$ and 3-fold $(H(e, [e'p\pi^+])_{FD})$ cases. Through these approaches, we aim to assess the CD tracking efficiency. The following two sub-sections will discuss the 3-fold and 4-fold cases separately.

4-fold case - $H(e, [e'p\pi^+]_{FD}[\pi^-]_{CD})$

We begin by examining the distributions of missing total mass and missing total energy in the event sample where e, p, and π^+ are detected in the FD while π^- is detected in the CD $(H(e, [e'p\pi^+]_{FD}[\pi^-]_{CD})$, assuming that π^- in the CD is the missing particle in the reaction.

$$MM^2_{(e'p\pi^+)_{FD}(\pi^-)_{CD}} = (k_{beam} + P_{target} - k_{e'} - P'_p - p_{\pi^+} - p_{\pi^-})^2. \tag{123}$$

Fig. 55 illustrates the Missing total mass square and Missing total energy plots for the event sample where e, p, and π^+ are detected in the FD while π^- is detected in the CD $(H(e, [e'p\pi^+]FD[\pi^-]CD)$, assuming that π^- in the CD is the missing particle in the reaction.

To select exclusive events, we apply two exclusivity cuts, $|M_X^2| < 0.1$ GeV^2 and $|E_X| < 0.5$ GeV, which are illustrated by a red line in Fig. 55:

To address the current issue of poor CD tracking, we employed a method to calculate the tracking χ^2 using CTOF hits that are consistent with the exclusivity of the missing π^- in the CD. The process of calculating the helical trajectory for the CTOF hits in the CD is detailed in Appendix E, and involves determining the (t, ϕ, z) coordinates of the CTOF

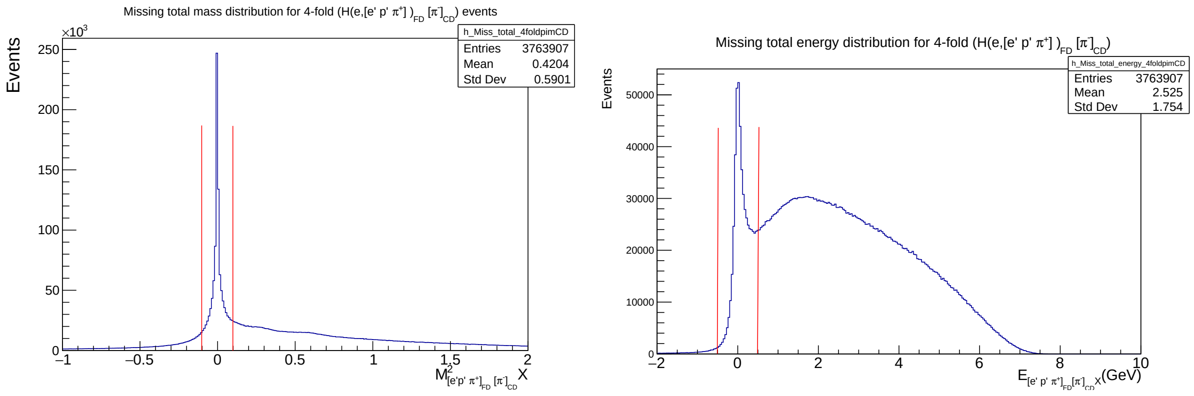

(a) (b)

FIG. 55. The plots depict the missing total mass square and missing total energy distributions for $H(e,[e'p\pi^+]FD[\pi^-]CD)X$ events in the fall 2018 in-bending RGA data. The left plot (Fig. (a)) displays the missing total mass square distribution, with the exclusivity cuts of $-0.1 < M_X^2(\text{GeV}^2) < 0.1$ marked by a red line. The right plot (Fig. (b)) shows the missing total energy distribution, with the exclusivity cut of -0.5 $< E_X$ (GeV) < 0.5 marked by a red line.

hit point based on the predicted hit coordinate of the CTOF. This can be expressed using cylinder coordinates, as shown in Eq. (124).

$$\chi^2 = \frac{(\phi(t_v+T)-\phi_{CTOF})^2}{\sigma_\phi^2} + \frac{(Z(t_v+T)-Z_{CTOF})^2}{\sigma_z^2} + \frac{((t_v+T)-t_{CTOF})^2}{\sigma_t^2}, \tag{124}$$

where: t_v=vertex time, T=Predicted time of the hit, $\sigma_\phi = 2\pi/(48\times\sqrt{12})$, $\sigma_z = 4.0$ cm, $\sigma_t = 0.065$ ns.

Substituting the value “T” from Appendix E into Eq. (124) yields the calculation of χ^2. The total χ^2 distribution is displayed in Fig. 56. To improve the accuracy of the pi-minus missing mass distribution, we created separate χ^2 distributions for each of the three terms in Eq. (124): χ^2_ϕ, χ^2_z, and χ^2_t, and applied separate χ^2 cuts. The separate χ^2 distributions are presented in Fig. 57. All ChiSq distributions are subject to Miss total MassSq ($-0.1 < M_X^2(\text{GeV}^2) < 0.1$) and Miss total energy ($-0.5 < E_X(\text{GeV}) < 0.5$) exclusivity cuts.

The missing π^- mass square distribution was examined using Eq. (125). Fig. 58a displays the missing π^- mass square distribution before any cuts were applied:

$$(MM^2_{(e'p\pi^+)_{FD}})_{4-fold} = (k_{beam} + P_{target} - k_{e'} - P'_p - p_{\pi^+})^2. \tag{125}$$

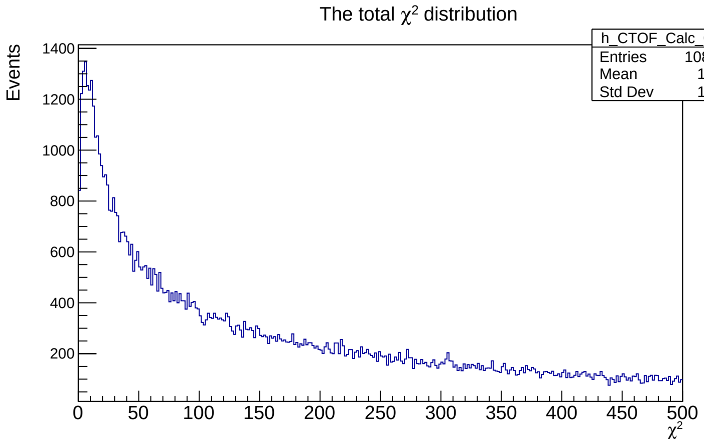

FIG. 56. The total χ^2 distribution (Eq. (124)) for the fall 2018 in-bending data after the exclusivity cuts.

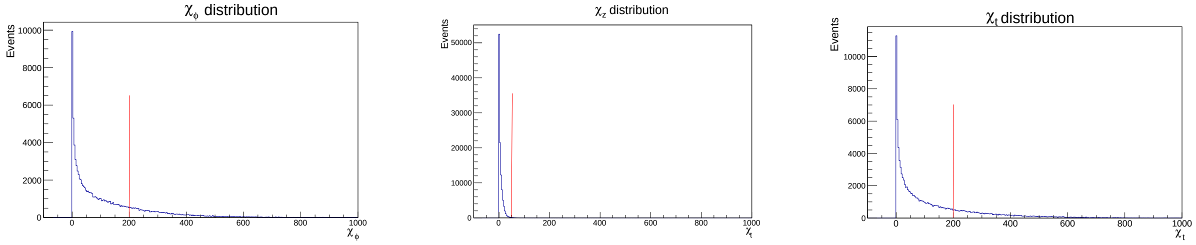

(a) (b) (c)

FIG. 57. The figure displays the separate χ^2 distributions for three terms in Eq. (124): (a) χ^2_ϕ, (b) χ^2_z, and (c) χ^2_t. The red line in each plot represents the respective χ^2 cut used, which are $\chi^2_\phi < 200$, $\chi^2_z < 50$, and $\chi^2_t < 200$. It is important to note that all these ChiSq distributions are made after applying the exclusivity cuts.

Then, the following cuts are applied in the missing pi-minus mass square distribution in CD. The Fig. 58(b) represents the distribution after the following cuts:

1. $\theta_{(e'p\pi^+)_{FD}}(4-fold) > 35°$–piminus in the CD.
2. $P_T((e'p\pi^+)_{FD})(4-fold) > 0.2$ GeV.
3. phi cut–this cut is shown in Fig. 59

   $-22.5° < \phi < 22.5°$, $37.5° < \phi < 82.5°$, $102.5° < \phi < 142.5°$, $-82.5° < \phi < -37.5°$, $-142.5° < \phi < -102.5°$, $-157.5° < \phi$, and $\phi < -157.5°$.
4. $-0.1 < M_X^2(X = \pi^-_{CD} + X)(4-fold)\mathrm{GeV}^2 < 0.29$.
5. $\chi^2_{phi} < 200, \chi^2_z < 50$, and $\chi^2_t < 200$.

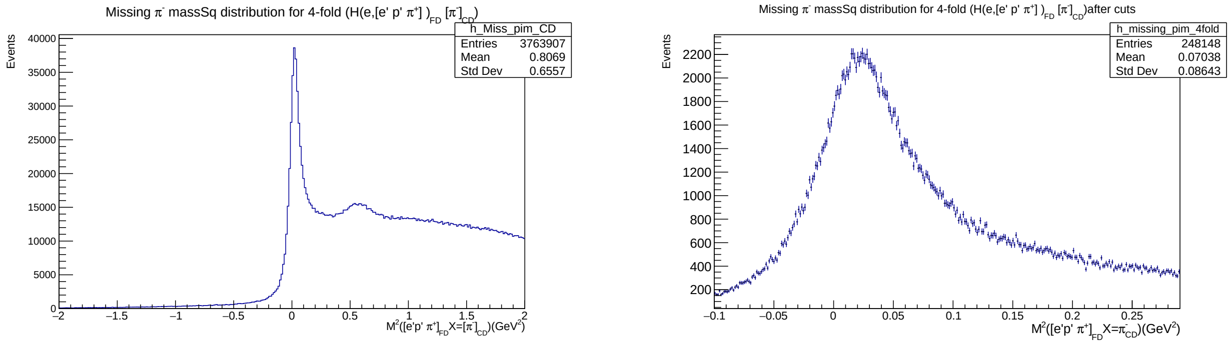

(a)

(b)

FIG. 58. The two plots depicting the distribution of missing mass squared $(M^2_{\pi^-})$ for the negative pion (π^-) in a certain type of event denoted as $H(e,[e'p\pi^+]_{FD}[\pi^-]_{CD})$. The plots correspond to data collected during the Fall of 2018 in the in-bending configuration. The plot on the left shows the $M^2_{\pi^-}$ distribution for all events before applying any selection cuts, while the plot on the right shows the $M^2_{\pi^-}$ distribution for events that pass certain selection criteria.

The "phi cut", has been incorporated to address the issue of poorly reconstructed tracks at the edges of the detector. This cut may involve removing tracks that have certain values of the detector azimuthal angle, ϕ. Fig. 59 depicts the effect of this cut, showing a graphical comparison of the missing π^- mass square distribution before and after the phi cut is applied. The phi cut is further detailed in item 3 (see section 5) of the analysis:

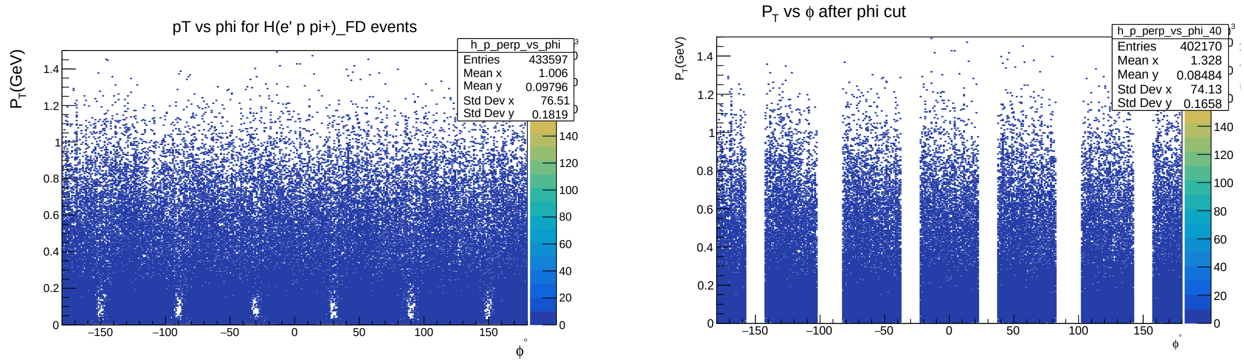

(a) (b)

FIG. 59. The two plots depicting the P_T vs. ϕ distribution before and after the application of the phi cuts. These plots are from fall-2018 in-bending data and are likely part of an analysis in experimental particle physics. The left plot displays the P_T vs. ϕ distribution before the phi cuts are applied, while the right plot shows the distribution after the phi cuts are implemented. These plots can provide insights into the effect of the phi cuts on the distribution of P_T vs. ϕ and may be used to assess the efficiency of the selection criteria.

3-fold case - $H(e, [e'p\pi^+]_{FD})$

Considering both FD and CD events in the 3-fold case. The analysis involves constructing a missing π^- mass square distribution for 3-fold events of the form $H(e, [e'p\pi^+]_{FD})$, as specified in Eq. (126). This equation likely represents the formula used to calculate the missing π^- mass square for the specified type of events:

$$(MM^2_{(e'p\pi^+)_{FD}})_{3-fold} = (k_{beam} + P_{target} - k_{e'} - P'_p - p_{\pi^+})^2. \tag{126}$$

In the context of a 3-fold case, Fig. 60 displays the missing mass distributions before and after cuts The cuts applied to the data are similar to those used in the 4-fold case, with the exception of the χ^2 cuts. The figure provides a visual representation of the distribution of missing masses for 3-fold events before and after the application of the selection criteria. By comparing the two sets of data, we can gather valuable information about how the applied cuts are affecting the characteristics of the 3-fold events.

1. $\theta_{(e'p\pi^+)_{FD}}(3-fold) > 35°$–piminus in the CD.
2. $P_{T(e'p\pi^+)_{FD}}(3-fold) > 0.2$ GeV
3. phi cut–this cut is shown in Fig. 59.

   $-22.5° < \phi < 22.5°$, $37.5° < \phi < 82.5°$, $102.5° < \phi < 142.5°$, $-82.5° < \phi < -37.5°$, $-142.5° < \phi < -102.5°$, $-157.5° < \phi$ and $\phi < -157.5°$.
4. $-0.1 < M^2_X(X = \pi^- + X)(3-fold)\,\mathrm{GeV}^2 < 0.29$.

Simulation for π^- in CD

The aim of this section is to elucidate the CD efficiency investigations conducted for simulations, which are vital in understanding the accuracy of simulation results. These investigations utilized the SIDIS MC data provided by Orlando Soto. Furthermore, similar studies were performed on additional MC simulation data to validate the findings. Two distinct data sets were utilized for this purpose.

1. True exclusive,
2. (SIDIS - true exclusive)=inclusive.

To study the scenario of “true exclusive” events, a Groovy script was implemented to extract these events from the “full SIDIS” dataset. In the context of “(SIDIS- true exclusive)”, the full SIDIS files were executed, and the true exclusive events were subsequently deduced by means of the implemented script. Fig. 61 illustrates the missing pi-minus mass square distributions obtained from 3-fold true exclusive, 4-fold true exclusive, 3-fold inclusive, and 4-fold inclusive MC simulations, where the distributions are depicted in different colors to differentiate between the various simulation categories.

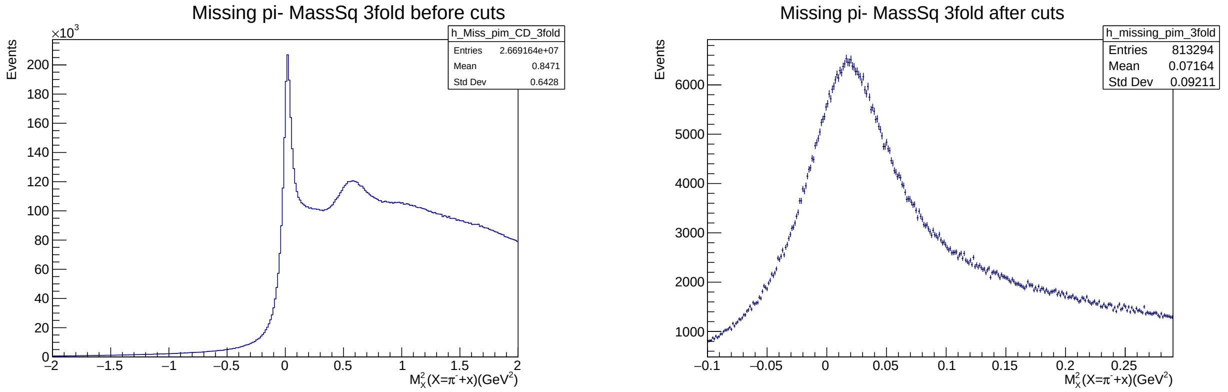

(a) (b)

FIG. 60. The two plots from an analysis of fall-2018 in-bending data, both of which display the missing π^- mass square distribution. The left plot shows the distribution before any cuts are applied, while the right plot shows the distribution after the cuts are implemented for the 3-fold case.

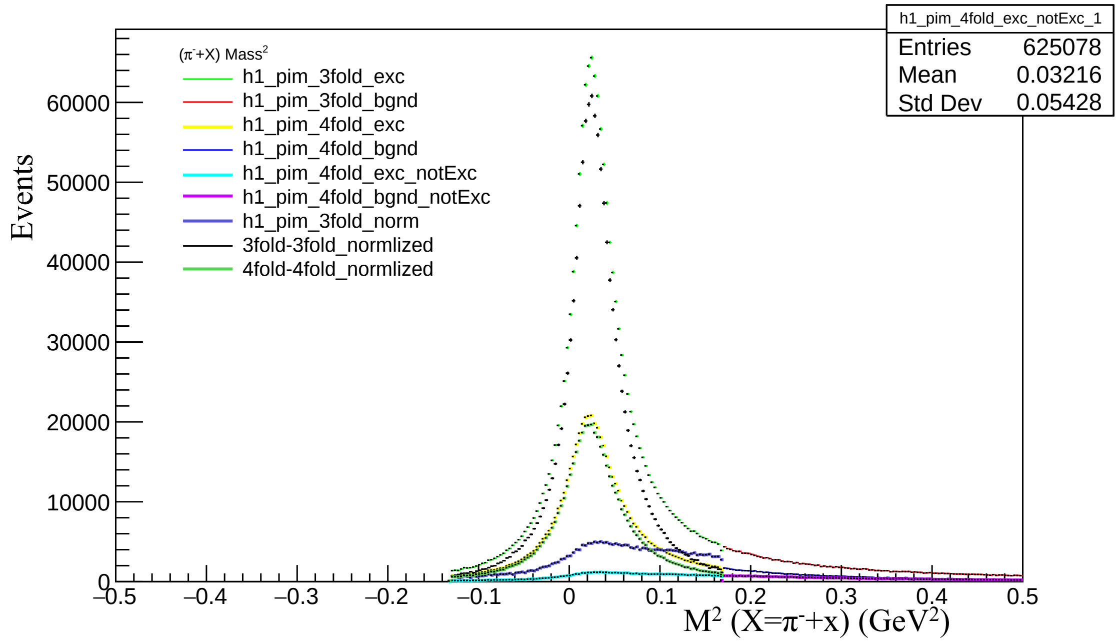

FIG. 61. Missing π^- massSq distribution for the simulation π^- in CD; 3-fold true exclusive (black), 4-fold true exclusive (red), 3-fold inclusive (green), and 4-fold inclusive (magenta).

Normilzation Procedure for π^- in CD

The objective of this section is to clarify the normalization procedure used for the data. Since the data lacks inclusive events, simulation was employed to establish a match between the data and simulation data. By using both inclusive and exclusive simulation data, a fit was obtained that closely corresponds to the data. The normalization of the data was accomplished by using two constants, as shown in the following formulas. Additionally, the "3-fold data" histogram was fitted over the range of $[-0.1, 0.29]$.

$$3 - fold\,Data = A \cdot [3 - fold\,exclusive]_{simu} + B \cdot [3 - fold\,inclusive]_{simu}. \tag{127}$$

The normalization constants A and B were utilized to normalize the data. The calculation procedure for these constants is illustrated in Appendix F. Similarly, the "4-fold histogram" was fitted within the range of $[-0.1, 0.29]$.

$$4 - fold\,Data = A' \cdot [3 - fold\,exclusive]_{simu} + B' \cdot [3 - fold\,inclusive]_{simu}. \tag{128}$$

The normalization constants A' and B' can be calculated using the method described in Appendix F. Additionally, the simulation histograms needed to be adjusted by adding smearing and peak offset to achieve a closer match with the experimental data.

Thus, in the case of π^-, the following smearing function was applied to the simulation plot.

$$smear\_sigma = 0.025,$$
$$smear\_offset = -0.0093.$$

Before filling the histogram with each simulation event, it is necessary to apply the specified smearing function to the Gaussian distribution. This ensures that the simulated events more closely resemble the experimental data.

$$smearRan = ran3.Gaus(smear\_offset.smear_sigma).$$

Then, need to fill the histogram:

$$hmissingmass- > Fill(MisspimCD.M2() + smearRan).$$

The resulting fitted plot (yellow plot) generated from the normalization constants is displayed in Fig. 62. This fit represents the closest match achievable between the simulation and experimental data.

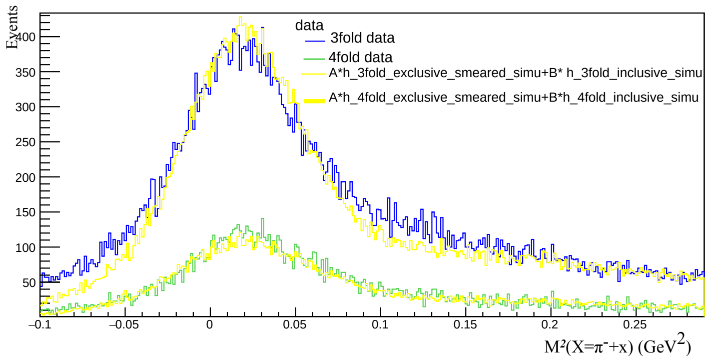

FIG. 62. The best-fitted plots (yellow) to the 3-fold and 4-fold data using simulation

The normalization constants for the 3-fold and 4-fold missing π^- events are as follows:
3-fold case → $A = 0.505660, B = 0.478655$,
4-fold case → $A' = 0.322414, B' = 0.413565$.

Next, the background must be removed from the data. This was achieved through the use of background normalization techniques. Once the background normalized plot was generated, it was subtracted from the fitted data plot to produce the true plots without background. These are displayed in Fig. 63 and are represented by the black line.

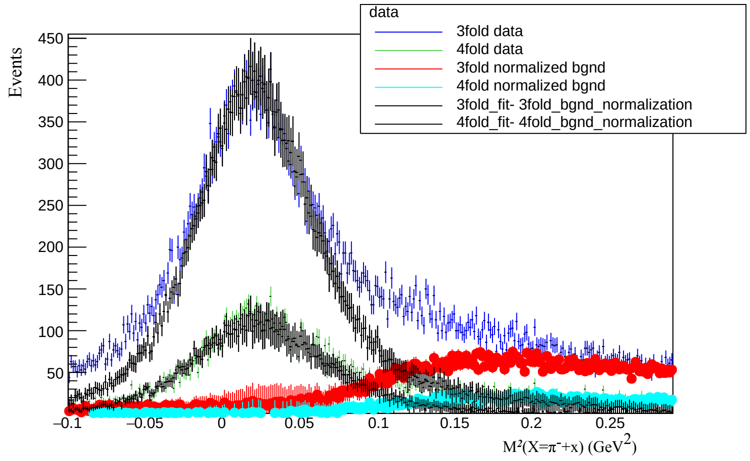

FIG. 63. The missing mass squared distribution of π^- in CD is displayed in the plots, with the background subtracted and represented by the black line.

The two black plots presented in Fig 63 are critical for determining the efficiency of the data. The efficiency was computed by integrating the area between −0.05 and 0.05 in the two aforementioned plots (Fig. 63). The efficiency value can be expressed mathematically as the integral of the region between −0.05 and 0.05 in the black plots shown in Fig. 63.

From Fig. 63

$$\begin{aligned} Data\ Efficiency &= \frac{\int_{-0.05}^{0.05} 4 - fold\, black\, plot}{\int_{-0.05}^{0.05} 3 - fold\, black\, plot}, \\ Data\ Efficiency &= 0.2876 \pm 0.0060. \end{aligned} \tag{129}$$

From Fig. 61

$$\begin{aligned} Simulation\ Efficiency &= \frac{\int_{-0.05}^{0.05} 4 - fold\, black\, plot}{\int_{-0.05}^{0.05} 3 - fold\, red\, plot}, \\ Simulation\ Efficiency &= 0.4706 \pm 0.0033. \end{aligned} \tag{130}$$

Bin-by-bin efficiency studies in π^- in CD

In order to improve the accuracy of the efficiency analysis, we repeated the above procedure using different (p, θ) binning configurations. Fig. 64 displays the π^- missing theta versus momentum plot with a red boundary line obtained as a result of this analysis.

The data for both the 3-fold and 4-fold cases were plotted in a similar manner as shown in Fig. 64. The resulting plot was then divided into 4 polar angle θ bins and 5 momentum bins, equi-spaced between the minimum and maximum polar angle θ as a function of momentum, and 5 equal bands in momentum from 0.2 to 2.0 GeV/c, as delineated by the red outline in Fig. 64.

The ratio of the tracking efficiency was then calculated for each bin in terms of the π^- extracted from the data to the value obtained from the simulation, bin-by-bin θ versus p, and is shown in Fig. 65. The ratios in all regions are less than unity due to the lack of improved CD tracking. Due to the limited statistics, we have removed most of the bins at the edges.

Efficiency ratios in π^+ in CD

The procedure used to estimate the tracking efficiency of π^+ particles in the CD is analogous to the method described earlier. The Fig. 66 shows the tracking efficiency values extracted from 3-fold vs. 4-fold coincidences of the data, to the same efficiency extracted

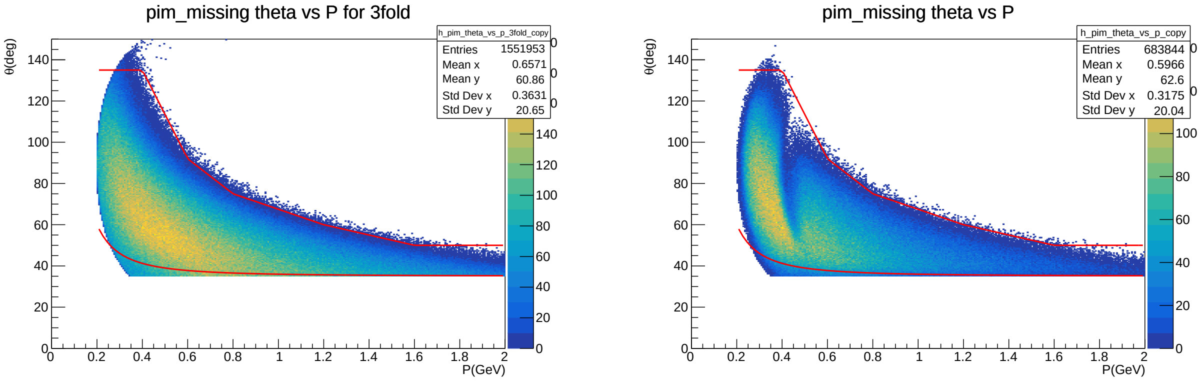

(a) (b)

FIG. 64. The π^- missing in theta versus momentum plot for the exclusive simulation, with the left and right panels displaying the 3-fold and 4-fold configurations, respectively, for the CD π^-. The red boundary line in each panel represents the results obtained from this analysis.

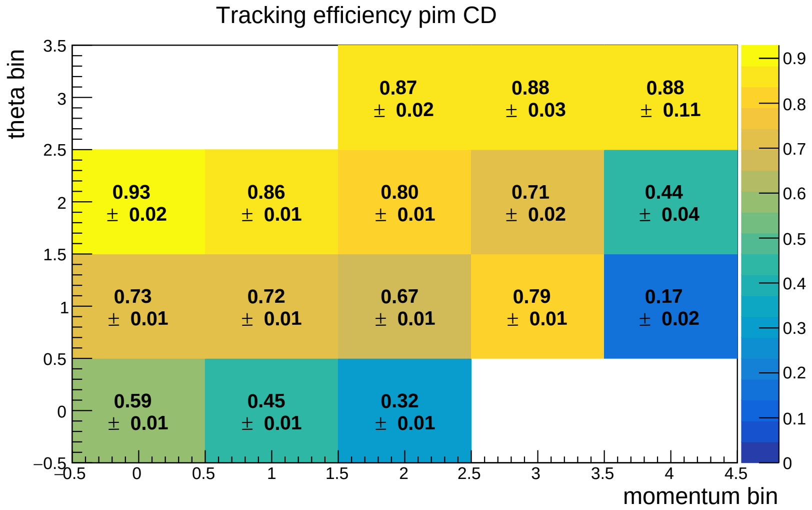

(a)

FIG. 65. Ratio of π^- efficiency extracted from 3-fold vs. 4-fold coincidences of the data, to the same efficiency extracted from simulation in CD.

from the simulation in CD. As shown in Fig. 66, the efficiency ratios obtained are not close to unity, indicating that there are some factors that affect the tracking performance of the CD and are not adequately accounted for in the simulations. These may include, for example, issues related to detector resolution, calibration, and alignment.

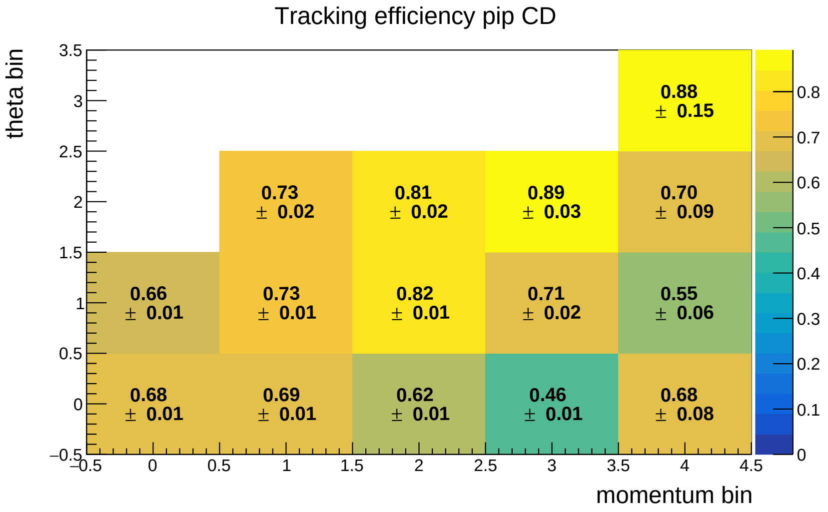

(a)

FIG. 66. Ratio of π^+ efficiency extracted from 3-fold vs. 4-fold coincidences of the data, to the same efficiency extracted from simulation in CD.

- **Efficiency ratios in proton in CD**

In this case, the same procedure has used. The tracking efficiency ratio values are calculated using the extracted from 3-fold vs. 4-fold coincidences of the data, to the same efficiency extracted from the simulation. Fig. 67 shows the efficiency ratio values calculated for the proton in the CD.

6.2.1 EFFICIENCY RATIO OF THREE PARTICLES

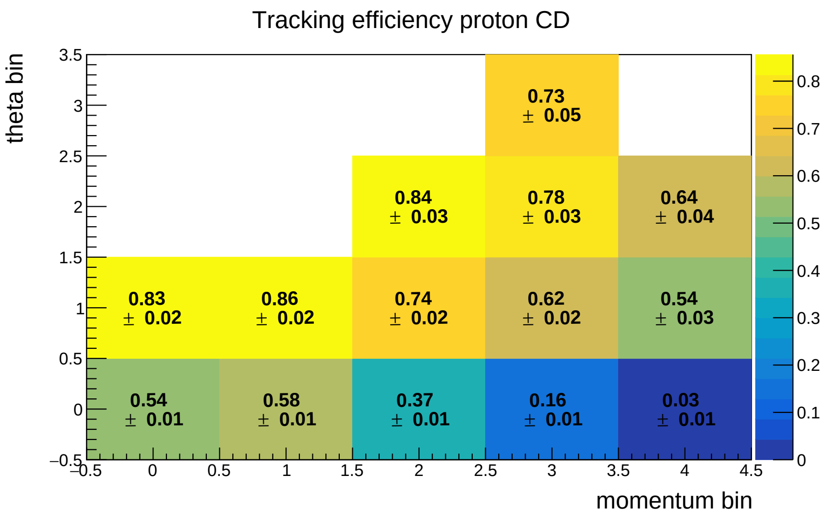

(a)

FIG. 67. Ratio of proton efficiency extracted from 3-fold vs. 4-fold coincidences of the data, to the same efficiency extracted from simulation in CD.

Subsequently, we examined the three particle ratios separately and calculated the corresponding weight factors, which we collectively referred to as the "weight-total" factors. The equation defining these factors is provided below.

$$weight\_total = \frac{\epsilon_{\pi^-}(p_{\pi^-}, \theta_{\pi^-})_{Data}}{\epsilon_{\pi^-}(p_{\pi^-}, \theta_{\pi^-})_{Simu}} \times \frac{\epsilon_{\pi^+}(p_{\pi^+}, \theta_{\pi^+})_{Data}}{\epsilon_{\pi^+}(p_{\pi^+}, \theta_{\pi^+})_{Simu}} \times \frac{\epsilon_p(p_p, \theta_p)_{Data}}{\epsilon_p(p_p, \theta_p)_{Simu}}. \tag{131}$$

The calculation of the weight total factor, as defined in Eq. (131), is a crucial step in the cross-section analysis, as outlined in Chapter 7 (see Eq. (140)). However, it should be noted that for the purpose of enhancing the accuracy of the cross-section analysis, we excluded the majority of low ratio values in previous bins and utilized only the ratio values exceeding 80%. This selection criterion was based on the consideration that the low ratio values could potentially introduce significant systematic uncertainties in the cross-section analysis, while the high ratio values are more likely to reflect the underlying physical processes of interest.

6.3 CONTROVERSY BETWEEN OTHER EFFICIENCY STUDIES IN CLAS12

Our calculation of the tracking efficiency has been subject to some debate, particularly in the results reported in the 2020-005 CLAS12 note [44]. According to this note, an 80% efficiency was achieved for each of the particles considered, namely protons, π^+, and π^-.

However, this value is in marked difference with the 1D efficiency calculation shown in Fig. 50, which was based on the ratio of 4-fold to 3-fold distributions.

It should be noted that the CLAS tech note [44] employed a different methodology for calculating efficiency, specifically by taking the ratio with and without background mixing. This approach is considered more precise at this stage of the data analysis and may help to reconcile some of the discrepancies observed between our study and that of the CLAS12 note.

Based on my interpretation, it seems that selecting a region with a higher number of events from the p vs θ distributions (as shown in Fig. 51) could help resolve the controversy surrounding my analysis. By focusing on a region with a larger statistical significance, it may be possible to reduce the impact of statistical fluctuations and improve the accuracy of the measurements. In my opinion, the red outline in the figure represents the area with the most statistics and may be a suitable choice for further investigation.

Despite having calculated my 1D tracking efficiency values, we chose not to use them in our cross-section analysis and instead relied on bin-by-bin studies. In particular, we focused on regions where the statistics were sufficient, and the acceptance was good, particularly in the middle bins. In these regions, my calculations showed that the efficiency was close to unity in the FD, which provided more than enough accuracy for our analysis. As a result, we did not encounter any issues or obtain unsatisfactory results.

CHAPTER 7

CROSS SECTION

7.1 CROSS-SECTION MODEL FITTING

In this section, our focus is on a more modest objective, which involves the fitting of the distributions of the cross- section in bins of $(Q^2, x_B, tmin - t)$ with respect to the variables $m_{\pi\pi}, \Theta_R, \Phi_R$, and Φ_h. It is noteworthy that, in this context, the rest frame angles are referred to as $\cos(\Theta_R)$ and Φ_R, where $\cos(\Theta_R)$ is the cosine angle in the $\pi\pi$ rest frame, Φ_R is the azimuth angle in the $\pi\pi$ rest frame and Φ_h is the relative azimuth between the electron scattering and hadron scattering plane. Our aim is to obtain a comprehensive understanding of the relationships between these variables and the cross-section, as well as any other underlying factors that may impact our results.

The virtual photon, denoted as γ^*, possesses three potential helicity states, namely $\lambda = \pm 1$, where the photon polarization is transverse (T), and $\lambda = 0$, where the polarization is longitudinal (L). It is imperative to differentiate the cross-section based on the polarization states of the virtual photon in order to analyze meson production in terms of Generalized Parton Distributions (GPDs). It should be noted that the factorization of meson production using GPDs has only been proven for longitudinal photons at twist 2. In accordance with the one-photon-exchange hypothesis, upon integrating over the $\pi\pi$ decay in phase space $d\Omega_R$, the cross-section for exclusive meson production on an unpolarized proton target can be expressed in its general form as follows:

$$\begin{aligned} d\sigma &= \Gamma\left[d\sigma_T + \epsilon d\sigma_L + \sqrt{\epsilon(1+\epsilon)}\cos\Phi_h d\sigma_{LT} + \epsilon\cos(2\Phi_h)d\sigma_{TT}\right], \\ \epsilon &= 1/\left[1 + 2\frac{\mathbf{q}^2}{Q^2}\tan^2(\theta_e/2)\right], \end{aligned} \tag{132}$$

where Γ is the virtual photon flux factor [45], and ϵ describes both the degree of longitudinal and transverse-linear polarization of the virtual photons. This target rest-frame definition of ϵ is equivalent to the Lorentz-invariant definition given in Eq. (132). In terms of the Lorentz invariant phase space defined in Eq. (48), the photon flux factor is:

$$\frac{d^3\Gamma}{dx_B dQ^2 d\phi_e} = \frac{\alpha}{4\pi}\frac{(W^2 - M^2)(q\cdot P)}{(k\cdot P)^2 x_B}\frac{1}{Q^2(1-\epsilon)}. \tag{133}$$

The more general angular forms are described in Schilling and Wolf [25] for production in a single vector meson channel. We develop the more general form below, including terms of interference between different spin-isospin channels. The general cross-section can be summarized as

$$d\sigma = \Gamma\left[d\mathfrak{R}_T + \epsilon d\mathfrak{R}_L + \sqrt{\epsilon(1+\epsilon)} f^{\alpha}_{TL} d\mathfrak{R}^{\alpha}_{TL} + \epsilon f^{\alpha}_{TT} d\mathfrak{R}^{\alpha}_{TT}\right], \tag{134}$$

where the factors f^{α}_{TL} and f^{α}_{TT} are linearly independent functions of $(m_{\pi\pi}, \Phi_R, \Theta_R, \Phi_h)$. For the cross-section (at fixed Q^2, x_B, t) the $(m_{\pi\pi}, \Theta_R, \Phi_R, \Phi_h)$ distribution has the form

$$\begin{aligned} d\mathfrak{R} = &\sum_{(J',I'),(J,I)} \sum_{(\lambda'_h,\lambda_h)(\lambda',\lambda)} \left[T^{(\lambda'_h,\lambda')}_{J',I'} D^{J'}_{0,\lambda'_h}(\Phi_R,\Theta_R,-\Phi_R)\Omega_{J',I'}(m_{\pi\pi})\right]^{\dagger} \rho^{(h)}_{\gamma}(\lambda',\lambda) \\ &\qquad T^{(\lambda_h,\lambda)}_{J,I} D^{J}_{0,\lambda_h}(\Phi_R,\Theta_R,-\Phi_R)\Omega_{J,I}(m_{\pi\pi}), \\ = &\, d^{J'}_{0,\lambda'_h}(\Theta_R) d^{J}_{0,\lambda_h}(\Theta_R) e^{i(\lambda_h-\lambda'_h)\Phi_R} \left[T^{(\lambda'_h,\lambda')}_{J',I'}\Omega_{J',I'}(m_{\pi\pi})\right]^{\dagger} \rho^{(h)}_{\gamma}(\lambda',\lambda) T^{(\lambda_h,\lambda)}_{J,I}\Omega_{J,I}(m_{\pi\pi}), \end{aligned} \tag{135}$$

with summation over all repeated indices. The $\mathfrak{R}_{TT}$ and $\mathfrak{R}_{TL}$ factors have a prefactor of ϵ. In practice, this was absorbed into the empirical $\bar{A}_i$ (Eq. (149)) values to simplify the analysis. This means that the fitted $\bar{A}_i$ (Eq. (149)) values include the effect of ϵ and are thus a combination of the true $\bar{A}_i$ (Eq. (149)) values and the ϵ pre-factor.

The specific terms $d\mathfrak{R}_{\Lambda}$ are given by a decomposition of the photon density matrix:

$$\begin{aligned} \rho_T(\lambda',\lambda) &= \delta_{\lambda',\lambda}\left[1-\delta_{\lambda,0}\right]\rho_{\gamma}(\lambda',\lambda) = \delta_{\lambda',\lambda}\left[1-\delta_{\lambda,0}\right], \\ \rho_L(\lambda',\lambda) &= \delta_{\lambda',0}\delta_{\lambda,0}\rho_{\gamma}(\lambda',\lambda) = 2\epsilon\,\delta_{\lambda',0}\delta_{\lambda,0}, \\ \rho_{TT}(\lambda',\lambda) &= \delta_{\lambda',-\lambda}\left[1-\delta_{\lambda,0}\right]\rho_{\gamma}(\lambda',\lambda) = -\epsilon e^{i\Phi_h(\lambda'-\lambda)}\delta_{\lambda',-\lambda}\left[1-\delta_{\lambda,0}\right], \\ \rho_{TL}(\lambda,\lambda') &= \left\{\delta_{\lambda',0}\left[1-\delta_{\lambda,0}\right] + \delta_{\lambda,0}\left[1-\delta_{\lambda',0}\right]\right\}\rho_{\gamma}(\lambda,\lambda'), \\ &= \sqrt{\epsilon(1+\epsilon+2\delta_C)}\left\{-\lambda\delta_{\lambda',0}\left[1-\delta_{\lambda,0}\right]e^{i\lambda\Phi_h} - \lambda'\delta_{\lambda,0}\left[1-\delta_{\lambda',0}\right]e^{-i\lambda'\Phi_h}\right\}. \end{aligned} \tag{136}$$

In the appendix labeled “Cross Section” (Appendix B), the calculations for the terms “Transverse and Longitudinal Terms” (Appendix B.0.1), “Transverse-Transverse Interference Terms” (Appendix B.0.2), and “Transverse-Longitudinal Interference Terms” (Appendix B.0.3) are carried out separately. Using the terms, we have separately extracted the following 34 linearly independent weight factors.

$$\begin{aligned}
wgt_0 &= \left|\Omega_{0,0}\right|^2 , \\
wgt_1 &= \left|\Omega_{1,1}\right|^2 , \\
wgt_2 &= \left|\Omega_{1,1}(m_{\pi\pi})\right|^2 P_2\left(\cos\Theta_R\right) , \\
wgt_3 &= \left|\Omega_{1,1}(m_{\pi\pi})\right|^2 \sin^2\Theta_R \cos(2\Phi_R), \\
wgt_4 &= \Re\left[\Omega_{1,1}(m_{\pi\pi})^\dagger \Omega_{0,0}(m_{\pi\pi})\right] \cos\left(\Theta_R\right) , \\
wgt_5 &= \Im\left[\Omega_{1,1}(m_{\pi\pi})^\dagger \Omega_{0,0}(m_{\pi\pi})\right] \cos\left(\Theta_R\right) ,
\end{aligned}$$

$$
\begin{aligned}
wgt_6 &= \left|\Omega_{0,0}(m_{\pi\pi})\right|^2 \cos\left(2\Phi_h\right), \\
wgt_7 &= \left|\Omega_{0,0}(m_{\pi\pi})\right|^2 \sin\left(2\Phi_h\right), \\
wgt_8 &= \left|\Omega_{1,1}(m_{\pi\pi})\right|^2 \cos^2\Theta_R \cos\left(2\Phi_h\right), \\
wgt_9 &= \left|\Omega_{1,1}(m_{\pi\pi})\right|^2 \cos^2\Theta_R \sin\left(2\Phi_h\right), \\
wgt_{10} &= \left|\Omega_{1,1}(m_{\pi\pi})\right|^2 \sin^2\Theta_R \cos\left(2\Phi_h\right), \\
wgt_{11} &= \left|\Omega_{1,1}(m_{\pi\pi})\right|^2 \sin^2\Theta_R \cos\left(2\Phi_R + 2\Phi_h\right), \\
wgt_{12} &= \left|\Omega_{1,1}(m_{\pi\pi})\right|^2 \sin^2\Theta_R \cos\left(2\Phi_R - 2\Phi_h\right), \\
wgt_{13} &= \left|\Omega_{1,1}(m_{\pi\pi})\right|^2 \sin\left(2\Theta_R\right) \cos\left(\Phi_R + 2\Phi_h\right), \\
wgt_{14} &= \left|\Omega_{1,1}(m_{\pi\pi})\right|^2 \sin\left(2\Theta_R\right) \cos\left(\Phi_R - 2\Phi_h\right), \\
wgt_{15} &= \Im\left[\Omega_{0,0}(m_{\pi\pi})^\dagger \Omega_{1,1}(m_{\pi\pi})\right] \cos\left(\Theta_R\right) \cos\left(2\Phi_h\right), \\
wgt_{16} &= \Re\left[\Omega_{0,0}(m_{\pi\pi})^\dagger \Omega_{1,1}(m_{\pi\pi})\right] \cos\left(\Theta_R\right) \cos\left(2\Phi_h\right), \\
wgt_{17} &= \Im\left[\Omega_{0,0}(m_{\pi\pi})^\dagger \Omega_{1,1}(m_{\pi\pi})\right] \sin\left(\Theta_R\right) \cos\left(\Phi_R + 2\Phi_h\right), \\
wgt_{18} &= \Re\left[\Omega_{0,0}(m_{\pi\pi})^\dagger \Omega_{1,1}(m_{\pi\pi})\right] \sin\left(\Theta_R\right) \cos\left(\Phi_R + 2\Phi_h\right), \\
wgt_{19} &= \Im\left[\Omega_{0,0}(m_{\pi\pi})^\dagger \Omega_{1,1}(m_{\pi\pi})\right] \sin\left(\Theta_R\right) \cos\left(\Phi_R - 2\Phi_h\right), \\
wgt_{20} &= \Re\left[\Omega_{0,0}(m_{\pi\pi})^\dagger \Omega_{1,1}(m_{\pi\pi})\right] \sin\left(\Theta_R\right) \cos\left(\Phi_R - 2\Phi_h\right),
\end{aligned}
$$

$$\begin{aligned}
wgt_{21} &= \left|\Omega_{0,0}(m_{\pi\pi})\right|^2 \cos\left(\Phi_h\right), \\
wgt_{22} &= \left|\Omega_{1,1}(m_{\pi\pi})\right|^2 \cos^2\Theta_R \cos\left(\Phi_h\right), \\
wgt_{23} &= \Re\left[\Omega_{0,0}(m_{\pi\pi})^\dagger \Omega_{1,1}(m_{\pi\pi})\right] \cos\left(\Theta_R\right)\cos\left(\Phi_h\right), \\
wgt_{24} &= \Im\left[\Omega_{0,0}(m_{\pi\pi})^\dagger \Omega_{1,1}(m_{\pi\pi})\right] \cos\left(\Theta_R\right)\cos\left(\Phi_h\right), \\
wgt_{25} &= \left|\Omega_{1,1}(m_{\pi\pi})\right|^2 sin^2\Theta_R \cos\left(\Phi_h\right), \\
wgt_{26} &= \left|\Omega_{1,1}(m_{\pi\pi})\right|^2 sin^2\Theta_R \cos\left(2\Phi_R+\Phi_h\right), \\
wgt_{27} &= \left|\Omega_{1,1}(m_{\pi\pi})\right|^2 sin^2\Theta_R \cos\left(2\Phi_R-\Phi_h\right), \\
wgt_{28} &= \left|\Omega_{1,1}(m_{\pi\pi})\right|^2 \sin(2\Theta_R) \cos\left(\Phi_R+\Phi_h\right), \\
wgt_{29} &= \left|\Omega_{1,1}(m_{\pi\pi})\right|^2 \sin(2\Theta_R) \cos\left(\Phi_R-\Phi_h\right), \\
wgt_{30} &= \Re\left[\Omega_{1,1}(m_{\pi\pi})^\dagger \Omega_{0,0}(m_{\pi\pi})\right] \sin\left(\Theta_R\right)\cos\left(\Phi_h-\Phi_R\right), \\
wgt_{31} &= \Re\left[\Omega_{1,1}(m_{\pi\pi})^\dagger \Omega_{0,0}(m_{\pi\pi})\right] \sin\left(\Theta_R\right)\cos\left(\Phi_h+\Phi_R\right), \\
wgt_{32} &= \Im\left[\Omega_{1,1}(m_{\pi\pi})^\dagger \Omega_{0,0}(m_{\pi\pi})\right] \sin\left(\Theta_R\right)\cos\left(\Phi_h-\Phi_R\right), \\
wgt_{33} &= \Im\left[\Omega_{1,1}(m_{\pi\pi})^\dagger \Omega_{0,0}(m_{\pi\pi})\right] \sin\left(\Theta_R\right)\cos\left(\Phi_h+\Phi_R\right).
\end{aligned}$$

The weight factors from wgt_0 to wgt_5 are found to contribute to both transverse and longitudinal terms. The weight factors wgt_6 to wgt_{20} are the transverse-transverse (TT) interference terms, while the weight factors from wgt_{21} to wgt_{33} are determined to be relevant for transverse-longitudinal (TL) terms. The uniform generator used in this study is discussed in Section 4.1. To simulate the data, we use a uniform weighting scheme for variables such as Q^2, x_B, ϕ_e, $t = \Delta^2$, Φ_h, $m^2_{\pi\pi}$, $\cos(\Theta_R)$, and Φ_R. The boundaries for Δ^2 and $m^2_{\pi\pi}$ are dynamically determined for each event. In our analysis, we construct bins for Q^2, x_B, and $(t_{\min} - t)$ as shown in Table 3, but we aim to develop an analytical model for the full distributions of Φ_h, $m^2_{\pi\pi}$, $\cos(\Theta_R)$, and Φ_R. It is worth noting that in the absence of a transversely polarized target, the cross-section is still differential in the electron azimuthal angle, though independent of this variable.

Based on the coherent sum of (J, I) amplitudes (0,0) and (1,1) in the final state $\pi\pi$ channel, we anticipate that the four-dimensional distribution $(m_{\pi\pi}, \Theta_R, \Phi_R, \Phi_h)$ will exhibit an explicit decomposition within each bin of $(Q^2, x_B, t_{\min} - t)$. To accomplish this decomposition, we initially consider only the σ_L and σ_T terms (i.e., the first six weight terms), which are independent of Φ_h, and subsequently extend our cross-section model to incorporate an additional 10 weight terms that account for the distribution of $(m_{\pi\pi}, \theta_{HS}, \Phi_R, \Phi_h)$.

Variable	Units	bin	Number of Bins	Bin width
Q^2	GeV^2	1.5-2.5	1	1
		2.5-4.0	1	1.5
		4.0-6.0	1	2.0
		6.0-10.0	1	4.0
x_B	-	(xMax-xMin)	3	(xMax-xMin)/3
$tmin - t$	GeV^2	0-0.6	1	0.6

TABLE 3. The binning for $(Q^2, x_B, t_{min} - t)$ is defined as above: the x_B binning is determined by setting the lower limit of x as $xMin = Q^2 * 0.75/12$ and the upper limit as $xMax = Q^2/(Q^2 + W^2_{min} - M^2_p)$, where W^2_{min} is equal to 4 GeV^2 and M_p represents the mass of the proton.

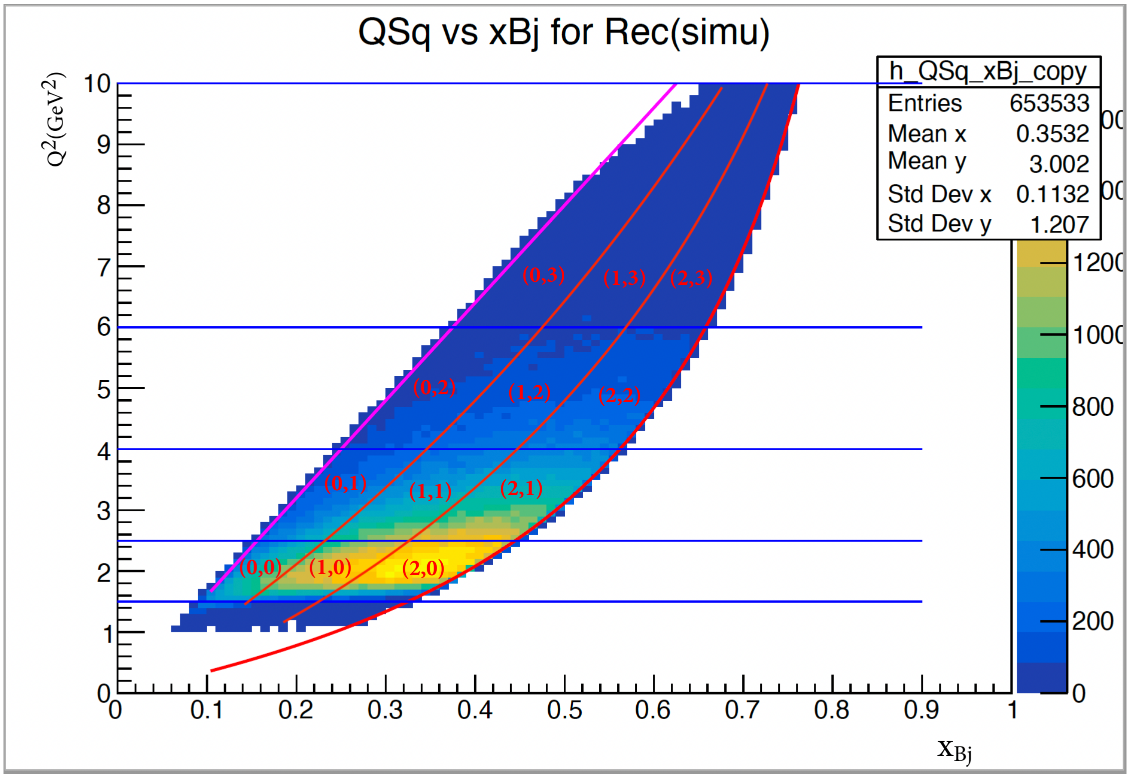

FIG. 68. The figure represents the Q^2 and x_B binning that we mentioned in Table 3.

If we use all 34 terms, we construct the following cross-section model.

$$d\sigma = \sum_{i=0}^{34} \bar{A}_i wgt_i(m_{\pi\pi}, \Theta_R, \Phi_R, \Phi_h)\mathcal{N}_0, \tag{137}$$

where $\tilde{A}_i$ is the extracted coefficient, and $wgt_i(m_{\pi\pi}, \Theta_R, \Phi_R)$ is the linearly independent weight factors, and $\mathcal{N}_0$ depends only on the electron scattering variables, defined in Eq. (145).

Our objective is to perform a linear regression analysis on the 10 kinematic terms, similar to the approach used by Schilling and Wolf [25], but with the inclusion of both $(J, I) = (0, 0)$ and $(1, 1)$ channels. The matrix that we generate from our events (prior to applying CLAS12 acceptance and resolution) for each bin of $(Q^2, x_B, t_{min} - t)$ is as follows:

$$\mathcal{M}_{i,j}^{GEN} = \frac{1}{N_{GEN}} \sum_{Events}^{GEN} wgt_i^{GEN}(m_{\pi\pi}, \Theta_R, \Phi_R, \Phi_h) wgt_i^{GEN}(m_{\pi\pi}, \Theta_R, \Phi_R, \Phi_h). \tag{138}$$

Using the orthogonality of the angular terms, we can expect the following off-diagonal terms in $\mathcal{M}_{GEN}$ to disappear:

$$\mathcal{M}_{2,i}^{Gen}, \quad \mathcal{M}_{i,2}^{Gen} \quad \mathcal{M}_{i,3}^{Gen} \quad \mathcal{M}_{3,i}^{Gen}, \quad \left\{ \mathcal{M}_{j,i}^{Gen}, \mathcal{M}_{i,j}^{Gen} \middle| i = 0, 1, 2, 3,\ j = 4, 5 \right\}. \tag{139}$$

The events generated in the previous step are subsequently subject to the complete simulation of the CLAS12 GEMC. As a result, a new matrix is constructed, which represents the effects of the CLAS12 acceptance and resolution on the kinematic variables $(Q^2, x_B, t_{min} - t)$ for each corresponding bin:

$$\mathcal{M}_{i,j}^{Simu} = \frac{1}{N_{\text{Gen}}} \sum_{\text{Events } n}^{\text{Simu}} \left[wgt_i^{\text{Simu}}(m_{\pi\pi}, \Theta_R, \Phi_R) \right] \left[wgt_j^{\text{Gen}}(m_{\pi\pi}, \Theta_R, \Phi_R) \right] \epsilon(n)\, \text{psf}(n) \mathcal{N}_0(n). \tag{140}$$

The superscripts "Simu" and "Gen" on the wgt factors indicate whether the kinematic variables are the reconstructed values of the simulation or the generated values. As a consequence $\mathcal{M}^{\text{Simu}}$ is non-symmetric. The factor $\epsilon(n)$ is an additional tracking efficiency derived for each particle type by comparing 3-fold and 4-fold coincidence events in both the simulation and data. The $psf(n)$ is the event-by-event phase space of the generator:

$$\text{psf}(event) = 2\pi \left(Q^2_{\text{Max}} - Q^2_{\text{Min}} \right) \left(x_{\text{B,Max}} - x_{\text{B,Min}} \right) (2\pi\Delta t) 4\pi \left(m^2_{\pi\pi,\text{Max}} - 4m^2_{\pi} \right). \tag{141}$$

7.2 CROSS SECTION EXTRACTION

7.2.1 ABSOLUTE NORMALIZATION

The absolute normalization of the cross-section is a critical aspect of experimental measurements and refers to determining the overall scale of the measured cross-section. This is typically achieved through various techniques, such as measuring the beam and target luminosity, using well-known cross-sections of certain processes as references, or comparing measurements with theoretical predictions.

The normalization procedure is crucial in order to compare experimental results with theoretical predictions and extract meaningful physics information. Without proper normalization, the extracted cross-sections may have significant uncertainties, making it difficult to draw meaningful conclusions from the data.

In order to achieve reliable normalization, careful calibration and monitoring of the experimental apparatus and conditions are required. This can involve detailed simulations of the detector response, precise beam, and target alignment, and other systematic studies to understand the impact of various experimental effects on the measurements.

As mentioned several times, the eight-fold differential cross-section for the reaction (Eq. (142)):

$$ep \to ep\pi^+\pi^-, \tag{142}$$

has the form

$$d^8\sigma = \frac{1}{4k\cdot P}\left|\mathcal{T}\right|^2 \frac{y dx_B dQ^2 d\phi_e^{\text{Lab}}}{4x_B}\frac{dt d\phi_{\pi\pi}^{\text{CM}}}{8\left|\mathbf{q}^{\text{CM}}\right|\sqrt{W^2}}\beta^{\text{Rest}} dM_{\pi\pi}^2 d\cos\Theta_R d\Phi_R, \tag{143}$$

with $\beta^{\text{Rest}} = \sqrt{1-4m_\pi^2/M_{\pi\pi}^2}$. The scattering matrix squared $|\mathcal{T}|^2$ has dimensions of cross-section per GeV^2, or $(\hbar c)^2/\text{GeV}^4$. To ensure the appropriate normalization of the model and extract the coefficients $\tilde{A}_i$, the model must take a specific form.

$$\begin{aligned}\frac{d^8\sigma}{d\phi_e dQ^2 dx_B dt d\Phi_h d^2\Omega_R dm_{\pi\pi}^2} &= \frac{y}{16(k\cdot P)x_B}\frac{\beta^{\text{Rest}}}{8\left|q^{\text{CM}}\right|\sqrt{W^2}}\sum_j A_j \text{wgt}_j, \\ &= \mathcal{N}_0 \sum_j A_j \text{wgt}_j,\end{aligned} \tag{144}$$

with

$$\mathcal{N}_0 = \frac{y}{16(k\cdot P)x_B}\frac{\beta^{\text{Rest}}}{8\left|q^{\text{CM}}\right|\sqrt{W^2}}, \qquad (\text{dimensions GeV}^{-4}). \tag{145}$$

The product of $\mathcal{N}_0$ and the phase space function (psf), denoted as $\mathcal{N}_0 * \text{psf}$ possesses units of GeV^2. Meanwhile, the psf alone has units of GeV^{-6}. If one evaluates the integrated luminosity in units of inverse micro-barns, then the resulting quantities have dimensions that include physical units.

- V_j has units of μb,
- $\mathcal{M}_{ij}$ has units of GeV^2,
- $\mathcal{M}^{-1}_{ij}$ has units of GeV^{-2},
- $\bar{A}_j$ has units of μb GeV^{-2},
- Model $= \mathcal{N}_0 \tilde{A}_i wgt_i$ has units of μb GeV^{-6}.

The fitted coefficients $\tilde{A}_i$ are averaged over the Q^2, x_B, t bin.

7.2.2 MODEL FITTING

Ideally, the data in a bin in Q^2, x_B, $(tmin - t)$ will have a distribution described by the following:

$$\text{Model}(m_{\pi\pi}, \Theta_R, \Phi_R, \Phi_h) = \sum_i A_i wgt_i(m_{\pi\pi}, \Theta_R, \Phi_R, \Phi_h)\mathcal{N}_0. \quad (146)$$

When analyzing electron scattering data, it is crucial to consider the $\mathcal{N}_0$ factor, which is solely dependent on the electron scattering variables, in order to obtain the best possible set of coefficients $\tilde{A}_i$. It is also helpful to define the inverse matrix $\mathcal{M}^{-1}$ of the simulation matrix $\mathcal{M}^{\text{Simu}}$ to aid in the analysis and determination of the coefficients $\tilde{A}_i$. We then construct the vector of weighted data as follows:

$$V_j^{\text{Data}} = \frac{1}{\int \mathcal{L}dt} \sum_{events}^{data} wgt_j(m_{\pi\pi}, \Theta_R, \Phi_R, \Phi_h)_{\text{Data}}. \quad (147)$$

The factor $\mathcal{N}_0$ is assumed to be intrinsic to the data, so it is not included in the vector of weighted data. Instead, to account for the integrated luminosity, the weighted sum is divided by the integrated luminosity. This results in each V_j term representing the cross-section integrated over the acceptance and weighted by wgt_j. If the model and simulation are accurate, then the vector V_j can be written as follows:

$$V_j \approx \mathcal{M}_{ji}^{\text{Simu}} \bar{A}_i. \quad (148)$$

The reconstructed coefficients $\{\overline{A}_i\}$ are obtained as follows:

$$\overline{A}_i = \left[\mathcal{M}^{-1}\right]_{ij}^{Simu} V_j^{\text{Data}}. \quad (149)$$

The covariance matrix of the statistical uncertainties in the extracted coefficients is obtained as

$$
\begin{aligned}
\left\langle \delta\overline{A}_i \delta\overline{A}_j \right\rangle &= \sum_n^{\text{data}} \frac{\partial A_i}{\partial n}\frac{\partial A_j}{\partial n}, \\
&= \left[\mathcal{M}^{-1}\right]_{ik}^{\text{Simu}} \sum_n^{\text{data}} \left\{ \frac{wgt_k(n)}{\int \mathcal{L}dt}\frac{wgt_l(n)}{\int \mathcal{L}dt} \right\} \left[\mathcal{M}^{-1}\right]_{jl}^{\text{Simu}}, \\
&= \frac{1}{\int \mathcal{L}dt} \left[\mathcal{M}^{-1}\right]_{ik}^{\text{Simu}} \mathcal{M}_{kl}^{\text{Data}} \left[\mathcal{M}^{-1}\right]_{jl}^{\text{Simu}},
\end{aligned} \tag{150}
$$

with

$$
\mathcal{M}_{kl}^{\text{Data}} = \frac{1}{\int \mathcal{L}dt} \sum_n^{\text{data}} wgt_k(n) wgt_l(n). \tag{151}
$$

The square root of the diagonal element at position (i, i) in the covariance matrix corresponds to the uncorrelated uncertainty in the parameter $\bar{A}_i$. This represents the standard deviation or the magnitude of the random error associated with the estimate of $\bar{A}_i$. These values are represented in Appendix G in this thesis for each nine bins.

Note that the sum is over the data, not the generated events. The extracted model and its error band and then described as:

$$
\begin{aligned}
\text{Model}(m_{\pi\pi}, \Theta_R, \Phi_R, \Phi_h) &= \sum_i A_i \text{wgt}_i(m_{\pi\pi}, \Theta_R, \Phi_R, \Phi_h)\mathcal{N}_0, \\
&\pm \mathcal{N}_0 \sqrt{\sum_{i,j} \text{wgt}_j(m_{\pi\pi}, \Theta_R, \Phi_R, \Phi_h) \left\langle \delta\overline{A}_j \delta\overline{A}_i \right\rangle \text{wgt}_i(m_{\pi\pi}, \Theta_R, \Phi_R)}.
\end{aligned} \tag{152}
$$

In certain circumstances where a large number of events have been generated, the statistical uncertainty may become too small to be discernible through conventional error bars or bands. It is crucial to recognize that small statistical uncertainty does not necessarily imply that the result is precise or accurate, as systematic errors may still be present and contribute to the overall uncertainty.

Upon computation of the $\overline{A}_i$ values, the model may be constructed in accordance with Eq. (146) for each of the Generated Events, Simulated Events, and Data individually. The following equations show separately for model calculation for Generated, Simulated, and Data:

$$
\text{Model\_GEN}(m_{\pi\pi}, \Theta_R, \Phi_R, \Phi_h) = \sum_i \bar{A}_i \text{wgt}_i^{GEN}(m_{\pi\pi}, \Theta_R, \Phi_R, \Phi_h)\mathcal{N}_0^{GEN}, \tag{153}
$$

$$\text{Model\_SIMU}(m_{\pi\pi}, \Theta_R, \Phi_R, \Phi_h) = \sum_i \bar{A}_i \text{wgt}_i^{SIMU}(m_{\pi\pi}, \Theta_R, \Phi_R, \Phi_h)\mathcal{N}_0^{SIMU}, \tag{154}$$

$$\text{Model\_DATA}(m_{\pi\pi}, \Theta_R, \Phi_R, \Phi_h) = \sum_i \bar{A}_i \text{wgt}_i^{DATA}(m_{\pi\pi}, \Theta_R, \Phi_R, \Phi_h)\mathcal{N}_0^{DATA}. \tag{155}$$

The current state of our calculations involves utilizing only 10 weight terms ($wgt_0 wgt_{10}$), owing to our need for more confidence in the extraction of all 34 weight terms Nevertheless, despite not considering all 34 weight terms, we have ensured that the first 10 weight terms encompass all dependencies on $m_{\pi\pi}$, Θ_R, Φ_R, and Φ_h. Henceforth, we shall employ 10 linearly independent weight factors in all our subsequent calculations.

I have now implemented two selection criteria in my analysis. Specifically, I have restricted the events to those falling within the range of $-0.8 < \cos(\Theta_R) < 0.8$ and with an invariant mass between $2m_\pi$ GeV and 0.9 GeV, based on the values present in my Omnés data set.

The cross-section has been studied in terms of several kinematic variables, namely $m_{\pi\pi}$, Θ_R, Φ_R, and Φ_h. Each of these variables has been weighted by a function called "ModelGEN", as given by Eq. (153). This weighting allows for the extraction of the cross-section in terms of each variable separately. We are initially striving to achieve a correlation between the data and simulation. This is because we can compute the extracted coefficient A_i as per Eq. (148), provided that the data and simulation are matched, as assumed.

7.2.3 FINAL CROSS SECTION RESULT

After completing the normalization and uncertainty analysis, the final result for the differential cross-section was obtained by averaging each value over the relevant (Q^2, x_B, t) bins of the independent variable. This process was performed with great care and attention to detail to ensure the accuracy and reliability of the final result:

$$\begin{aligned} \frac{d^8\sigma}{dQ^2 dx_B d\phi_e d\Delta^2 d\Phi_h dm_{\pi\pi}^2 d\Omega_{Rest}} &= \frac{1}{2\pi}\text{Model.} \\ &= \frac{1}{2\pi}\sum_j \bar{A}_j \, \text{wgt}_j(m_{\pi\pi}, \Theta_R, \Phi_R, \Phi_h), \end{aligned} \tag{156}$$

Equivalently,

$$\frac{d^7\sigma}{dQ^2 dx_B dt d\Phi_h dm_{\pi\pi}^2 d\Omega_{Rest}} = \sum_j \bar{A}_j \, \text{wgt}_j(m_{\pi\pi}, \Theta_R, \Phi_R, \Phi_h)\mathcal{N}_0. \tag{157}$$

7.2.4 MODEL VALIDATION USING DATA AND SIMULATIONS

The current section pertains to the validation of a simulation model. Specifically, the distributions of $m_{\pi\pi}$, $\cos(\Theta_R)$, Φ_R, and Φ_h have been examined separately for the simulation events. In addition, these events were analyzed after being processed through the CLAS12 GEMC software, which accounts for the detector's acceptance and resolution.

By studying these distributions, the performance of the simulation model in reproducing the real physics processes and the detector response can be evaluated. It is important to note that these simulated events are processed through the CLAS12 GEMC software, which accounts for the detector's acceptance and resolution. Therefore, the distributions obtained from these events represent the experimental data the CLAS12 detector would collect.

Overall, validating simulation models is crucial in ensuring the accuracy and reliability of their predictions. Furthermore , by examining the distributions of various variables, such as $m_{\pi\pi}$, $\cos(\Theta_R)$, Φ_R, and Φ_h, the performance of the simulation model can be assessed and compared with experimental data.

The initial step of this process involved examining weighted histograms of the distributions of $m_{\pi\pi}$, $\cos(\Theta_R)$, Φ_R, and Φ_h. The weights were calculated using the product of the generated model, ModelGEN, and the phase space factor (psf), and were used to account for various effects that could distort the true distribution. The histograms were then normalized by the number of trial events, which in this case was 10,000 physical events selected from a total of 22,000 trial events generated by the simulation and saved in a LUND file. (Note that these LUND files do not have exact 10,000 events but are very close). Following the generation of the weighted histograms from the simulation, un-weighted data distributions were analyzed. The data distributions were divided by the integrated experimental luminosity to ensure normalization, and a comparison was made with the Monte Carlo simulation results. Then the normalized distributions for each $m_{\pi\pi}$, $\cos(\Theta_R)$, Φ_R, and Φ_h variable were compared separately for the experimental data and the Monte Carlo simulation.

The figure shown in Fig. 69 compares between the data and simulation for $m_{\pi\pi}$ distributions. The plot colored in blue represents the data, while the plot colored in magenta represents the simulated data. It can be observed that the data and simulation plots under consideration are in agreement with the Lehmann-Dronke paper [24]. Specifically, the σ channel exhibits a discernible variation with increasing x_B range, showing less structure in the low x_B range and more clear structure in the high x_B range. Although the data and simulation plots in the figure appear to be in agreement, it cannot be assured that our model accurately represents the data since the N^* resonances have not been incorporated in our model calculation.

Further discussion regarding this issue will be presented in section 7.3.1 of this thesis.

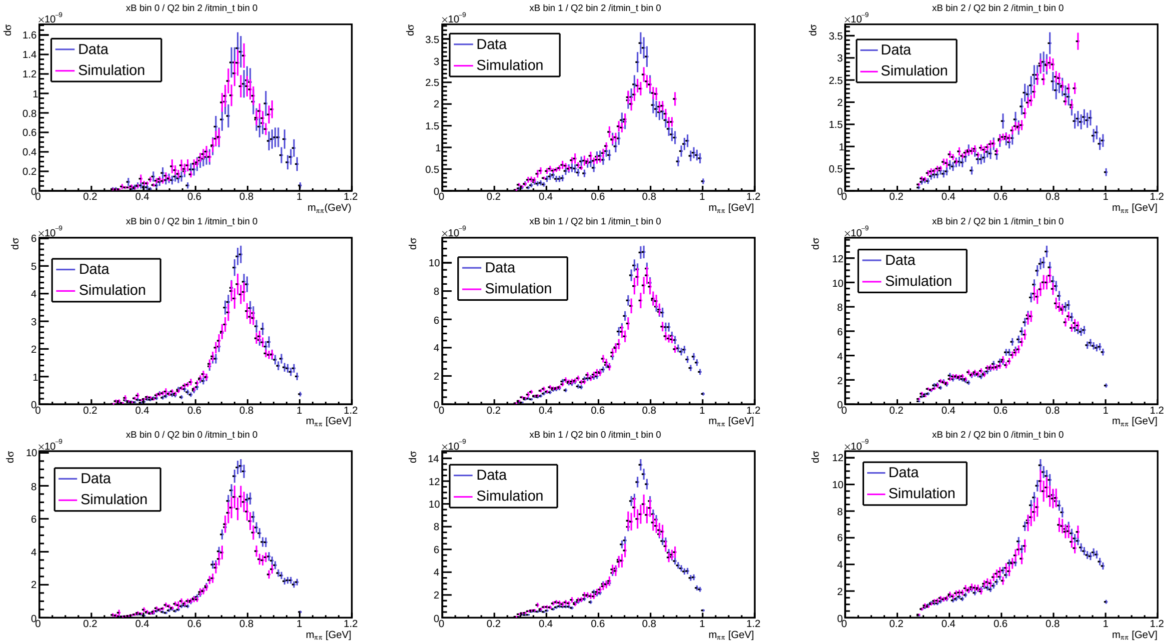

FIG. 69. This figure depicts the distributions of $m_{\pi\pi}$ for both the simulated and experimental data. The simulation data is weighted by “ModelGEN*psf” and normalized by the number of trial events in each bin. The experimental data is normalized by the Integrated Luminosity. Both plots are segmented into several $(Q^2, x_B, t_{min} - t)$ bins. The blue plot represents the experimental data, whereas the magenta plot represents the simulated data. Here x_B bins increase from left to right, and Q^2 bins increase from bottom to top.

Similarly, the $\cos(\Theta_R)$ distributions were compared between simulation and data. The simulation histograms were weighted by “ModelGEN * psf” and normalized by the number of trial events in the generator for each bin, while the integrated luminosity normalized the data distributions. The figure displayed in Fig. 70 indicates that the data and simulation are in reasonable agreement with each other. Then Φ_R and Φ_h distributions are made separately

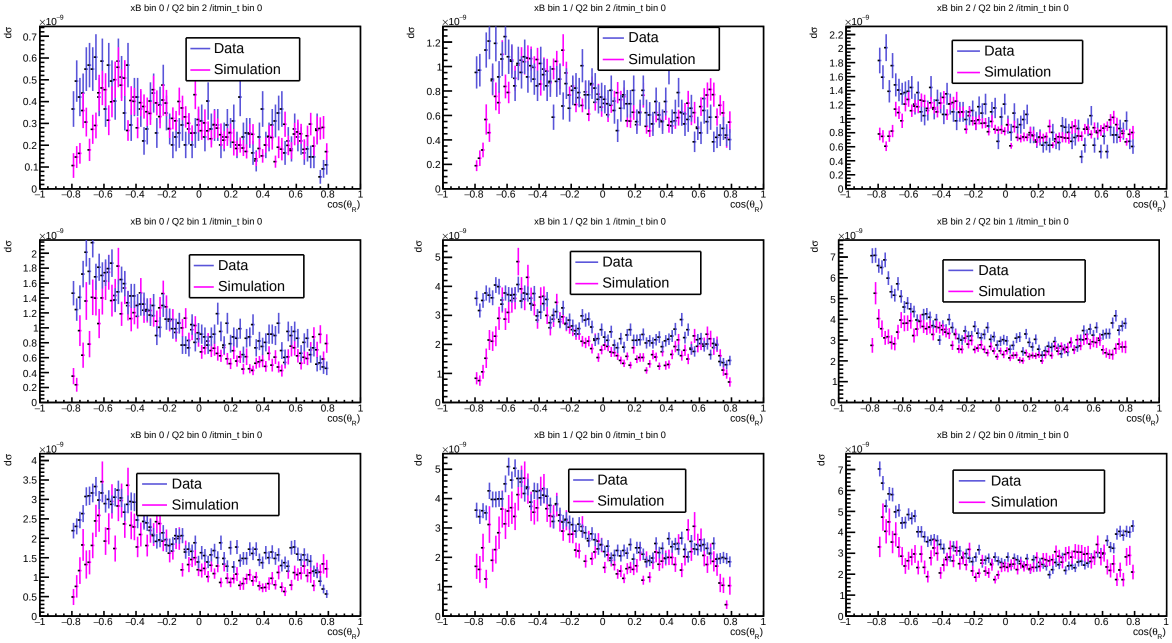

FIG. 70. This figure depicts the distributions of $\cos(\Theta_R)$ for both the simulated and experimental data. The simulation data is weighted by "ModelGEN*psf" and normalized by the number of trial events in each bin. The experimental data is normalized by the Integrated Luminosity. Both plots are segmented into several $(Q^2, x_B, t_{min} - t)$ bins. The blue plot represents the experimental data, whereas the magenta plot represents the simulated data. Here x_B bins increase from left to right, and Q^2 bins increase from bottom to top.

for simulation and data. First distribution is based on simulation that has been weighted by "ModelGEN * psf" and normalized by the number of trial events, while the data distribution is based on actual data and has been normalized by the integrated luminosity. The distributions for Φ_R and Φ_h are shown in Fig. 71 and Fig. 72, respectively. The experimental and

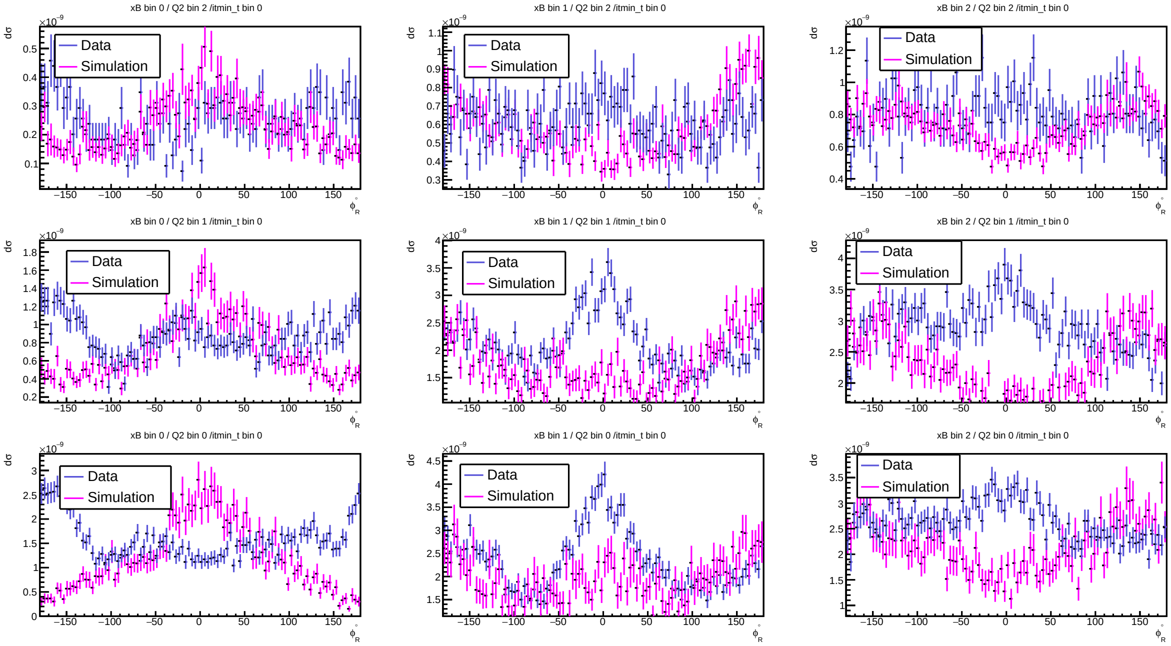

FIG. 71. This figure depicts the distributions of Φ_R for both the simulated and experimental data. The simulation data is weighted by “ModelGEN*psf” and normalized by the number of trial events in each bin. The experimental data is normalized by the Integrated Luminosity. Both plots are segmented into several $(Q^2, x_B, t_{min} - t)$ bins. The blue plot represents the experimental data, whereas the magenta plot represents the simulated data. Here x_B bins increase from left to right, and Q^2 bins increase from bottom to top.

simulated data for the Φ_R and Φ_h distributions exhibit a significant discrepancy, particularly in the higher bins of Φ_h corresponding to higher x_B values. Several possible explanations exist for this observation. One hypothesis is that the simulation used to generate the data inadequately models the underlying physical processes, leading to differences between the simulated and experimental data. We also noticed that on the left side of Fig. 72, negative values of the model can be observed in the first column’s three bins. Negative values of a model are often an indication of the limitations of the model itself. In some cases, negative values may arise due to the instability of the results and the limited number of fitted parameters. This means that the model may not be able to effectively constrain the model parameters to generate a strictly positive cross-section. In other cases, negative values may be due to the weighting of V_i factors, which includes the effect of N* resonances. Referring to Fig. 72, it is possible that the inclusion of resonances in the model has resulted in negative

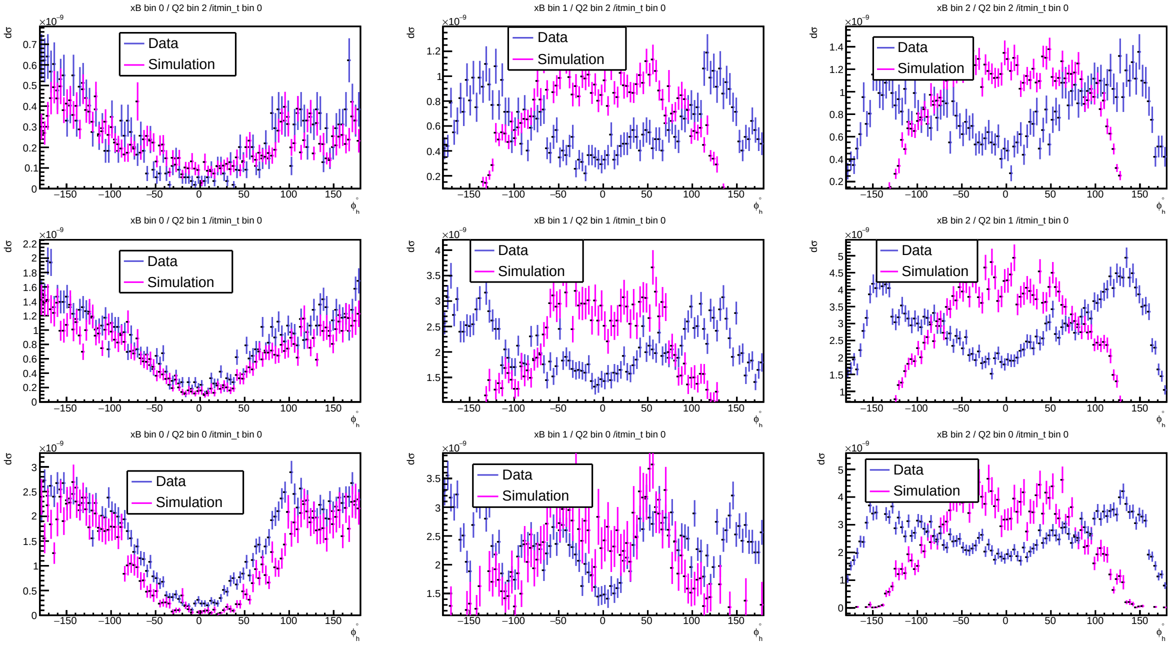

FIG. 72. This figure depicts the distributions of phi_h for both the simulated and experimental data. The simulation data is weighted by "ModelGEN*psf" and normalized by the number of trial events in each bin. The experimental data is normalized by the Integrated Luminosity. Both plots are segmented into several $(Q^2, x_B, t_{min} - t)$ bins. The blue plot represents the experimental data, whereas the magenta plot represents the simulated data. Here x_B bins increase from left to right, and Q^2 bins increase from bottom to top.

values due to the difficulty in accurately modeling their effect on the cross-section.

Despite good agreement between the $m_{\pi\pi}$ and $\cos(\Theta_R)$ data and simulation distributions, the model cannot be considered trustworthy due to its lack of inclusion of N^* resonances. This could be a potential reason. The forthcoming section 7.3.1 will provide a description of the N^* resonances that are expected to influence our analysis.

Then we can look at the actual results of extracted cross-section using the generated events weighted by the "ModelGEN". The "ModelGEN" is a model used to generate events, where each event is assigned a weight based on its contribution to the overall distribution of $m_{\pi\pi}$. This represented the theoretical distributions of the extracted cross-section. By examining the distributions of these weighted variables, the dependence of the cross-section on each of them can be determined. This provides insight into the underlying physics of the interaction and can be used to test theoretical models of the process. Fig. 73 displays the distribution of $m_{\pi\pi}$, weighted by the "ModelGEN" and segmented into various $(Q^2, x_B, t_{min} - t)$ bins, as defined in Table 3. The Fig. 73 includes four different colored plots, each representing the sum of the weight terms corresponding to different physical processes and resonances. Specifically, the blue color plot shows the contribution of all weight terms, the green color plot represents the contribution of weight terms solely from the ρ-resonance (wgt_1, wgt_2, wgt_3, wgt_8, wgt_9, and wgt_{10}), the red color plot shows the contribution of weight terms solely from the *sigma*- resonance (wgt_0, wgt_6, and wgt_7), and the Magenta plot displays only the interference terms (wgt_4 and wgt_5).

The different weight terms represent distinct physical processes and resonances that contribute to the distribution. The bins of $(Q^2, x_B, t_{min} - t)$ are used to segment the distribution, which suggests that the distribution of $m_{\pi\pi}$ is dependent on these variables. Thus, Fig. 73 provides a visual representation of how different the resonances contribute to the distribution of $m_{\pi\pi}$ in various $(Q^2, x_B, t_{min} - t)$ bins. The results displayed in Fig. 73 indicate significant variations in the physics under investigation. Specifically, the behavior of the σ channel appears to be affected by the Bjorken x value (x_B). Notably, as x_B increases, there is a statistically significant rise in the σ channel. This observation aligns with the findings reported by Lehmann-Dronke in their paper [24], which suggest a strong dependence of physics on x_B, particularly in the σ channel when $x_B > 0.3$ GeV. We have observed minimal dependence on Q^2 for these channels. The interference plot of the "Sigma-Rho" (denoted by the color magenta) in Fig. 73 appears to be close to zero. However, it is important to note that it is not exactly zero but rather averaged to zero in the depicted Fig. 73. While the t dependence is less significant in the σ channel, the mass dependence is paramount.

Similarly, the cross-section extracted as a function of $\cos(\Theta_R)$ is shown in Fig. 74. This figure was generated by weighting $cos\Theta_R$ using the "ModelGEN"(Eq. (153)). The plots depicting the differential cross-section ($d\sigma$) as a function of the scattering angle ($\cos(\Theta_R)$) hold great significance. In particular, the pure sigma-meson signal exhibits isotropic, resulting in flat "red" curves when plotted against $\cos(\Theta_R)$. On the other hand, the interference terms

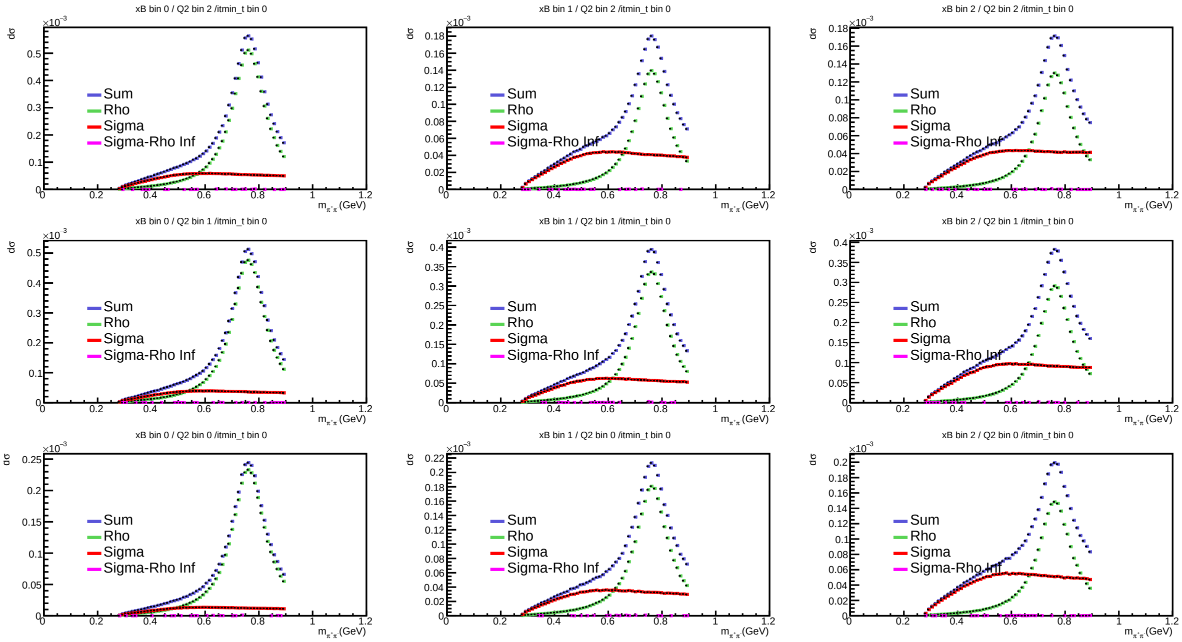

FIG. 73. This figure displays the distributions of $m_{\pi\pi}$, which have been weighted by the “ModelGEN” and segmented into various $(Q^2, x_B, t_{min} - t)$ bins. The “blue” plot represents the total sum of all 10 weight terms, while the “Green” plot displays only the “rho” terms, the “Red” plot displays only the “sigma” terms, and the “Magenta” plot displays the interference terms. Here x_B bins increase from left to right, and Q^2 bins increase from bottom to top.

between the sigma and rho mesons, denoted as “Sigma-Rho” interference, are all proportional to $-\cos(\Theta_R)$. As a consequence, these interference terms are represented by straight lines that exhibit negativity for values of $\cos(\Theta_R)$ greater than zero.

The cross-section extracted as a function of Φ_R in various $(Q^2, x_B, t_{min} - t)$ bins, is shown in the Fig. 75. This figure also generated by weighting Φ_R using the “ModelGEN”. Similar to the behavior observed in Fig. 74, the plots illustrating the differential cross-section ($d\sigma$) as a function of the azimuthal angle (Φ_R) in Fig. 75 are of great significance. In the case of the pure sigma-meson signal, we observe isotropy, resulting in flat “red” curves when plotted against both $\cos(\Theta_R)$ and Φ_R.

The cross-section extracted as a function of Φ_h in various $(Q^2, x_B, t_{min} - t)$ bins, is shown in Fig. 76. This figure is also generated by weighting Φ_R using the “ModelGEN”. But in

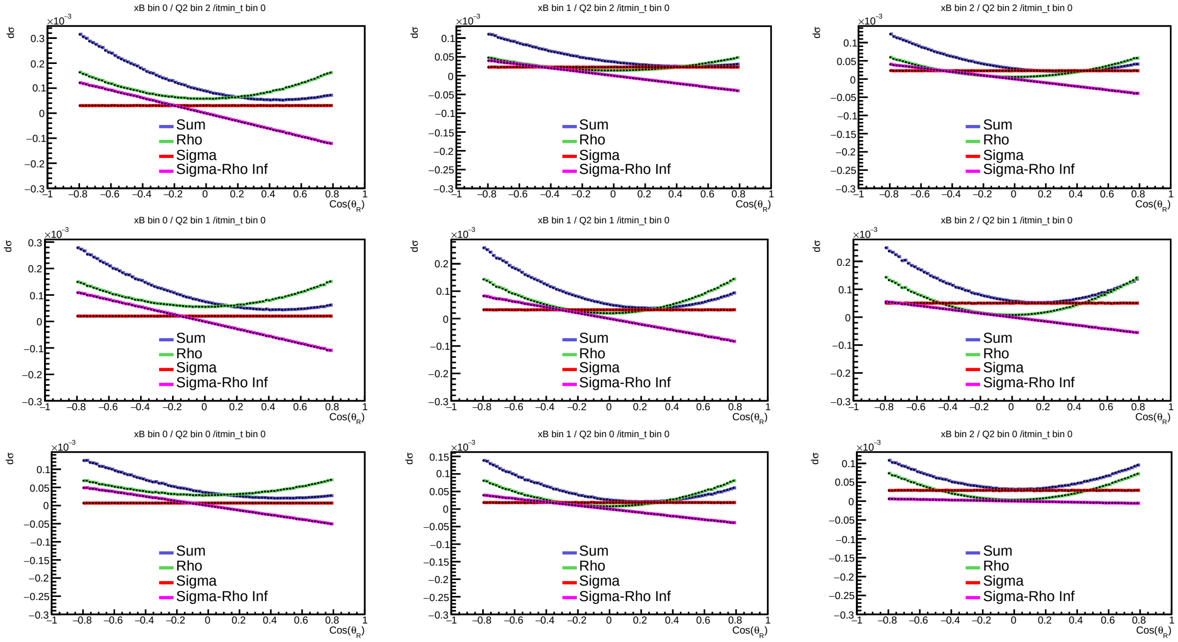

FIG. 74. This figure displays the distributions of $\cos(\Theta_R)$, which have been weighted by the "ModelGEN" and segmented into various $(Q^2, x_B, t_{min} - t)$ bins. The "blue" plot represents the total sum of all 10 weight terms, while the "Green" plot displays only the "rho" terms, the "Red" plot displays only the "sigma" terms, and the "Magenta" plot displays the interference terms. Here x_B bins increase from left to right, and Q^2 bins increase from bottom to top.

these plots the sigma-meson is not flat vs. Φ_h, because the the virtual photon can have any helicity, and still produce a sigma meson. The dependence on Φ_h (see Eq. (132)) arises due to the presence of the wave function of the virtual photon with helicity $\lambda = 0, \pm 1$, which carries a phase factor of $\exp(i\lambda\phi_h)$. Consequently, the term involving $\cos(\phi_h)$ (see Eq. (132)) in the equation represents the real part of the interference between scattering amplitudes with helicities $\lambda = 0$ and $\lambda = \pm 1$. Moreover, the term $\cos(2\phi_h)$ (see Eq. (132)) corresponds to the interference between terms involving helicities $\lambda = +1$ and $\lambda = -1$. This interference term reflects the difference in the cross-sections for linear polarization of the virtual photon. By considering the contributions from different helicity states and their corresponding interference, the angular dependence of the cross-section can be understood in terms of these Φ_h terms.

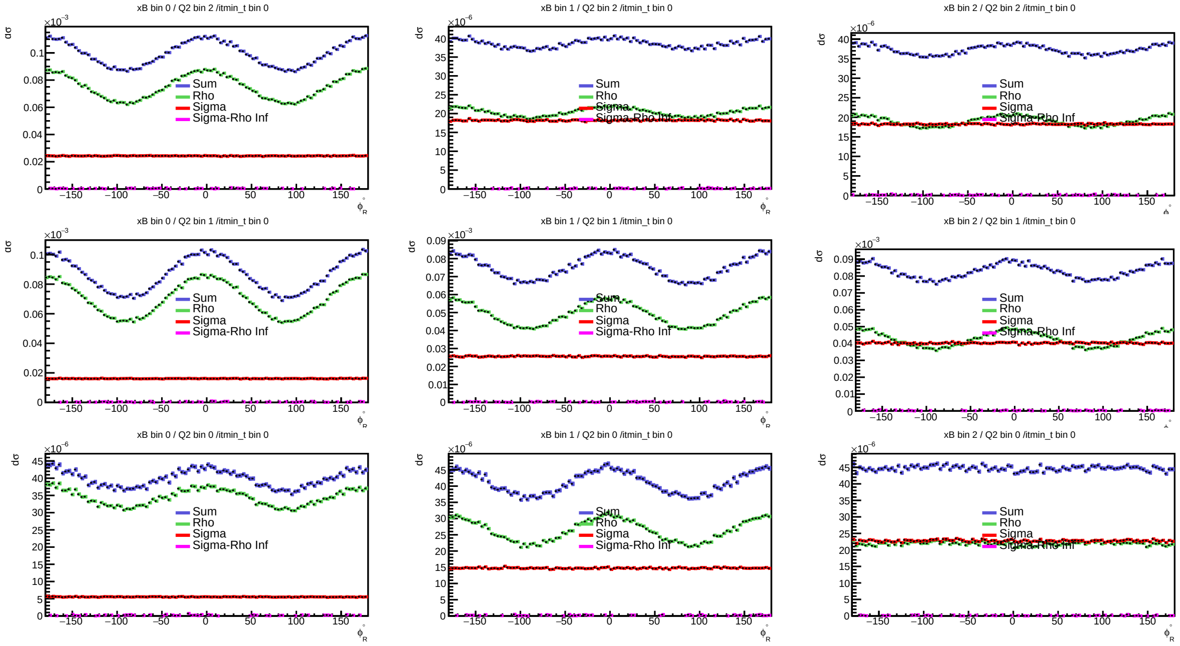

FIG. 75. This figure displays the distributions of Φ_h, which have been weighted by the "ModelGEN" and segmented into various $(Q^2, x_B, t_{min} - t)$ bins. The "blue" plot represents the total sum of all 10 weight terms, while the "Green" plot displays only the "rho" terms, the "Red" plot displays only the "sigma" terms, and the "Magenta" plot displays the interference terms. Here x_B bins increase from left to right, and Q^2 bins increase from bottom to top.

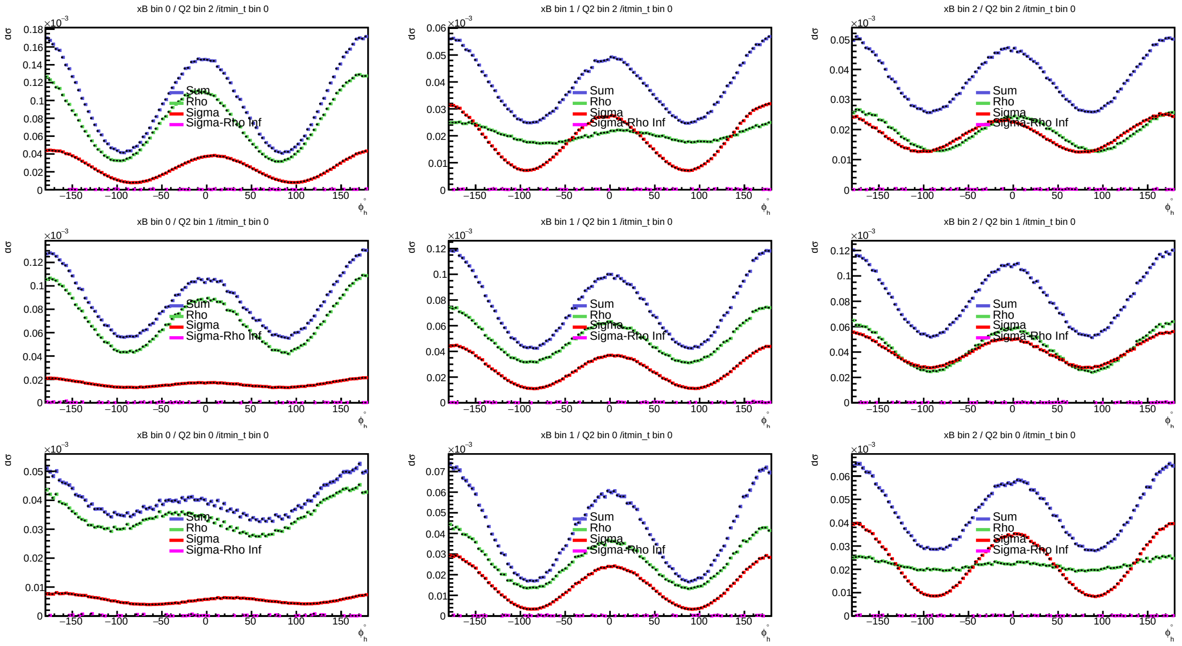

FIG. 76. This figure displays the distributions of Φ_h, which have been weighted by the "ModelGEN" and segmented into various $(Q^2, x_B, t_{min} - t)$ bins. The "blue" plot represents the total sum of all 10 weight terms, while the "Green" plot displays only the "rho" terms, the "Red" plot displays only the "sigma" terms, and the "Magenta" plot displays the interference terms. Here x_B bins increase from left to right, and Q^2 bins increase from bottom to top.

7.3 EXTRACTED CROSS-SECTION FOR ρ RESONANCE

To determine the cross-section for the ρ channel, the variables $m_{\pi\pi}$, $\cos(\Theta_R)$, Φ_R, and Φ_h were plotted using experimental data that was collected and analyzed with a specialized apparatus. A selection was made in the ρ window ($0.67\,\mathrm{GeV} < m_{\pi\pi} < 0.87\,\mathrm{GeV}$) and the resulting plots represent the extracted cross-section for the ρ mesons.

The extracted cross-section distributions for the selected ρ window were compared to simulated events that were weighted by "ModelGen *psf" and shown in red, as well as actual data shown in green, in Fig. 77, Fig. 78, Fig. 79 and Fig. 80 respectively for the $m_{\pi\pi}$, $\cos(\Theta_R)$, Φ_R and Φ_h. The comparison indicated a significantly improved agreement between the simulated events and the actual data for this selected region, with the exception of some bins in the Φ_h distributions.

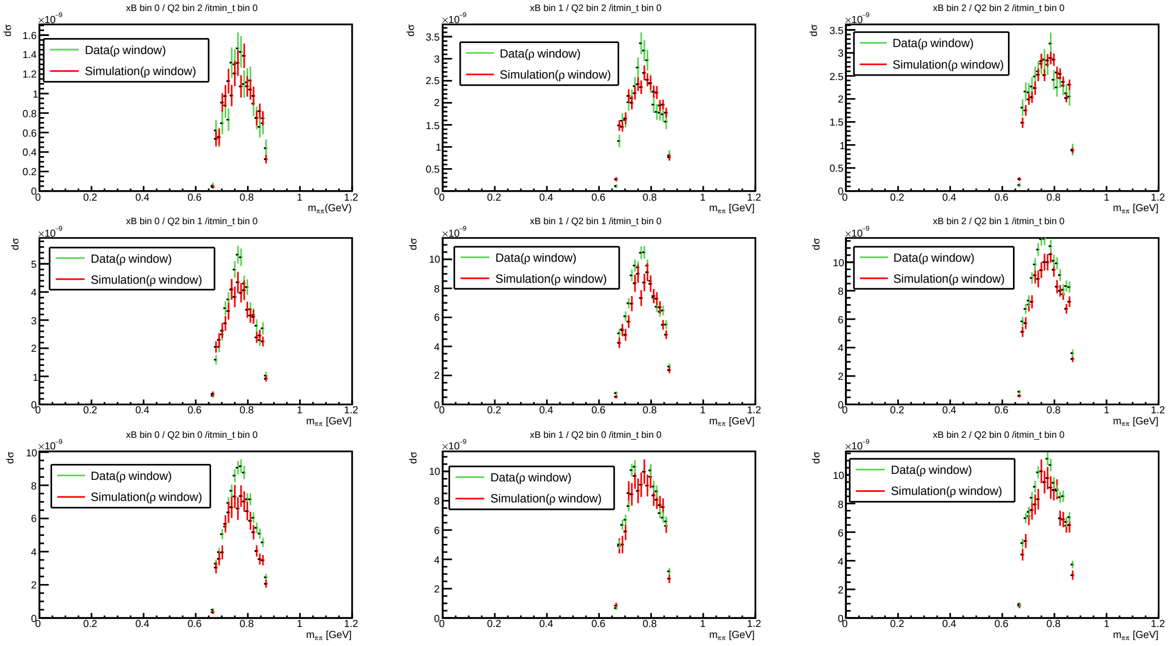

FIG. 77. This figure depicts the distributions of $m_{\pi\pi}$ in the region of ρ region($m_{\pi\pi}$ with values 0.67 GeV $< m_{\pi\pi} <$ 0.87 GeV) for both the simulated and experimental data. The simulation data is weighted by "ModelGEN*psf" and normalized by the number of trial events in each bin. The experimental data is normalized by the Integrated Luminosity. Both plots are segmented into several $(Q^2, x_B, t_{min} - t)$ bins. The green plot represents the experimental data, whereas the red plot represents the simulated data. Here x_B bins increase from left to right, and Q^2 bins increase from bottom to top.

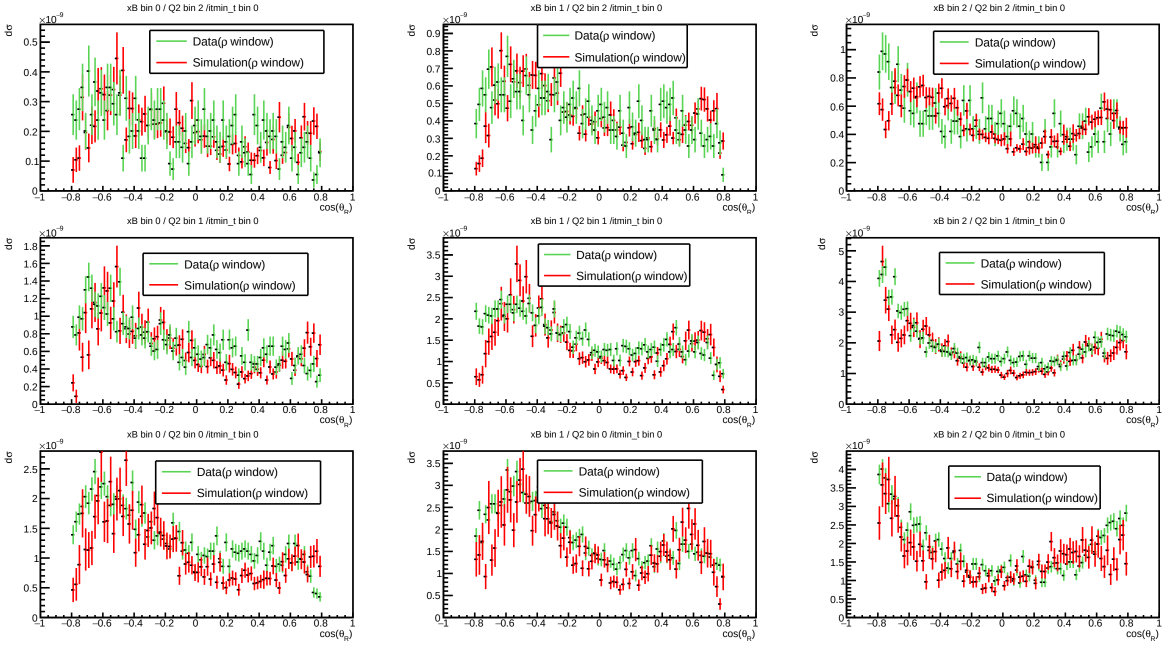

FIG. 78. This figure depicts the distributions of $cos(\Theta_R)$ in the region of ρ window ($m_{\pi\pi}$ with values 0.67 GeV $< m_{\pi\pi} <$ 0.87 GeV) for both the simulated and experimental data. The simulation data is weighted by “ModelGEN*psf” and normalized by the number of trial events in each bin. The experimental data is normalized by the Integrated Luminosity. Both plots are segmented into several $(Q^2, x_B, t_{min} - t)$ bins. The green plot represents the experimental data, whereas the red plot represents the simulated data. Here x_B bins increase from left to right, and Q^2 bins increase from bottom to top.

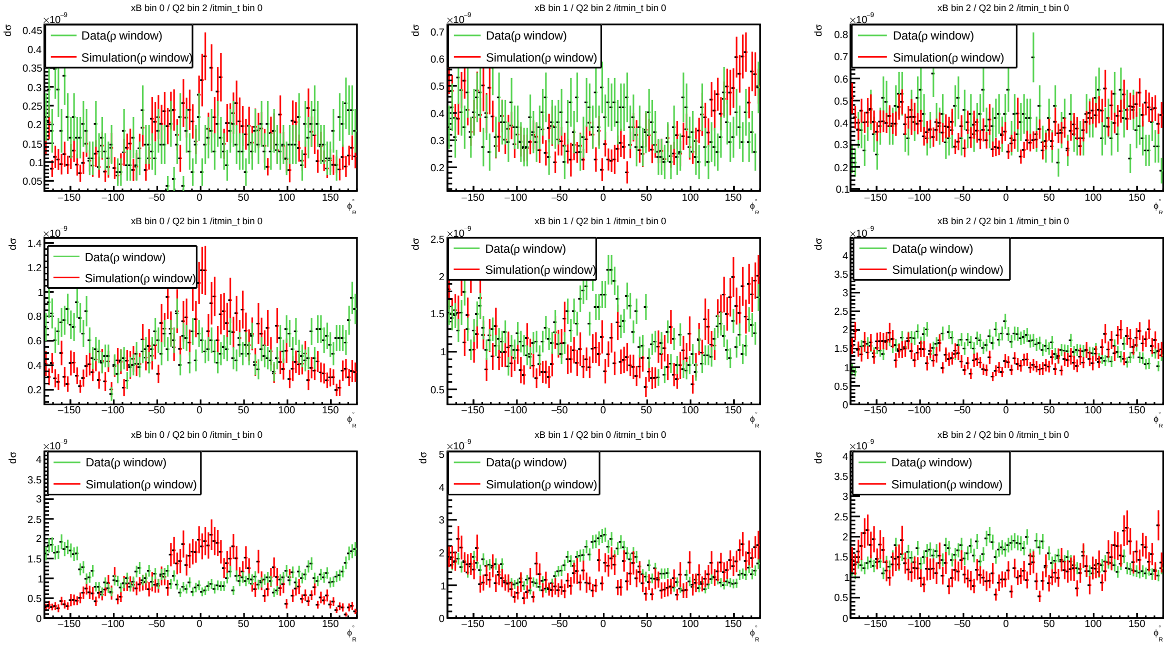

xB bin 0 / Q2 bin 2 /itmin_t bin 0

xB bin 1 / Q2 bin 2 /itmin_t bin 0

xB bin 2 / Q2 bin 2 /itmin_t bin 0

xB bin 0 / Q2 bin 1 /itmin_t bin 0

xB bin 1 / Q2 bin 1 /itmin_t bin 0

xB bin 2 / Q2 bin 1 /itmin_t bin 0

xB bin 0 / Q2 bin 0 /itmin_t bin 0

xB bin 1 / Q2 bin 0 /itmin_t bin 0

xB bin 2 / Q2 bin 0 /itmin_t bin 0

FIG. 79. This figure depicts the distributions of Φ_R in the region of ρ window ($m_{\pi\pi}$ with values 0.67 GeV $< m_{\pi\pi} <$ 0.87 GeV) for both the simulated and experimental data. The simulation data is weighted by "ModelGEN*psf" and normalized by the number of trial events in each bin. The experimental data is normalized by the Integrated Luminosity. Both plots are segmented into several $(Q^2, x_B, t_{min} - t)$ bins. The green plot represents the experimental data, whereas the red plot represents the simulated data. Here x_B bins increase from left to right, and Q^2 bins increase from bottom to top.

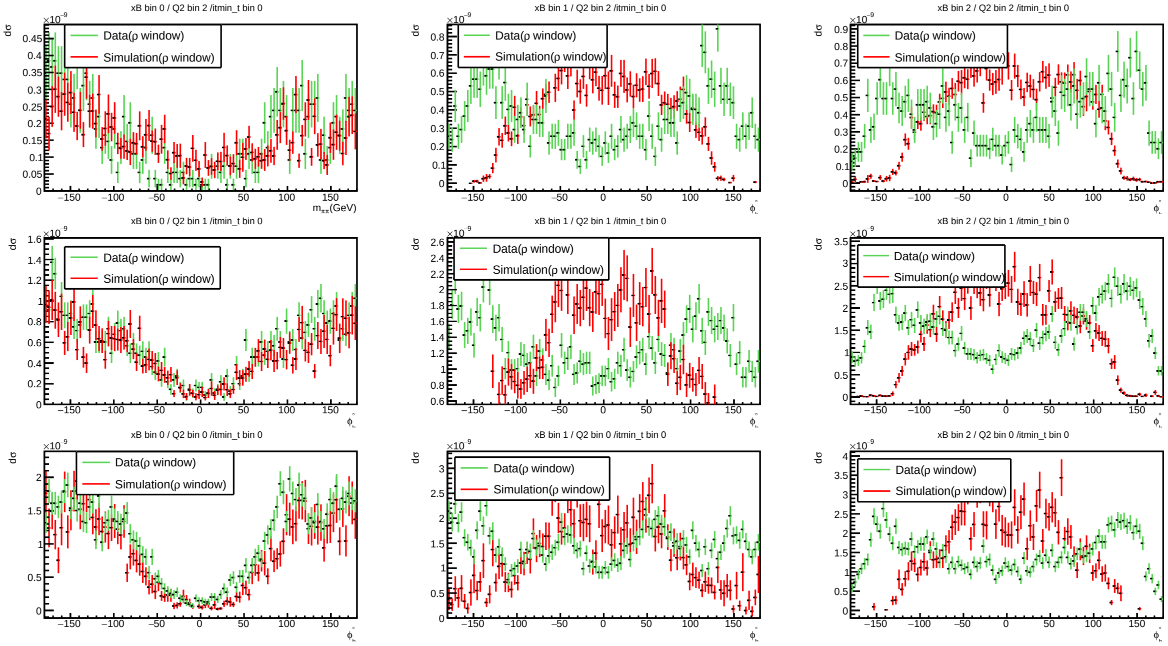

FIG. 80. This figure depicts the distributions of Φ_h in the region of ρ region ($m_{\pi\pi}$ with values 0.67 GeV $< m_{\pi\pi} <$ 0.87 GeV) for both the simulated and experimental data. The simulation data is weighted by “ModelGEN*psf” and normalized by the number of trial events in each bin. The experimental data is normalized by the Integrated Luminosity. Both plots are segmented into several $(Q^2, x_B, t_{min} - t)$ bins. The green plot represents the experimental data, whereas the red plot represents the simulated data. Here x_B bins increase from left to right and Q^2 bins increase from bottom to top.

7.3.1 N^* RESONANCES

The $e'p'\pi^+\pi^-$ final state can arise from various reactions, including meson decay ($ep \rightarrow e'p'M$) and the decay of an excited state of the nucleon ($ep \rightarrow e'\pi N^* \rightarrow p\pi^-\pi^+$). In meson decay, the incoming electron and proton interact, producing an intermediate meson (M) which subsequently decays into a pair of pions ($\pi^+\pi^-$), along with the scattered electron (e') and the recoiling proton (p'). In the case of excited nucleon decay, the incoming electron and proton collide, exciting the nucleon (N^*) to a higher energy state, which subsequently decays into a pion (π^-) and a virtual photon, which then converts into a second pion (π^+), in addition to the scattered electron and recoiling proton. Both meson decay and excited nucleon decay can contribute to the production of the $e'p'\pi^+\pi^-$ final state, and their relative contributions depend on the kinematics and energy regime of the reaction. Therefore, when analyzing experimental data for the $e'p'\pi^+\pi^-$ final state, it is important to consider not only meson decays but also the various possible combinations of final-state particles that can arise from the decay of baryonic resonances. These resonances are shown in the Dalitz plots of Fig. 81 for the experimental data used to create Dalitz plots, which visually represent particle decay. The red arrows on the plot indicate the major mesonic and baryonic resonances, which correspond to peaks in the plot. These resonances provide insight into the masses and decay properties of the particles involved in the decay process. The Fig. 81 shows that the process $ep \rightarrow e'\pi^-\Delta^{++} \rightarrow p\pi^+$ has a significant contribution that overlaps with the region where $\rho(770)$ is present, and it also shows evidence of production of other resonances, including $\Delta^{++} \rightarrow p\pi^+$, $D_{13}(1520) \rightarrow p\pi^-$, and $F_{15}(1680) \rightarrow p\pi^-$.

Fig. 82 displays the 1D plots of the $M_{p\pi^+}$ and $M_{p\pi^-}$ distributions for the experimental data, which reveal the resonance structures present in these distributions. The prominent peaks observed in the plots correspond to the production and decay of specific particles, such as the Delta baryon (Δ^{++}, Δ^+, Δ^0, Δ^-) and the $N^*(1440)$ resonance, the $N^*(1520)$ resonance, and the $N^*(1700)$.

Then we conducted an analysis comparing the invariant mass distributions of $M_{p\pi^+}$ and $M_{p\pi^-}$ between simulated and experimental data in various $(Q^2, x_B, t_{min} - t)$ binning. The simulation plots are weighted by "ModelGEN·psf" and normalized by the trial events generated from each bin, while the data plots are normalized by the integrated luminosity. The results are presented in Fig. 83 for the $p\pi^+$ channel and in Fig. 84 for the $p\pi^-$ channel. The simulation cross-section per bin is shown in magenta, and the data cross-section per bin is shown in blue. Not surprisingly, key N^* structures in the data are not precisely reproduced by the fitted model (simulation). However, the qualitative agreement is gratifying, given that

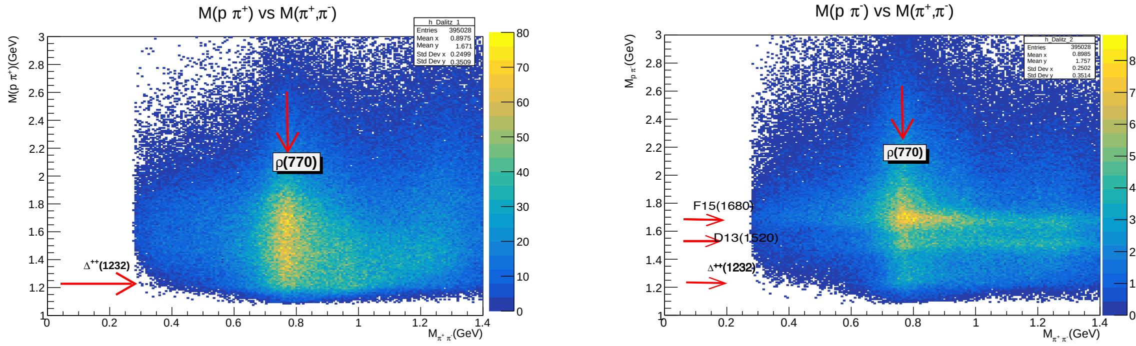

(a)

(b)

FIG. 81. The Dalitz plots are created from the experimental data, which visually represent the particle decay. The red arrows in the plots represents the major mesonic and baryonic resonances that overlap with the $\rho(770)$ resonance.

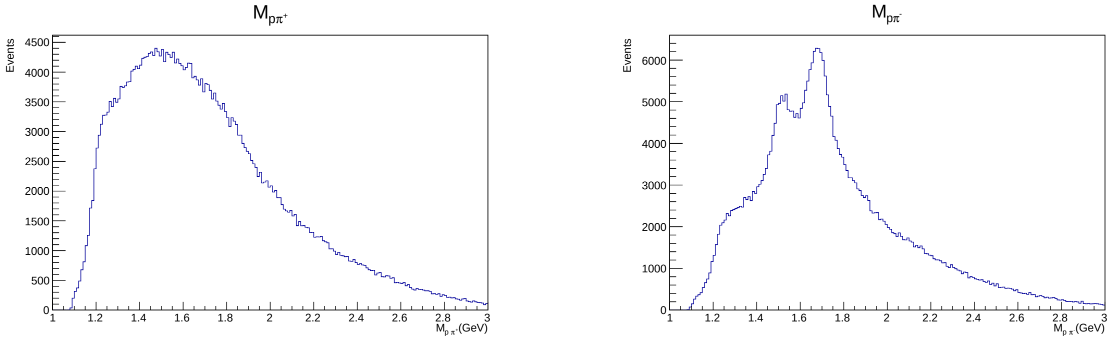

(a)

(b)

FIG. 82. The invariant mass distributions of $M_{p\pi^+}$(left) and $M_{p\pi^-}$(right). We do clearly see major baryonic resonances.

there is no explicit N^* dynamics in the model used to fit the data. Upon comparing the

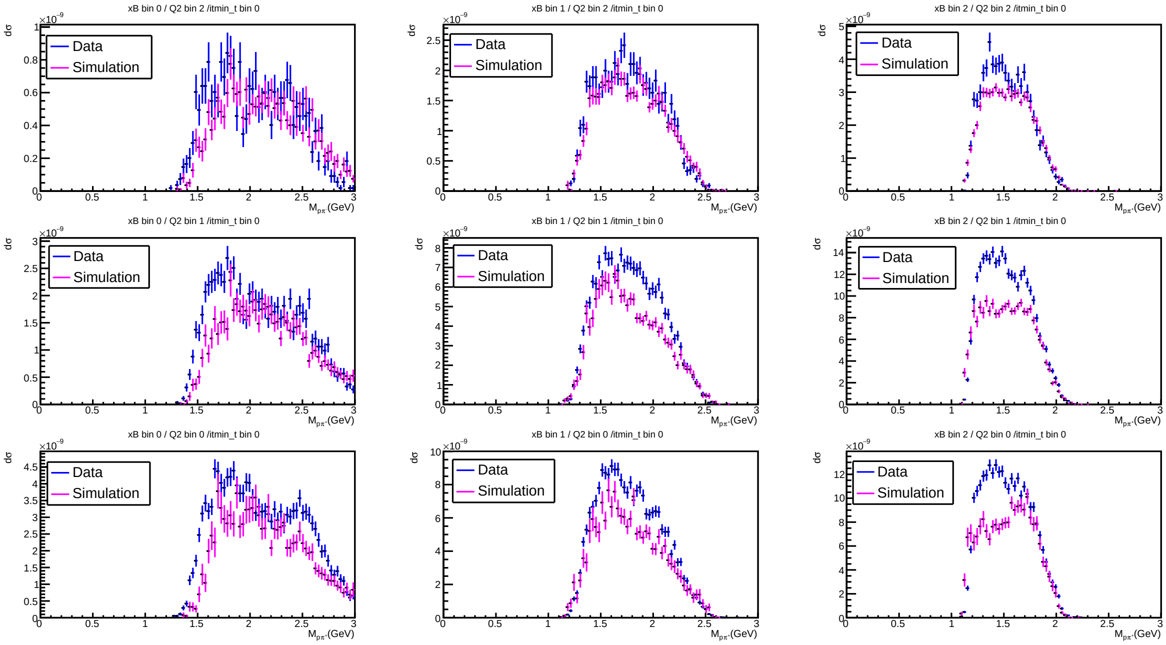

FIG. 83. The figure illustrates the comparison of the invariant mass distributions of $M_{p\pi^+}$ between experimental data and simulation in each of the defined $(Q^2, x_B, t_{min} - t)$ bins. The data plots are represented in blue, while the simulation plots are in magenta. Here x_B bins increase from left to right, and Q^2 bins increase from bottom to top.

resonance plot (Fig. 82) with the proton-pion invariant mass plots (Fig. 84 and Fig. 83), it is evident that the resonances exhibit considerable variability and appear less pronounced. The established threshold value is 1.1 GeV; however, some cases indicate the absence of events until 1.4 GeV, especially in the left column plots of Fig. 83 and Fig. 84. This observation is contingent upon the selected bin. Although we observed some resonance structures, no narrow resonances were identified initially. The addition of these resonances, as depicted

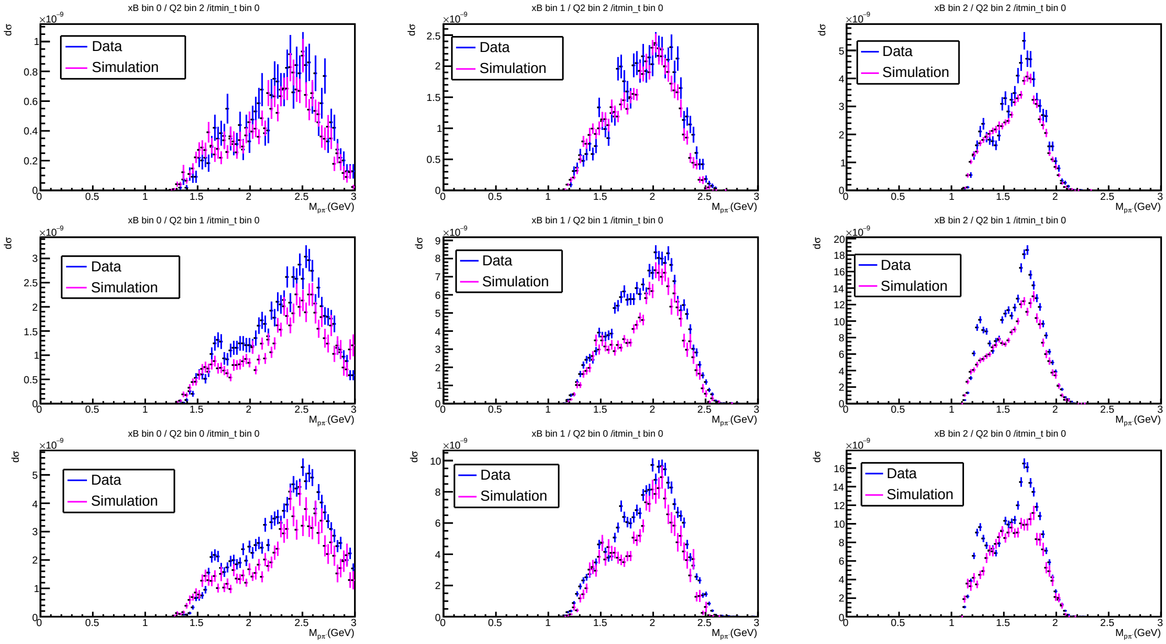

FIG. 84. The figure illustrates the comparison of the invariant mass distributions of $M_{p\pi^-}$ between experimental data and simulation in each of the defined $(Q^2, x_B, t_{min} - t)$ bins. The data plots are represented in blue, while the simulation plots are in magenta. Here x_B bins increase from left to right and Q^2 bins increase from bottom to top.

in Fig. 82, results in the emergence of more pronounced resonance structures. In Section 7.1, we discussed a model that examines the process of two pions in the final state that do not interact with the proton. This assumption is a fundamental aspect of the Schilling and Wolf [25] calculation, as depicted in Fig. 85. However, in reality, further interactions may occur, as illustrated by the purple lines in Fig. 86. Fig. 86(a) indicates that there may be an interaction between the recoil proton (p') and pion, leading to their decay into a pion (π) and nucleon (N). The diagram on the right-hand side of Fig. 86(b) illustrates how excited

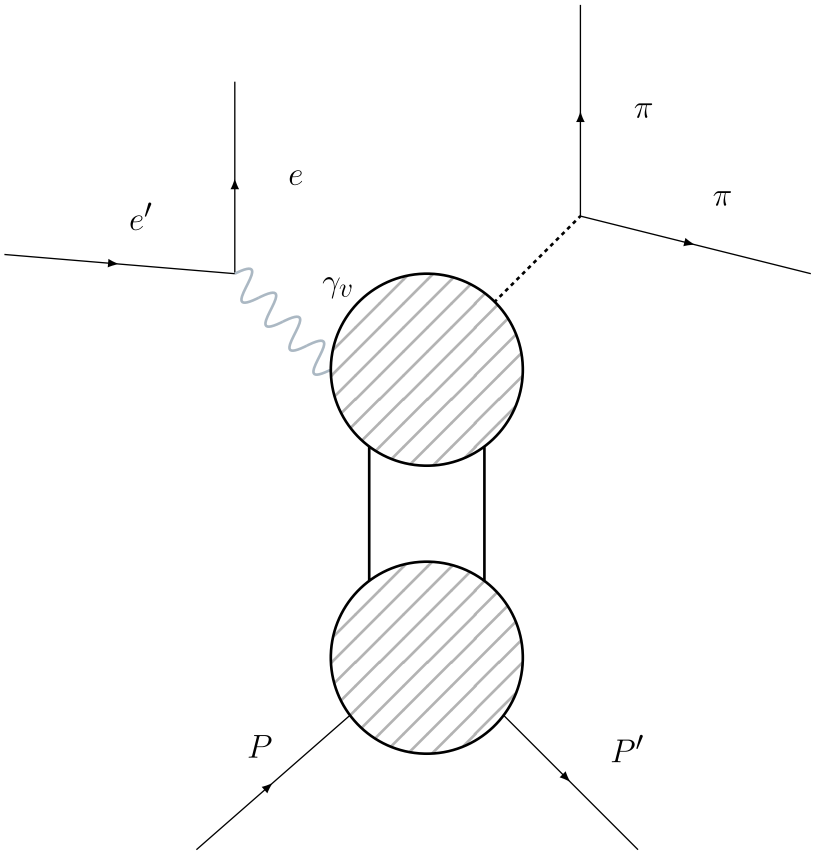

FIG. 85. The rough sketch of the Feynman diagram for $e'p'\pi^+\pi^-$ final state by assuming there is no interaction between the hard part and soft part.

baryons decay into a pion and proton. These additional interactions undermine the analysis conducted by Schilling and Wolf [25]. Our model calculation, as depicted in Fig. 86(a), includes a set of Feynman diagrams. However, we have excluded the purple part and the diagram on the left and right from our analysis. Neglecting these secondary interactions leads to a discrepancy between our model and the observed data. In order to improve the model's agreement with the experimental results, it is necessary to incorporate these interactions into the model amplitude in a coherent manner with the Generalized Parton Distribution (GPD) model. To solve this problem and make our model more accurate, we need to consistently include these interactions in the model's amplitude with the Generalized Parton Distribution (GPD) model. However, this task presents a significant challenge due to the potential violation of unitarity when adding these interactions to the model. Such violations may lead to unphysical results, such as an amplitude that is excessively large.

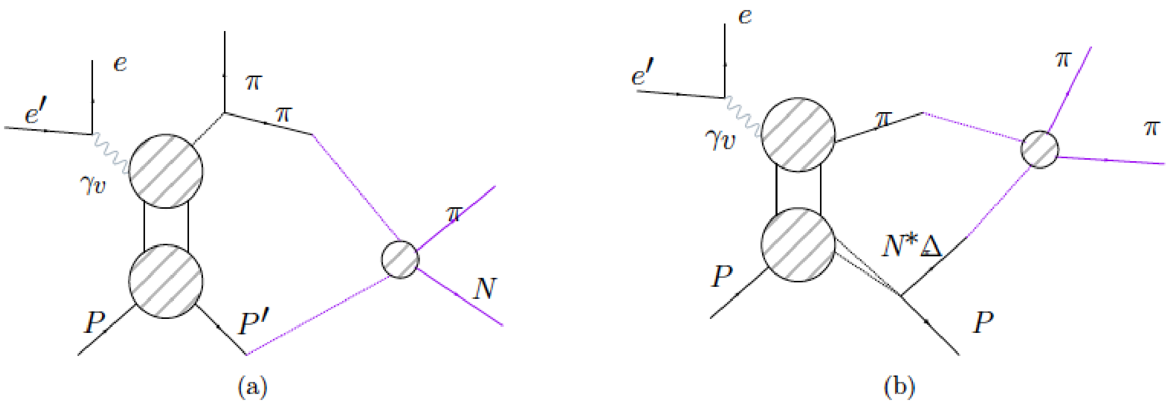

FIG. 86. The figures depict rough sketches of Feynman diagrams representing the $e'p'\pi^+\pi^-$ final state interacting with both the soft and hard parts. In both diagrams, two pions are produced, indicated by the $\pi\pi$ labels. The purple lines represent additional interactions that occur after the initial interaction between the electron and proton. These interactions are significant because they contribute to the overall production of the final state.

CHAPTER 8

CONCLUSION

The preliminary cross-sections for the σ and ρ mesons were obtained using the available RG-A fall 2018 pass-1 data in the CLAS12 experiment. While this experiment provided valuable insights into the behavior of the system under investigation, the accuracy of the results was limited by several factors.

One of the main limitations was the inadequacy of the efficiency studies. Specifically, the Forward Detector (FD) tracking efficiency was found to be approximately 80%, while the Central Detector (CD) tracking efficiency ranged from 50% to 80%. These efficiency limitations resulted in high systematic uncertainty for each track and likely contributed to the limited accuracy of the preliminary cross-section results. In order to improve the accuracy of the analysis and overcome these limitations, it is necessary to conduct proper efficiency studies.

In addition to the limitations imposed by the efficiency studies, the inadequate description of the model calculation also contributed to the limited accuracy of the preliminary cross-section results. While the implemented model clearly represented the measurement of the eight-fold differential cross-section for the electroproduction of σ and ρ mesons using CLAS12 pass-1 data (RG-A fall 2018), there were doubts about the model's accuracy since final state proton-pion interactions in the $ep \rightarrow e'p'\pi^+\pi^-$ reaction were skipped. Efforts to improve the analysis by adding resonance cuts to the analysis, specifically an invariant mass of $M_{p\pi^+} > 1.4$ GeV and $M_{p\pi^-} > 1.8$ GeV, did not yield the desired results due to insufficient statistics in the data. To address these limitations and enhance these studies, higher statistics are required. These efforts will be critical to improving the accuracy and reliability of the model calculations

To overcome the limitation of the preliminary cross-section results, one step will be to implement a maximum likelihood analysis (iterating on the parameter values) to enforce positivity of the model at all kinematic points. This would also potentially enable fitting all 34 parameters, including correlation between the azimuthal angles of the scattering plane and two-pion decay plane.

The RG-A pass2 analysis in CLAS12 has the potential for significant improvement through collaboration-wide efforts aimed at refining various aspects such as tracking efficiency, momentum correction, calibration, and alignment. These collective endeavors are expected to yield much better results compared to the current stage of the study.

In addition, the Monte Carlo generator will be updated with several changes to enhance the understanding of the electroproduction of ρ and σ mesons. These updates will include improvements in the modeling of the final-state interactions, as well as a more accurate treatment of the detector response.

The current collaborative endeavor focused on refining the analysis of electroproduction in CLAS12 presents a significant opportunity to enhance our understanding of the production mechanisms involved in generating ρ and σ mesons. This joint effort involves incorporating additional statistical data, investigating the outcomes of out-bending experiments, and strategically planning for future runs. By leveraging these advancements, our objective is to surpass the initially anticipated results and achieve more comprehensive and insightful findings in this particular study.

BIBLIOGRAPHY

[1] B. Pire and L. Szymanowski, “Hard exclusive reactions and hadron structure,” Nuclear Physics A **782**, 9–15 (2007).

[2] K. A. Olive et al., “(particle data group),” Chinese Physics C **38** (2014), 10.1088/1674-1137/38/9/090001.

[3] J. W. Qiu, Felix Ringer, Nobuo Sato, and Pia Zurita, “QCD factorization and universality of jet cross sections in heavy-ion collisions,” Nuclear Physics A **1005**, 121853 (2021).

[4] E. Rutherford, “The scattering of alpha and beta particles by matter and the structure of the atom,” Phil. Mag. Ser. 6 **21**, 669–688 (1911).

[5] M. Thomson, *Modern particle physics* (Cambridge University Press, New York, 2013).

[6] F. Jegerlehner, *The Anomalous Magnetic Moment of the Muon*, Vol. 274 (Springer Tracts in Modern Physics, Cambridge, UK, 2017).

[7] M. N. Rosenbluth, “High energy elastic scattering of electrons on protons,” Physical Review **79** (1950), 10.1103/PhysRev.79.615.

[8] C. F. Perdrisat, V. Punjabi, and M. Vanderhaeghen, “Nucleon Electromagnetic Form Factors,” Prog. Part. Nucl. Phys. **59**, 694–764 (2007), arXiv:hep-ph/0612014 .

[9] M. K. Jones, Kevin Fissum, Z. L. Zhou, and The Jefferson Lab Hall A Collaboration, “GEp/GMp Ratio by Polarization Transfer in $\vec{e}p \to e\vec{p}$,” Physical Review Letters **84**, 1398–1402 (2000).

[10] V. Punjabi *et al.*, “Proton elastic form-factor ratios to Q**2 = 3.5-GeV**2 by polarization transfer,” Phys. Rev. C **71**, 055202 (2005), [Erratum: Phys.Rev.C 71, 069902 (2005)], arXiv:nucl-ex/0501018 .

[11] I. A. Qattan *et al.*, “Precision Rosenbluth measurement of the proton elastic form-factors,” Phys. Rev. Lett. **94**, 142301 (2005), arXiv:nucl-ex/0410010 .

[12] M. E. Christy *et al.* (E94110), “Measurements of electron proton elastic cross-sections for 0.4 < Q**2 < 5.5 (GeV/c)**2,” Phys. Rev. C **70**, 015206 (2004), arXiv:nucl-ex/0401030 .

[13] L. L. Pappalardo, *Transverse spin effects in polarized semi inclusive deep inelastic scattering*, Tech. Rep. (Deutsches Elektronen-Synchrotron (DESY), Ph.D. Thesis Ferrara U., 2008).

[14] B. Guegan, *Study of Generalized Parton Distributions and Deeply Virtual Compton Scattering on the nucleon with the CLAS and CLAS12 detectors at the Jefferson Laboratory*, Tech. Rep. (Ph.D. Thesis, Universite Paris-Sud, Rensselaer Polytechnic Institute,), 2013).

[15] Y. L. Dokshitzer, "Calculation of the Structure Functions for Deep Inelastic Scattering and e+ e- Annihilation by Perturbation Theory in Quantum Chromodynamics." Sov. Phys. JETP **46**, 641–653 (1977).

[16] H. Abramowicz *et al.* (H1, ZEUS), "Combination of measurements of inclusive deep inelastic $e^{\pm}p$ scattering cross sections and QCD analysis of HERA data," Eur. Phys. J. C **75**, 580 (2015), arXiv:1506.06042 [hep-ex] .

[17] M. Guidal, H. Moutarde, and M. Vanderhaeghen, "Generalized Parton Distributions in the valence region from Deeply Virtual Compton Scattering," Rept. Prog. Phys. **76**, 066202 (2013), arXiv:1303.6600 [hep-ph] .

[18] C. E. Hyde, M. Guidal, and A. V. Radyushkin, "Deeply virtual exclusive processes and generalized parton distributions," Journal of Physics: Conference Series **299**, 012006 (2011).

[19] B. Zhao, *Beam Spin Asymmetry Measurements from Deeply Virtual Meson Production*, Ph.D. thesis, Connecticut U. (2008).

[20] D. Müller, D. Robaschik, B. Geyer, F. M. Dittes, and J. Hořejši, "Wave functions, evolution equations and evolution kernels from light ray operators of QCD," Fortsch. Phys. **42**, 101–141 (1994), arXiv:hep-ph/9812448 .

[21] X. Ji, "Gauge-invariant decomposition of nucleon spin," Physical Review Letters **78**, 610–613 (1997).

[22] A. V. Radyushkin, "Nonforward parton distributions," Physical Review D **56**, 5524–5557 (1997).

[23] J. Ashman, F. Lettenström, and K. Ziemons, "An investigation of the spin structure of the proton in deep inelastic scattering of polarised muons on polarised protons," Nuclear Physics B **328**, 1–35 (1989).

[24] B. Lehmann-Dronke, P. V. Pobylitsa, M.V. Polyakov, A. Schäfer, and K. Goeke, "Hard exclusive electroproduction of two pions," Physics Letters B **475**, 147–156 (2000).

[25] K. Schilling and G. Wolf, "How to analyse vector-meson production in inelastic lepton scattering," Nucl. Phys., B, v. B61, pp. 381-413 (1973), 10.1016/0550-3213(73)90371-4.

[26] K. Goeke, M. V. Polyakov, and M. Vanderhaeghen, "Hard exclusive reactions and the structure of hadrons," Progress in Particle and Nuclear Physics **47**, 401–515 (2001).

[27] M. R. Pennington, "Sigma coupling to photons: Hidden scalar in $\gamma\gamma \to \pi^0\pi^0$," Phys. Rev. Lett. **97**, 011601 (2006).

[28] *L. Y. Dai, private communication 2016*.

[29] M. Jacob and G. C. Wick, "On the General Theory of Collisions for Particles with Spin," Annals Phys. **7**, 404–428 (1959).

[30] L. Y. Dai and M. R. Pennington, "Comprehensive amplitude analysis of γ $\gamma\to$ π+ π-, π 0 π 0 and k$^-$ k below 1.5 gev," Physical Review D **90**, 036004 (2014).

[31] L. Y. Dai and M. R. Pennington, "Two photon couplings of the lightest isoscalars from BELLE data," Physics Letters B **736**, 11–15 (2014).

[32] J. R. Pelaez, "From controversy to precision on the sigma meson: a review on the status of the non-ordinary $f_0(500)$ resonance," Phys. Rept. **658**, 1 (2016), arXiv:1510.00653 [hep-ph] .

[33] A. Radyushkin and P. Stoler, *Exclusive Reactions at High Momentum Transfer IV* (World Scientific Publishing Company; Illustrated edition (February 25, 2011), 2011).

[34] "CLAS12 RG-A - Analysis Note Overview and Procedures Phase I Towards SIDIS CLAS12 First Publications," (2020).

[35] V. D. Burkert *et al.*, "The CLAS12 Spectrometer at Jefferson Laboratory," Nucl. Instrum. Meth. A **959**, 163419 (2020).

[36] V. Ziegler *et al.*, “The CLAS12 software framework and event reconstruction,” Nucl. Instrum. Meth. A **959**, 163472 (2020).

[37] M. Ungaro *et al.*, “The CLAS12 Geant4 simulation,” Nucl. Instrum. Meth. A **959**, 163422 (2020).

[38] *A Geant4 simulation framework*, `https://gemc.jlab.org`.

[39] `https://clasweb.jlab.org/wiki/index.php/CLAS12_Momentum_Corrections_from_richcap:All_Channels#tab=Correction_Code__28All_29`.

[40] I. Akushevich, “Radiative effects in processes of diffractive vector meson electroproduction,” The European Physical Journal C Particles and Fields **8**, 457–463 (1998).

[41] *Radiative Correction HelpDesk*, `https://www.jlab.org/RC/`.

[42] L. Tiator, “The MAID legacy and future,” Few-Body Systems **59** (2018), 10.1007/s00601-018-1343-5.

[43] A. Afanasev, I. Akushevich, V. Burkert, and K. Joo, “QED radiative corrections in processes of exclusive pion electroproduction,” Physical Review D **66** (2002), 10.1103/physrevd.66.074004.

[44] S. Stepanyan et al, “Clas12 forward detector charge particle reconstruction efficiency and the beam background merging,” (2020), CLAS12 note 2020-005.

[45] L. N. Hand, “Experimental investigation of pion electroproduction,” Phys. Rev. **129**, 1834–1846 (1963).

[46] A. Bacchetta, U. D’Alesio, M. Diehl, and C. Andy Miller, “Single-spin asymmetries: The Trento conventions,” Phys. Rev. D **70**, 117504 (2004), arXiv:hep-ph/0410050 .

[47] CLAS-12 Drift Chambers: `https://www.jlab.org/Hall-B/clas12-web/specs/dc.pdf`.

[48] M. D. Mestayer *et al.*, “The CLAS12 drift chamber system,” Nucl. Instrum. Meth. A **959**, 163518 (2020).

[49] CLAS Collaboration, CLAS12 DC Calibrations `https://clasweb.jlab.org/wiki/index.php/CLAS12_DC_Calibration#tab=Current_Version`.

[50] CLAS Collaboration, (accessed 3/2023), CLAS12 DC Calibration Software, `https://github.com/JeffersonLab/clas12calibration-dc`.

APPENDIX A

INDEPENDENT VARIABLES IN PHASE-SPACE

The choice of a specific set of independent variables in the final state is flexible, but the specific relationships amongst the dependent variables are complicated. What follows is a specific choice.

- Define a series of rotated coordinate systems. The initial system is the laboratory system with $\hat{z}$ along the electron beam direction, $\hat{y}$ vertically up, and $\hat{x}$ horizontal, defined by $\hat{y} \times \hat{z}$, to ensure the $x - y - z$ coordinate system is right-handed. Next, define a coordinate system determined by the electron scattering kinematics:

$$\begin{aligned}\hat{z}_q &\equiv \frac{\mathbf{q}_{\rm Rest}}{\sqrt{\mathbf{q}^2_{\rm Rest}}}, \\ \hat{y}_q &\equiv \left[\frac{\mathbf{k}\times\mathbf{k}'}{|\mathbf{k}\times\mathbf{k}'|}\right]_{\rm Rest}, \\ \hat{x}_q &\equiv \hat{y}_q \times \hat{z}_q. \end{aligned} \tag{158}$$

  Note that the vectors $\{\hat{x}_q, \hat{y}_q, \hat{z}_q\}$ vary event-by-event, according the electron scattering kinematics.

- Apply the following identity [2]:

$$\begin{aligned}\Phi^{(4)}(k+P;k',P',p_1,p_2) &= d\Phi^{(3)}(k+P;k',P',P_{1,2})d\Phi^{(2)}(P_{1,2};p_1,p_2)(2\pi)^3 dP^2_{1,2}, \\ &= \frac{\delta^{(4)}\left(k^\mu + P^\mu - k'^\mu - P'^\mu - P^\mu_{1,2}\right)}{(2\pi)^9}[\frac{d^3\mathbf{k}'}{2E'_e}][\frac{d^3\mathbf{P}'}{2E'_p}][\frac{d^3\mathbf{P}_{1,2}}{2E_{1,2}}] \\ &\quad\times \frac{\delta^{(4)}\left(P^\mu_{1,2} - p^\mu_1 - p^\mu_2\right)}{(2\pi)^6}\left[\frac{d^3\mathbf{p}_1}{2E_1}\right]\left[\frac{d^3\mathbf{p}_2}{2E_2}\right] dM^2_{1,2}(2\pi)^3. \end{aligned} \tag{159}$$

- Since the factors $d^3\mathbf{P}_{1,2}/(2E_{1,2})$ and $d^3\mathbf{p}_1/(2E_1)$ are each separately Lorentz-invariant, we can evaluate each one in distinct convenient reference frames.

- Evaluate the invariant factor

$$F_{\gamma^* P} = \delta^{(4)}\left(q^\mu + P^\mu - P'^\mu - P^\mu_{1,2}\right)\left[\frac{d^3\mathbf{P}'}{2E'_p}\right]\left[\frac{d^3\mathbf{P}_{1,2}}{2E_{1,2}}\right], \tag{160}$$

in the $\gamma^* + P$ Center-of-Mass (CM) frame. Note that this is also the $P' + P_{1.2}$ CM frame:

$$\begin{aligned}
[q+P]^{\mu}_{\gamma^* P \text{ CM}} &= \left[\sqrt{W^2}, \mathbf{0}\right], \\
\mathbf{P}_{\gamma^* P \text{ CM}} &= -\mathbf{q}_{\gamma^* P \text{ CM}}, \\
[E_P]_{\gamma^* P \text{ CM}} &= \sqrt{M^2 + \mathbf{q}^2_{\gamma^* P \text{ CM}}}, \\
\left[q^0\right]_{\gamma^* P \text{ CM}} &= \sqrt{-Q^2 + \mathbf{q}^2_{\gamma^* P \text{ CM}}}, \\
[E_P]^2_{\gamma^* P \text{ CM}} &= \left(\sqrt{W^2} - \left[q^0\right]_{\gamma^* P \text{ CM}}\right)^2, \\
M^2 + [q^0]^2_{\gamma^* P \text{ CM}} &= W^2 - 2\sqrt{W^2}\left[q^0\right]_{\gamma^* P \text{ CM}} - Q^2 + \mathbf{q}^2_{\gamma^* P \text{ CM}}, \\
\left[q^0\right]_{\gamma^* P \text{ CM}} &= \frac{W^2 - M^2 - Q^2}{2\sqrt{W^2}}, \\
[E_p]_{\gamma^* P \text{ CM}} &= \frac{W^2 + M^2 + Q^2}{2\sqrt{W^2}}.
\end{aligned} \tag{161}$$

Applying the same analysis to P'^{μ} and $P^{\mu}_{1,2}$ in this same reference frame, we obtain:

$$\begin{aligned}
[P' + P_{1,2}]^{\mu}_{\gamma^* P \text{ CM}} &= \left[\sqrt{W^2}, \mathbf{0}\right], \\
[E_{1,2}]_{\gamma^* P \text{ CM}} &= \sqrt{M^2_{1,2} + [\mathbf{P}_{1,2}]^2_{\gamma^* P \text{ CM}}}, \\
\left[E'_p\right]_{\gamma^* P \text{ CM}} &= \sqrt{M^2 + [\mathbf{P}_{1,2}]^2_{\gamma^* P \text{ CM}}}, \\
\left[E'_p\right]_{\gamma^* P \text{ CM}} &= \frac{W^2 + M^2 - M^2_{1,2}}{2\sqrt{W^2}}, \\
[E_{1,2}]_{\gamma^* P \text{ CM}} &= \frac{W^2 - M^2 + M^2_{1,2}}{2\sqrt{W^2}}.
\end{aligned} \tag{162}$$

In the $\gamma^* P$ CM frame, the the momentum 3-vector of the $\pi\pi$ system can be expressed as:

$$\mathbf{P}_{1,2} \equiv \mathrm{P}^*_{12}\left[\hat{z}_q \cos\theta^*_{12} + \sin\theta^*_{12}\left(\hat{x}_q \cos\phi^*_{12} + \hat{y}_q \sin\phi^*_{12}\right)\right]. \tag{163}$$

In the definition of $F_{\gamma^* P}$, integrate over d^3P':

$$\begin{aligned}
F_{\gamma^* P} &= \delta\left(\left[q^0 + E_p - E'_p - E_{1,2}\right]_{\gamma^* P \text{ CM}}\right)\left[\frac{d^3\mathbf{P}_{1,2}}{4E_{1,2}E'_p}\right]_{\gamma^* P \text{ CM}}, \\
&= \delta\left(f(\mathrm{P}^*_{1,2})\right)\frac{\left(\mathrm{P}^*_{1,2}\right)^2 d\mathrm{P}^*_{1,2} d\cos\theta^*_{1,2} d\phi^*_{1,2}}{\left[4E_{1,2}E'_p\right]_{\gamma^* P \text{ CM}}},
\end{aligned} \tag{164}$$

with

$$f\left(\mathrm{P}^*_{1,2}\right) = \sqrt{W^2} - \sqrt{M^2 + \left[\mathrm{P}^*_{1,2}\right]^2} - \sqrt{M^2_{1,2} + \left[\mathrm{P}^*_{1,2}\right]^2}. \tag{165}$$

Then

$$
\begin{aligned}
F_{\gamma^* P} &= \frac{1}{\left|f'\left(\mathrm{P}^*_{1,2}\right)\right|_{f=0}} \frac{\left(\mathrm{P}^*_{1,2}\right)^2 d\cos\theta^*_{1,2} d\phi^*_{1,2}}{\left[4E_{1,2}E'_p\right]_{\gamma^* P\ \mathrm{CM}}}, \\
\left|f'\left(\mathrm{P}^*_{1,2}\right)\right|_{f=0} &= \left[\frac{\mathrm{P}^*_{1,2}}{E'^*_p} + \frac{\mathrm{P}^*_{1,2}}{E^*_{1,2}}\right]_{f=0} = \left[E^*_{1,2} + E'^*_p\right] \frac{\mathrm{P}^*_{1,2}}{E'^*_p E^*_{1,2}}, \\
&= \frac{\mathrm{P}^*_{1,2}\sqrt{W^2}}{E'^*_p E^*_{1,2}}.
\end{aligned} \tag{166}
$$

Therefore

$$
F_{\gamma^* P} = \frac{\left(\mathrm{P}^*_{1,2}\right) d\cos\theta^*_{1,2} d\phi^*_{1,2}}{4\sqrt{W^2}}. \tag{167}
$$

Furthermore, the invariant variable t has the form:

$$
\begin{aligned}
t &= (P' - P)^2 = 2M^2 - 2P' \cdot P, \\
&= 2M^2 - 2\left[E'_p E_p\right]_{\gamma^* P\ \mathrm{CM}} + 2\left[\mathbf{P}' \cdot \mathbf{P}\right]_{\gamma^* P\ \mathrm{CM}}.
\end{aligned} \tag{168}
$$

Note, however, that

$$
\begin{aligned}
\left[\mathbf{P}'\right]_{\gamma^* P\ \mathrm{CM}} &= -\left[\mathbf{P}_{1,2}\right]_{\gamma^* P\ \mathrm{CM}}, \\
\left[\mathbf{P}'\right]_{\gamma^* P\ \mathrm{CM}} &= -\left[\mathbf{q}\right]_{\gamma^* P\ \mathrm{CM}},
\end{aligned} \tag{169}
$$

and therefore

$$
t = 2M^2 - 2\left[E'_p E_p\right]_{\gamma^* P\ \mathrm{CM}} + 2\left[\left|\mathbf{q}\right|_{\gamma^* P\ \mathrm{CM}} \mathrm{P}^*_{1,2} \cos\theta^*_{1,2}\right], \tag{170}
$$

$$
\frac{\partial t}{\partial \cos\theta^*_{1,2}} = 2\left|\mathbf{q}\right|_{\gamma^* P\ \mathrm{CM}} \mathrm{P}^*_{1,2}. \tag{171}
$$

As a consequence:

$$
\begin{aligned}
d\cos\theta^*_{1,2} &= dt\left[\frac{\partial t}{\partial\cos\theta^*_{1,2}}\right]^{-1} = \frac{dt}{2\left|\mathbf{q}\right|_{\gamma^* P\ \mathrm{CM}} \mathrm{P}^*_{1,2}}, \\
F_{\gamma^* P} &= \frac{dt\, d\phi^*_{1,2}}{8\left|\mathbf{q}\right|_{\gamma^* P\ \mathrm{CM}} \sqrt{W^2}}.
\end{aligned} \tag{172}
$$

Eq. (170) is also useful for defining the minimum value of $-t$ (recall t is strictly negative). In the $\gamma^* P$ CM frame the values of E'_p, E_p, $|\mathbf{q}|$, and $\mathbf{P}_{1.2}$ are determined by

W^2, Q^2, and $M_{1,2}^2$ (as well as the proton mass). The only remaining variable in the definition of t is $\cos\theta_{1,2}^*$. The minimum value of $-t$ occurs for $\theta_{1,2}^* = 0$:

$$t_{\min} = 2M^2 - 2\left[E'_p E_p\right]_{\gamma^* P\ \mathrm{CM}} + 2\left[|\mathbf{q}|_{\gamma^* P\ \mathrm{CM}}\,\mathrm{P}_{1,2}^*\right], \tag{173}$$

and maximum value of $-t$ occurs at $\theta_{1,2}^* = \pi$:

$$t_{\min} = 2M^2 - 2\left[E'_p E_p\right]_{\gamma^* P\ \mathrm{CM}} - 2\left[|\mathbf{q}|_{\gamma^* P\ \mathrm{CM}}\,\mathrm{P}_{1,2}^*\right]. \tag{174}$$

This is a slight misnomer, because this is the maximum value of t:

$$t \le t_{\min} < 0. \tag{175}$$

The maximum possible value of $-t$ is obtained for $\theta_{1,2}^* = \pi$:

$$2M^2 - 2\left[E'_p E_p\right]_{\gamma^* P\ \mathrm{CM}} - 2\left[|\mathbf{q}|_{\gamma^* P\ \mathrm{CM}}\,\mathrm{P}_{1,2}^*\right] \le t. \tag{176}$$

- It now remains to define the decay of the σ-meson into the two final state pions: $P_{1,2}^\mu = p_1^\mu + p_2^\mu$. For this, define a new coordinate system in the $\gamma^* P = P' + P_{1,2}$ CM frame: Define $\hat{z}_{1,2}^*$ parallel to $\mathbf{P}_{1,2}^*$:

$$\hat{z}_{1,2}^* = \hat{z}_q \cos\theta_{1,2}^* + \sin\theta_{1,2}^* \left[\hat{x}_q \cos\phi_{1,2}^* + \hat{y}_q \sin\phi_{1,2}^*\right]. \tag{177}$$

The unit vector $\hat{x}_{1,2}^*$ will be perpendicular to $\hat{z}_{1,2}^*$, but in the plane defined by $[\mathbf{q} \otimes \mathbf{P}_{1,2}]$ in this $P' + P_{1,2}$ CM frame. First, define the unit vector perpendicular to this plane:

$$\hat{y}_{1,2}^* = \frac{\hat{z}_q \times \hat{z}_{1,2}^*}{\left|\hat{z}_q \times \hat{z}_{1,2}^*\right|}. \tag{178}$$

Then:

$$\hat{x}_{1,2}^* = \hat{y}_{1,2}^* \times \hat{z}_{1,2}^*. \tag{179}$$

Boost along the $\hat{z}_{1,2}^*$ direction to the σ-meson rest frame:

$$[P_{1,2}]_{\sigma\text{-Rest}} = [M_{1,2}, 0, 0, 0]. \tag{180}$$

Define the polar and azimuthal angles of pion-1 in the σ-meson rest frame:

$$\mathbf{p}_{1,\sigma\text{-Rest}} = |\mathbf{p}_{\sigma\text{-Rest}}| \left[\hat{z}_{1,2}^* \cos\theta_{\sigma\text{-Rest}} + \sin\theta_{\sigma\text{-Rest}} \left(\hat{x}_{1,2}^*\right)\right]. \tag{181}$$

In this frame, the two pions have equal and opposite three-momenta:

$$\mathbf{p}_{2,\sigma\text{-Rest}} = -\mathbf{p}_{1,\sigma\text{-Rest}} \qquad |\mathbf{p}_{1,\sigma\text{-Rest}}|^2 = \frac{1}{4}M_{1,2}^2 - m_\pi^2, \tag{182}$$

and

$$E_{1,\sigma\text{-Rest}} = E_{2,\sigma\text{-Rest}} = M_{1,2}/2, \tag{183}$$

Recall $M_{1,2}^2 > 4m_\pi^2$.

Limit on Λ^2

For fixed values of (Q^2, x_B, t), there is a bound on the value of Λ^2. In calculating this bound, we will use the kinematic bounds on t at fixed Q^2, x_B and $\Lambda^2 = M^2$:

$$\begin{aligned}
t_0 &= -Q^2 + m_V^2 - 2\left(\nu^{CM} E_V^{CM} - \left|\mathbf{q}^{CM}\right| \left|\mathbf{p}_V^{CM}\right|\right)_{\Lambda^2=M^2}, \\
t_\pi &= -Q^2 + m_V^2 - 2\left(\nu^{CM} E_V^{CM} + \left|\mathbf{q}^{CM}\right| \left|\mathbf{p}_V^{CM}\right|\right)_{\Lambda^2=M^2}, \\
(t_0 - t)(t - t_\pi) &= -\left(t + Q^2 - m_V^2 + 2\nu^{CM} E_V^{CM} - 2\left|\mathbf{q}^{CM}\right| \left|\mathbf{p}_V^{CM}\right|\right)_{\Lambda^2=M^2}, \\
&\quad \times \left(t + Q^2 - m_V^2 + 2\nu^{CM} E_V^{CM} + 2\left|\mathbf{q}^{CM}\right| \left|\mathbf{p}_V^{CM}\right|\right)_{\Lambda^2=M^2}, \\
&= \left[4\left|\mathbf{q}^{CM}\right|^2 \left|\mathbf{p}_V^{CM}\right|^2 - \left(t + Q^2 - m_V^2 + 2\nu^{CM} E_V^{CM}\right)^2\right]_{\Lambda^2=M^2}. \qquad (184)
\end{aligned}$$

The bound on Λ^2, as a function of t is determined by the constraint that $\left|\cos\theta_{\gamma V}^{CM}\right| \le 1$. Inverting the expression for t:

$$-1 \le \cos\theta_{\gamma V}^{CM} = \frac{t + Q^2 - m_V^2 + 2\nu^{CM}\left[E_V^{CM}\right]_{\Lambda^2}}{2\left|\mathbf{q}^{CM}\right| \left|\mathbf{p}_V^{CM}\right|_{\Lambda^2}} \le 1. \qquad (185)$$

Only the upper limit is relevant:

$$\begin{aligned}
2\left|\mathbf{q}^{CM}\right| \left|\mathbf{p}_V^{CM}\right|_{\Lambda^2} &\ge t + Q^2 - m_V^2 + 2\nu^{CM}\left[E_V^{CM}\right]_{\Lambda^2}, \\
4\left|\mathbf{q}^{CM}\right|^2 \left|\mathbf{p}_V^{CM}\right|_{\Lambda^2}^2 &\ge \left[t + Q^2 - m_V^2 + 2\nu^{CM}\left[E_V^{CM}\right]_{\Lambda^2}\right]^2. \qquad (186)
\end{aligned}$$

To simplify this, note that

$$\begin{aligned}
\left(E_V^{CM}\right)_{\Lambda^2} &= \left(E_V^{CM}\right)_{M^2} - \frac{\Lambda^2 - M^2}{2W}, \\
\left(E_V^{CM}\right)_{\Lambda^2}^2 &= \left(E_V^{CM}\right)_{M^2}^2 - 2\left(E_V^{CM}\right)_{M^2} \frac{\Lambda^2 - M^2}{2W} + \left[\frac{\Lambda^2 - M^2}{2W}\right]^2, \\
\left|\mathbf{p}_V^{CM}\right|_{\Lambda^2}^2 &= \left|\mathbf{p}_V^{CM}\right|_{M^2}^2 - 2\left(E_V^{CM}\right)_{M^2} \frac{\Lambda^2 - M^2}{2W} + \left[\frac{\Lambda^2 - M^2}{2W}\right]^2. \qquad (187)
\end{aligned}$$

The bound on Λ^2 is now expressed as:

$$\begin{aligned}
4\left|\mathbf{q}^{CM}\right|^2 & \left(\left|\mathbf{p}_V^{CM}\right|^2_{M^2} - \left(E_V^{CM}\right)_{M^2}\frac{\Lambda^2 - M^2}{W} + \left[\frac{\Lambda^2 - M^2}{2W}\right]^2\right) \\
&\geq \left[t + Q^2 - m_V^2 + 2\nu^{CM}\left(\left[E_V^{CM}\right]_{M^2} - \frac{\Lambda^2 - M^2}{2W}\right)\right]^2 \\
&\geq \left[t + Q^2 - m_V^2 + 2\nu^{CM}\left(E_V^{CM}\right)_{M^2}\right]^2 + \left[\frac{\nu^{CM}}{W}\left(\Lambda^2 - M^2\right)\right]^2 \\
&\quad - 2\left[t + Q^2 - m_V^2 + 2\nu^{CM}\left(E_V^{CM}\right)_{M^2}\right]\frac{\nu^{CM}}{W}\left(\Lambda^2 - M^2\right), \\
0 &\leq 4\left|\mathbf{q}^{CM}\right|^2\left|\mathbf{p}_V^{CM}\right|^2_{M^2} - \left[t + Q^2 - m_V^2 + 2\nu^{CM}\left(E_V^{CM}\right)_{M^2}\right]^2 + \frac{Q^2}{W^2}\left(\Lambda^2 - M^2\right)^2 \\
&\quad - \left\{4Q^2\frac{\left(E_V^{CM}\right)_{M^2}}{W} - 2\left[t + Q^2 - m_V^2\right]\frac{\nu^{CM}}{W}\right\}\left(\Lambda^2 - M^2\right), \\
0 &\leq (t_0 - t)(t - t_\pi) \\
&\quad - 4\left\{Q^2\frac{\left(E_V^{CM}\right)_{M^2}}{W} - \left[t + Q^2 - m_V^2\right]\frac{\nu^{CM}}{2W}\right\}\left(\Lambda^2 - M^2\right) \\
&\quad + \frac{Q^2}{W^2}\left(\Lambda^2 - M^2\right)^2.
\end{aligned} \tag{188}$$

Substitute the invariant expressions for the CM variables:

$$\begin{aligned}
0 &\leq (t_0 - t)(t - t_\pi) \\
&\quad - 4\left\{\frac{Q^2}{W}\left[\nu^{CM} + \frac{m_V^2 + Q^2}{2W}\right] - \frac{\nu^{CM}}{2W}\left(t + Q^2 - m_V^2\right)\right\}\left(\Lambda^2 - M^2\right) \\
&\quad + \frac{Q^2}{W^2}\left(\Lambda^2 - M^2\right)^2, \\
0 &\leq (t_0 - t)(t - t_\pi) \\
&\quad - \frac{1}{W^2}\left\{2Q^2\left[W^2 - M^2 + m_V^2\right] - \left[W^2 - M^2 - Q^2\right]\left(t + Q^2 - m_V^2\right)\right\}\left(\Lambda^2 - M^2\right) \\
&\quad + \frac{Q^2}{W^2}\left(\Lambda^2 - M^2\right)^2 \\
&\leq (t_0 - t)(t - t_\pi) \\
&\quad - \frac{Q^2}{W^2}\left\{\frac{Q^2 - t + m_V^2}{x_B} + 2t\right\}\left(\Lambda^2 - M^2\right) \\
&\quad + \frac{Q^2}{W^2}\left(\Lambda^2 - M^2\right)^2.
\end{aligned} \tag{189}$$

Solving the limiting quadratic:

$$\begin{aligned}\left(\Lambda^2 - M^2\right)_{\text{Max}} &= \frac{W^2}{2Q^2}\left\{ \frac{Q^2}{W^2}\left[\frac{Q^2 - t + m_V^2}{x_B} + 2t\right]\right.\\ &\left.\pm\sqrt{\left[\frac{Q^2}{W^2}\right]^2\left[\frac{Q^2 - t + m_V^2}{x_B} + 2t\right]^2 - 4(t_0 - t)(t - t_\pi)\frac{Q^2}{W^2}}\right\},\\ &= \left[\frac{Q^2 - t + m_V^2}{2x_B} + t\right]\left\{1 \pm \sqrt{1 - \frac{W^2}{Q^2}\frac{(t_0 - t)(t - t_\pi)}{\left[t + \left(Q^2 - t + m_V^2\right)/(2x_B)\right]^2}}\right\}. \end{aligned} \qquad (190)$$

Only the '−' solution is relevant.

Radiative Lineshape Generation

For the generation of the radiative lineshape, we need to generate random numbers u with probability distribution

$$P(x)dx = \delta_S x^{\delta_S - 1}\, dx\,, \qquad 0 \le x < 1. \qquad (191)$$

The integrated distribution is

$$F(y) = \int_0^y \delta_S x^{\delta_S - 1} dx = y^{\delta_S}. \qquad (192)$$

1. Generate a uniform deviate $0 \le u < 1$.
2. Define $y = u^{1/\delta_S}$.

The deviate y has the desired probability distribution.

APPENDIX B

CROSS SECTION

B.0.1 TRANSVERSE AND LONGITUDINAL TERMS

The following is limited to $J, J' \leq 1$. The generalization to higher spin channels is straightforward, though tedious. Applying parity symmetry 67:

$$\begin{aligned}
d\Re_T &= \sum_{\lambda=\pm1} d^{J'}_{0,\lambda'_h}(\Theta_R) d^{J}_{0,\lambda_h}(\Theta_R) e^{i(\lambda_h-\lambda'_h)\Phi_R} \left[T^{(\lambda'_h,\lambda)}_{J',I'}\Omega_{J',I'}(m_{\pi\pi})\right]^{\dagger} T^{(\lambda_h,\lambda)}_{J,I}\Omega_{J,I}(m_{\pi\pi}),\\
&= \sum_{\lambda=\pm1}\left\{\sum_{\lambda_h=-1}^{1} d^{J'}_{0,\lambda_h}(\Theta_R) d^{J}_{0,\lambda_h}(\Theta_R)\Re\left[T^{(\lambda_h,\lambda)\dagger}_{J',I'}T^{(\lambda_h,\lambda)}_{J,I}\Omega_{J',I'}(m_{\pi\pi})^{\dagger}\Omega_{J,I}(m_{\pi\pi})\right]\right.\\
&+ \sum_{\lambda_h=\pm1} d^{J'}_{0,-\lambda_h}(\Theta_R) d^{J}_{0,\lambda_h}(\Theta_R) e^{2i\lambda_h\Phi_R}\left[T^{(-\lambda_h,\lambda)}_{J',I'}\Omega_{J',I'}(m_{\pi\pi})\right]^{\dagger} T^{(\lambda_h,\lambda)}_{J,I}\Omega_{J,I}(m_{\pi\pi})\\
&+ \sum_{\lambda_h=\pm1} d^{J'}_{0,0}(\Theta_R) d^{J}_{0,\lambda_h}(\Theta_R) e^{i\lambda_h\Phi_R}\left[T^{(0,\lambda)}_{J',I'}\Omega_{J',I'}(m_{\pi\pi})\right]^{\dagger} T^{(\lambda_h,\lambda)}_{J,I}\Omega_{J,I}(m_{\pi\pi})\\
&\left.+ \sum_{\lambda'_h=\pm1} d^{J'}_{0,\lambda'_h}(\Theta_R) d^{J}_{0,0}(\Theta_R) e^{-i\lambda'_h\Phi_R}\left[T^{(\lambda'_h,\lambda)}_{J',I'}\Omega_{J',I'}(m_{\pi\pi})\right]^{\dagger} T^{(0,\lambda)}_{J,I}\Omega_{J,I}(m_{\pi\pi})\right\}. \qquad (193)
\end{aligned}$$

Combining terms with $(J', I') \leftrightarrow (J, I)$, $\lambda \leftrightarrow -\lambda$, *etc.* and suppressing the arguments of the d-functions and Omnés functions:

$$\begin{aligned}
d\Re_T = \sum_{\lambda=\pm1}\sum_{\lambda_h=-1}^{1} d^{J'}_{0,\lambda_h} d^{J}_{0,\lambda_h} &\left\{\Re\left[T^{(\lambda_h,\lambda)\dagger}_{J',I'}T^{(\lambda_h,\lambda)}_{J,I}\Omega_{J',I'}{}^{\dagger}\Omega_{J,I}\right]\right.\\
&\left.+ (1-\delta_{\lambda_h,0})\cos(2\lambda_h\Phi_R)\,\Re\left[T^{(-\lambda_h,\lambda)\dagger}_{J',I'}T^{(\lambda_h,\lambda)}_{J,I}\Omega_{J',I'}{}^{\dagger}\Omega_{J,I}\right]\right\}\\
+ \sum_{\lambda=\pm1}\sum_{\lambda_h=\pm1} d^{J'}_{0,0} d^{J}_{0,\lambda_h} &\left\{\cos(\lambda_h\Phi_R)\,\Re\left[T^{(0,\lambda)\dagger}_{J',I'}T^{(\lambda_h,\lambda)}_{J,I}\Omega_{J',I'}{}^{\dagger}\Omega_{J,I}\right]\right.\\
&\left.- \sin(\lambda_h\Phi_R)\,\Im\left[T^{(0,\lambda)\dagger}_{J',I'}T^{(\lambda_h,\lambda)}_{J,I}\Omega_{J',I'}{}^{\dagger}\Omega_{J,I}\right]\right\}\\
+ \sum_{\lambda=\pm1}\sum_{\lambda_h=\pm1} d^{J'}_{0,\lambda_h} d^{J}_{0,0} &\left\{\cos(\lambda_h\Phi_R)\,\Re\left[T^{(\lambda_h,\lambda)\dagger}_{J',I'}T^{(0,\lambda)}_{J,I}\Omega_{J',I'}{}^{\dagger}\Omega_{J,I}\right]\right.\\
&\left.- \sin(\lambda_h\Phi_R)\,\Im\left[T^{(\lambda_h,\lambda)\dagger}_{J',I'}T^{(0,\lambda)}_{J,I}\Omega_{J',I'}{}^{\dagger}\Omega_{J,I}\right]\right\}. \qquad (194)
\end{aligned}$$

Notice that terms such as $\left[T'^{\dagger}T\Omega'^{\dagger}\Omega\right]$ should be expanded as *e.g.*,

$$\begin{aligned}\Re\left[T^{(\lambda_h,\lambda)\dagger}_{J',I'}T^{(\lambda_h,\lambda)}_{J,I}\Omega_{J',I'}{}^{\dagger}\Omega_{J,I}\right] &= \Re\left[T^{(\lambda_h,\lambda)\dagger}_{J',I'}T^{(\lambda_h,\lambda)}_{J,I}\right]\Re\left[\Omega_{J',I'}{}^{\dagger}\Omega_{J,I}\right] \\ &\quad - \Im\left[T^{(\lambda_h,\lambda)\dagger}_{J',I'}T^{(\lambda_h,\lambda)}_{J,I}\right]\Im\left[\Omega_{J',I'}{}^{\dagger}\Omega_{J,I}\right], \\ \Im\left[T^{(0,\lambda)\dagger}_{J',I'}T^{(\lambda_h,\lambda)}_{J,I}\Omega_{J',I'}{}^{\dagger}\Omega_{J,I}\right] &= \Re\left[T^{(0,\lambda)\dagger}_{J',I'}T^{(\lambda_h,\lambda)}_{J,I}\right]\Im\left[\Omega_{J',I'}{}^{\dagger}\Omega_{J,I}\right] \\ &\quad + \Im\left[T^{(0,\lambda)\dagger}_{J',I'}T^{(\lambda_h,\lambda)}_{J,I}\right]\Re\left[\Omega_{J',I'}{}^{\dagger}\Omega_{J,I}\right]. \end{aligned} \tag{195}$$

The longitudinal term has a similar form

$$\begin{aligned} d\mathfrak{R}_L &= 2d^{J'}_{0,\lambda'_h}(\Theta_R)d^{J}_{0,\lambda_h}(\Theta_R)e^{i(\lambda_h-\lambda'_h)\Phi_R}\left[T^{(\lambda'_h,0)}_{J',I'}\Omega_{J',I'}(m_{\pi\pi})\right]^{\dagger}\left[T^{(\lambda_h,0)}_{J,I}\Omega_{J,I}(m_{\pi\pi})\right], \\ &= 2\sum_{\lambda_h=-1}^{1} d^{J'}_{0,\lambda_h}d^{J}_{0,\lambda_h}\left[T^{(\lambda_h,0)}_{J',I'}\Omega_{J',I'}\right]^{\dagger}\left[T^{(\lambda_h,0)}_{J,I}\Omega_{J,I}\right] \\ &+ 2\sum_{\lambda_h=\pm1} d^{J'}_{0,-\lambda_h}(\Theta_R)d^{J}_{0,\lambda_h}(\Theta_R)e^{2i\lambda_h\Phi_R}\left[T^{(-\lambda_h,0)}_{J',I'}\Omega_{J',I'}\right]^{\dagger}\left[T^{(\lambda_h,0)}_{J,I}\Omega_{J,I}\right] \\ &+ 2\sum_{\lambda_h=\pm1}\Bigg\{e^{i\lambda_h\Phi_R}d^{J'}_{0,0}d^{J}_{0,\lambda_h}\left[T^{(0,0)}_{J',I'}\Omega_{J',I'}\right]^{\dagger}\left[T^{(\lambda_h,0)}_{J,I}\Omega_{J,I}\right] \\ &\qquad + e^{-i\lambda_h\Phi_R}d^{J'}_{\lambda_h,0}d^{J}_{0,0}\left[T^{(\lambda_h,0)}_{J',I'}\Omega_{J',I'}\right]^{\dagger}\left[T^{(0,0)}_{J,I}\Omega_{J,I}\right]\Bigg\}. \end{aligned} \tag{196}$$

Expanding the sums over λ_h, λ:

$$\begin{aligned} d\mathfrak{R}_L = 2d^{J'}_{0,0}d^{J}_{0,0}&\Bigg\{\Re\left[\left(T^{(0,0)}_{J',I'}\right)^{\dagger}T^{(0,0)}_{J,I}\right]\Re\left[\Omega^{\dagger}_{J',I'}\Omega_{J,I}\right]\Bigg\} \\ &+ 4d^{J'}_{0,1}d^{J}_{0,1}\left[1-\cos\left(2\lambda_h\Phi_R\right)\right]\Re\left\{\left[T^{(1,0)}_{J',I'}\Omega_{J',I'}\right]^{\dagger}\left[T^{(1,0)}_{J,I}\Omega_{J,I}\right]\right\} \\ &\quad + 4d^{J'}_{0,1}d^{J}_{0,0}\sin\left(\Phi_R\right)\Im\left\{\left[T^{(1,0)}_{J',I'}\Omega_{J',I'}\right]^{\dagger}\left[T^{(0,0)}_{J,I}\Omega_{J,I}\right]\right\} \\ &\quad - 4d^{J'}_{0,0}d^{J}_{0,1}\sin\left(\Phi_R\right)\Im\left\{\left[T^{(0,0)}_{J',I'}\Omega_{J',I'}\right]^{\dagger}\left[T^{(1,0)}_{J,I}\Omega_{J,I}\right]\right\}. \end{aligned} \tag{197}$$

Writing out the sum over $J, J' \leq 1$ explicitly:

$$\begin{aligned} d\mathbf{R}_T = 2\left|T^{(0,1)}_{0,0}\right|^2\left|\Omega_{0,0}(m_{\pi\pi})\right|^2 + \left|\Omega_{1,1}(m_{\pi\pi})\right|^2&\Bigg(\left[1+\cos\left(2\Theta_R\right)\right]\left|T^{(0,1)}_{1,1}\right|^2 \\ + \frac{\left[1-\cos\left(2\Theta_R\right)\right]}{2}&\left\{\left|T^{(1,1)}_{1,1}\right|^2 + \left|T^{(1,-1)}_{1,1}\right|^2 + 4\cos\left(2\Phi_R\right)\Re\left[T^{(-1,1)\dagger}_{1,1}T^{(1,1)}_{1,1}\right]\right\}\Bigg) \\ + 4\cos\left(\Theta_R\right)\Re\left[T^{(0,1)\dagger}_{0,0}T^{(0,1)}_{1,1}\Omega^{\dagger}_{0,0}\Omega_{1,1}\right]&. \end{aligned} \tag{198}$$

Converting the angular distribution to linearly independent Legendre Polynomials:

$$\begin{aligned} d\mathfrak{R}_T &= 2\left|T_{0,0}^{(0,1)}\right|^2 |\Omega_{0,0}(m_{\pi\pi})|^2 + \frac{2}{3}\left\{\left|T_{1,1}^{(0,1)}\right|^2 + \left|T_{1,1}^{(1,1)}\right|^2 + \left|T_{1,1}^{(1,-1)}\right|^2\right\} |\Omega_{1,1}(m_{\pi\pi})|^2 \\ &+ \frac{2}{3}\left\{2\left|T_{1,1}^{(0,1)}\right|^2 - \left|T_{1,1}^{(1,1)}\right|^2 - \left|T_{1,1}^{(1,-1)}\right|^2\right\} P_2\left(\cos\Theta_R\right) |\Omega_{1,1}(m_{\pi\pi})|^2 \\ &+ 4\sin^2\Theta_R\cos\left(2\Phi_R\right)\Re\left[T_{1,1}^{(-1,1)\dagger}T_{1,1}^{(1,1)}\right] |\Omega_{1,1}(m_{\pi\pi})|^2 \\ &+ 4\cos\Theta_R\left\{\Re\left[T_{0,0}^{(0,1)\dagger}T_{1,1}^{(0,1)}\right]\Re\left[\Omega_{0,0}^{\dagger}\Omega_{1,1}\right] - \Im\left[T_{0,0}^{(0,1)\dagger}T_{1,1}^{(0,1)}\right]\Im\left[\Omega_{0,0}^{\dagger}\Omega_{1,1}\right]\right\}. \end{aligned} \tag{199}$$

In conclusion, the six linearly independent terms of $d\mathfrak{R}_T$ are the coefficients of:

$$\begin{gathered} |\Omega_{0,0}(m_{\pi\pi})|^2, \qquad |\Omega_{1,1}(m_{\pi\pi})|^2, \qquad |\Omega_{1,1}(m_{\pi\pi})|^2 P_2\left(\cos\Theta_R\right) \\ |\Omega_{1,1}(m_{\pi\pi})|^2 \sin^2\left(\Theta_R\right)\cos\left(2\Phi_R\right), \\ \Re\left[\Omega_{1,1}(m_{\pi\pi})^{\dagger}\Omega_{0,0}(m_{\pi\pi})\right]\cos\left(\Theta_R\right), \qquad \Im\left[\Omega_{1,1}(m_{\pi\pi})^{\dagger}\Omega_{0,0}(m_{\pi\pi})\right]\cos\left(\Theta_R\right). \end{gathered} \tag{200}$$

Similarly,

$$\begin{aligned} d\mathfrak{R}_L &= 2\left|T_{0,0}^{(0,0)}\right|^2 |\Omega_{0,0}|^2 + \left[1+\cos(2\Theta_R)\right]\left|T_{1,1}^{(0,0)}\right|^2 |\Omega_{1,1}|^2 \\ &+ 4\cos\Theta_R\Re\left[T_{0,0}^{(0,0)\dagger}T_{1,1}^{(0,0)}\right]\Re\left[\Omega_{0,0}^{\dagger}\Omega_{1,1}\right] \\ &+ \left[1-\cos(2\Theta_R)\right]\left|T_{1,1}^{(0,0)}\right|^2 |\Omega_{1,1}|^2. \end{aligned} \tag{201}$$

Thus the longitudinal term does not introduce any new Θ_R, Φ_R dependence to the Φ_h-independent part of the cross-section.

B.0.2 THE TT INTERFERENCE TERM

The TT interference term has an important dependence on Φ_h, Θ_R, and Φ_R.

$$\begin{aligned} \epsilon f_{TT}^{\alpha} d\mathfrak{R}_{TT}^{\alpha} &= \sum_{J',I'}\sum_{J,I}\sum_{\lambda'_h=-J'}^{J'}\sum_{\lambda_h=-J}^{J}\sum_{\lambda',\lambda} d_{0,\lambda'_h}^{J'}(\Theta_R)d_{0,\lambda_h}^{J}(\Theta_R)e^{i(\lambda_h-\lambda'_h)\Phi_R}\rho_{TT}(\lambda',\lambda) \\ &\qquad \left[T_{J',I'}^{(\lambda'_h,\lambda')}\Omega_{J',I'}(m_{\pi\pi})\right]^{\dagger}\left[T_{J,I}^{(\lambda_h,\lambda)}\Omega_{J,I}(m_{\pi\pi})\right], \\ &= -\epsilon\sum_{J,J'}\left[\Omega_{J',I'}^{\dagger}\Omega_{J,I}\right]\sum_{\lambda'_h=-J'}^{J}\sum_{\lambda_h+J}^{J} e^{i(\lambda_h-\lambda'_h)\Phi_R}d_{0,\lambda'_h}^{J'}(\Theta_R)d_{0,\lambda_h}^{J}(\Theta_R)\sum_{\lambda'=-\lambda=\mp1} \\ &\qquad \left[T_{J',I'}^{(\lambda'_h,1)\dagger}T_{J,I}^{(\lambda_h,-1)}e^{2i\Phi_h} + T_{J',I'}^{(\lambda'_h,-1)\dagger}T_{J,I}^{(\lambda_h,1)}e^{-2i\Phi_h}\right]. \end{aligned} \tag{202}$$

The complete form of $f_{TT}d\mathfrak{R}_{TT}$ is derived in §B.0.4 and written out in Eq. (252), equivalently Eq. (253). This introduces a total of 15 new linearly-independent terms.

B.0.3 THE TL INTERFERENCE TERM

The TL components of the virtual photon spin density matrix are

$$\rho_{TL}(\lambda,\lambda') = \sqrt{\epsilon(1+\epsilon+2\delta_C)}\left\{-\lambda\delta_{\lambda',0}\left[1-\delta_{\lambda,0}\right]e^{i\lambda\Phi_h} - \lambda'\delta_{\lambda,0}\left[1-\delta_{\lambda',0}\right]e^{-i\lambda'\Phi_h}\right\}. \tag{203}$$

Thus TL interference term has the form $\sqrt{\epsilon(1+\epsilon+2\delta_C)}f^{\alpha}_{TL}d\Re^{\alpha}_{TL}$ with,

$$\begin{aligned}
f^{\alpha}_{TL}d\Re^{\alpha}_{TL} = & \sum_{J',I'}\sum_{J,I}\sum_{\lambda'_h=-J'}^{J'}\sum_{\lambda_h=-J}^{J} d^{J'}_{0,\lambda'_h}(\Theta_R)d^{J}_{0,\lambda_h}(\Theta_R)e^{i(\lambda_h-\lambda'_h)\Phi_R} \\
& \sum_{\lambda',\lambda}\left[T^{(\lambda'_h,\lambda')}_{J',I'}\Omega_{J',I'}(m_{\pi\pi})\right]^{\dagger}\left[T^{(\lambda_h,\lambda)}_{J,I}\Omega_{J,I}(m_{\pi\pi})\right]\frac{\rho_{TL}(\lambda,\lambda')}{\sqrt{\epsilon(1+\epsilon+2\delta_C)}}, \\
= & -\sum_{\substack{J',I'\\J,I}}\sum_{\lambda'_h=-J'}^{J'}\sum_{\lambda_h=-J}^{J} d^{J'}_{0,\lambda'_h}(\Theta_R)d^{J}_{0,\lambda_h}(\Theta_R)e^{i(\lambda_h-\lambda'_h)\Phi_R} \\
& \left\{\sum_{\lambda=\pm1}\lambda e^{i\lambda\Phi_h}\left[T^{(\lambda'_h,0)}_{J',I'}\Omega_{J',I'}(m_{\pi\pi})\right]^{\dagger}\left[T^{(\lambda_h,\lambda)}_{J,I}\Omega_{J,I}(m_{\pi\pi})\right],\right. \\
& \left.+\sum_{\lambda'=\pm1}\lambda' e^{-i\lambda'\Phi_h}\left[T^{(\lambda'_h,\lambda')}_{J',I'}\Omega_{J',I'}(m_{\pi\pi})\right]^{\dagger}\left[T^{(\lambda_h,0)}_{J,I}\Omega_{J,I}(m_{\pi\pi})\right]\right\}.
\end{aligned} \tag{204}$$

There are a total of 13 linearly independent TL terms (see Appendix B.0.4).

$$
\begin{aligned}
f^{\alpha}_{TL} d\Re^{\alpha}_{TL} = & -4\left|\Omega_{0,0}\right|^2 \Re\left[T^{(0,0)\dagger}_{0,0} T^{(0,1)}_{0,0}\right]\cos(\Phi_h) \\
& -4\left|\Omega_{1,1}\right|^2 \cos^2\Theta_R \Re\left[T^{(0,0)\dagger}_{1,1} T^{(0,1)}_{1,1}\right]\cos(\Phi_h)\\
& -4\cos\Theta_R\Big\{\Re\left[\Omega^\dagger_{0,0}\Omega_{1,1}\right]\Re\left[T^{(0,0)\dagger}_{0,0}T^{(0,1)}_{1,1}\right]\\
& \qquad -\Im\left[\Omega^\dagger_{0,0}\Omega_{1,1}\right]\Im\left[T^{(0,0)\dagger}_{0,0}T^{(0,1)}_{1,1}\right]\Big\}\cos\Phi_h\\
& -2\left|\Omega_{1,1}\right|^2\sin^2\Theta_R\Big\{\Re\left[T^{(1,0)\dagger}_{1,1}T^{(1,1)}_{1,1}\right] + \Re\left[T^{(-1,0)\dagger}_{1,1}T^{(-1,1)}_{1,1}\right]\Big\}\cos\Phi_h\\
& +2\left|\Omega_{1,1}\right|^2\sin^2\Theta_R\Big\{\cos\left(2\Phi_R+\Phi_h\right)\Re\left[T^{(-1,0)\dagger}_{1,1}T^{(1,1)}_{1,1}\right]\\
& \qquad -\cos\left(2\Phi_R-\Phi_h\right)\Re\left[T^{(-1,0)\dagger}_{1,1}T^{(1,-1)}_{1,1}\right]\Big\}\\
& +4\left|\Omega_{1,1}\right|^2\frac{\sin(2\Theta_R)}{2\sqrt{2}}\Big(\cos(\Phi_R+\Phi_h)\Re\left[T^{(0,0)\dagger}_{1,1}T^{(1,1)}_{1,1} - T^{(0,-1)\dagger}_{1,1}T^{(1,0)}_{1,1}\right]\\
& \qquad +\cos(\Phi_R-\Phi_h)\Re\left[T^{(0,1)\dagger}_{1,1}T^{(1,0)}_{1,1} - T^{(0,0)\dagger}_{1,1}T^{(1,-1)}_{1,1}\right]\Big)\\
& +2\sqrt{2}\sin\Theta_R\Big\{\\
& \qquad \cos(\Phi_h-\Phi_R)\Re\left[\Omega^\dagger_{1,1}\Omega_{0,0}\right]\Re\left[T^{(1,1)\dagger}_{1,1}T^{(0,0)}_{0,0} - T^{(1,0)\dagger}_{1,1}T^{(0,1)}_{0,0}\right]\\
& \qquad -\cos(\Phi_h-\Phi_R)\Im\left[\Omega^\dagger_{1,1}\Omega_{0,0}\right]\Im\left[T^{(1,1)\dagger}_{1,1}T^{(0,0)}_{0,0} - T^{(1,0)\dagger}_{1,1}T^{(0,1)}_{0,0}\right]\\
& \qquad +\cos(\Phi_h+\Phi_R)\Re\left[\Omega^\dagger_{1,1}\Omega_{0,0}\right]\Re\left[T^{(1,0)\dagger}_{1,1}T^{(0,-1)}_{0,0} - T^{(1,1)\dagger}_{1,1}T^{(0,0)}_{0,0}\right]\\
& \qquad -\cos(\Phi_h+\Phi_R)\Im\left[\Omega^\dagger_{1,1}\Omega_{0,0}\right]\Im\left[T^{(1,0)\dagger}_{1,1}T^{(0,-1)}_{0,0} - T^{(1,1)\dagger}_{1,1}T^{(0,0)}_{0,0}\right]\Big\}.
\end{aligned} \tag{205}
$$

Coordinate Systems

Given the initial four vectors k^μ, P^μ of the electron and proton, respectively, we define several sets of coordinate systems to describe the kinematics of the $ep \to ep\pi\pi$ reaction. I will proceed in a completely general way, without explicit reference to either the proton rest frame or a head-on ep collision frame.

Start with the following detector frame four-vectors

$$
X^{0,1,2,3}_{\text{Det}} = [0,1,0,0]\,,\; Y^{0,1,2,3}_{\text{Det}} = [0,0,1,0]\,,\; Z^{0,1,2,3}_{\text{Det}} = [0,0,0,1]\,,\; T^{0,1,2,3}_{\text{Det}} = [1,0,0,0]\,. \tag{206}
$$

Then $X_{\text{Det}}\cdot X_{\text{Det}} = -1 = Y_{\text{Det}}\cdot Y_{\text{Det}} = Z_{\text{Det}}\cdot Z_{\text{Det}}$ Also, this is a four-dimensional right-handed coordinate system with:

$$\epsilon_{\mu\nu\rho\delta} T^{\mu}_{\mathrm{Det}} X^{\nu}_{\mathrm{Det}} Y^{\rho}_{\mathrm{Det}} Z^{\sigma}_{\mathrm{Det}} = 1, \tag{207}$$

provided the original unit 3-vectors satisfy $(\hat{x} \wedge \hat{y}) \cdot \hat{z} = 1$. I assume the beams are approximately parallel or antiparallel to Z^{i}_{Det} with the electron beam approximately in the $-Z^{i}_{\mathrm{Det}}$ direction, and Y^{i}_{Det} is up in the laboratory.

The electron plus proton coordinate system

Define a pair of light cone vectors which will define a coordinate system in which the electron and proton are head-ons:

$$\begin{aligned} n(e)^{\mu} &= \left[k^{\mu} - \frac{m_e^2}{k \cdot P} \frac{1}{\left(1 + \sqrt{1 - \delta_e}\right)} P^{\mu} \right] \frac{M/(k \cdot P)}{\sqrt{2(1 - \delta_e)}}, \qquad \text{with } \delta_e = \frac{m_e^2 M^2}{(k \cdot P)^2} \ll 1; \\ \widetilde{n}(e)^{\mu} &= \left[-k^{\mu} + \frac{k \cdot P}{M^2} \left(1 + \sqrt{1 - \delta_e}\right) P^{\mu} \right] \frac{M/(k \cdot P)}{\sqrt{2(1 - \delta_e)}}, \\ n \cdot \widetilde{n} &= 1, \qquad n^2 = 0 = \widetilde{n}^2. \end{aligned} \tag{208}$$

In the limit $m_e \to 0$

$$n(e)^{\mu} \to k^{\mu} \frac{M}{(k \cdot P)\sqrt{2}}, \qquad \widetilde{n}(e)^{\mu} \to P^{\mu} \frac{\sqrt{2}}{M} - k^{\mu} \frac{M}{(k \cdot P)\sqrt{2}}. \tag{209}$$

In addition to the ultrarelativistic limit, if $\mathbf{k}$ is exactly in the $-\hat{z}$ direction and the target is at rest then

$$n(e)^{0123} \to \frac{1}{\sqrt{2}} \left[1, 0, 0, -1\right], \qquad \widetilde{n}(e)^{0123} \to \frac{1}{\sqrt{2}} \left[1, 0, 0, 1\right]. \tag{210}$$

The lightcone components of k and P are in general:

$$\begin{aligned} k \cdot n(e) &= m_e^2 \frac{M}{(k \cdot P)} \frac{1}{\left(1 + \sqrt{1 - \delta_e}\right) \sqrt{2}}, \\ k \cdot \widetilde{n}(e) &= \frac{(k \cdot P)}{M} \frac{\left(1 + \sqrt{1 - \delta_e}\right)}{\sqrt{2}}, \\ P \cdot n(e) &= \frac{M}{\sqrt{2}} = P \cdot \widetilde{n}(e). \end{aligned} \tag{211}$$

Generating the Scattered Electron

In order to properly generate the azimuthal variation of the scattered electron, we define the followings:

$$\begin{aligned}
X(e)^\mu &= \frac{X^\mu_{\text{Det}} - [X_{\text{Det}}\cdot n(e)]\widetilde{n}(e)^\mu - [X_{\text{Det}}\cdot \widetilde{n}(e)]n(e)^\mu}{1+2[X_{\text{Det}}\cdot n(e)][X_{\text{Det}}\cdot \widetilde{n}(e)]}, \\
Y(e)_\alpha &= \epsilon_{\alpha\beta\gamma\delta}X(e)^\beta n(e)^\gamma \widetilde{n}(e)^\delta, \qquad \text{with } \epsilon_{0123}=1, \\
X(e)^2 &= -1 = Y(e)^2.
\end{aligned} \tag{212}$$

The scattered electron four vector is

$$k'^\mu = [k'\cdot n(e)]\widetilde{n}(e)^\mu + [k'\cdot \widetilde{n}(e)]n(e)^\nu + \sqrt{|\mathbf{k}|^2_\perp}\left[\cos\phi_e X(e)^\mu + \sin\phi_e Y(e)^\mu\right]. \tag{213}$$

This provides a Lorentz-invariant definition of the electron azimuthal angle ϕ_e. In a collider with a crossing angle, ϕ_e is not a simple azimuth around the electron beam in the detector coordinate system. The coefficients $k'\cdot n(e)$ and $k'\cdot \widetilde{n}(e)$ are determined from any choice of the pairs

$$(Q^2, x_B), \qquad (Q^2, y = q\cdot P/k\cdot P), \qquad (x_B, y). \tag{214}$$

Specifically:

$$\begin{aligned}
\mathbf{k}'^2_\perp &= 2[k'\cdot n(e)]\,[k'\cdot \widetilde{n}(e)] - m_e^2, \\
k'\cdot n(e) &= \frac{x_B y M}{\sqrt{2(1-\delta_e)}} + \frac{m_e^2 M}{(k\cdot P)\sqrt{2}}\left(\frac{1+y/\sqrt{1-\delta_e}}{1+\sqrt{1-\delta_e}}\right), \\
k'\cdot \widetilde{n}(e) &= \frac{2(k\cdot P)\,(1-y)}{M\sqrt{2}} - k'\cdot n(e).
\end{aligned} \tag{215}$$

The Virtual Photon plus Proton Coordinate System

Define the first lightcone vectors for the virtual photon + proton system:

$$\begin{aligned}
n(q)^\mu &= \alpha\left[q^\mu - \frac{q\cdot P}{M^2}\left(1-\sqrt{1+\delta_Q}\right)P^\mu\right] = \alpha\left[q^\mu + \frac{Q^2}{q\cdot P}\frac{1}{\left(1+\sqrt{1+\delta_Q}\right)}P^\mu\right], \\
\widetilde{n}(q)^\mu &= \widetilde{\alpha}\left[-q^\mu + \frac{q\cdot P}{M^2}\left(1+\sqrt{1+\delta_Q}\right)P^\mu\right], \\
&\text{with} \quad \delta_Q = \frac{M^2Q^2}{(q\cdot P)^2} = \frac{4M^2x_B^2}{Q^2} \\
\alpha &= \alpha_0\Lambda, \qquad \widetilde{\alpha} = \frac{\alpha_0}{\Lambda}, \qquad \alpha_0 = \frac{M}{(q\cdot P)\sqrt{2(1+\delta_Q)}}.
\end{aligned} \tag{216}$$

For the $q + P$ CM system:

$$\Lambda^2 = \frac{1 + M^2/(q \cdot P) + \sqrt{1 + \delta_Q}}{1 + M^2/(q \cdot P) - \sqrt{1 + \delta_Q}}, \tag{217}$$

such that

$$\begin{aligned} \frac{1}{\sqrt{2}} \left(P \cdot n(q) + P \cdot \widetilde{n}(q)\right) &= E_p^{\mathrm{CM}} = \frac{W^2 + M^2 + Q^2}{2W}, \\ \frac{1}{\sqrt{2}} \left(q \cdot n(q) - q \cdot \widetilde{n}(q)\right) &= \left|\mathbf{q}^{\mathrm{CM}}\right|. \end{aligned} \tag{218}$$

Now define a transverse space-like unit-vector orthogonal to the scattering hyper-plane

$$\begin{aligned} Y(q)_\alpha &= \epsilon_{\alpha\beta\gamma\delta} P^\beta k^\gamma k'^\delta / \mathcal{N}_Y = \epsilon_{\alpha\beta\gamma\delta} P^\beta q^\gamma K^\delta / (2\mathcal{N}_Y), \\ \mathcal{N}_Y &= \sqrt{2(k \cdot k')(k \cdot P)(k' \cdot P) - M^2 (k \cdot k')^2 - m_e^2 \left[(k \cdot P)^2 + (k' \cdot P)^2 - M^2 m_e^2\right]}, \\ &= (k \cdot P) \sqrt{Q^2 \left[1 - y - \frac{M^2 Q^2}{4(k \cdot P)^2}\right] - m_e^2 y^2 \left[1 + \delta_Q\right]}, \\ Y(q) \cdot Y(q) &= -1. \end{aligned} \tag{219}$$

In the target rest frame, $Y(q)$ simplifies to

$$Y(q)^{[0123]} = \left[0, \frac{\mathbf{k} \times \mathbf{k}'}{|\mathbf{k} \times \mathbf{k}'|}\right]. \tag{220}$$

The final basis vector is

$$\begin{aligned} X(q)_\alpha &= \epsilon_{\alpha\beta\gamma\delta} Y(q)^\beta q^\gamma P^\delta / \mathcal{N}_X, \\ \mathcal{N}_X &= q \cdot P \sqrt{1 + \delta_Q}. \end{aligned} \tag{221}$$

We can also define time-like and space-like longitudinal vectors:

$$\begin{aligned} T(q)^\mu &= \frac{1}{\sqrt{2}} \left[n(q)^\mu + \widetilde{n}(q)^\mu\right], \\ Z(q)^\mu &= \frac{1}{\sqrt{2}} \left[n(q)^\mu - \widetilde{n}(q)^\mu\right], \end{aligned} \tag{222}$$

such that $T^2 = 1$ and $Z^2 = -1$. The overall sign conventions are chosen such that

$$\epsilon_{\mu\nu\rho\sigma} T^\mu X^\nu Y^\rho Z^\sigma = 1, \tag{223}$$

which generalizes the concept of a right-handed coordinate system into Minkowski space. The coordinate system is also consistent with the Trento convention for the kinematics of SIDIS and DVES processes [46].

Hadron Production Coordinate System

If the four-momentum of the hadronic system (*e.g.*, $h = \pi\pi$) is denoted by $P(h)^\mu$, then the Lorentz invariant definition of the azimuth Φ_h is

$$\Phi_h = \tan^{-1}\left(\frac{-Y(q)\cdot P(h)}{-X(q)\cdot P(h)}\right). \tag{224}$$

More explicity:

$$\begin{aligned}\cos(\Phi_h) &= \frac{-X(q)\cdot P(h)}{\sqrt{[X(q)\cdot P(h)]^2 + [Y(q)\cdot P(h)]^2}},\\ \sin(\Phi_h) &= \frac{-Y(q)\cdot P(h)}{\sqrt{[X(q)\cdot P(h)]^2 + [Y(q)\cdot P(h)]^2}}.\end{aligned} \tag{225}$$

In order to describe the decay of the mesonic system, we introduce an additional covariant coordinate system, which generalizes the concept of the final state meson plus nucleon CM system. We start with the four-vector orthogonal to P^μ, P_h^μ, and q^μ:

$$Y(h)_\alpha = \epsilon_{\alpha\beta\gamma\delta}q^\beta P^\gamma P_h^\delta. \tag{226}$$

Hadron Decay Angular Variables

In order to describe the decay of the mesonic system, we introduce an additional covariant coordinate system, which generalizes the concept of the final state meson plus nucleon CM system. We start with the four-vector orthogonal to P^μ, P_h^μ, and q^μ:

$$Y(h)_\alpha = \epsilon_{\alpha\beta\gamma\delta}q^\beta P^\gamma P_h^\delta. \tag{227}$$

B.0.4 PHOTON POLARIZATION VECTORS

For virtual photon helicity $\lambda = \pm 1$, the photon polarization four-vectors are:

$$\epsilon(\lambda)^\mu = \frac{-\lambda}{\sqrt{2}}\left[X(q)^\mu + i\lambda Y(q)^\mu\right]. \tag{228}$$

In the Lorentz Gauge $\partial_\mu A^\mu = 0$, the longitudinal polarization vector satisfies:

$$\begin{aligned}&q\cdot\epsilon(0) = 0, \qquad \epsilon(0)^2 = 1,\\ &\epsilon(0)^\mu = \frac{1}{\sqrt{Q^2(1+\delta_Q)}}\left[q^\mu + \frac{Q^2}{(q\cdot P)}P^\mu\right] \qquad \text{with} \quad \delta_Q = \frac{Q^2M^2}{(q\cdot P)^2}.\end{aligned} \tag{229}$$

In the target rest frame, this reduces to

$$[\epsilon(0)^\mu]_{\text{Rest}} = \frac{1}{\sqrt{Q^2(1+\delta_Q)}}\left[\frac{\mathbf{q}^2}{\nu}, \mathbf{q}\right], = \frac{1}{\sqrt{Q^2}}\left[|\mathbf{q}|\,, \hat{q}\nu\right]. \tag{230}$$

Wigner d-functions

The lowest-order Wigner d-functions of interest here are

$$
\begin{aligned}
d^0_{0,0} &= 1, \\
d^1_{0,0} &= \cos(\theta), \qquad d^1_{0,\pm 1} = \pm \frac{1}{\sqrt{2}} \sin\theta, \\
d^1_{1,\pm 1} &= \frac{1}{2}\left[1 \pm \cos\theta\right].
\end{aligned} \tag{231}
$$

The d-functions have orthogonality

$$
\int_0^{\pi} \sin\beta d\beta d^J_{m',m}(\beta)^* d^{J'}_{m',m}(\beta) = \frac{2}{2J+1}\delta_{J,J'}. \tag{232}
$$

Hadron Tensor Φ_h-Dependence

We provide here additional details on the decomposition of the Hadron Tensor.

The $d\Re_{TL}$ Interference Term

The TL interference term is

$$
\begin{aligned}
f^{\alpha}_{TL} d\Re^{\alpha}_{TL} = &- \sum_{\substack{J',I' \\ J,I}} \sum_{\lambda'_h=-J'}^{J'} \sum_{\lambda_h=-J}^{J} d^{J'}_{0,\lambda'_h}(\Theta_R) d^{J}_{0,\lambda_h}(\Theta_R) e^{i(\lambda_h-\lambda'_h)\Phi_R} \\
&\left\{ \sum_{\lambda=\pm 1} \lambda e^{i\lambda\Phi_h} \left[T^{(\lambda'_h,0)}_{J',I'} \Omega_{J',I'}(m_{\pi\pi})\right]^{\dagger} \left[T^{(\lambda_h,\lambda)}_{J,I} \Omega_{J,I}(m_{\pi\pi})\right] \right. \\
&\left. + \sum_{\lambda'=\pm 1} \lambda' e^{-i\lambda'\Phi_h} \left[T^{(\lambda'_h,\lambda')}_{J',I'} \Omega_{J',I'}(m_{\pi\pi})\right]^{\dagger} \left[T^{(\lambda_h,0)}_{J,I} \Omega_{J,I}(m_{\pi\pi})\right] \right\}.
\end{aligned} \tag{233}
$$

Restricting (J, I) to just $(0, 0)$ and $(1, 1)$ channels, and grouping the terms according to $(\lambda'_h, \lambda_h) = (0, 0)$, $(\pm 1, \pm 1)$, $(\mp 1, \pm 1)$, $(0, \pm 1) \oplus (\pm 1, 0)$

$$
\begin{aligned}
f_{TL}(\Phi_h) d\Re^{(0,0)}_{TL} = &-4\left|\Omega_{0,0}\right|^2 \Re\left[T^{(0,0)\dagger}_{0,0} T^{(0,1)}_{0,0}\right] \cos(\Phi_h) \\
&- 4\left|\Omega_{1,1}\right|^2 \cos^2\Theta_R \Re\left[T^{(0,0)\dagger}_{1,1} T^{(0,1)}_{1,1}\right] \cos(\Phi_h) \\
&- 4\cos\Theta_R \left\{ \Re\left[\Omega^{\dagger}_{0,0}\Omega_{1,1}\right] \Re\left[T^{(0,0)\dagger}_{0,0} T^{(0,1)}_{1,1}\right] \right. \\
&\left. - \Im\left[\Omega^{\dagger}_{0,0}\Omega_{1,1}\right] \Im\left[T^{(0,0)\dagger}_{0,0} T^{(0,1)}_{1,1}\right] \right\} \cos\Phi_h,
\end{aligned} \tag{234}
$$

$$\begin{aligned}
f_{TL} d\mathcal{R}_{TL}^{(\pm,\pm)} &= -\left|\Omega_{1,1}\right|^2 \frac{\sin^2\Theta_R}{2} \sum_{\lambda_h'=\lambda_h=\pm1} \Bigg\{ \left[T_{1,1}^{(\lambda_h,0)\dagger} T_{1,1}^{(\lambda_h,1)}\right] e^{i\Phi_h} - \left[T_{1,1}^{(\lambda_h,0)\dagger} T_{1,1}^{(\lambda_h,-1)}\right] e^{-i\Phi_h} \\
&\qquad + \left[T_{1,1}^{(\lambda_h,1)\dagger} T_{1,1}^{(\lambda_h,0)}\right] e^{-i\Phi_h} - \left[T_{1,1}^{(\lambda_h,-1)\dagger} T_{1,1}^{(\lambda_h,0)}\right] e^{i\Phi_h} \Bigg\} \\
&= -\left|\Omega_{1,1}\right|^2 \sin^2\Theta_R \sum_{\lambda_h'=\lambda_h=\pm1} \Bigg\{ \Re\left[T_{1,1}^{(\lambda_h,0)\dagger} T_{1,1}^{(\lambda_h,1)}\right] - \Re\left[T_{1,1}^{(\lambda_h,0)\dagger} T_{1,1}^{(\lambda_h,-1)}\right] \Bigg\} \cos\Phi_h \\
&= -2\left|\Omega_{1,1}\right|^2 \sin^2\Theta_R \Bigg\{ \Re\left[T_{1,1}^{(1,0)\dagger} T_{1,1}^{(1,1)}\right] + \Re\left[T_{1,1}^{(-1,0)\dagger} T_{1,1}^{(-1,1)}\right] \Bigg\} \cos\Phi_h,
\end{aligned} \tag{235}$$

$$\begin{aligned}
f_{TL}(\Phi_h) d\mathcal{R}_{TL}^{(\mp,\pm)} &= \left|\Omega_{1,1}\right|^2 \frac{\sin^2\Theta_R}{2} \sum_{-\lambda_h'=\lambda_h}^{\pm1} e^{2i\lambda_h\Phi_R} \Bigg\{ \left[T_{1,1}^{(-\lambda_h,0)\dagger} T_{1,1}^{(\lambda_h,1)}\right] e^{i\Phi_h} \\
&\qquad - \left[T_{1,1}^{(-\lambda_h,0)\dagger} T_{1,1}^{(\lambda_h,-1)}\right] e^{-i\Phi_h} \\
&\qquad + \left[T_{1,1}^{(-\lambda_h,1)\dagger} T_{1,1}^{(\lambda_h,0)}\right] e^{-i\Phi_h} - \left[T_{1,1}^{(-\lambda_h,-1)\dagger} T_{1,1}^{(\lambda_h,0)}\right] e^{i\Phi_h} \Bigg\} \\
&= \left|\Omega_{1,1}\right|^2 \sin^2\Theta_R \sum_{\lambda_h}^{\pm1} e^{2i\lambda_h\Phi_R} \Bigg\{ \Re\left[T_{1,1}^{(-\lambda_h,0)\dagger} T_{1,1}^{(\lambda_h,1)}\right] e^{i\Phi_h} \\
&\qquad - \Re\left[T_{1,1}^{(-\lambda_h,0)\dagger} T_{1,1}^{(\lambda_h,-1)}\right] e^{-i\Phi_h} \Bigg\} \\
&= \left|\Omega_{1,1}\right|^2 \sin^2\Theta_R \Bigg\{ e^{2i\Phi_R} \left(e^{i\Phi_h} \Re\left[T_{1,1}^{(-1,0)\dagger} T_{1,1}^{(1,1)}\right] - e^{-i\Phi_h} \Re\left[T_{1,1}^{(-1,0)\dagger} T_{1,1}^{(1,-1)}\right] \right) \\
&\qquad e^{-2i\Phi_R} \left(e^{i\Phi_h} \Re\left[T_{1,1}^{(1,0)\dagger} T_{1,1}^{(-1,1)}\right] - e^{-i\Phi_h} \Re\left[T_{1,1}^{(1,0)\dagger} T_{1,1}^{(-1,-1)}\right] \right) \Bigg\} \\
&= 2\left|\Omega_{1,1}\right|^2 \sin^2\Theta_R \Bigg\{ \cos\left(2\Phi_R + \Phi_h\right) \Re\left[T_{1,1}^{(-1,0)\dagger} T_{1,1}^{(1,1)}\right] \\
&\qquad - \cos\left(2\Phi_R - \Phi_h\right) \Re\left[T_{1,1}^{(-1,0)\dagger} T_{1,1}^{(1,-1)}\right] \Bigg\}.
\end{aligned} \tag{236}$$

Consider next the $|\Omega_{1,1}|^2$ terms of $(0,\pm) \oplus (\pm,0)$:

$$\begin{aligned}
f_{TL} d\mathcal{R}_{TL(1,1)}^{(0,\pm)\oplus(\pm,0)} &= \left|\Omega_{1,1}\right|^2 \frac{\sin(2\Theta_R)}{2\sqrt{2}} \Bigg(\sum_{\lambda_h}^{\pm1} \lambda_h e^{i\lambda_h\Phi_R} \Bigg\{ \\
&\qquad \sum_{\lambda}^{\pm1} \lambda e^{i\lambda\Phi_h} T_{1,1}^{(0,0)\dagger} T_{1,1}^{(\lambda_h,\lambda)} + \sum_{\lambda'}^{\pm1} \lambda' e^{-i\lambda'\Phi_h} T_{1,1}^{(0,\lambda')\dagger} T_{1,1}^{(\lambda_h,0)} \Bigg\} \\
&\quad + \sum_{\lambda_h'}^{\pm1} \lambda_h' e^{-i\lambda_h'\Phi_R} \Bigg\{ \\
&\qquad \sum_{\lambda}^{\pm1} \lambda e^{i\lambda\Phi_h} T_{1,1}^{(\lambda_h',0)\dagger} T_{1,1}^{(0,\lambda)} + \sum_{\lambda'}^{\pm1} \lambda' e^{-i\lambda'\Phi_h} T_{1,1}^{(\lambda_h',\lambda')\dagger} T_{1,1}^{(0,0)} \Bigg\} \Bigg).
\end{aligned} \tag{237}$$

Expanding the summations:

$$\begin{aligned} f_{TL} d\mathcal{R}_{TL(1,1)}^{(0,\pm)\oplus(\pm,0)} = |\Omega_{1,1}|^2 \frac{\sin(2\Theta_R)}{2\sqrt{2}} \Bigg(& e^{i\Phi_R} \Bigg\{ e^{i\Phi_h} T_{1,1}^{(0,0)\dagger} T_{1,1}^{(1,1)} - e^{-i\Phi_h} T_{1,1}^{(0,0)\dagger} T_{1,1}^{(1,-1)} \\ & \qquad + e^{-i\Phi_h} T_{1,1}^{(0,1)\dagger} T_{1,1}^{(1,0)} - e^{i\Phi_h} T_{1,1}^{(0,-1)\dagger} T_{1,1}^{(1,0)} \Bigg\} \\ & - e^{-i\Phi_R} \Bigg\{ e^{i\Phi_h} T_{1,1}^{(0,0)\dagger} T_{1,1}^{(-1,1)} - e^{-i\Phi_h} T_{1,1}^{(0,0)\dagger} T_{1,1}^{(-1,-1)} \\ & \qquad + e^{-i\Phi_h} T_{1,1}^{(0,1)\dagger} T_{1,1}^{(-1,0)} - e^{i\Phi_h} T_{1,1}^{(0,-1)\dagger} T_{1,1}^{(-1,0)} \Bigg\} \\ & + e^{-i\Phi_R} \Bigg\{ e^{i\Phi_h} T_{1,1}^{(1,0)\dagger} T_{1,1}^{(0,1)} - e^{-i\Phi_h} T_{1,1}^{(1,0)\dagger} T_{1,1}^{(0,-1)} \\ & \qquad + e^{-i\Phi_h} T_{1,1}^{(1,1)\dagger} T_{1,1}^{(0,0)} - e^{i\Phi_h} T_{1,1}^{(1,-1)\dagger} T_{1,1}^{(0,0)} \Bigg\} \\ & - e^{i\Phi_R} \Bigg\{ e^{i\Phi_h} T_{1,1}^{(-1,0)\dagger} T_{1,1}^{(0,1)} - e^{-i\Phi_h} T_{1,1}^{(-1,0)\dagger} T_{1,1}^{(0,-1)} \\ & \qquad + e^{-i\Phi_h} T_{1,1}^{(-1,1)\dagger} T_{1,1}^{(0,0)} - e^{i\Phi_h} T_{1,1}^{(-1,-1)\dagger} T_{1,1}^{(0,0)} \Bigg\} \Bigg). \end{aligned} \tag{238}$$

Combining terms:

$$\begin{aligned} f_{TL} d\mathcal{R}_{TL(1,1)}^{(0,\pm)\oplus(\pm,0)} = 4\,|\Omega_{1,1}|^2 \frac{\sin(2\Theta_R)}{2\sqrt{2}} \Bigg(& \cos(\Phi_R + \Phi_h) \Re \left[T_{1,1}^{(0,0)\dagger} T_{1,1}^{(1,1)} - T_{1,1}^{(0,-1)\dagger} T_{1,1}^{(1,0)} \right] \\ & + \cos(\Phi_R - \Phi_h) \Re \left[T_{1,1}^{(0,1)\dagger} T_{1,1}^{(1,0)} - T_{1,1}^{(0,0)\dagger} T_{1,1}^{(1,-1)} \right] \Bigg). \end{aligned} \tag{239}$$

There are also the interference terms between $(J, I) = (0,0)$ and $(1,1)$:

$$\begin{aligned} f_{TL} d\mathcal{R}_{TL}^{(0,\pm)\oplus(\pm,0)}(0,1) = -\Omega_{1,1}^{\dagger} \Omega_{0,0} \sum_{\lambda'_h}^{\pm 1} d_{0,\lambda'_h}^{1} d_{0,0}^{0} e^{-i\lambda'_h \Phi_R} & \Bigg\{ \\ & \sum_{\lambda}^{\pm 1} \lambda e^{i\lambda\Phi_h} \left[T_{1,1}^{(\lambda'_h,0)\dagger} T_{0,0}^{(0,\lambda)} \right] + \sum_{\lambda'}^{\pm 1} \lambda' e^{-i\lambda'\Phi_h} \left[T_{1,1}^{(\lambda'_h,\lambda')\dagger} T_{0,0}^{(0,0)} \right] \Bigg\} \\ - \Omega_{0,0}^{\dagger} \Omega_{1,1} \sum_{\lambda_h}^{\pm 1} d_{0,0}^{0} d_{0,\lambda}^{1} e^{i\lambda_h \Phi_R} & \Bigg\{ \\ & \sum_{\lambda}^{\pm 1} \lambda e^{i\lambda\Phi_h} \left[T_{0,0}^{(0,0)\dagger} T_{1,1}^{(\lambda_h,\lambda)} \right] + \sum_{\lambda'}^{\pm 1} \lambda' e^{-i\lambda'\Phi_h} \left[T_{0,0}^{(0,\lambda')\dagger} T_{1,1}^{(\lambda_h,0} \right] \Bigg\}. \end{aligned} \tag{240}$$

Expanding terms:

$$\begin{aligned}
f_{TL} d\mathfrak{R}^{(0,\pm)\oplus(\pm,0)}_{TL\,0,0,1,1} = {}& -\Omega^{\dagger}_{1,1}\Omega_{0,0}\frac{\sin\Theta_R}{\sqrt{2}}\Bigg(e^{-i\Phi_R}\Bigg\{e^{i\Phi_h}\left[T^{(1,0)\dagger}_{1,1}T^{(0,1)}_{0,0}\right] - e^{-i\Phi_h}\left[T^{(1,0)\dagger}_{1,1}T^{(0,-1)}_{0,0}\right] \\
& + e^{-i\Phi_h}\left[T^{(1,1)\dagger}_{1,1}T^{(0,0)}_{0,0}\right] - e^{i\Phi_h}\left[T^{(1,-1)\dagger}_{1,1}T^{(0,0)}_{0,0}\right]\Bigg\} \\
& - e^{i\Phi_R}\Bigg\{e^{i\Phi_h}\left[T^{(-1,0)\dagger}_{1,1}T^{(0,1)}_{0,0}\right] - e^{-i\Phi_h}\left[T^{(-1,0)\dagger}_{1,1}T^{(0,-1)}_{0,0}\right] \\
& + e^{-i\Phi_h}\left[T^{(-1,1)\dagger}_{1,1}T^{(0,0)}_{0,0}\right] - e^{i\Phi_h}\left[T^{(-1,-1)\dagger}_{1,1}T^{(0,0)}_{0,0}\right]\Bigg\}\Bigg) \\
& - \Omega^{\dagger}_{0,0}\Omega_{1,1}\frac{\sin\Theta_R}{\sqrt{2}}\Bigg(e^{i\Phi_R}\Bigg\{e^{i\Phi_h}\left[T^{(0,0)\dagger}_{0,0}T^{(1,1)}_{1,1}\right] - e^{-i\Phi_h}\left[T^{(0,0)\dagger}_{0,0}T^{(1,-1)}_{1,1}\right] \\
& + e^{-i\Phi_h}\left[T^{(0,1)\dagger}_{0,0}T^{(1,0)}_{1,1}\right] - e^{i\Phi_h}\left[T^{(0,-1)\dagger}_{0,0}T^{(1,0)}_{1,1}\right]\Bigg\} \\
& - e^{-i\Phi_R}\Bigg\{e^{i\Phi_h}\left[T^{(0,0)\dagger}_{0,0}T^{(-1,1)}_{1,1}\right] - e^{-i\Phi_h}\left[T^{(0,0)\dagger}_{0,0}T^{(-1,-1)}_{1,1}\right] \\
& + e^{-i\Phi_h}\left[T^{(0,1)\dagger}_{0,0}T^{(-1,0)}_{1,1}\right] - e^{i\Phi_h}\left[T^{(0,-1)\dagger}_{0,0}T^{(-1,0)}_{1,1}\right]\Bigg\}\Bigg). \qquad (241)
\end{aligned}$$

Applying parity symmetry and combining terms:

$$\begin{aligned}
f_{TL} d\mathfrak{R}^{(0,\pm)\oplus(\pm,0)}_{TL\,(0,0)(1,1)} = {}& -\Omega^{\dagger}_{1,1}\Omega_{0,0}\frac{\sin\Theta_R}{\sqrt{2}}\Bigg\{2\cos(\Phi_h - \Phi_R)\left(\left[T^{(1,0)\dagger}_{1,1}T^{(0,1)}_{0,0}\right] - \left[T^{(1,-1)\dagger}_{1,1}\right]\left[T^{(0,0)\dagger}_{0,0}\right]\right) \\
& - 2\cos(\Phi_h + \Phi_R)\left(\left[T^{(1,0)\dagger}_{1,1}T^{(0,-1)}_{0,0}\right] - \left[T^{(1,1)\dagger}_{1,1}T^{(0,0)}_{0,0}\right]\right)\Bigg\} \\
& - \Omega^{\dagger}_{0,0}\Omega_{1,1}\frac{\sin\Theta_R}{\sqrt{2}}\Bigg\{2\cos(\Phi_h + \Phi_R)\left(\left[T^{(0,0)\dagger}_{0,0}T^{(1,1)}_{1,1}\right] - \left[T^{(0,-1)\dagger}_{0,0}T^{(1,0)}_{1,1}\right]\right) \\
& - 2\cos(\Phi_h - \Phi_R)\left(\left[T^{(0,0)\dagger}_{0,0}T^{(1,-1)}_{1,1}\right] - \left[T^{(0,1)\dagger}_{0,0}T^{(1,0)}_{1,1}\right]\right)\Bigg\}. \qquad (242)
\end{aligned}$$

Combining complex conjugate terms:

$$\begin{aligned}
f_{TL} d\Re^{(0,\pm)\oplus(\pm,0)}_{TL\,(0,0)(1,1)} &= 2\sqrt{2}\sin\Theta_R \Bigg\{ \cos(\Phi_h - \Phi_R) \Re\left[\Omega^\dagger_{1,1}\Omega_{0,0}\left(T^{(1,1)\dagger}_{1,1} T^{(0,0)}_{0,0} - T^{(1,0)\dagger}_{1,1} T^{(0,1)}_{0,0}\right)\right] \\
&\qquad + \cos(\Phi_h + \Phi_R) \Re\left[\Omega^\dagger_{1,1}\Omega_{0,0}\left(T^{(1,0)\dagger}_{1,1} T^{(0,-1)}_{0,0} - T^{(1,1)\dagger}_{1,1} T^{(0,0)}_{0,0}\right)\right] \Bigg\} \\
&= 2\sqrt{2}\sin\Theta_R \Bigg\{ \\
&\qquad \cos(\Phi_h - \Phi_R) \Re\left[\Omega^\dagger_{1,1}\Omega_{0,0}\right] \Re\left[T^{(1,1)\dagger}_{1,1} T^{(0,0)}_{0,0} - T^{(1,0)\dagger}_{1,1} T^{(0,1)}_{0,0}\right] \\
&\qquad - \cos(\Phi_h - \Phi_R) \Im\left[\Omega^\dagger_{1,1}\Omega_{0,0}\right] \Im\left[T^{(1,1)\dagger}_{1,1} T^{(0,0)}_{0,0} - T^{(1,0)\dagger}_{1,1} T^{(0,1)}_{0,0}\right] \\
&\qquad + \cos(\Phi_h + \Phi_R) \Re\left[\Omega^\dagger_{1,1}\Omega_{0,0}\right] \Re\left[T^{(1,0)\dagger}_{1,1} T^{(0,-1)}_{0,0} - T^{(1,1)\dagger}_{1,1} T^{(0,0)}_{0,0}\right] \\
&\qquad - \cos(\Phi_h + \Phi_R) \Im\left[\Omega^\dagger_{1,1}\Omega_{0,0}\right] \Im\left[T^{(1,0)\dagger}_{1,1} T^{(0,-1)}_{0,0} - T^{(1,1)\dagger}_{1,1} T^{(0,0)}_{0,0}\right] \Bigg\}. \qquad (243)
\end{aligned}$$

In total, the TL contribution to the cross-section contributes 13 linearly independent terms

The $d\Re_{TT}$ Interference Term

$$\begin{aligned}
\epsilon f_{TT}(\Phi_h) d\Re_{TT} &= \sum_{J',I'}\sum_{J,I}\sum_{\lambda'_h=-J'}^{J'}\sum_{\lambda_h=-J}^{J}\sum_{\lambda'=-\lambda=\mp 1} d^{J'}_{0,\lambda'_h}(\Theta_R) d^{J}_{0,\lambda_h}(\Theta_R) e^{i(\lambda_h-\lambda'_h)\Phi_R}\rho_{TT}(\lambda',\lambda) \\
&\qquad \left[T^{(\lambda'_h,\lambda')}_{J',I'}\Omega_{J',I'}(m_{\pi\pi})\right]^\dagger \left[T^{(\lambda_h,\lambda)}_{J,I}\Omega_{J,I}(m_{\pi\pi})\right]; \\
&= -\epsilon\sum_{J,J'}\left[\Omega^\dagger_{J',I'}\Omega_{J,I}\right]\sum_{\lambda'_h=-J'}^{J}\sum_{\lambda_h+J}^{J} e^{i(\lambda_h-\lambda'_h)\Phi_R} d^{J'}_{0,\lambda'_h}(\Theta_R) d^{J}_{0,\lambda_h}(\Theta_R) \\
&\qquad \left[T^{(\lambda'_h,1)\dagger}_{J',I'} T^{(\lambda_h,-1)}_{J,I} e^{2i\Phi_h} + T^{(\lambda'_h,-1)\dagger}_{J',I'} T^{(\lambda_h,1)}_{J,I} e^{-2i\Phi_h}\right]. \qquad (244)
\end{aligned}$$

Restricting (J, I) to $(0,0)$ and $(1,1)$:

$$\begin{aligned}
f_{TT}(\Phi_h)\mathcal{R}_{TT} = & -4\left|\Omega_{0,0}(m_{\pi\pi})\right|^2 \left\{\Re\left[T_{0,0}^{(0,1)\dagger}T_{0,0}^{0,-1}\right]\cos\left(2\Phi_h\right) - \Im\left[T_{0,0}^{(0,1)\dagger}T_{0,0}^{0,-1}\right]\sin\left(2\Phi_h\right)\right\} \\
& - 4\left|\Omega_{1,1}(m_{\pi\pi})\right|^2 \cos^2\Theta_R \left\{\Re\left[T_{1,1}^{(0,1)\dagger}T_{1,1}^{0,-1}\right]\cos\left(2\Phi_h\right) - \Im\left[T_{1,1}^{(0,1)\dagger}T_{1,1}^{0,-1}\right]\sin\left(2\Phi_h\right)\right\} \\
& - \left|\Omega_{1,1}(m_{\pi\pi})\right|^2 \frac{\sin^2\Theta_R}{2}\left\{\sum_{\lambda'_h=\lambda_h}^{\pm 1}\left[T_{1,1}^{(\lambda_h,1)\dagger}T_{1,1}^{(\lambda_h,-1)}e^{2i\Phi_h} + T_{1,1}^{(\lambda_h,-1)\dagger}T_{1,1}^{(\lambda_h,1)}e^{-2i\Phi_h}\right]\right. \\
& \qquad \left. - \sum_{-\lambda'_h=\lambda_h}^{\pm 1} e^{2i\lambda_h\Phi_R}\left[T_{1,1}^{(-\lambda_h,1)\dagger}T_{1,1}^{(\lambda_h,-1)}e^{2i\Phi_h} + T_{1,1}^{(-\lambda_h,-1)\dagger}T_{1,1}^{(\lambda_h,1)}e^{-2i\Phi_h}\right]\right\} \\
& - \left|\Omega_{1,1}(m_{\pi\pi})\right|^2 \frac{\sin(2\Theta_R)}{2\sqrt{2}}\left\{\sum_{\lambda_h=\pm 1}\lambda_h e^{i\lambda_h\Phi_R}\left[T_{1,1}^{(0,1)\dagger}T_{1,1}^{\lambda_h,-1}e^{2i\Phi_h} + T_{1,1}^{(0,-1)\dagger}T_{1,1}^{\lambda_h,1}e^{-2i\Phi_h}\right]\right. \\
& \qquad \left. + \sum_{\lambda'_h=\pm 1}\lambda'_h e^{-i\lambda'_h\Phi_R}\left[T_{1,1}^{(\lambda'_h,1)\dagger}T_{1,1}^{0,-1}e^{2i\Phi_h} + T_{1,1}^{(\lambda'_h,-1)\dagger}T_{1,1}^{0,1}e^{-2i\Phi_h}\right]\right\} \\
& - \Omega_{0,0}^{\dagger}\Omega_{1,1}\sum_{\lambda_h} d_{0,\lambda_h}^{1} e^{i\lambda_h\Phi_R}\left[T_{0,0}^{(0,1)\dagger}T_{1,1}^{(\lambda_h,-1)}e^{2i\Phi_h} + T_{0,0}^{0,-1)\dagger}T_{1,1}^{(\lambda_h,1)}e^{-2i\Phi_h}\right] \\
& - \Omega_{1,1}^{\dagger}\Omega_{0,0}\sum_{\lambda'_h} d_{0,\lambda'_h}^{1} e^{-i\lambda'_h\Phi_R}\left[T_{1,1}^{(\lambda'_h,1)\dagger}T_{0,0}^{(0,-1)}e^{2i\Phi_h} + T_{1,1}^{(\lambda'_h,-1)\dagger}T_{1,1}^{(0,0)}e^{-2i\Phi_h}\right].
\end{aligned} \tag{245}$$

In order to properly average and sum over the initial and final state nucleon helicities, respectively, we can only apply the parity symmetry of Eq. (67) to bilinear combinations $T^{\dagger}T$, not to individual factors. The term proportional to $\sin(2\Theta_R)$ expands to

$$\begin{aligned}
-\left|\Omega_{1,1}(m_{\pi\pi})\right|^2 \frac{\sin(2\Theta_R)}{2\sqrt{2}}\Bigg\{ & e^{i\Phi_R}\left[T_{1,1}^{(0,1)\dagger}T_{1,1}^{1,-1}e^{2i\Phi_h} + T_{1,1}^{(0,-1)\dagger}T_{1,1}^{1,1}e^{-2i\Phi_h}\right] \\
& - e^{-i\Phi_R}\left[T_{1,1}^{(0,1)\dagger}T_{1,1}^{-1,-1}e^{2i\Phi_h} + T_{1,1}^{(0,-1)\dagger}T_{1,1}^{-1,1}e^{-2i\Phi_h}\right] \\
& + e^{-i\Phi_R}\left[T_{1,1}^{(1,1)\dagger}T_{1,1}^{0,-1}e^{2i\Phi_h} + T_{1,1}^{(1,-1)\dagger}T_{1,1}^{0,1}e^{-2i\Phi_h}\right] \\
& - e^{i\Phi_R}\left[T_{1,1}^{(-1,1)\dagger}T_{1,1}^{0,-1}e^{2i\Phi_h} + T_{1,1}^{(-1,-1)\dagger}T_{1,1}^{0,1}e^{-2i\Phi_h}\right]\Bigg\}.
\end{aligned} \tag{246}$$

Now apply parity symmetry to select bilinear combinations. The expression in curly brackets of Eq. (246) simplifies to

$$\begin{aligned}
\Big\{\Big\} = & \Bigg\{T_{1,1}^{(0,1)\dagger}T_{1,1}^{1,-1}\left[e^{i(\Phi_R+2\Phi_h)} + e^{-i(\Phi_R+2\Phi_h)}\right] + T_{1,1}^{(0,-1)\dagger}T_{1,1}^{1,1}\left[e^{i(\Phi_R-2\Phi_h)} + e^{-i(\Phi_R-2\Phi_h)}\right] \\
& + T_{1,1}^{(1,1)\dagger}T_{1,1}^{0,-1}\left[e^{-i(\Phi_R-2\Phi_h)} + e^{i(\Phi_R-2\Phi_h)}\right] + T_{1,1}^{(1,-1)\dagger}T_{1,1}^{0,1}\left[e^{-i(\Phi_R+2\Phi_h)} + e^{i(\Phi_R+2\Phi_h)}\right]\Bigg\} \\
= & \, 4\Bigg\{\Re\left[T_{1,1}^{(0,1)\dagger}T_{1,1}^{1,-1}\right]\cos\left(\Phi_R+2\Phi_h\right) + \Re\left[T_{1,1}^{(0,-1)\dagger}T_{1,1}^{1,1}\right]\cos\left(\Phi_R-2\Phi_h\right)\Bigg\}.
\end{aligned} \tag{247}$$

Similarly, the $\sin^2\Theta_R$ term expands to

$$\begin{aligned}
-|\Omega_{1,1}(m_{\pi\pi})|^2\,\frac{\sin^2\Theta_R}{2}\Bigg\{ & \left[T_{1,1}^{(1,1)\dagger}T_{1,1}^{(1,-1)}e^{2i\Phi_h}+T_{1,1}^{(1,-1)\dagger}T_{1,1}^{(1,1)}e^{-2i\Phi_h}\right]\\
& +\left[T_{1,1}^{(-1,1)\dagger}T_{1,1}^{(-1,-1)}e^{2i\Phi_h}+T_{1,1}^{(-1,-1)\dagger}T_{1,1}^{(-1,1)}e^{-2i\Phi_h}\right]\\
& -e^{2i\Phi_R}\left[T_{1,1}^{(-1,1)\dagger}T_{1,1}^{(1,-1)}e^{2i\Phi_h}+T_{1,1}^{(-1,-1)\dagger}T_{1,1}^{(1,1)}e^{-2i\Phi_h}\right]\\
& -e^{-2i\Phi_R}\left[T_{1,1}^{(1,1)\dagger}T_{1,1}^{(-1,-1)}e^{2i\Phi_h}+T_{1,1}^{(1,-1)\dagger}T_{1,1}^{(-1,1)}e^{-2i\Phi_h}\right]\Bigg\}. \qquad (248)
\end{aligned}$$

The curly bracket factor of Eq. (248) simplifies to

$$\begin{aligned}
\Big\{\Big\} = \Bigg\{ & 2\left[T_{1,1}^{(1,1)\dagger}T_{1,1}^{(1,-1)}+T_{1,1}^{(1,-1)\dagger}T_{1,1}^{(1,1)}\right]\cos\left(2\Phi_h\right)\\
& -2\left[T_{1,1}^{(-1,1)\dagger}T_{1,1}^{(1,-1)}\right]\cos\left(2\Phi_R+2\Phi_h\right)-2\left[T_{1,1}^{(-1,-1)\dagger}T_{1,1}^{(1,1)}\right]\cos\left(2\Phi_R-2\Phi_h\right)\Bigg\}.
\end{aligned}$$

Each term in square brackets is real:

$$\begin{aligned}
\Big\{\Big\} = \Bigg\{ & 4\Re\left[T_{1,1}^{(1,1)\dagger}T_{1,1}^{(1,-1)}\right]\cos\left(2\Phi_h\right)-2\Re\left[T_{1,1}^{(-1,1)\dagger}T_{1,1}^{(1,-1)}\right]\cos\left(2\Phi_R+2\Phi_h\right)\\
& -2\Re\left[T_{1,1}^{(-1,-1)\dagger}T_{1,1}^{(1,1)}\right]\cos\left(2\Phi_R-2\Phi_h\right)\Bigg\}. \qquad (249)
\end{aligned}$$

All of the terms above with $|\Omega_{1,1}|^2$ are defined in [25]. The final TT terms are the interference terms between $(J,I)=(0,0)$ and $(1,1)$:

$$\begin{aligned}
\left[f_{TT}\mathcal{R}_{TT}\right]^{\Im} &= -\Omega^{\dagger}_{0,0}\Omega_{1,1}\Bigg\{\cos(\Theta_R)\left[T^{(0,1)\dagger}_{0,0}T^{(0,-1)}_{1,1}e^{2i\Phi_h}+T^{(0,-1)\dagger}_{0,0}T^{(0,1)}_{1,1}e^{-2i\Phi_h}\right]\\
&\qquad+\sum_{\lambda_h=\pm1}\frac{\lambda_h\sin(\Theta_R)}{\sqrt{2}}e^{i\lambda_h\Phi_R}\left[T^{(0,1)\dagger}_{0,0}T^{(\lambda_h,-1)}_{1,1}e^{2i\Phi_h}+T^{0,-1)\dagger}_{0,0}T^{(\lambda_h,1)}_{1,1}e^{-2i\Phi_h}\right]\Bigg\}\\
&\quad-\Omega^{\dagger}_{1,1}\Omega_{0,0}\Bigg\{\cos\Theta_R\left[T^{(0,1)\dagger}_{1,1}T^{(0,-1)}_{0,0}e^{2i\Phi_h}+T^{(0,-1)\dagger}_{1,1}T^{(0,1)}_{0,0}e^{-2i\Phi_h}\right]\\
&\qquad+\sum_{\lambda'_h=\pm1}\frac{\lambda'_h\sin(\Theta_R)}{\sqrt{2}}e^{-i\lambda'_h\Phi_R}\left[T^{(\lambda'_h,1)\dagger}_{1,1}T^{(0,-1)}_{0,0}e^{2i\Phi_h}+T^{(\lambda'_h,-1)\dagger}_{1,1}T^{(0,1)}_{0,0}e^{-2i\Phi_h}\right]\Bigg\}\\
&= -2\cos\Theta_R\Bigg\{\left[\Omega^{\dagger}_{0,0}\Omega_{1,1}T^{(0,1)\dagger}_{0,0}T^{(0,-1)}_{1,1}\right]+c.c\Bigg\}\cos(2\Phi_h)\\
&\quad-\Omega^{\dagger}_{0,0}\Omega_{1,1}\frac{\sin\Theta_R}{\sqrt{2}}\Bigg\{e^{i\Phi_R}\left[T^{(0,1)\dagger}_{0,0}T^{(1,-1)}_{1,1}e^{2i\Phi_h}+T^{(0,-1)\dagger}_{0,0}T^{(1,1)}_{1,1}e^{-2i\Phi_h}\right]\\
&\qquad-e^{-i\Phi_R}\left[T^{(0,1)\dagger}_{0,0}T^{(-1,-1)}_{1,1}e^{2i\Phi_h}+T^{(0,-1)\dagger}_{0,0}T^{(-1,1)}_{1,1}e^{-2i\Phi_h}\right]\Bigg\}\\
&\quad-\Omega^{\dagger}_{1,1}\Omega_{0,0}\frac{\sin\Theta_R}{\sqrt{2}}\Bigg\{e^{-i\Phi_R}\left[T^{(1,1)\dagger}_{1,1}T^{(0,-1)}_{0,0}e^{2i\Phi_h}+T^{(1,-1)\dagger}_{1,1}T^{(0,1)}_{0,0}e^{-2i\Phi_h}\right]\\
&\qquad-e^{i\Phi_R}\left[T^{(-1,1)\dagger}_{1,1}T^{(0,-1)}_{0,0}e^{2i\Phi_h}+T^{(-1,-1)\dagger}_{1,1}T^{(0,1)}_{0,0}e^{-2i\Phi_h}\right]\Bigg\}.
\end{aligned}\tag{250}$$

Combining terms, and applying parity symmetry to both factors in the bilinear combinations $T^{\dagger}T$:

$$\begin{aligned}
\left[f_{TT}\mathcal{R}_{TT}\right]^{\Im} &= 4\cos\Theta_R\cos(2\Phi_h)\Bigg\{\Im\left[\Omega^{\dagger}_{0,0}\Omega_{1,1}\right]\Im\left[T^{(0,1)\dagger}_{0,0}T^{(0,-1)}_{1,1}\right]-\Re\left[\Omega^{\dagger}_{0,0}\Omega_{1,1}\right]\Re\left[T^{(0,1)\dagger}_{0,0}T^{(0,-1)}_{1,1}\right]\Bigg\}\\
&\quad-2\left[\Omega^{\dagger}_{0,0}\Omega_{1,1}\right]\frac{\sin\Theta_R}{\sqrt{2}}\Bigg\{T^{(0,1)\dagger}_{0,0}T^{(1,-1)}_{1,1}\cos(\Phi_R+2\Phi_h)+T^{(0,-1)\dagger}_{0,0}T^{(1,1)}_{1,1}\cos(\Phi_R-2\Phi_h)\Bigg\}\\
&\quad-2\left[\Omega^{\dagger}_{1,1}\Omega_{0,0}\right]\frac{\sin\Theta_R}{\sqrt{2}}\Bigg\{T^{(1,1)\dagger}_{1,1}T^{(0,-1)}_{0,0}\cos(\Phi_R-2\Phi_h)+T^{(1,-1)\dagger}_{1,1}T^{(0,1)}_{0,0}\cos(\Phi_R+2\Phi_h)\Bigg\}\\
&= 4\cos\Theta_R\cos(2\Phi_h)\Bigg\{\Im\left[\Omega^{\dagger}_{0,0}\Omega_{1,1}\right]\Im\left[T^{(0,1)\dagger}_{0,0}T^{(0,-1)}_{1,1}\right]\\
&= -\Re\left[\Omega^{\dagger}_{0,0}\Omega_{1,1}\right]\Re\left[T^{(0,1)\dagger}_{0,0}T^{(0,-1)}_{1,1}\right]\Bigg\}\\
&\quad+2\sqrt{2}\sin\Theta_R\Bigg\{\\
&\cos(\Phi_R+2\Phi_h)\left(\Im\left[\Omega^{\dagger}_{0,0}\Omega_{1,1}\right]\Im\left[T^{(0,1)\dagger}_{0,0}T^{(1,-1)}_{1,1}\right]-\Re\left[\Omega^{\dagger}_{0,0}\Omega_{1,1}\right]\Re\left[T^{(0,1)\dagger}_{0,0}T^{(1,-1)}_{1,1}\right]\right)\\
&+\cos(\Phi_R-2\Phi_h)\left(\Im\left[\Omega^{\dagger}_{0,0}\Omega_{1,1}\right]\Im\left[T^{(0,-1)\dagger}_{0,0}T^{(1,1)}_{1,1}\right]-\Re\left[\Omega^{\dagger}_{0,0}\Omega_{1,1}\right]\Re\left[T^{(0,-1)\dagger}_{0,0}T^{(1,1)}_{1,1}\right]\right)\\
&\qquad\qquad\Bigg\}.
\end{aligned}\tag{251}$$

The complete TT interference term is then

$$
\begin{aligned}
f_{TT}(\Phi_h)\mathcal{R}_{TT} = {}& -4\left|\Omega_{0,0}(m_{\pi\pi})\right|^2 \Big\{\Re\left[T_{0,0}^{(0,1)\dagger}T_{0,0}^{0,-1}\right]\cos\left(2\Phi_h\right) - \Im\left[T_{0,0}^{(0,1)\dagger}T_{0,0}^{0,-1}\right]\sin\left(2\Phi_h\right)\Big\} \\
& - 4\left|\Omega_{1,1}(m_{\pi\pi})\right|^2\cos^2\Theta_R \Big\{\Re\left[T_{1,1}^{(0,1)\dagger}T_{1,1}^{0,-1}\right]\cos\left(2\Phi_h\right) - \Im\left[T_{1,1}^{(0,1)\dagger}T_{1,1}^{0,-1}\right]\sin\left(2\Phi_h\right)\Big\} \\
& - \left|\Omega_{1,1}(m_{\pi\pi})\right|^2\sin^2\Theta_R \Bigg\{2\Re\left[T_{1,1}^{(1,1)\dagger}T_{1,1}^{(1,-1)}\right]\cos\left(2\Phi_h\right) - \\
& \quad \Re\left[T_{1,1}^{(-1,1)\dagger}T_{1,1}^{(1,-1)}\right]\cos\left(2\Phi_R+2\Phi_h\right) - \Re\left[T_{1,1}^{(-1,-1)\dagger}T_{1,1}^{(1,1)}\right]\cos\left(2\Phi_R-2\Phi_h\right)\Bigg\} \\
& \quad - \sqrt{2}\left|\Omega_{1,1}\right|^2\sin(2\Theta_R)\Bigg\{ \\
& \qquad \Re\left[T_{1,1}^{(0,1)\dagger}T_{1,1}^{1,-1}\right]\cos\left(\Phi_R+2\Phi_h\right) + \Re\left[T_{1,1}^{(0,-1)\dagger}T_{1,1}^{1,1}\right]\cos\left(\Phi_R-2\Phi_h\right)\Bigg\} \\
& + 4\cos\Theta_R\cos(2\Phi_h)\Bigg\{\Im\left[\Omega_{0,0}^{\dagger}\Omega_{1,1}\right]\Im\left[T_{0,0}^{(0,1)\dagger}T_{1,1}^{(0,-1)}\right] \\
& - \Re\left[\Omega_{0,0}^{\dagger}\Omega_{1,1}\right]\Re\left[T_{0,0}^{(0,1)\dagger}T_{1,1}^{(0,-1)}\right]\Bigg\} \\
& + 2\sqrt{2}\sin\Theta_R\Bigg\{ \\
& \cos(\Phi_R+2\Phi_h)\Big(\Im\left[\Omega_{0,0}^{\dagger}\Omega_{1,1}\right]\Im\left[T_{0,0}^{(0,1)\dagger}T_{1,1}^{(1,-1)}\right] - \Re\left[\Omega_{0,0}^{\dagger}\Omega_{1,1}\right]\Re\left[T_{0,0}^{(0,1)\dagger}T_{1,1}^{(1,-1)}\right]\Big) \\
& + \cos(\Phi_R-2\Phi_h)\Big(\Im\left[\Omega_{0,0}^{\dagger}\Omega_{1,1}\right]\Im\left[T_{0,0}^{(0,-1)\dagger}T_{1,1}^{(1,1)}\right] - \Re\left[\Omega_{0,0}^{\dagger}\Omega_{1,1}\right]\Re\left[T_{0,0}^{(0,-1)\dagger}T_{1,1}^{(1,1)}\right]\Big) \\
& \qquad\qquad \Bigg\}.
\end{aligned} \tag{252}
$$

This is a total of 15 linearly independent terms. Regrouping by Legendre polynomials of

$u = \cos\Theta_R$:

$$
\begin{aligned}
f_{TT}(\Phi_h)\mathcal{R}_{TT} = & -4\left|\Omega_{0,0}(m_{\pi\pi})\right|^2 \left\{\Re\left[T_{0,0}^{(0,1)\dagger}T_{0,0}^{0,-1}\right]\cos\left(2\Phi_h\right) - \Im\left[T_{0,0}^{(0,1)\dagger}T_{0,0}^{0,-1}\right]\sin\left(2\Phi_h\right)\right\} \\
& + \frac{4}{3}\left|\Omega_{1,1}(m_{\pi\pi})\right|^2 \Bigg\{\left(\Re\left[T_{1,1}^{(1,1)\dagger}T_{1,1}^{(1,-1)}\right] - \Re\left[T_{1,1}^{(0,1)\dagger}T_{1,1}^{0,-1}\right]\right)\cos\left(2\Phi_h\right) \\
& \qquad + \Im\left[T_{1,1}^{(0,1)\dagger}T_{1,1}^{0,-1}\right]\left[1 + 2P_2(u)\right]\sin\left(2\Phi_h\right) \\
& \qquad + P_2(u)\left(\Re\left[T_{1,1}^{(1,1)\dagger}T_{1,1}^{(1,-1)}\right] - 2\Re\left[T_{1,1}^{(0,1)\dagger}T_{1,1}^{0,-1}\right]\right)\cos\left(2\Phi_h\right)\Bigg\} \\
& - \left|\Omega_{1,1}(m_{\pi\pi})\right|^2 \sin^2\Theta_R \Bigg\{ \\
& \quad \Re\left[T_{1,1}^{(-1,1)\dagger}T_{1,1}^{(1,-1)}\right]\cos\left(2\Phi_R + 2\Phi_h\right) - \Re\left[T_{1,1}^{(-1,-1)\dagger}T_{1,1}^{(1,1)}\right]\cos\left(2\Phi_R - 2\Phi_h\right)\Bigg\} \\
& \quad - \sqrt{2}\left|\Omega_{1,1}\right|^2 \sin(2\Theta_R)\Bigg\{ \\
& \qquad \Re\left[T_{1,1}^{(0,1)\dagger}T_{1,1}^{1,-1}\right]\cos\left(\Phi_R + 2\Phi_h\right) + \Re\left[T_{1,1}^{(0,-1)\dagger}T_{1,1}^{1,1}\right]\cos\left(\Phi_R - 2\Phi_h\right)\Bigg\} \\
& + 4\cos\Theta_R\cos(2\Phi_h)\Bigg\{\Im\left[\Omega_{0,0}^{\dagger}\Omega_{1,1}\right]\Im\left[T_{0,0}^{(0,1)\dagger}T_{1,1}^{(0,-1)}\right] \\
& - \Re\left[\Omega_{0,0}^{\dagger}\Omega_{1,1}\right]\Re\left[T_{0,0}^{(0,1)\dagger}T_{1,1}^{(0,-1)}\right]\Bigg\} \\
& + 2\sqrt{2}\sin\Theta_R\Bigg\{ \\
& \cos(\Phi_R + 2\Phi_h)\left(\Im\left[\Omega_{0,0}^{\dagger}\Omega_{1,1}\right]\Im\left[T_{0,0}^{(0,1)\dagger}T_{1,1}^{(1,-1)}\right] - \Re\left[\Omega_{0,0}^{\dagger}\Omega_{1,1}\right]\Re\left[T_{0,0}^{(0,1)\dagger}T_{1,1}^{(1,-1)}\right]\right) \\
& + \cos(\Phi_R - 2\Phi_h)\left(\Im\left[\Omega_{0,0}^{\dagger}\Omega_{1,1}\right]\Im\left[T_{0,0}^{(0,-1)\dagger}T_{1,1}^{(1,1)}\right] - \Re\left[\Omega_{0,0}^{\dagger}\Omega_{1,1}\right]\Re\left[T_{0,0}^{(0,-1)\dagger}T_{1,1}^{(1,1)}\right]\right) \\
& \qquad \Bigg\}. \qquad (253)
\end{aligned}
$$

APPENDIX C

DC CALIBRATION PROJECT

The CLAS12 service project involves my involvement as the main Drift Chamber (DC) calibrator. Currently, I am calibrating data for four different run groups: RG-A, RG-B, RG-M, and RG-C. Our focus at the moment (January 2023) is on DC calibration for Pass2 data preparation.

C.0.1 CLAS12 DRIFT CHAMBER

The CLAS12 Drift Chamber (DC) measures trajectories (path curvature in a magnetic field). Since it is possible to calculate the momentum of a charged particle emerging from the target. There are three regions in the Drift Chamber system. The six chambers of "region 1" are located approximately 2 m radially from the target, before the torus. The six chambers of "region 2" are located between the six coils of the torus at a radius of about 3 m, while the six chambers of "region 3" are located radially outward of the torus at the radius of about 4 m [47]. The DC system includes 18 wire chambers, each with 2 superlayers of 6 layers and 112 cells in polar angle and total of 24,192 wires [48]. Each cell gives spacial resolution of $250 - 350$ μ m [48]. Small cells and fast drift velocity meet the luminosity requirement of 10^{35} cm^{-2}s^{-1} [48]. The cell structure is hexagonal, that is, each sense wire is surrounded by six field wires. The superlayers have their wires arranged with a plus or minus 6^o stereo angle [48]. The choice of gases Argon:CO_2, $90:10$ mixture should result in a higher and more constant drift velocity [48]. It has very good momentum and angular resolution for the scattered electron on the order of $dp/p < 1\%$ and $\Delta\theta = 1$ mrad. Table 4 summarizes the specifications for the forward tracking system.

There are two gases Ar and CO_2, Ar is the one that going to be ionized. When molecules are ionized along the trajectory, ions move in the opposite direction to the sense wire, while electrons move in the same direction. As a result, an electron avalanche occurs around the sense wire. Drift time can be measured for distance between wire and the trajectory. The six cathode wires approximate the cylindrical geometry of this stroke tube, Fig. 88 shows the clear picture of this process. There are two separate track reconstruction are implemented. Those are "Hit-based" tracking and "Time-based" tracking. "Hit-based" tracking uses hit

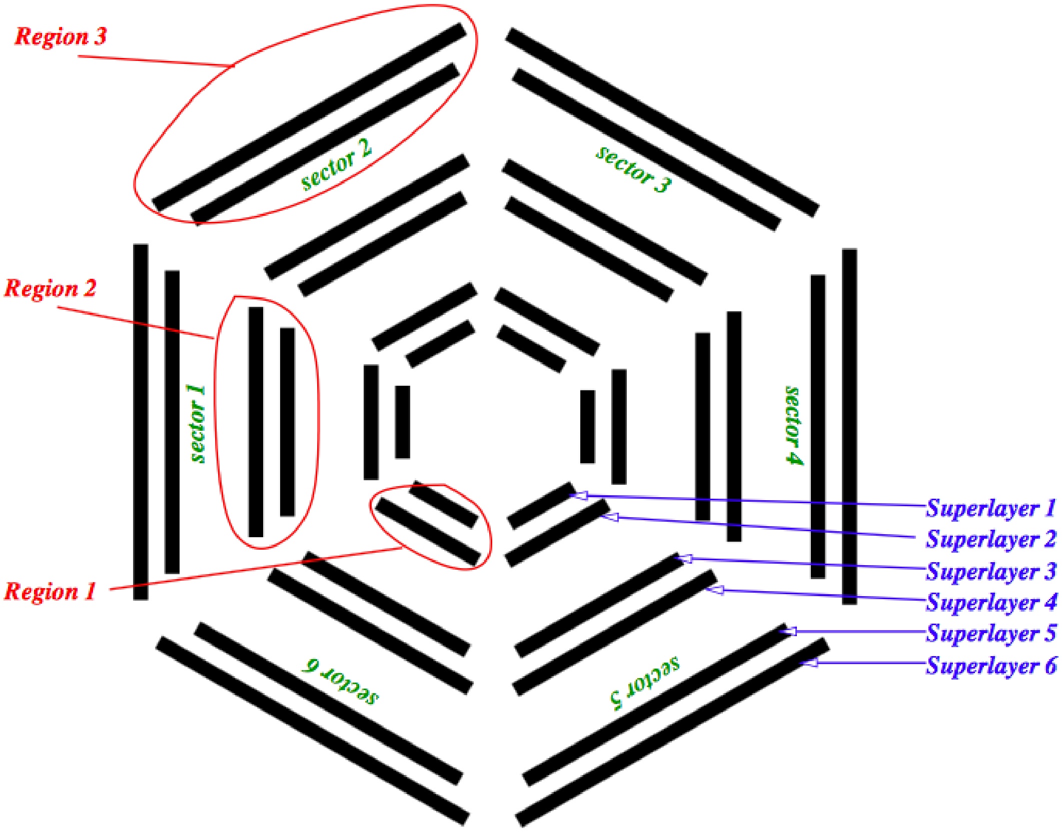

FIG. 87. Diagram of the CLAS12 Drift Chamber illustrating the names of the regions and superlayers.

Parameter	Specification
Angular Coverage	5^o-40^o
Momentum resolution	$dp/p < 1\%$
θ resolution	1 mrad
ϕ resolution	$1\text{mrad}/\sin(\theta)$
Luminosity	$10^{35}\text{cm}^{-2}\text{s}^{-1}$

TABLE 4. Specifications for CLAS12 drift chamber system [48].

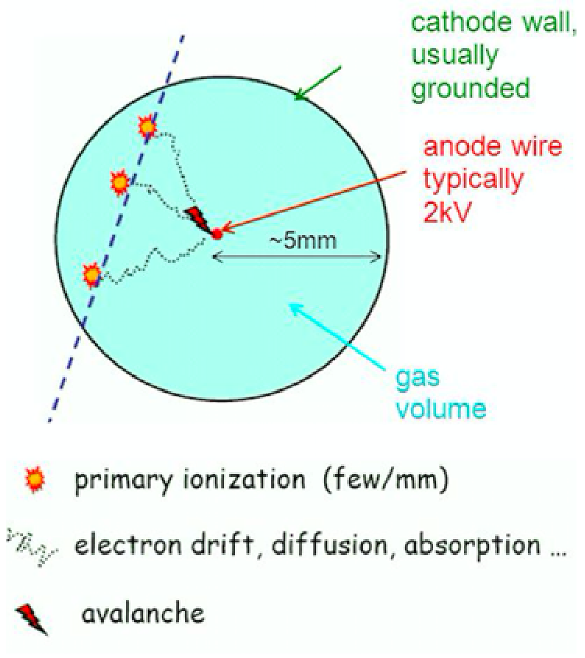

FIG. 88. Sketch of drift cell (note that drift cell is a hexagonal shape, not a circle).

position information and “Time-based” tracking uses timing information. In Fig. 89 shows the hit-based tracking and time-based tracking. Two terms are used to describe the distance between a charged particle track and a sense wire (see Fig. 90):

- trkDoca-Calculate Distance of Closest Approach (DOCA) from Hit Based tracking,
- calcDoca-Calculate Distance of Closest Approach (DOCA) from Time-Based tracking.

Therefore, calibration is necessary to achieve convergence on time-residuals, where

$$TimeResidual = trkDoca - calcDoca. \tag{254}$$

The following section C.0.2 will describe the DC calibration process.

C.0.2 DC CALIBRATION

A description of the DC calibration process, primarily the calibration of the time-to-distance function, can be found in this section. The “hit-based” tracking system, as described in section C.0.2, does not simply calculate the position of the wire but rather calculates it based on the wire’s distance-of-closest-approach (DOCA), as calculated from the wire’s

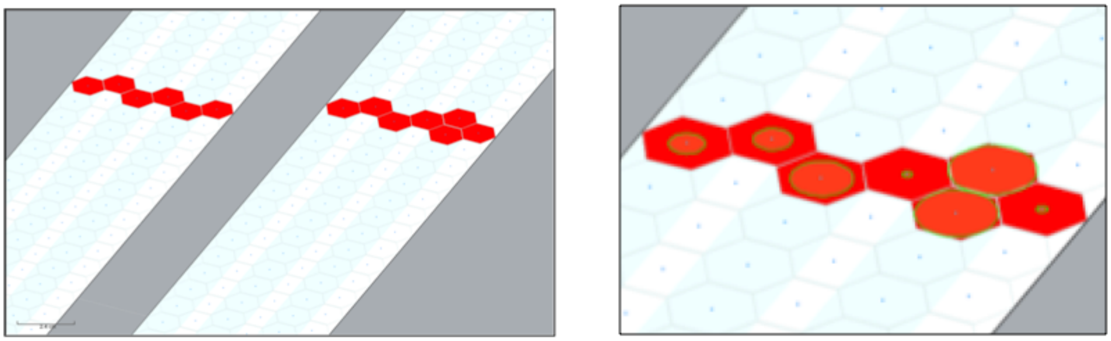

(Hit Based)

(Time Based)

FIG. 89. Diagrams of hit-based and time-based tracking.

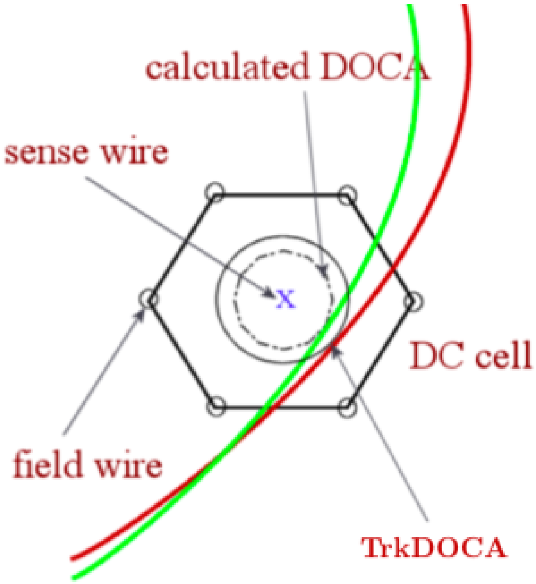

FIG. 90. Schematic of “trkDoca” and “CalcDoca”.

recorded time-to-Digital converters(TDCs) , which measures time. TDC digits are the raw data from the drift chambers, which can be converted to nanoseconds by measuring the signal times of the sense wire. When these times are corrected for various delays, they can be converted into drift times of the ions received by the corresponding wires. These delays include signal propagation delays due to cable lengths, sense wire lengths, particle flight time used to trigger events, and particle flight time being tracked, among others. Thus, drift time can be written as follows(see Eq. (255)[48]).

$$t_{drift} = t_{tdc} - t_{start} - t_0 - t_{flight} - t_{prop} - t_{walk}, \tag{255}$$

where, t_{tdc}- raw time measured by the TDC, t_{start}- event start time, t_0- fixed-time (cable) delay for the wire, t_{flight}- flight time of the particle from the interaction vertex to the wire, t_{prop}-signal propagation time along the wire, and t_{walk}- shift of the recorded hit time and the distance of the track to the wire
The start time can be determined using the Forward Time of Flight (FTOF) system's counter time for the scattered electron. To determine the t_0, which is the fixed time delay for each wire, was quite challenging. For that, they produced a histogram for the $t_{tdc} - t_{start} - t_{flight} - t_{prop} - t_{walk}$ for all his used in the tracks. The result was a characteristic plot of an out-of-time drift chamber signal on a flat background. Using a sigmoid with linear extrapolation as a fit to the leading edge, the value of t0 was obtained [48]. This

It was necessary to convert the corrected time from the wire to an estimated DOCA after the raw TDC had been corrected. As mentioned in previous section C.0.2, there are two "DOCA" terms used. The "TRKDOCA" value represents the track's closest approach to the wire, while "DOCA" is calculated from the measured time for the wire. It was previously understood that the "DOCA" terms are referred to as "CalcDoca". However, under the CLAS12 notation, the CalcDoca term is no longer used.

Fitting Procedure

Our goal is to fit the observed time as a function of distance, which is the distance between a track and a wire. There is no doubt that time increases with distance, but the function is not linear. Ionized electrons are attracted to the wire by an electric field that is strong near the wire and decreases as distance increases. As the track approaches the outer corners of the cell, the field increases again due to the field wires. As a result, we have an inflection point in our function. In order to model the relationship between time and distance, we use a fourth-order polynomial. The four variables are transformed into four (physically meaningful) variables using simple calculus. Those are **V0**- Slope of the curvature at 0, **R**- Distance (normalized to the maximum distance) of the inflection point, **Vmid**- Slope at R, and **Tmax**- The maximum time occurring at the maximum distance.

Furthermore, there is a "timewalk" function that increases the observation time for small values of distance; the parameter **distBeta** controls this function. Observation time is increased in Region 2 due to the strong magnetic field (compared to the case without a magnetic field). The function's shape is controlled by four parameters, and the overall scale by one, **DelBf**. Currently, we only allow $V0$, $Vmid$, $Tmax$, and $DelBf$ to vary to maintain a more stable resolution. At this time DC team follows the following calibration protocols to achieve consistent residuals across all runs of a Run Group:(Occasionally, this protocol may be modified).

Nominal (current) protocol)Updated on 09/13/2021 [49]
Keep **R** fixed at a value of 0.66 for all super-layers.
Keep **DelBf = 0** fixed for Regions 1 and 3. This parameter varies for Region 2.
b1 – b4 are kept fixed at default/preloaded values.
Fix **distbeta** = 0.08 for all super-layers.
If we "fix" the variable it will be held as a fixed variable and if it varying it will be varied by chi-squared minimization routine.

Those variables that are "fixed" will be retained as fixed variables, and those that are varying will be varied by the chi-square minimization procedure.

DC Calibration Steps

During the CLAS12 Drift Chamber Calibration, the following steps are performed iteratively. Fig. 91 shows the flow chart of the process. The first step in the decoding process is to convert raw data into decoded data. Then cooked data is then created as a result of the reconstruction process. In order to reconstruct a decoded file, you may simply use the standard builds that are already installed and ready for use. These builds (of COATJAVA, CLARA, etc.) can be used by loading the modules that are available.

First logon to the Jlab farm and follow the following procedure, source command will setup the environment, and module command will load the necessary software in CLAS12

```
source /group/clas12/packages/setup.csh
```

```
module load clas12/pro
```

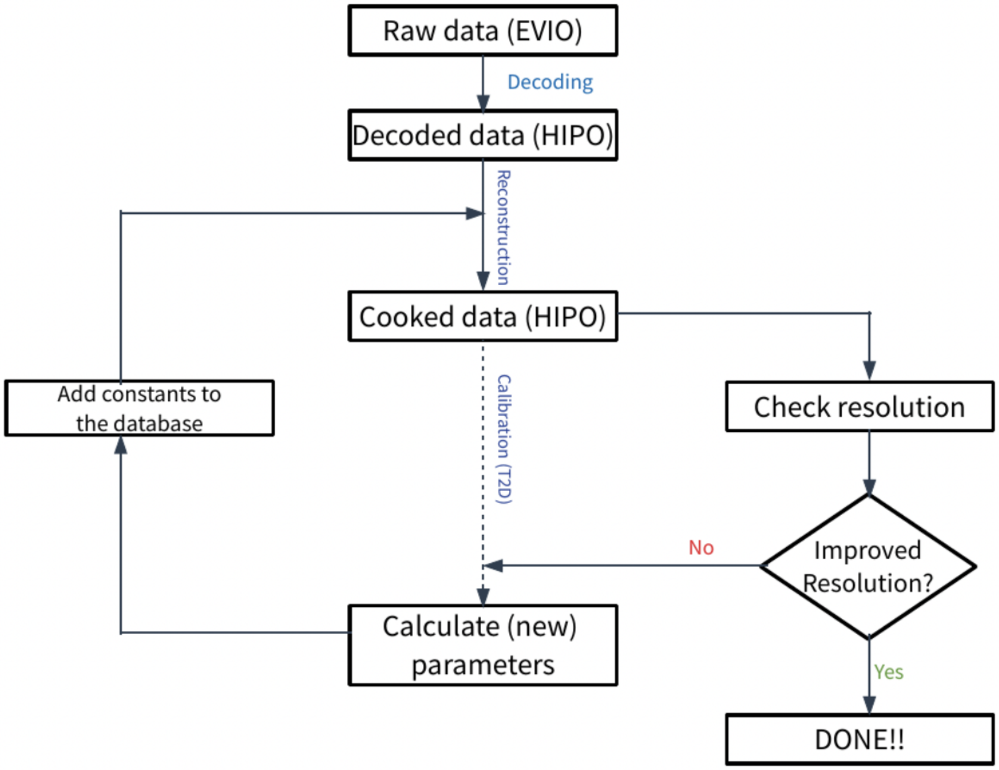

FIG. 91. The iterative process of calibration.

Now we're ready to cook the decoded file. Next, time-to-distance calibration must be conducted (see the following section C.0.2 for more information about DC Calibration GUI) and calculate the new parameters. These parameters must be uploaded to the CLAS12 Constant Database (CCDB). It is necessary to cook the data and check the resolution using these parameters. The calibration process is complete if the resolution has been improved; otherwise, we need to iterate the procedure as shown in Fig. 91.

DC Calibration GUI

The calibration software is currently available on the [50]. First, we need to install this software. In order to install the calibration software, follow the steps below91.

```
git clone https://github.com/JeffersonLab/clas12calibration-dc.git
cd clas12calibration-dc
```

```
mvn install
```

Once the software package is installed, run the following command.

```
./script.sh
```

This interface (see Fig. 92) appears first when the program is launched and allows us to perform various functions. The time-to-distance calibration process is initiated by selecting the “T2D” button. Once clicked on “T2D”, the “Configuration Calibration Setting window” will launch(see Fig. 93). This needs to be configured according to our requirements, such as variation, number of events to run, etc. After that, close it by pressing the “Finish” button on the “Configure Calibration Setting” window. When the user interface appears(see Fig. 94), select the “HIPO” data file using the H4 button (red outlined H4 button). The play arrow button (encircled in red) becomes clickable when a hipo file has been selected. Once start the process, the DC-GUI navigates through the TBHits bank, and a 2-dimensional histogram of time versus TRKDoca is loaded from all of the single-segment fits in the TBHits bank. It is important to note that “time” represents the fully-corrected time value for each hit (ns), while “trkDoca” represents the closest approach (cm) of the fit to the hits in a track segment. Now there is a new “Fit control” window (see Fig. 95 (left)) visible. When all events in the file have been processed, the “FIT TIME TO DISTANCE” tab will change color from red to green. Once the “FIT TIME TO DISTANCE” tab has become green, follow the “Calibration protocol” described in the previous section C.0.2 (Note that this protocol may change time to time). Then click on the “FIT TIME TO DISTANCE” button, and this will fit the time to distance distributions. After that, click on “REDO SEGMENT FIT”, which do the function minimization. In order to see the fits over-plotted on the TrackDoca vs. T histograms, click on the tab “TrackDoca vs. T Graphs” and select the layer for the specific component (equivalent to different bins) (see Fig. 96). Finally, click on the “PLOT RESIDUALS”(yellow button) button, and it will draw the time residual distributions. Once reprocessing is done, click on the “Time Residuals” tab on the ’DC Calibration’ main GUI. This procedure needs to continue for both “pass1” and “pass2”. The Time Residual distributions “pass1” and “pass2” examples are shown in Fig. 96 and Fig. 97. Note that, Fig. 96 and Fig. 97 are from RGM 15045 run calibration for the recent pass2 data preparation. Fig. 97 shows three rows; the top row shows the time residuals from default parameters directly taken from the CCDB, the middle row shows the time residuals from pass1 parameters and the third row shows the time residuals from pass2 parameters.

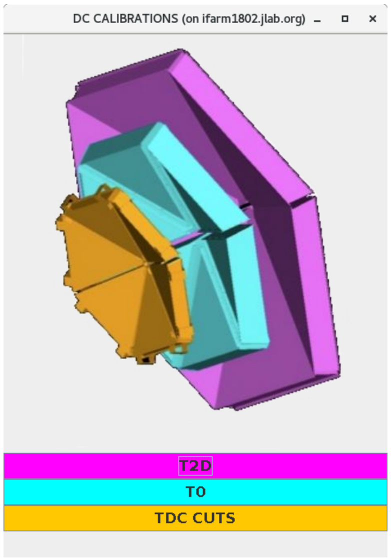

FIG. 92. Calibration Suite's main GUI as it currently appears.

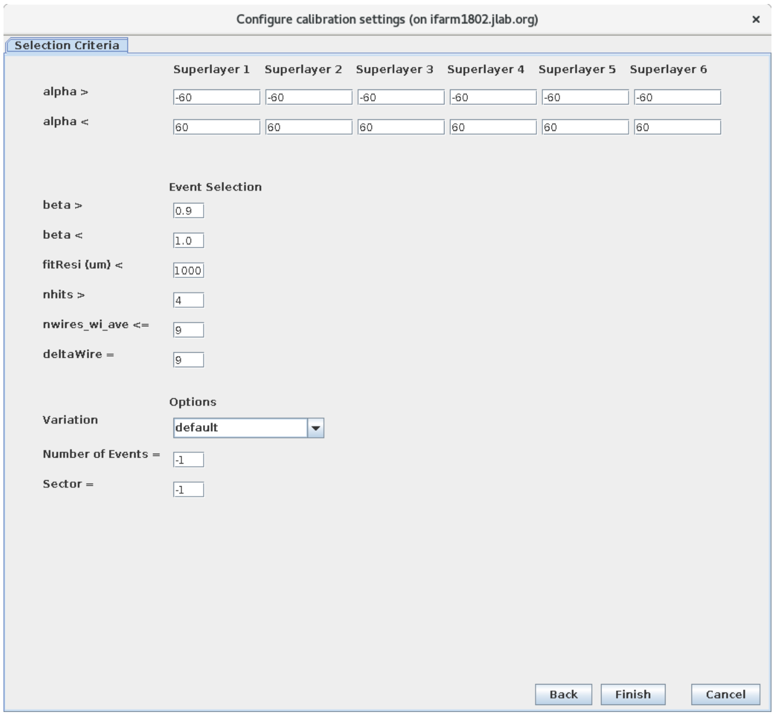

	Superlayer 1	Superlayer 2	Superlayer 3	Superlayer 4	Superlayer 5	Superlayer 6
alpha >	-60	-60	-60	-60	-60	-60
alpha <	60	60	60	60	60	60

Event Selection

beta > 0.9
beta < 1.0
fitResi (um) < 1000
nhits > 4
nwires_wi_ave <= 9
deltaWire = 9

Options

Variation default
Number of Events = -1
Sector = -1

FIG. 93. Configure the calibration Setting window.

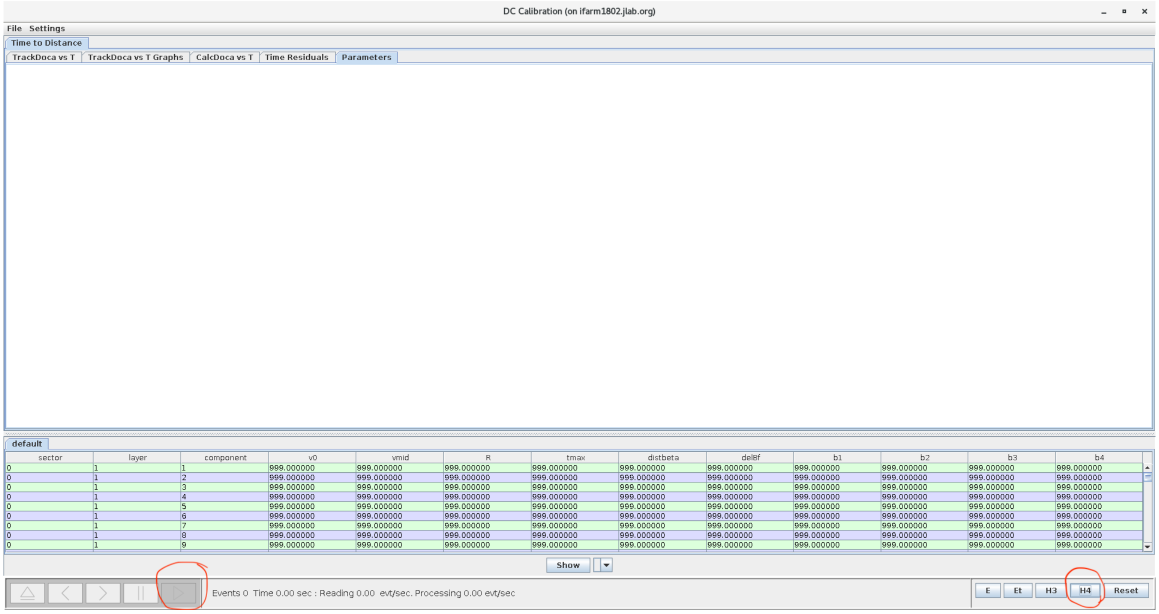

sector	layer	component	v0	vmid	R	tmax	distbeta	delBf	b1	b2	b3	b4
0	1	1	999.000000	999.000000	999.000000	999.000000	999.000000	999.000000	999.000000	999.000000	999.000000	999.000000
0	1	2	999.000000	999.000000	999.000000	999.000000	999.000000	999.000000	999.000000	999.000000	999.000000	999.000000
0	1	3	999.000000	999.000000	999.000000	999.000000	999.000000	999.000000	999.000000	999.000000	999.000000	999.000000
0	1	4	999.000000	999.000000	999.000000	999.000000	999.000000	999.000000	999.000000	999.000000	999.000000	999.000000
0	1	5	999.000000	999.000000	999.000000	999.000000	999.000000	999.000000	999.000000	999.000000	999.000000	999.000000
0	1	6	999.000000	999.000000	999.000000	999.000000	999.000000	999.000000	999.000000	999.000000	999.000000	999.000000
0	1	7	999.000000	999.000000	999.000000	999.000000	999.000000	999.000000	999.000000	999.000000	999.000000	999.000000
0	1	8	999.000000	999.000000	999.000000	999.000000	999.000000	999.000000	999.000000	999.000000	999.000000	999.000000
0	1	9	999.000000	999.000000	999.000000	999.000000	999.000000	999.000000	999.000000	999.000000	999.000000	999.000000

Events 0 Time 0.00 sec : Reading 0.00 evt/sec. Processing 0.00 evt/sec

FIG. 94. DC Calibration interface.

	Super Layer 1	Super Layer 2	Super Layer 3	Super Layer 4	Super Layer 5	Super Layer 6
v0	0.00547 ☐ Fix	0.00497 ☐ Fix	0.00521 ☐ Fix	0.00509 ☐ Fix	0.00356 ☐ Fix	0.00358 ☐ Fix
vmid	0.00475 ☐ Fix	0.00457 ☐ Fix	0.00336 ☐ Fix	0.00310 ☐ Fix	0.00169 ☐ Fix	0.00159 ☐ Fix
R	0.66000 ☑ Fix	0.66000 ☑ Fix	0.66000 ☑ Fix	0.66000 ☑ Fix	0.66000 ☑ Fix	0.66000 ☑ Fix
tmax	159.105 ☐ Fix	167.545 ☐ Fix	299.235 ☐ Fix	334.874 ☐ Fix	666.957 ☐ Fix	735.479 ☐ Fix
distbeta	0.08000 ☑ Fix	0.08000 ☑ Fix	0.08000 ☑ Fix	0.08000 ☑ Fix	0.08000 ☑ Fix	0.08000 ☑ Fix
delBf	0.00000 ☑ Fix	0.00000 ☑ Fix	0.25805 ☑ Fix	0.26601 ☑ Fix	0.00000 ☑ Fix	0.00000 ☑ Fix
b1	0.40000 ☑ Fix	0.40000 ☑ Fix	0.40000 ☑ Fix	0.40000 ☑ Fix	0.40000 ☑ Fix	0.40000 ☑ Fix
b2	-2.00000 ☑ Fix	-2.00000 ☑ Fix	-2.00000 ☑ Fix	-2.00000 ☑ Fix	-2.00000 ☑ Fix	-2.00000 ☑ Fix
b3	10.00000 ☑ Fix	10.00000 ☑ Fix	10.00000 ☑ Fix	10.00000 ☑ Fix	10.00000 ☑ Fix	10.00000 ☑ Fix
b4	-6.50000 ☑ Fix	-6.50000 ☑ Fix	-6.50000 ☑ Fix	-6.50000 ☑ Fix	-6.50000 ☑ Fix	-6.50000 ☑ Fix

Fit range min 0.0
Fit range max 2.0

	Super Layer 1	Super Layer 2	Super Layer 3	Super Layer 4	Super Layer 5	Super Layer 6
v0	0.00547 ☐ Fix	0.00497 ☐ Fix	0.00521 ☐ Fix	0.00509 ☐ Fix	0.00356 ☐ Fix	0.00358 ☐ Fix
vmid	0.00475 ☐ Fix	0.00457 ☐ Fix	0.00336 ☐ Fix	0.00310 ☐ Fix	0.00169 ☐ Fix	0.00159 ☐ Fix
R	0.66000 ☑ Fix	0.66000 ☑ Fix	0.66000 ☑ Fix	0.66000 ☑ Fix	0.66000 ☑ Fix	0.66000 ☑ Fix
tmax	159.105 ☐ Fix	167.545 ☐ Fix	299.235 ☐ Fix	334.874 ☐ Fix	666.957 ☐ Fix	735.479 ☐ Fix
distbeta	0.08000 ☑ Fix	0.08000 ☑ Fix	0.08000 ☑ Fix	0.08000 ☑ Fix	0.08000 ☑ Fix	0.08000 ☑ Fix
delBf	0.00000 ☑ Fix	0.00000 ☑ Fix	0.25805 ☑ Fix	0.26601 ☑ Fix	0.00000 ☑ Fix	0.00000 ☑ Fix
b1	0.40000 ☑ Fix	0.40000 ☑ Fix	0.40000 ☑ Fix	0.40000 ☑ Fix	0.40000 ☑ Fix	0.40000 ☑ Fix
b2	-2.00000 ☑ Fix	-2.00000 ☑ Fix	-2.00000 ☑ Fix	-2.00000 ☑ Fix	-2.00000 ☑ Fix	-2.00000 ☑ Fix
b3	10.00000 ☑ Fix	10.00000 ☑ Fix	10.00000 ☑ Fix	10.00000 ☑ Fix	10.00000 ☑ Fix	10.00000 ☑ Fix
b4	-6.50000 ☑ Fix	-6.50000 ☑ Fix	-6.50000 ☑ Fix	-6.50000 ☑ Fix	-6.50000 ☑ Fix	-6.50000 ☑ Fix

Fit range min 0.0
Fit range max 2.0

FIG. 95. Fit panel before (left) processed all events, and Fit panel after (right) processed events.

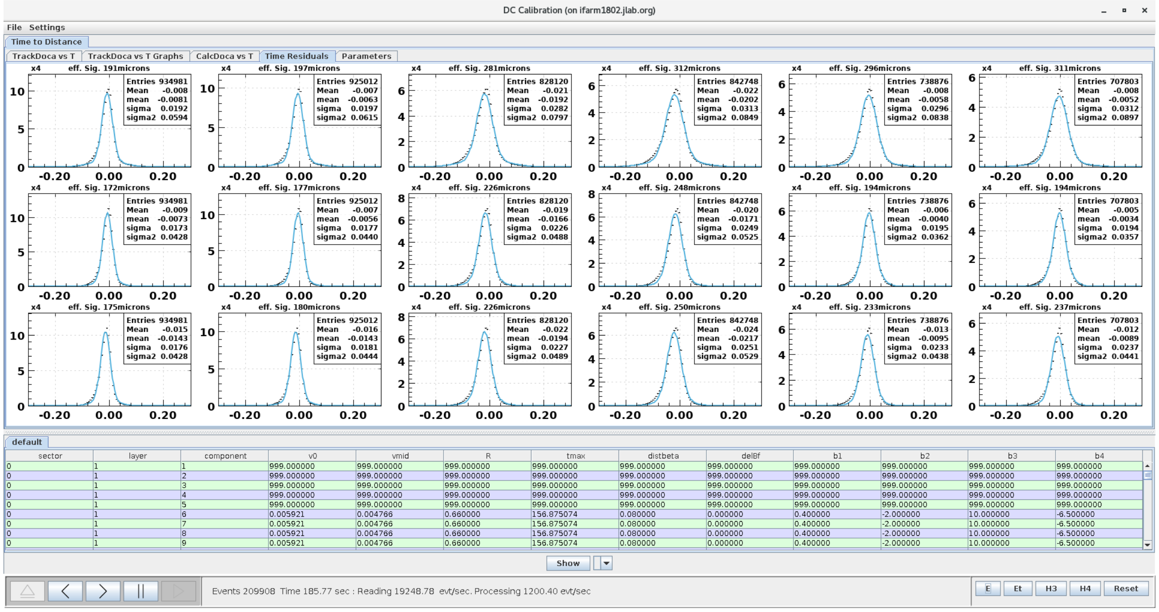

sector	layer	component	v0	vmid	R	tmax	distbeta	delBf	b1	b2	b3	b4
0	1	1	999.000000	999.000000	999.000000	999.000000	999.000000	999.000000	999.000000	999.000000	999.000000	999.000000
0	1	2	999.000000	999.000000	999.000000	999.000000	999.000000	999.000000	999.000000	999.000000	999.000000	999.000000
0	1	3	999.000000	999.000000	999.000000	999.000000	999.000000	999.000000	999.000000	999.000000	999.000000	999.000000
0	1	4	999.000000	999.000000	999.000000	999.000000	999.000000	999.000000	999.000000	999.000000	999.000000	999.000000
0	1	5	999.000000	999.000000	999.000000	999.000000	999.000000	999.000000	999.000000	999.000000	999.000000	999.000000
0	1	6	0.005921	0.004766	0.660000	156.875074	0.080000	0.000000	0.400000	-2.000000	10.000000	-6.500000
0	1	7	0.005921	0.004766	0.660000	156.875074	0.080000	0.000000	0.400000	-2.000000	10.000000	-6.500000
0	1	8	0.005921	0.004766	0.660000	156.875074	0.080000	0.000000	0.400000	-2.000000	10.000000	-6.500000
0	1	9	0.005921	0.004766	0.660000	156.875074	0.080000	0.000000	0.400000	-2.000000	10.000000	-6.500000

```
Events 209908  Time 185.77 sec : Reading 19248.78  evt/sec. Processing 1200.40 evt/sec
```

FIG. 96. Time residual distributions for pass1.

.

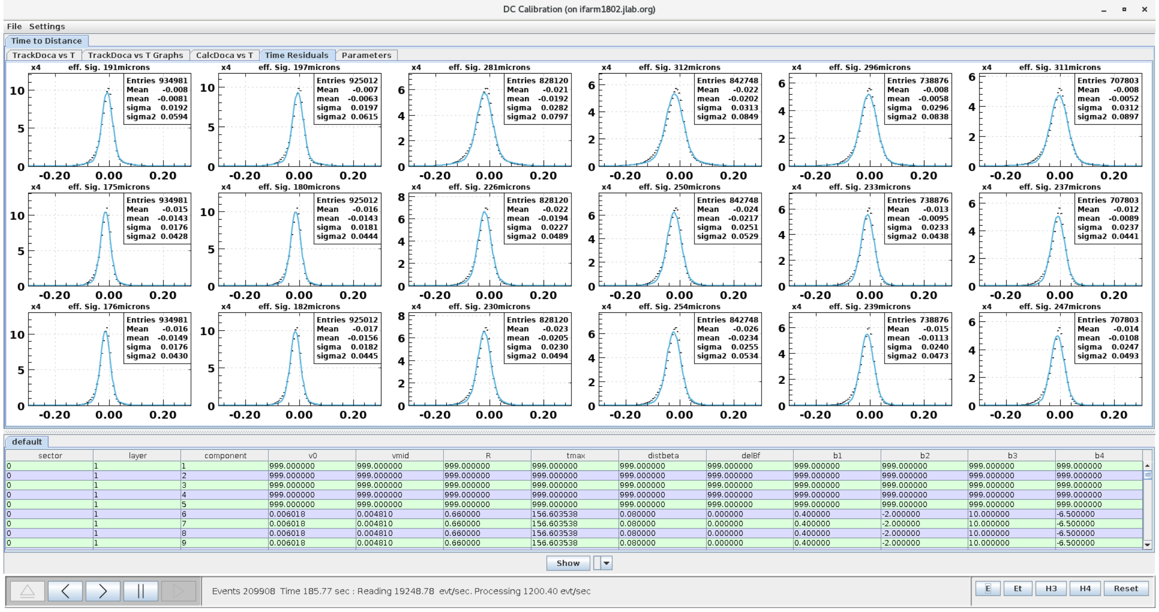

sector	layer	component	v0	vmid	R	tmax	distbeta	delBf	b1	b2	b3	b4
0	1	1	999.000000	999.000000	999.000000	999.000000	999.000000	999.000000	999.000000	999.000000	999.000000	999.000000
0	1	2	999.000000	999.000000	999.000000	999.000000	999.000000	999.000000	999.000000	999.000000	999.000000	999.000000
0	1	3	999.000000	999.000000	999.000000	999.000000	999.000000	999.000000	999.000000	999.000000	999.000000	999.000000
0	1	4	999.000000	999.000000	999.000000	999.000000	999.000000	999.000000	999.000000	999.000000	999.000000	999.000000
0	1	5	999.000000	999.000000	999.000000	999.000000	999.000000	999.000000	999.000000	999.000000	999.000000	999.000000
0	1	6	0.006018	0.004810	0.660000	156.603538	0.080000	0.000000	0.400000	-2.000000	10.000000	-6.500000
0	1	7	0.006018	0.004810	0.660000	156.603538	0.080000	0.000000	0.400000	-2.000000	10.000000	-6.500000
0	1	8	0.006018	0.004810	0.660000	156.603538	0.080000	0.000000	0.400000	-2.000000	10.000000	-6.500000
0	1	9	0.006018	0.004810	0.660000	156.603538	0.080000	0.000000	0.400000	-2.000000	10.000000	-6.500000

```
Events 209908  Time 185.77 sec : Reading 19248.78  evt/sec. Processing 1200.40 evt/sec
```

FIG. 97. Time residual distributions for pass2.

APPENDIX D

ATTEMPT TO IDENTIFY PARTICLES(OWN PID)

This study has done the year 2019 for a few files for $skim8_{ep}$ train using coatjava version 5b.7.8 to get better particle identification. Although, The CLAS12 common analysis note had achieved a more acceptable quality level, which forced me to skip this study.

D.0.1 ELECTRON IDENTIFICATION

For electron identification, the following cut has been used.

- ECAL deposited energy cut- Fig. 98 shows the energy deposited in EC_{inner} as a function of energy deposited in EC_{outer}. A constant signal(see left from the red vertical line in Fig. 98) is produced by high-energy pions, and a cut at 0.03 GeV gets rid of the majority of them.

- Sampling fraction (E_{total}/p) cut- An illustration of the sampling fraction cut as a function of momentum can be found in Fig. 99. There are two hard cuts applied around $\pm 3\sigma$(red horizontal lines) and the $P > 2$ GeV (blue vertical line) region.

- HTCC number of photo-electron cut ($nphe > 2phe$). Fig 100 shows the number of photo-electron distribution fitted with $Fitfunction = Poisson \circledast Gausserror$. The following reasons may explain why this is not exactly fit with Poisson distribution. (Please note that this analysis is based on an old version of coatjava)
  - There were some events that came from clusters two, three, and four
  - The path length is a slightly different event within a single mirror. As a result, Cherenkov's radiation is different.
  - There could be some miscalibration between PMTs

- Veterx cut- Fig. 101 shows the electron vertex distribution.

- PCAL fiducial cuts- PCAL $U > 30$, $30 < V < 390$, $30 < W < 390$ (three independent readout layers) cuts used as in the Fig. 102. Because of the leakage from the shower, this method removes events close to the edge.

- DC Fiducial cut for Region 2-The following geometrical cuts were applied in order to eliminate low rejection efficiency at the edges of the DC.

$$(XS * XS + YS * YS) > r_{cut} * r_{cut}, \tag{256}$$

$$|\phi_s| < \frac{\pi}{3}, \tag{257}$$

where,

$$\begin{aligned} r_{th} &= (S-1)\frac{\pi}{3}, \\ X_S &= \cos(r_{th})X + \sin(r_{th})Y, \\ Y_S &= -\sin(r_{th})X + \cos(r_{th})Y, \\ \phi_s &= \text{atan2}(Y_S, X_S - \frac{r_{cut}}{2}), \end{aligned} \tag{258}$$

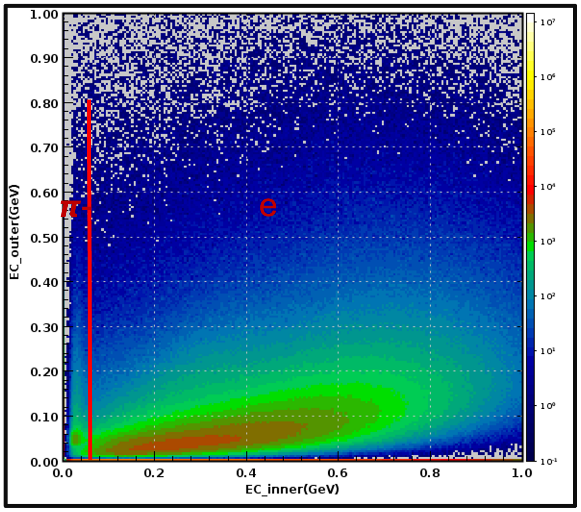

FIG. 98. Deposited energy distribution for EC_{inner} vs. EC_{outer}. The red vertical line represents the cut that was applied (0.03 GeV).

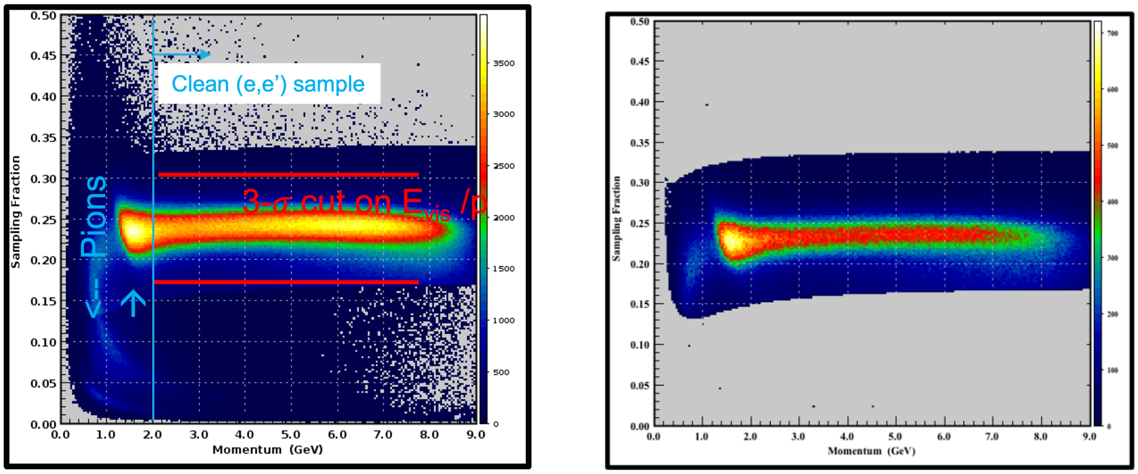

FIG. 99. Sampling fraction as a function of momentum. There is a hard cut for $p > 2$ GeV (blue vertical line) and a hard cut for $\pm 3\sigma$ (red horizontal line) in order to identify a clean electron sample and suppress pion misidentification.

D.0.2 HADRON IDENTIFICATION

For hadron identification following cuts have been used.

- Time of Flight (TOF) distributions- Fig. 103 and Fig. 104 show the distributions of β vs. momentum (p) for both FTOF and CTOF. Note that, the path length and time were used to calculate $\beta = \frac{l}{tof*c}$, which overlapped with the β value in event builder. There are clear signals of proton, kaon, and π^+ and $\beta = 1$ for the positron (see Fig. 103. The following cuts were used to identify the proton in Fig. 103.

$$\beta_1(p) = \frac{\beta(proton)(p) + \beta(deuteron)(p)}{2}, \tag{259}$$

$$\beta_2(p) = \frac{\beta(kaon)(p) + \beta(proton)(p)}{2}, \tag{260}$$

Cut applied $\beta_1(p) < \beta(p) < \beta_2(p)$, where $\beta(kaon) = \frac{p}{\sqrt{(p^2 + m_{kaon}^2)}}$, similarly for proton and deuterium. As shown in Fig. 103 and Fig. 104 (right), proton signals are extracted

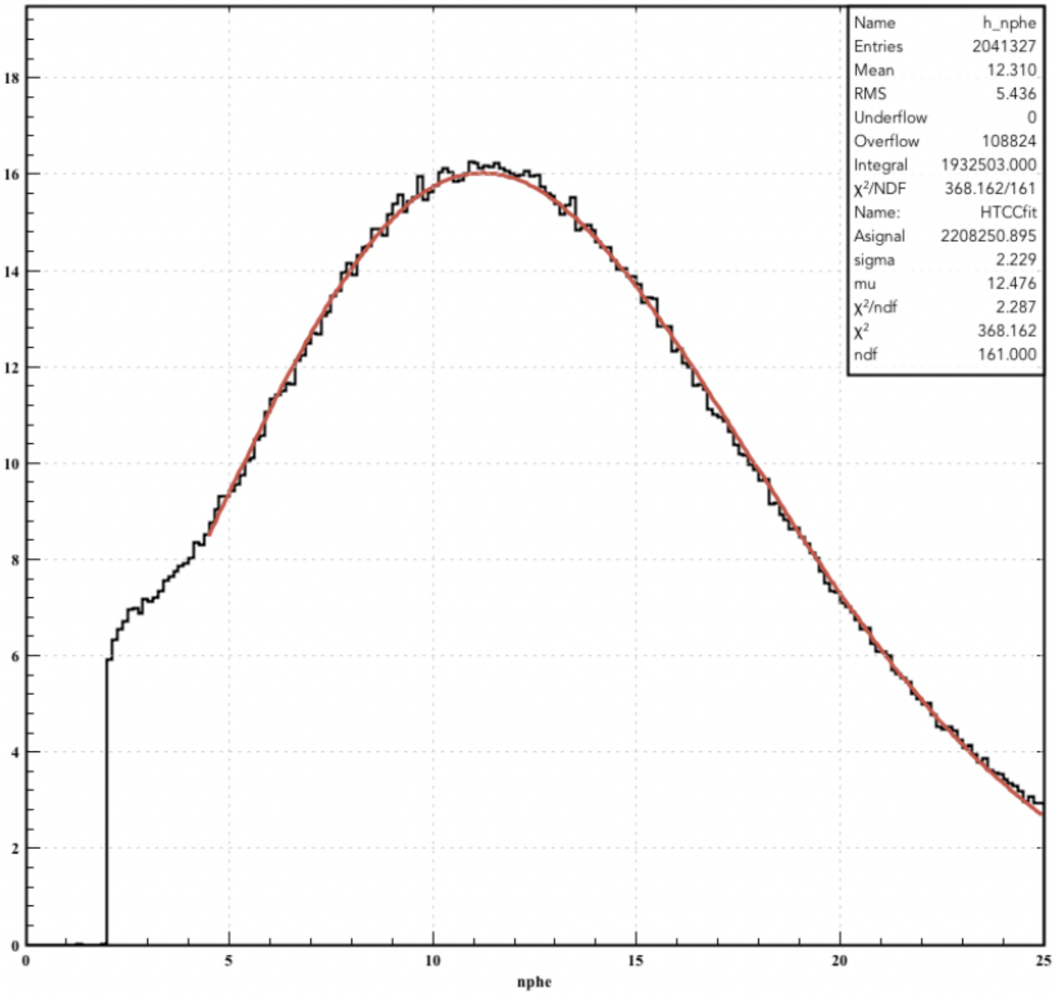

FIG. 100. Number of photo-electron in HTCC. $Nphe > 2$ cut has been used to identify the electron. The red line is the $Fitfunction = Poisson \circledast Gausserror$

using the cut. The accidentals from pions and protons are clearly visible in Fig. 103. This is due to the fact that there are several beam bunches separated by 2 ns.

We could not work on pion identifications, so we opted to identify π^- where all events that did not satisfy the electron and used $\beta(p)) > \beta_2(p)$ for the π^+ identifications.

- DC fiducial cuts applied for the positive particles shown in Fig. 105.

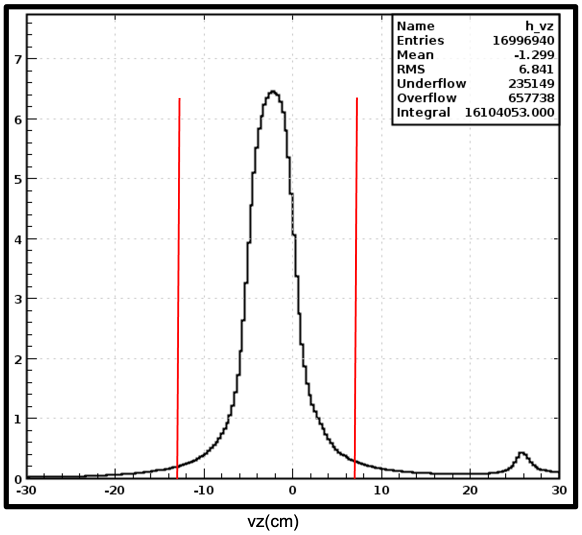

FIG. 101. Electron v_z distribution. The red vertical lines represent cut -13 cm $< v_z <$ 7 cm.

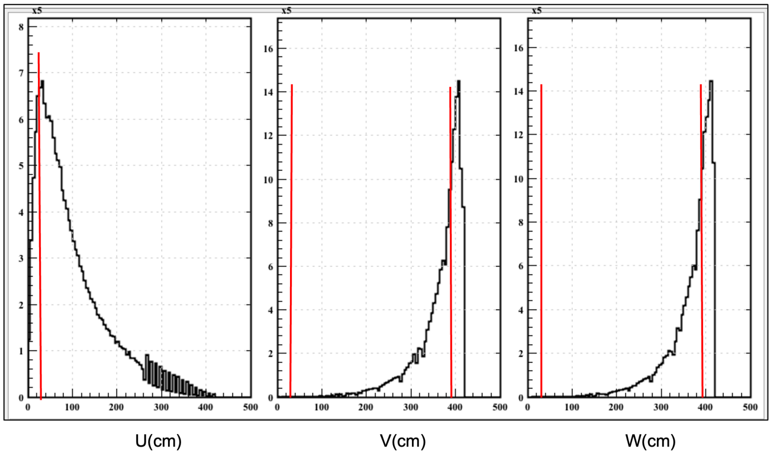

FIG. 102. PCAL fiducial cuts from U, V, and W individual layers. The red vertical lines represent $U >$ 30 cm, 30 cm $< V <$390 cm, and 30 cm $< W <$ 390 cm.

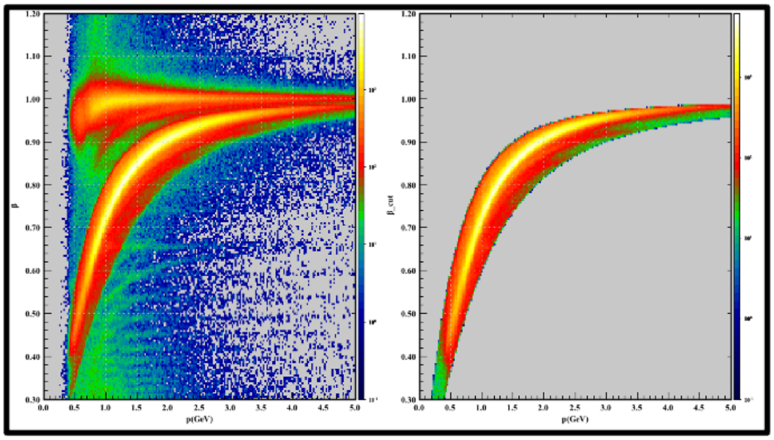

FIG. 103. β vs. p distribution for FTOF (left) and selection of proton (right).

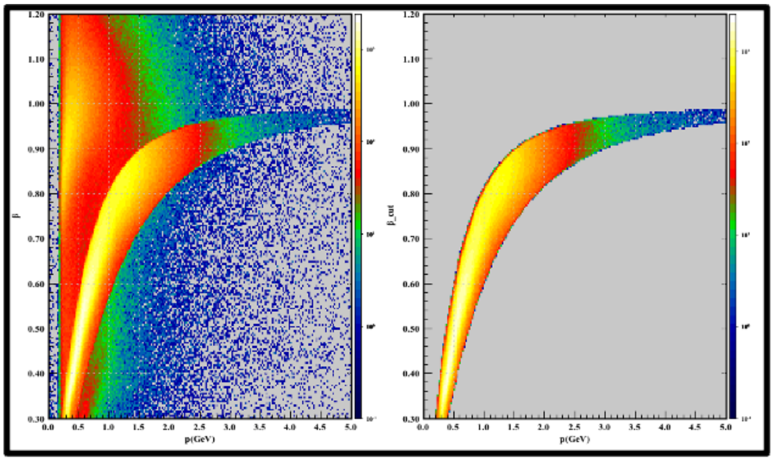

FIG. 104. β vs. p distribution for CTOF (left) and selection of proton (right).

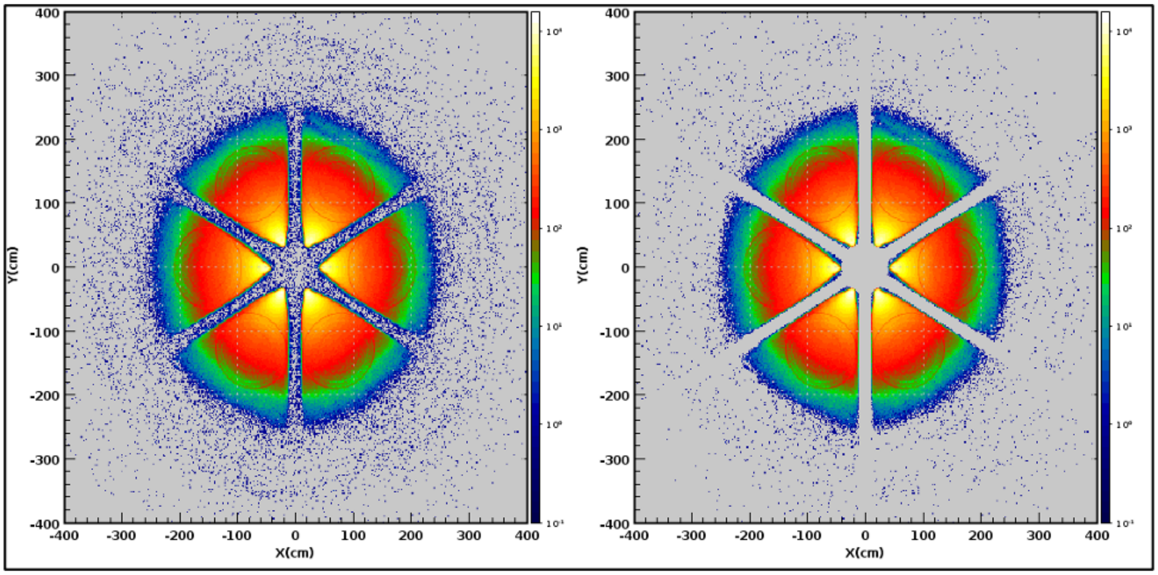

FIG. 105. DC region 2 for positive particles before (left) and after (right) fiducial cuts.

APPENDIX E

CHISQ CALCULATION FOR CTOF HIT

Helix Constant can be defined as follows (see Eq. (261))

$$r_{\perp}(\text{cm}) = \frac{\sqrt{P_X^2 + P_Y^2} \times 10^2(\text{cm/m})}{eB_{field} \times \text{speed-of-light(Gm/s)}}. \tag{261}$$

The actual magnitude of the charge is subsumed into the units of momentum (GeV/c). Velocity can be written as:

$$\vec{V}_V = \text{speed\_of\_light(cm/ns)} \times \frac{\vec{P}_{Miss}}{\sqrt{(P_{Miss}^2 + m_\pi^2)}}. \tag{262}$$

Then we can write angular velocity $\omega = \frac{V_\perp}{r_\perp}$. The helix is either clockwise or counter-clockwise, looking downstream, depending on the pion charge. For a $\pi+$, with B-field pointing in $+Z$ direction (downstream) the omega vector is in $-Z$ direction and $\frac{dv}{dt} = \omega \times v$.

Try $-$ for pim, $+$ for pip

- $\omega_{\pi^-} = -\frac{V_\perp}{r_\perp}$,
- $\omega_{\pi^+,p} = +\frac{V_\perp}{r_\perp}$,

The velocity equation is

$$\begin{aligned} V_x &= V_\perp \cos(\omega t + \delta), \\ V_y &= V_\perp \sin(\omega t + \delta). \end{aligned} \tag{263}$$

After integration

$$\begin{aligned} x &= x_0 + \frac{V_\perp}{\omega} \sin(\omega t + \delta), \\ y &= y_0 - \frac{V_\perp}{\omega} \cos(\omega t + \delta). \end{aligned} \tag{264}$$

At the vertex $t = 0$,

$$V_x(0) = V_{v,x} = V_\perp \cos(\delta), \tag{265}$$

$$V_y(0) = V_{v,y} = V_\perp \sin(\delta), \tag{266}$$

$$\boxed{\delta = atan2(V_{v,y}, V_{v,x})}. \tag{267}$$

Position of the vertex

$$x_v = x_0 + \frac{V_\perp}{\omega}\sin(\delta), \tag{268}$$

$$y_v = y_0 - \frac{V_\perp}{\omega}\cos(\delta). \tag{269}$$

Therefore x_0 and y_0

$$x_0 = x_v - \frac{V_\perp}{\omega}\sin(\delta), \tag{270}$$

$$y_0 = y_v + \frac{V_\perp}{\omega}\cos(\delta). \tag{271}$$

E.0.1 CALCULATE T

Consider the following condition and continue to find the time interval T from the vertex to the CTOF.

$$\begin{aligned} r_{CTOF}^2 &= x^2 + y^2, \\ &= \Big(x_0 + \frac{V_\perp}{\omega}\sin(\omega T + \delta)\Big)^2 + \Big(y_0 - \frac{V_\perp}{\omega}\cos(\omega T + \delta)\Big)^2, \\ &= x_0^2 + y_0^2 + \frac{V_\perp^2}{\omega^2} + 2x_0\frac{V_\perp}{\omega}\sin(\omega T + \delta) - 2y_0\frac{V_\perp}{\omega}\cos(\omega T + \delta). \end{aligned} \tag{272}$$

By defining $r_0^2 = x_0^2 + y_0^2$:

$$r_{CTOF}^2 = r_0^2 + \frac{V_\perp^2}{\omega^2} + 2r_0\frac{V_\perp}{\omega}\left[\frac{x_0}{r_0}\sin(\omega T + \delta) - \frac{y_0}{r_0}\cos(\omega T + \delta)\right]. \tag{273}$$

We chose our testing 4 Define $\delta_0 = \text{atan2}(y_0, x_0)$:

$$\begin{aligned} \frac{r_{CTOF}^2 - r_0^2 - \frac{V_\perp^2}{\omega}}{2r_0\frac{V_\perp}{\omega}} &= \cos(\delta_0)\sin(\omega T + \delta) - \sin(\delta_0)\cos(\omega T + \delta) \\ &= \sin(\omega T + \delta - \delta_0) \\ &= \sin(\omega T)\cos(\delta - \delta_0) + \cos(\omega T)\sin(\delta - \delta_0), \end{aligned} \tag{274}$$

$$\begin{aligned} \cos(\delta - \delta_0) = &= \cos(\delta)\cos(\delta_0) + \sin(\delta)\sin(\delta_0) \\ &= \frac{V_{v,x}}{V_\perp}\frac{x_0}{r_0} + \frac{V_{v,y}}{V_\perp}\frac{y_0}{r_0} \\ &= \frac{1}{r_0 V_\perp}[x_0 V_{v,x} + y_0 V_{v,y}], \end{aligned} \tag{275}$$

$$\begin{aligned}\sin(\delta-\delta_0) &= \sin(\delta)\cos(\delta_0) - cos(\delta)\sin(\delta_0) \\ &= \frac{V_{v,y}}{V_\perp}\frac{x_0}{r0} - \frac{V_{v,x}}{V_\perp}\frac{y_0}{r_0} \\ &= \frac{1}{r_0 V_\perp}[x_0 V_{v,y} - y_0 V_{v,x}],\end{aligned} \tag{276}$$

$$\delta-\delta_0 = atan2(\sin(\delta-\delta_0), \cos(\delta-\delta_0)). \tag{277}$$

Corrected formula

$$\omega T + \delta - \delta_0 = asin\left[\frac{r_{CTOF}^2 - r_0^2 - \frac{V_\perp^2}{\omega^2}}{2r_0(V_T/\omega)}\right] = \Theta_T, \tag{278}$$

$$\boxed{T = \frac{\Theta_T + \delta_0 - \delta}{\omega}}. \tag{279}$$

E.0.2 PREDICTED HIT COORDINATES AT CTOF

The projected x, and y hit coordinates at CTOF are

$$\begin{aligned}x_{\text{proj}} = x(T) &= x_0 + \frac{V_\perp}{\omega}\sin(\omega T + \delta) \\ &= x_v - \frac{V_\perp}{\omega}[\sin\delta - \sin(\omega T + \delta)] \\ &= x_v - \frac{V_\perp}{\omega}[\sin\delta - \sin(\Theta_T + \delta_0)].\end{aligned} \tag{280}$$

Substituted x_0 from the equation $x_0 = x_v + \frac{V_\perp}{\omega}\sin(\delta)$ Similarly for y_{proj},

$$\begin{aligned}y_{\text{proj}} = y(T) &= y_0 - \frac{V_\perp}{\omega}\cos(\omega T + \delta), \\ &= y_0 - \frac{V_\perp}{\omega}\cos(\Theta_T + \delta_0') \\ &= y_v + \frac{V_\perp}{\omega}(\cos(\delta) + \cos(\Theta_T + \delta_0)).\end{aligned} \tag{281}$$

Substituted y_0 from the equation $y_0 = y_v + \frac{V_\perp}{\omega}\cos(\delta)$, The projected ϕ_{CTOF} value is

$$\phi_{\text{CTOF}}^{\text{proj}} = \text{atan2}(y_{\text{proj}}, x_{\text{proj}}). \tag{282}$$

APPENDIX F

NORMALIZATION CONSTANTS CALCULATION FOR THE CD

This calculation shows only for the pi-minus 3-fold case. It is also possible to use this method to find the constants for the 4-fold case. To begin, define the sum of the exclusive and inclusive regions $[-0.05, 0.05]$ and $[0.19, 0.29]$ separately for data and exclusive simulation and inclusive simulation.

D-Data
S-Simulation
exc- exclusive
inc- inclusive

$$D_{exc} = \sum_{[-0.05,0.05]} h - data - 3 - fold, \tag{283}$$

$$D_{inc} = \sum_{[0.19,0.29]} h - data - 3 - fold, \tag{284}$$

$$S^{exc}_{exc} = \sum_{[-0.05,0.05]} h - simu - exc - 3 - fold, \tag{285}$$

$$S^{inc}_{exc} = \sum_{[0.19,0.29]} h - simu - exc - 3 - fold, \tag{286}$$

$$S^{exc}_{inc} = \sum_{[-0.05,0.05]} h - simu - inc - 3 - fold, \tag{287}$$

$$S^{inc}_{inc} = \sum_{[0.19,0.29]} h - simu - inc - 3 - fold, \tag{288}$$

$$D_{exc} = A \cdot S^{exc}_{exc} + B \cdot S^{inc}_{exe}, \tag{289}$$

$$D_{inc} = A \cdot S^{exc}_{inc} + B \cdot S^{inc}_{inc}, \tag{290}$$

$$\begin{pmatrix} D_{exc} \\ D_{inc} \end{pmatrix} = \begin{pmatrix} S^{exc}_{exc} & S^{inc}_{exc} \\ S^{exc}_{inc} & S^{inc}_{inc} \end{pmatrix} \begin{pmatrix} A \\ B \end{pmatrix}. \tag{291}$$

By solving Eq. (291) can be used to solve for A and B.

APPENDIX G

EXTRACTED COEFFICIENT AND ERROR

$\bar{A}_i \pm \sqrt{(\left\langle \delta\overline{A}_i \delta\overline{A}_i \right\rangle)}$ for Bin $(Q^2, x_B, t_{min} - t)$		
Bin [0 0 0]	Bin [1 0 0]	Bin[2 0 0]
$6.15295e - 07 \pm 5.80851e - 08$	$1.2764e - 06 \pm 1.24235e - 07$	$1.93345e - 06 \pm 2.81905e - 07$
$8.32049e - 07 \pm 1.40463e - 08$	$1.26415e - 06 \pm 2.90111e - 08$	$1.28971e - 06 \pm 5.97161e - 08$
$7.36893e - 07 \pm -3.49781e - 08$	$1.2019e - 06 \pm 6.66171e - 08$	$1.26487e - 06 \pm 1.30552e - 07$
$8.2059e - 08 \pm 1.31766e - 08$	$2.63573e - 07 \pm 2.36743e - 08$	$2.25046e - 07 \pm 3.96187e - 08$
$-3.41522e - 06 \pm 9.05685e - 08$	$-5.44227e - 06 \pm 1.78223e - 07$	$-5.57248e - 06 \pm 3.15018e - 07$
$4.55019e - 07 \pm 9.60227e - 08$	$5.82633e - 07 \pm 1.82409e - 07$	$1.50811e - 06 \pm 2.98421e - 07$
$7.25618e - 08 \pm 8.30877e - 08$	$1.84654e - 07 \pm 1.63291e - 07$	$1.2422e - 06 \pm 3.85241e - 07$
$1.14666e - 07 \pm 6.13557e - 08$	$-1.29507e - 08 \pm 1.26384e - 07$	$2.71497e - 07 \pm 2.26059e - 07$
$1.92335e - 08 \pm 5.76707e - 08$	$1.44672e - 07 \pm 9.83969e - 08$	$9.02406e - 07 \pm 2.05439e - 07$
$-3.63669e - 07 \pm 4.7118e - 08$	$-4.1546e - 08 \pm 9.69383e - 08$	$-7.61213e - 07 \pm 1.58991e - 07$
$7.00389e - 08 \pm 1.98872e - 08$	$4.52785e - 07 \pm 3.54783e - 08$	$4.93832e - 07 \pm 7.05321e - 08$

$\bar{A}_i \pm \sqrt{(\left\langle \delta\overline{A}_i\delta\overline{A}_i \right\rangle)}$ for Bin $(Q^2, x_B, t_{min} - t)$		
Bin [0 1 0]	Bin [1 1 0]	Bin[2 1 1]
$3.21528e - 06 \pm 1.17157e - 07$	$4.59164e - 06 \pm 1.57771e - 07$	$3.05119e - 06 \pm 1.60379e - 07$
$1.63886e - 06 \pm 2.89745e - 08$	$2.24993e - 06 \pm 4.15949e - 08$	$7.85963e - 07 \pm 3.01937e - 08$
$2.73551e - 06 \pm 6.65504e - 08$	$3.54184e - 06 \pm 9.97252e - 08$	$9.03586e - 07 \pm 7.35204e - 08$
$2.40605e - 07 \pm 1.43537e - 08$	$3.63151e - 07 \pm 2.47754e - 08$	$6.2942e - 08 \pm 2.34828e - 08$
$-5.20947e - 06 \pm 1.12799e - 07$	$-8.46867e - 06 \pm 1.94478e - 07$	$-3.83465e - 06 \pm 1.73018e - 07$
$1.78356e - 06 \pm 1.47681e - 07$	$3.81541e - 06 \pm 2.22115e - 07$	$1.7331e - 06 \pm 1.85968e - 07$
$2.47589e - 06 \pm 1.55458e - 07$	$2.45655e - 06 \pm 2.20938e - 07$	$1.82335e - 06 \pm 2.12843e - 07$
$8.20701e - 08 \pm 9.5669e - 08$	$5.19268e - 07 \pm 1.47381e - 07$	$-1.16702e - 07 \pm 1.44966e - 07$
$2.4793e - 06 \pm 1.23265e - 07$	$2.31871e - 06 \pm 1.70535e - 07$	$-2.09974e - 09 \pm 1.15058e - 07$
$1.18515e - 07 \pm 9.34216e - 08$	$-1.30512e - 07 \pm 1.36258e - 07$	$7.38911e - 08 \pm 1.052e - 07$
$9.39125e - 08 \pm 2.40514e - 08$	$1.48421e - 07 \pm 3.71558e - 08$	$1.02895e - 07 \pm 3.49606e - 08$

$\bar{A}_i \pm \sqrt{(\left\langle \delta\overline{A}_i\delta\overline{A}_i \right\rangle)}$ for Bin $(Q^2, x_B, t_{min} - t)$		
Bin [0 2 0]	Bin [1 2 0]	Bin[2 2 0]
$7.33358e - 06 \pm 1.66911e - 07$	$9.59915e - 06 \pm 1.86826e - 07$	$3.69625e - 06 \pm 1.28058e - 07$
$1.92547e - 06 \pm 3.53229e - 08$	$2.53977e - 06 \pm 4.35796e - 08$	$9.0116e - 07 \pm 3.1487e - 08$
$3.40414e - 06 \pm 7.62901e - 08$	$4.40622e - 06 \pm 1.00577e - 07$	$1.50971e - 06 \pm 7.69231e - 08$
$-2.50045e - 08 \pm 2.26511e - 08$	$3.10407e - 07 \pm 2.99982e - 08$	$7.58997e - 08 \pm 2.1049e - 08$
$2.27352e - 07 \pm 1.67637e - 07$	$-6.52442e - 06 \pm 1.94623e - 07$	$-4.23163e - 06 \pm 1.58433e - 07$
$7.49271e - 06 \pm 2.60788e - 07$	$1.03098e - 05 \pm 3.21389e - 07$	$2.65342e - 06 \pm 2.02806e - 07$
$4.66162e - 06 \pm 2.18878e - 07$	$2.79011e - 06 \pm 2.38992e - 07$	$1.05361e - 06 \pm 1.61448e - 07$
$3.59321e - 08 \pm 1.56084e - 07$	$-4.90775e - 07 \pm 2.10279e - 07$	$-4.25979e - 07 \pm 1.54196e - 07$
$2.70155e - 06 \pm 1.45763e - 07$	$3.20185e - 06 \pm 1.82736e - 07$	$9.61432e - 07 \pm 1.25537e - 07$
$2.55114e - 07 \pm 1.22628e - 07$	$-3.64158e - 07 \pm 1.7067e - 07$	$3.28516e - 08 \pm 1.22604e - 07$
$-4.49313e - 07 \pm 3.04978e - 08$	$-2.09384e - 08 \pm 3.85837e - 08$	$-3.02571e - 09 \pm 2.96423e - 08$

VITA

Dilini Lakshani Bulumulla
Department of Physics
Old Dominion University
Norfolk, VA 23529

EDUCATION:

- 2017-2023 Ph.D. Candidate (Physics), Old Dominion University, Norfolk, Virginia, USA.
- 2017 Master of Science (Physics), Old Dominion University, Norfolk, Virginia, USA.
- 2014 Bachelor of Science (Physics), University of Peradeniya, Sri Lanka.

AWARDS:

- Academic Excellence Award (University of Peradeniya) -May 2014

Typeset using LaTeX.